Multiscale Models of VEGF-mediated Molecular Signaling Pathways in Intratumoral Angiogenesis

by

Harsh Vardhan Jain

A dissertation submitted in partial fulfillment
of the requirements for the degree of
Doctor of Philosophy
(Mathematics)
in The University of Michigan
2008

Doctoral Committee:

Associate Professor Trachette Levon Jackson, Chair
Professor Robert Krasny
Professor Jacques Eduardo Nör
Assistant Professor Daniel Barclay Forger
Professor Helen Byrne, The University of Nottingham

To my parents.

ACKNOWLEDGEMENTS

I would like to express the deepest appreciation to my advisor, Professor Trachette Jackson, without whose guidance and persistent help this dissertation would not have been possible. Professor Jackson epitomizes all the qualities that one seeks from ones advisor, but that are rarely found in a single person. I also owe a huge thank you to Professor Jacques Nor for the tremendous opportunity to work on this project, and for the immense support and encouragement he has provided throughout. I am grateful to my committee members, Professor Daniel Forger, Professor Robert Krasny and Professor Helen Byrne for their exceedingly valuable comments and ideas. I would also like to express my gratitude to Professor Howard Levine for his support and guidance in conducting my research.

I am grateful to Dr Sukumar Natarajan and Dr Pinaki Biswas for offering me personal and professional advice along the way. I would like to thank my sisters for their encouragement and patience. I would also like to thank my wife who was there for me at every step of the way.

TABLE OF CONTENTS

LIST OF FIGURES

Figure

LIST OF TABLES

Table

LIST OF APPENDICES

Appendix

CHAPTER I

Introduction

Cancer accounts for nearly one-quarter of deaths in the United States, exceeded only by heart disease. In 2005, there were over half a million cancer deaths in the US. It is estimated that about 1.4 million new cases of cancer will be diagnosed in 2008. Although cancer death rates have declined since the 1990s, the rate of decline currently remains comparatively low; at 2.6% for men and 1.8% for women[1].

Cancer is a distinct type of genetic disease in which a cell must acquire a number of mutations in order to transform from a normal to a cancerous phenotype. In a seminal review published in 2000, Hanahan and Weinberg (49) characterized six hallmarks of cancer. These include self-sufficiency in growth signal, insensitivity to anti-growth signals, evading apoptosis, limitless replicative potential, sustained angiogenesis and invasion and metastasis. A solid tumor must undergo a phase of sustained angiogenesis, in order to progress from a relatively benign stage to an invasive and potentially fatal phenotype. Conversely, without a vascular system, tumors can not grow beyond a critical size or metastasize to another organ (19). Therefore, the field of angiogenesis continues to generate intense interest, in an effort to develop and maximize the effects of anti-angiogenic therapies.

Tumor-induced angiogenesis is a highly complex process operating on several time

[1]Data taken from Cancer Facts and Figures 2008 report by the American Cancer Society.

and length scales. It involves an intricate interplay between biochemical and biomechanical processes. At the biochemical level, there is transcription and release of pro-angiogenic factors by the tumor cells, their uptake by vascular endothelial cells (ECs) lining neighboring vasculature, the activation of cell surface receptors and the myriad downstream signalling pathways initiated as a result. These translate into specific behavior by the cells, such as proliferation, migration, differentiation, gene transcription, and the release of factors further regulation angiogenesis. Biomechanical mechanisms such as cell-cell interactions, cell-matrix interactions, result in cooperative interactions of the cells with their micro-environments and play a key role in regulating angiogenesis.

Experimental investigations into the processes governing angiogenesis have been carried out in earnest over the last few decades and have resulted in the accumulation of a large volume of data. This information exists at various levels; at the tissue level, where tumors grow and vascular networks are formed, at the cellular level, where cell behavior such as migration, proliferation, survival, differentiation are studied, and at the molecular level, where pro- and anti-angiogenic molecules and their downstream signalling pathways are investigated. The integration of this information with the aim of developing anti-cancer and anti-angiogenic therapies is a major challenge facing the scientific community today. Mathematical modelling provides a powerful tool in elucidating the mechanisms of interactions between tumor and endothelial cells with the host environment, while taking into account the mechanical and chemical aspects of angiogenesis. Consequently, it has an enormous potential in the development and testing of therapeutic strategies targeting angiogenesis.

The research conducted for this dissertation concentrates on the development of a multiscale model of tumor-induced angiogenesis, with particular emphasis on in-

corporating key molecular signalling pathways at the sub-cellular level, and the biochemical interactions between pro-angiogenic molecules such as VEGF and CXCL8 and endothelial cells, that regulate these pathways. The model then integrates the sub-cellular and cellular level responses into a tissue level behavior. The therapeutic potential of specific proteins and chemokines is also investigated as possible targets of anti-angiogenic therapy.

The dissertation is organized in the following manner. Chapter II provides a background to the biology of tumor-induced angiogenesis. The importance of angiogenesis in the progression of a tumor from a benign avascular stage to a malignant vascularized cancer is highlighted. The significance of VEGF, CXCL8, and extracellular matrix in promoting and regulating angiogenesis is discussed in particular.

In Chapter III, we present a survey of existing mathematical techniques used to model various aspects of angiogenesis. These models are divided into two categories; continuum models that treat endothelial cell density and chemokine concentrations as continuous variables, that evolve according to reaction-diffusion systems, and discrete, cell-based models that track the movements of individual cells or sprout tips. The strengths and limitations of these models are discussed. The need for incorporation of greater biological and biochemical detail in order to keep up with the current state of knowledge in the field forms the motivation for our choice of a delay differential equation model of angiogenesis.

VEGF has been the most studied pro-angiogenic chemokine. In Chapter IV, we present a detailed molecular model of the uptake of VEGF by its cell surface receptors. We begin with a biological background of the VEGF molecule and its transmembrane receptor tyrosine kinases. This is followed by an overview of the mathematical models of angiogenesis that have focussed on the role of chemokines

such as VEGF. However, these models make a number of simplifying assumptions when dealing with VEGF-endothelial cell interactions that can potentially effect simulation results. We present a detailed mathematical investigation of the validity of these assumptions, while presenting our own model of VEGF-VEGF receptor interactions. In particular, the validity of the quasi steady state assumption in the context of VEGF binding to its cell surface receptors is investigated.

Recent experiments show that VEGF is the crucial mediator of downstream events that ultimately lead to enhanced endothelial cell survival and increased vascular density within many tumors. The newly discovered pathway involves up-regulation of the anti-apoptotic protein Bcl-2, which in turn leads to increased production of CXCL8. The VEGF - Bcl- 2 - CXCL8 pathway suggests new targets for the development of anti-angiogenic strategies. In Chapter V, we present and validate a mathematical model designed to predict the effect of the therapeutic blockage of VEGF, CXCL8, and Bcl-2 at different stages of tumor progression. Specifically, a system of delay-differential equations is derived to describe the temporal dynamics of the cells, growth factors and chemokines involved in tumor induced angiogenesis. Techniques developed in Chapter IV to model VEGF-receptor interaction are applied here.

Endothelial cell apoptosis plays a critical role in the disruption of blood vessels mediated by natural inhibitors of angiogenesis and by anti-vascular drugs. In Chapter VI, we apply the model of angiogenesis developed in Chapter V, to answer a critical question that arises with regards to the evaluation of these anti-angiogenic agents. What is the minimum percentage requirement of vascular endothelial cell apoptosis for microvascular regression? We adapt the model developed in the previous chapter so that it represents the experimental system designed to answer this question. It

is then used to evaluate experimentally inaccessible ratios. The combined use of biological experimentation with our mathematical modelling highlights the flexibility and applicability of our modelling framework.

Pro- and anti- apoptotic proteins in the Bcl family, such as Bad and Bcl-2, are key regulators of programmed cell death. It is the interaction between these molecules that determine cellular response to apoptotic signals, making them attractive targets for therapeutic intervention. In recent experiments designed to study intra-tumoral angiogenesis, Bcl-2 up-regulation in endothelial cells was shown to be a critical mediator of vascular development. In Chapter VII, we extend the model of intra-tumoral angiogenesis developed in Chapter V to explicitly incorporate the cellular response to variations in pro- and anti-apoptotic proteins in the Bcl family, as well as the administration of specific anti-angiogenic therapy in the form of a small molecule inhibitor BL193 targeted against the Bcl-2 molecule. The model is validated by comparing its predictions to in vitro experimental data. Finally, a sensitivity analysis carried out on drug design parameters reveals that developing a better inhibitor of Bcl-2 has greater therapeutic potential than improving its permeability across the cell membrane.

Thus far, we have concentrated on a delay differential equation model of tumor angiogenesis, and assumed spatial homogeneity. However, the vascular structure within a tumor is highly unorganized and spatially heterogeneous, and it would be instructive to extend our model to include spatial variations in cell densities, chemical concentrations and vascular development. To this end, in Chapter VIII we develop a hybrid model of tumor-induced angiogenesis, based on the theory of reinforced random walks. We include in our model, the chemotactic response of endothelial cells to VEGF bound to cell-surface receptors, rather than approximating this as a function

of free VEGF concentrations. We also propose a novel and more biologically reasonable functional form for the chemotactic sensitivity of cells, than those currently used. We begin with the motion of a single endothelial cell under the influence of a gradient of VEGF. Biologically observed phenomena such as the ability of ECs to sense a chemical gradient as low as 1% across their lengths and their resulting polarization and movement is captured by our model. To our knowledge, this is the first instance of the inclusion of this level of molecular detail in a spatial model of tumor angiogenesis. Later, we modify the motion of a single endothelial cell to model the capillary network formation under the influence of VEGF. Events such as branching and anastomoses, which are observed to occur in vivo, are incorporated explicitly in the model. Empirically observed proliferative regions behind developing sprout tips match those in our simulations, thereby validating our model. This multiscale model is a first step in incorporating cellular and sub-cellular events in hybrid models of tumor angiogenesis, in an effort to understanding relationship between intra-cellular molecular pathways and multicellular behavior.

We conclude with a summary chapter which discusses the impact of this research and proposes future directions for the extension of our model.

CHAPTER II

Biological Background to Angiogenesis

2.1 Stages of Tumor Growth

The growth of solid tumors can be characterized as having three distinct stages; an avascular stage of diffusion limited growth, a phase of blood vessel growth, and a vascularized stage where the tumor cells may become highly invasive and metastatic (Figure 2.1). In the first stage, solid tumors begin as avascular spheroids, and rely on diffusion for the supply of oxygen and nutrients, as well as waste product removal from neighboring vessels for growth. As they grow, nutrient requirements of the tumor cells increase and the flux of nutrients through the tumor surface is unable to meet these demands. Consequently, the interior of these spheroids becomes progressively lacking in oxygen (hypoxic), and in glucose (hypoglycemic). This results in the formation of a necrotic core, and the tumor reaches a steady state size of 1-3 mm in diameter. This may be termed as the avascular growth stage, and is diffusion limited (63; 84).

Sustained tumor growth requires an adequate supply of nutrients and an effective means of the removal of metabolic wastes. This need is met by the establishment of a blood supply to the tumor, which the tumor cells may accomplish in a variety of ways. For instance, the tumor cells may themselves grow around existing vessels,

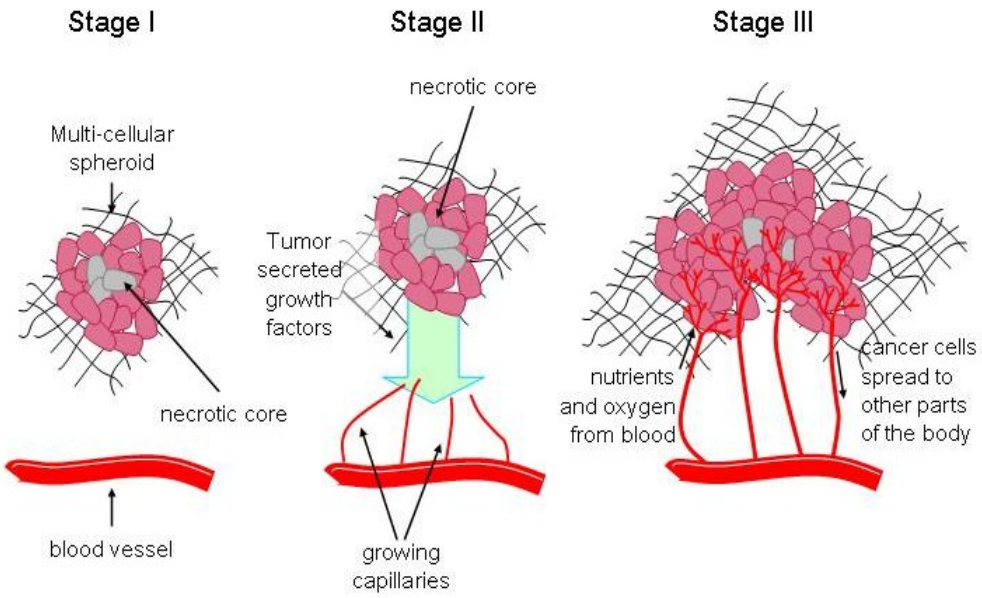

Figure 2.1: Figure showing the cascade of events leading to intra-tumoral angiogenesis adapted from (57)

forming a perivascular cuff in a process known as vessel co-option (8). Alternatively, extra-cellular matrix-rich vascular channels may develop, that lack endothelial cells, but contain circulating red blood cells. This is known as vascular mimicry (124). Circulating endothelial cell precursors derived from the bone marrow may also contribute to vascular development within the tumor (109). Frequently, the tumor will stimulate new blood vessel growth from existing vasculature, in a process known as angiogenesis, described in greater detail below.

Often, in response to the hypoxia, the tumor cells begin to secrete a variety of polypeptidic angiogenic factors, such as such as Vascular Endothelial Growth Factor (VEGF) and basic Fibroblast Growth Factor (bFGF) (135). These factors diffuse from the tumor to nearby vessels, and result in the activation of endothelial cells (ECs) lining vessel walls. The vasculature surrounding the tumor undergoes the angiogenic switch. At first, vascular permeability increases, resulting in extravascular

deposition of fibrin. This is followed by the removal of pericytes that comprise the vessel wall. Next, basement membrane and extra cellular matrix (ECM) are degraded by proteases such as matrix metalloproteinases. New matrix may be laid down, and existing ECM remodelled to facilitate the migration and proliferation of the ECs. This is aided by the presence of growth factors sequestered in the matrix and released due to its degradation, or released by the tumor cells. The ECs will migrate chemotactically up the gradient of the growth factors, towards the tumor. After sufficient division, the ECs are able to organize themselves into a monolayer and form tube like structures or the capillary lumen. Neighboring capillary sprouts may fuse together (anastomosis) resulting in the circulation of blood. The immature vessels may further branch or fuse creating a complex vascular network, that will eventually reach and penetrate the tumor. The process of sprouting is followed by a phase of maturation in which cell proliferation is inhibited, and migration ceases. Pericytes or smooth muscle cells are recruited to form the basement membrane and vessel walls. Vessels uncovered by pericytes regress. This process of vessel maturation is controlled by the angiopoietin/Tie system (84; 109; 124).

Angiogenesis results in the vascularization of the spheroid. Thus the tumor has established an effective means for the supply of nutrients for growth of the tumor cells, and waste product removal. The newly formed vasculature is also a route for the tumor cells to spread to other parts of the body in a process known as metastasis (84). Angiogenesis is thus a crucial step in the progression of cancer, and a better understanding of the processes which control it is vital for the development of effective anti-tumor therapy. In the sections that follow, the principle aspects of tumor angiogenesis are discussed in greater detail.

2.2 The Role of VEGF in Angiogenesis

The most common angiogenic factor released by tumor cells is Vascular Endothelial Growth Factor (VEGF). VEGF is the most crucial regulator of angiogenesis and is highly up-regulated in most human cancers (37; 96; 106; 109; 124). As mentioned earlier, oxygen tension plays a key role in the regulation of VEGF gene expression. Briefly, oxygen promotes the hydroxylation of the hypoxia-inducible factor (HIF-1α), which leads to its eventual proteosomal degradation. However, under conditions of hypoxia, this fails to occur, and there is a resultant build up in HIF-1α levels. HIF-1α is then able to form dimers with HIF-1β, and initiate the transcription of target genes including the VEGF gene (37; 124). Several growth factors including fibroblast growth factor (FGF), platelet-derived growth factor (PDGF), transforming growth factor (TGF-β), and epidermal growth factor (EGF) have also been shown to up-regulate VEGF expression. Furthermore, mutations of the Ras proto-oncogene which occur in a variety of human cancers, lead to increased VEGF expression via the activation of the Ras-Mek-Erk MAP kinase pathway (124).

VEGF diffuses from the tumor to nearby vessels, and binds to receptors on the surface of the vascular endothelial cells. These are transmembrane receptor tyrosine kinases (RTKs) including VEGFR-1 (flt-1) and VEGFR-2 (KDR/flk-1), which are activated through ligand binding. This facilitates receptor dimerization and autophosphorylation of tyrosine residues in the cytoplasmic portion. The phosphotyrosine residues either enhance receptor catalytic activity or provide docking sites for downstream signaling proteins (85). VEGF mediates multiple responses from activated endothelial cells, which are illustrated in Figure 2.2.

It has been demonstrated that VEGF increases vascular permeability, which al-

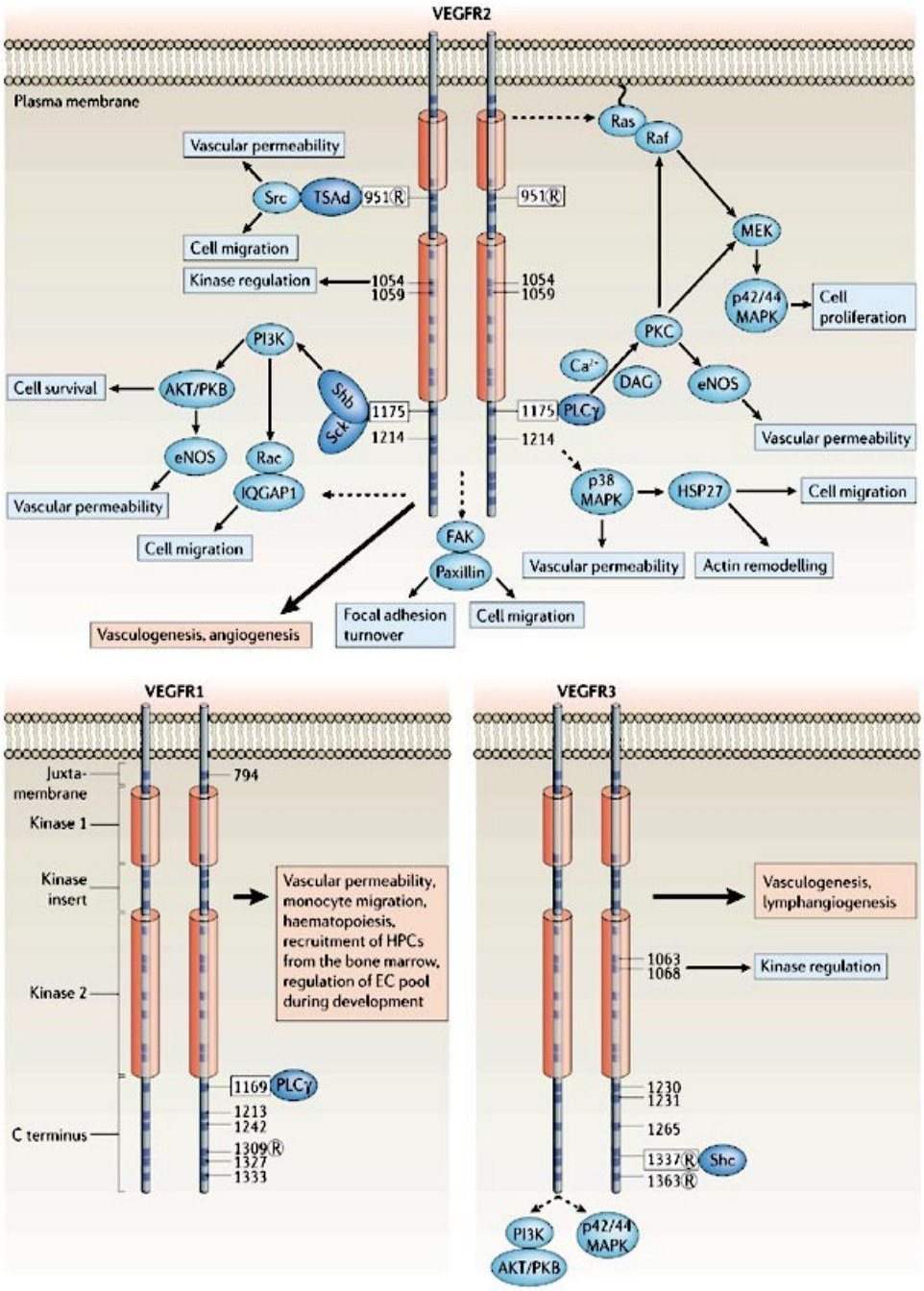

Figure 2.2: Figure showing the intracellular domains of dimerized and activated VEGF receptors (VEGFR1/2/3), taken from (102). Binding of signalling molecules to certain phosphorylation sites initiates downstream signalling pathways, resulting in specific biological responses.

lows for the extravasation of plasma proteins, such as fibrinogen, and other clotting proteins. This results in the deposition of fibrin in the avascular space, which leads

to the formation of ECM, facilitating EC migration (17; 52). VEGF has also been shown to increase the expression of urokinase and tissue-type plasminogen activators (uPA and tPA). These are serine proteases involved in the degradation of ECM. The expression of plasminogen activator inhibitor (PAI) type-1 is also increased, which is an inhibitor of uPA and tPA. Additionally, VEGF stimulates the production of matrix degrading metalloproteinases, interstitial collagenase. All these components actively participate in the remodelling of the ECM, aiding in EC migration and sprouting (84; 109).

VEGF exerts a number of different effects on EC, including inducing changes in EC morphology, cytoskeleton alteration, and stimulation of EC migration. VEGF is also a highly specific mitogen for vascular endothelial cells and stimulates their proliferation (52). It also acts as a survival factor for ECs by activating the PI3K-Akt (Phosphoinositide 3-kinase/protein kinase B) pathway. This results in the up-regulation of anti-apoptotic proteins such as Bcl-2, which in turn prevents cellular apoptosis (52; 97; 138).

VEGF and its receptors have been shown to play a pivotal role in angiogenesis. Activation of the VEGF-receptor pathway triggers a variety of downstream signalling events that promote EC survival, proliferation, and migration. VEGF also enhances vascular permeability and plays an important role in ECM remodelling. In the model of angiogenesis developed here, VEGF will be treated as the principal tumor-secreted chemokine that promotes angiogenesis. The effects of the VEGF-receptor pathway on ECs will be explicitly incorporated in our model.

2.3 Interleukin-8 in Tumoral Angiogenesis

CXCL8 or Interleukin-8 is a member of the chemokine family. These are small cytokines produced by a variety of cells including macrophages and endothelial cells. They are characterized by their ability to induce chemotaxis in responsive cells. In particular, CXCL8 is a potent chemotactic factor for neutrophils, basophils, T lymphocytes, and microvascular endothelial cells (15; 97). It is known to play an important role in autoimmune, inflammatory, and infectious diseases. Therefore, its production is tightly regulated, and its constitutive levels in normal tissue are very low (15).

CXCL8 is also a potent mediator of tumor angiogenesis. Its expression is found to be up-regulated in certain cancers, such as non-small cell lung cancer, and melanoma (109). Further, it has been shown that VEGF is able to induce over-expression of CXCL8 mRNA in human dermal microvascular endothelial cells (HDMECs), via the PI3K/Akt signalling pathway. Activation of this pathway results in the increased intra-cellular levels of IκB kinase-α and -β (IKKBs), which in turn cause phosphorylation of I-κB, leading to its proteosomal degradation. I-κB is a natural cytosolic inhibitor of the transcription factor nuclear factor-κB (NF-κB). Thus, NF-κB is released into the nucleus of the EC, where it initiates transcription of the CXCL8 gene (15; 59).

CXCL8 mediates its biological functions by interacting with specific G-protein-coupled CXC chemokine receptors CXCR1 and CXCR2 (Figure 2.3). These are expressed on a variety of cell types including macrophages and endothelial cells (15). CXCL8 acts as a promoter of angiogenesis by inducing EC proliferation, migration and survival. It is believed that the pro-angiogenic effects of CXCL8 are due to the presence of a Glu-Leu-Arg (ELF) domain. This has been demonstrated by observing

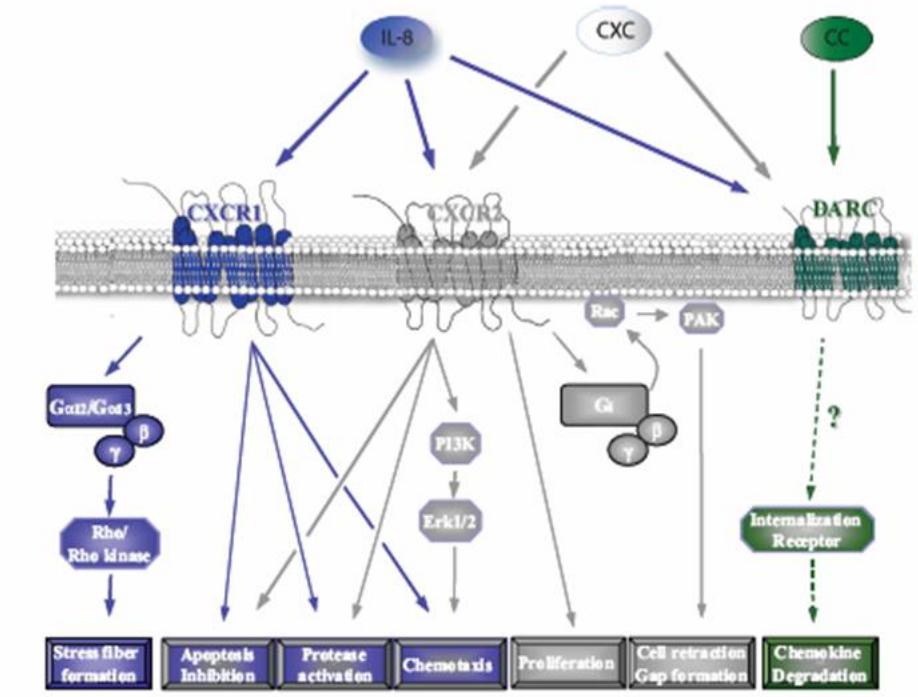

Figure 2.3: Figure showing the CXCL8 mediated signaling pathways in endothelial cells, taken from (15). Binding of CXCL8 to its transmembrane G-protein-coupled receptors CXCR1/2 induces angiogenic properties including cell proliferation, chemotaxis, survival, and protease activation.

that mutant forms of CXCL8 lacking in the ELF domain are unable to stimulate angiogenesis in vivo, while its introduction into an ELF-negative chemokine bestows angiogenic properties on the chemokine (15). Finally, CXCL8 has also been shown to stimulate the expression of matrix metalloproteinases-2 and -9 (MMP-2/9) in ECs. As mentioned earlier, the MMPs degrade basement membranes of vessels, as well as ECM, promoting cell invasion and migration (15; 109).

CXCL8 has been demonstrated to be a potent pro-angiogenic chemokine. It is therefore incorporated explicitly in our model of tumoral angiogenesis. In particular, we will focus on the role of CXCL8 as a mitogenic and chemotactic factor for ECs, and investigate its therapeutic potential as a possible target for the development of

anti-angiogenic therapy.

2.4 Extra Cellular Matrix in Tumoral Angiogenesis

The ECM is a dynamic macromolecular system integral to the structure and function of vessels. In addition to providing structural support to the vessel, the ECM is responsible for the mechanical properties of the vessel wall. Two critical steps in angiogenesis - the proliferation of ECs, and their migration into the stroma also require the adherence of the cells to the ECM (137; 150). Therefore, there has been considerable interest in elucidating the mechanisms by which the ECM modulates angiogenesis.

The ECM is comprised of various types of molecules. These include structural proteins such as collagen and elastin, and specialized proteins such as fibronectin, laminin, thrombospondins, and proteoglycans (84). Each of these molecules is a key determinant in triggering specific cellular responses. For instance, fibronectin effects endothelial cell adhesion, growth, migration, and survival. It binds to VEGF and enhances VEGF-induced angiogenesis. Other matrix molecules such as laminin, collagens, and vitronectin also promote EC adhesion and survival (137). On the other hand, some ECM proteins including thrombospondin-1 (TSP-1), and thrombospondin-2 (TSP-2) can function as inhibitors of angiogenesis. Additionally, the proteolytic fragments of matrix molecules have been identified as having antiangiogenic properties. Two such fragments are angiostatin, which is generated on cleavage of plasminogen, and endostatin, which is generated on the cleavage of the ECM protein, collagen type XVIII (150). The ECM also functions as a reservoir of angiogenic factors such as FGF-2 and heparin- binding forms of VEGF, that bind to and remain sequestered in the ECM until their release due to ECM degradation. This has the

effect of further promoting angiogenesis (137).

During the process of angiogenesis, the ECM is continually remodelled and conditioned by endothelial cells. In response to growth factors such as VEGF, ECs release proteolytic enzymes like the MMPs that cleave the matrix. This could have the effect of releasing growth factors or inhibitors sequestered in the matrix. They can also synthesize ECM components like fibronectin and collagen (84). Thus, a full understanding of the interactions between ECM and ECs, and how ECM proteins influence EC behaviors is essential in providing a complete picture of angiogenesis.

2.5 Other Factors affecting Angiogenesis

2.5.1 The Angiopoietins and Tie Receptors

In addition to the chemokines and proteins discussed above, several other factors have been shown to mediate tumoral angiogenesis. These include the angiopoietins and Tie receptors, that are implicated in vessel maturation. Two Tie receptors (Tie1 and Tie2) have been identified so far. These are receptor tyrosine kinases, and are specific to vascular endothelial cells. Genetic studies have demonstrated that initial vessel growth occurs in Tie1 deficient mice. However, this vasculature fails to mature and undergo remodelling. Thus Tie1 is necessary for vascular integrity and EC survival. Tie2 deficient mice have exhibited underdeveloped hearts, and vasodilation. Furthermore, Tie2 has been found to be crucial for vessel branching and sprouting. The ligands for Tie2 are the angiopoietins (Ang1-4), while those for Tie1 are not known. Ang1 is the most extensively characterized angiopoietin. It's overexpression induces vessel branching and increases vessel girth, while making them resistant to leakage by agents such as VEGF. Ang2 blocks Ang1-mediated activation of Tie2 on endothelial cells, and acts as a check to prevent excessive branching of blood vessels by promoting their destabilization. It has also been postulated that

Ang1 makes ECs more sensitive to VEGF signalling by antagonizing Ang2/Tie1 function (84; 109).

2.5.2 Additional Membrane-bound Molecules

Membrane-bound molecules such as integrins, cadherins and ephrins also play an important role in angiogenesis. For instance, the Eph receptor family together with their membrane bound ligand ephrin controls positional guidance cues on vascular endothelial cells aiding in the establishment of arterio-venous asymmetry (51). The integrins are transmembrane receptors that act as adhesion molecules, allowing the anchorage of the EC to the ECM. Binding of integrins to the ECM also triggers the expression of numerous cytosolic kinases such as mitogen-activated protein kinase which elicits a range of cellular responses including promoting cell survival, cell migration, and inducing cell proliferation (143). Finally, endothelial cells must be able to adhere to each other tightly in order to maintain a barrier between the blood in the blood vessels and extravascular space, and to control the permeability of blood vessel walls. The mechanism for such adherence is through an adhesion molecule located at junctions between ECs, called vascular endothelial (VE)-cadherin (149).

In 1971, Judah Folkman postulated that blocking tumor angiogenesis would prevent expansion of the tumor or, at best cause it to regress to a manageable size. Since the publication of this visionary hypothesis, angiogenesis has remained a field of intense research. Today there are over 20 anti-angiogenic compounds in various phases of clinical trials. However the survival benefits of these treatments are relatively modest. In addition the cost and potential toxic side effects due to chronic use are indicative of problems that still remain in the clinical applications of angiogenic inhibitors (63). In order to develop effective strategies for the treatment of angiogenesis-dependent diseases such as cancer, a better understanding of their

pathogenesis at a molecular and cellular level is essential. Mathematical modelling such as that developed in this research provides a powerful tool to elucidate the mechanisms of angiogenesis.

In the following chapters, we will develop continuous and hybrid models of tumor-induced angiogenesis to gain deeper understanding of the processes that operate at multiple scales to make tumor vascularization possible. Our model operates on three scales:

- **Intracellular Signalling**: We investigate signal transduction pathways operating within a single endothelial cell, eliciting pro-angiogenic responses from the cell such as proliferation, migration, differentiation and survival. In particular, we focus on the VEGF - Bcl-2 - CXCL8 signaling pathway. The response of the cell to these chemical cues will be the output of this model.

- **Cellular Level**: We model the uptake of chemokines such as VEGF and CXCL8 by ECs, and the production and release of CXCL8 into the tumor microenvironment by the ECs. Upon uptake by the ECs, these chemokines lead to the activation of downstream signalling pathways, thus providing input to the intracellular model.

- **Tissue Level**: We scale the model up to a population level, so that the behavior predicted by the single cell model may be used to determine the response of a population of cells to their microenviroment.

A primary objective of our modelling effort is to provide us with a better quantitative understanding of the role of the intra-cellular molecular pathways mentioned above, in determining vascular development in tumors. This information will then be used to suggest and theoretically test new anti-angiogenic therapies targeted against

these pathways.

CHAPTER III

Mathematical Models of Angiogenesis

The use of mathematical models to describe various aspects of tumor growth began in earnest several decades ago. Modelling techniques paralleled the surge in the understanding of the mechanisms driving the progression of cancer. Today, cancer is recognized to be a disease that operates at various scales; at intracellular, intercellular, and tissue levels. This has led to the development of novel multiscale quantitative models of tumorigenesis, with the aim of facilitating a deeper understanding of the onset and progression of the disease, and evaluating the potential of treatment strategies.

In this chapter, we present a brief overview of a few of these models, that have pioneered innovative approaches to modelling cancer, and have motivated several others. Since the central theme of this research is the biochemical forces driving angiogenesis in tumors, we will limit our review to models of angiogenesis.

Models describing tumor-induced angiogenesis can be broadly classified into two categories.

1. Continuum models that treat model variable densities as continuous, and track their temporal and/or spatial evolution governed by reaction-diffusion systems.

2. Discrete or hybrid models, that track the motion of individual endothelial cell

and capillary sprouts densities, while treating chemical species as continuous variables.

3.1 Continuum Models

Continuous mathematical models of angiogenesis can be dated back to at least the late 1970's (29). These models rely on the principles of mass conservation and chemical kinetics, and can predict the behavior of certain averaged quantities such as vessel and tip densities and capillary extension speeds.

One of the first models of tumor-induced capillary growth was proposed by Balding and McElwain in 1985 (11). Their model comprised of three equations in 1 dimension, for the sprout tip density, the capillary density, and tumor angiogenic factor (TAF) concentration. This approach had the novel idea that sprout tips guide capillary formation, thereby accounting for the experimental observation that EC proliferation occurs mainly behind the sprout tip. It captured the fact that there is an increased frequency of branching at the edge of the network as the capillary sprouts get closer to the tumor, termed as the brush-border effect (93). Model parameters could be fitted to reproduce observed vessel lengths and tip speeds.

Byrne and Chaplain (18) modified the above approach to incorporate explicitly for the first time in models of tumor angiogenesis, the experimentally observed phenomena of branching, and tip-sprout anastomoses. Tip proliferation was assumed to occur only above a certain threshold TAF concentration, and was localized behind the moving tip. Also, a term was incorporated for the uptake of TAF by the tip cells.

One of the first two-dimensional models of tumor angiogenesis was developed by Orme and Chaplain in 1997 (103). A square domain geometry was used ($D = [0, L] \times$

$[0, L]$), with the parent vessel located at $y = 0$, and a line of tumor cells, (source of the TAFs) at $y = L$. A novel feature of this model was that it accounted for for cell-matrix interactions by incorporating haptotaxis, a process by which ECs migrate up gradients of fibronectin. The model described the evolution of endothelial cell density that comprised newly developing vasculature, TAF concentration (assumed to be at steady state), and fibronectin concentration. EC growth was assumed to occur logistically. An important result of the paper was that haptotaxis was important for successful angiogenesis, and in its absence, anastomoses occurred too early for normal development of the vasculature.

In 1998, Anderson and Chaplain published another continuous two-dimensional model of tumor-induced angiogenesis (5). As in (103), EC density and fibronectin concentration were kept track of, while the TAF was assumed to be quasi steady state. The same domain geometry as in (103) was used. A receptor kinetic law was used to model the chemotaxis sensitivity of ECs to the TAF, reflecting the desensitization of EC receptors at high chemical concentrations. Two kinds of tumor sources were considered a small circular tumor and a row of tumor cells. Numerical simulations of this model were performed and several interesting observations were made. In the absence of haptotaxis, the endothelial cells migrated directly across the domain towards the tumor, with very little lateral motion. Including haptotaxis slowed down the migration, and lateral movement became very apparent, interpreted by the authors as branching of the vasculature. Further, by choosing appropriate concentrations of tumor angiogenic factors at which endothelial cells become desensitized, the authors were able to reproduce experimental observations that endothelial cells will not reach the tumor when cells are not allowed to proliferate.

While these models represented significant advances in terms of simulating neo-

vascularization, they had some major drawbacks:

- A number of models ignored chemokine uptake by the ECs, and many used steady state profiles of the TAFs. The justification for this was that the diffusion time-scale for the TAFs is much smaller than that for ECs or sprout tips. However, in biologically realistic situations, the source of TAFs may not be constant. Factors effecting TAF production rates include increased levels of local oxygen concentration provided by newly developed vasculature, and anti-angiogenic therapy targeted against the TAFs or their receptors. Further, as mentioned earlier, a significant percentage of TAFs such as VEGF may remain sequestered by the ECM and is biologically unavailable to the cells. In this case, uptake of the unbound TAFs by the ECs could create steep local gradients in the chemokine profile and alter the resulting vascular development significantly.

- A generic chemokine was used to represent an entire set of angiogenic factors. Whilst different chemokines can produce similar qualitative effects, such as inducing cell proliferation or migration, the degree of the effect varies and makes the choice of parameters difficult. For instance, the numbers of cell surface receptors, the rate constants for receptor-ligand interaction, the degree of proliferative and chemotactic response can vary considerably between a wide variety of angiogenic factors. Further, a key motivation behind simulating angiogenesis in silico is to provide valuable insights into understanding the processes that govern it so that new methods of promoting or reversing it may be investigated. In the case of tumoral angiogenesis, for example, the development of anti-angiogenic therapy is the focus of much interest. Such therapy may target a particular chemokine, or its receptors. For VEGF in particular, a number of antagonist compounds are currently undergoing clinical trials. To accurately

simulate these, specific characteristics of VEGF would have to be modelled instead of a generic growth factor that combines the traits of many diffusible angiogenic chemokines.

- The biochemistry of interactions between ligands and their receptors has often not been considered. With an increasing availability of experimental data, our knowledge of the cellular and sub-cellular processes governing angiogenesis is growing, and a number of new targets for the development of pro- and anti-angiogenic therapy have come to light. One such example is the VEGFR2-mediated VEGF-Bcl-2-CXCL8 signaling pathway (98), which elicits a pro-angiogenic and pro-survival response in ECs. Bcl-2 has been identified as a promising target for anti-angiogenic therapy. The incorporation of a molecular level of detail in quantitative models is required if we are to accurately simulate such pro- or anti-angiogenic compounds that target the TAFs, their receptors, or act further downstream. It is essential that Mathematics keeps up with the recent advances in this field, in order to be useful as a predictive tool in an in vivo setting.

3.1.1 A Biochemically Motivated Approach

The first few models of tumor-induced angiogenesis to incorporate the detailed interactions between growth factors such as VEGF and their cell surface receptors were developed by Levine et al (73; 74; 75). A distinguishing feature of their models was the fact that the movement of cells was based on the theory of reinforced random walks. Phenomenological choices of the chemotactic sensitivity function were made, to mimic a receptor-kinetic law of the form $\frac{\chi}{(1+\gamma_1 v)(1+\gamma_2 v)}$, where v is the chemokine concentration. Using this approach, in (74), the authors presented a

model of the initiation and development of vasculature in tumors, under the influence of a number of factors, including VEGF, a proteolytic enzyme, protease inhibitor, fibronectin and angiostatin. In (73), this model was extended to incorporate the dynamics of angiostatin, pericytes and macrophages. The law of mass action was used in these models to derive the set of equations governing receptor-ligand reactions. However, for the sake of simplicity, Michaelis-Menten kinetics were assumed for these reactions where cell-surface receptors function the same way an enzyme functions in classical enzymatic catalysis. Further, it was assumed that a single molecule of VEGF binds and activates a receptor monomer and results in the production of a single proteolytic enzyme molecule. This issue was partly addressed in (75), where a single molecule of VEGF signalled a cascade of intracellular events, that resulted in the production of several (perhaps hundreds) of molecules of proteolytic enzymes.

The level of detail of the biochemistry of angiogenesis incorporated meant that these models were a significant improvement over previous models. They were able to account for capillary sprout initiation from parent vessels based solely on biochemical considerations, and the subsequent vascular development. However, there were a few issues with this approach. It did not account for the fact that VEGF induces receptor dimerization, and that it is these dimerized receptors that are in an activated state. Further, Michaelis-Menten like kinetics were assumed throughout. However, it is not necessary that in in vivo systems, the ligand concentration will always be significantly greater than receptor density, in which case the quasi-steady state assumption is no longer valid. The degradation of a number of the protein was not included, whereas they could have very short half-lives in tissue. For instance, the half-life of VEGF in tissue is approximately 60 min (132). The diffusion of the chemokines is ignored, with the justification that it takes place on a much slower time-scale than the reactions.

However, diffusion of ECs is incorporated even though this occurs at even slower time-scale than that of the chemokines.

3.2 Discrete Models

Models of the continuum, deterministic framework were capable of capturing some features of angiogenesis such as average sprout density and network expansion rates, permitting a detailed qualitative comparison with in vivo observations concerning the spatio-temporal distribution of capillary sprouts within the network. However, they were unable to provide more detailed information concerning the actual structure and morphology of the capillary network. In order to capture certain important events such as repeated sprout branching and hence the overall dendritic structure of the network, the model should recognize the existence of individual sprouts. This has been made possible by the advent of hybrid models of tumor angiogenesis.

One of the first discrete models of angiogenesis was published by Stokes and Lauffenburger in 1991 (140). They based their model on stochastic differential equations that governed the velocity of each tip. Thus, the motion of individual sprouts could be followed, thereby allowing realistic capillary networks to be generated based on rules for sprout branching and looping. The model incorporated random motility and chemotaxis as mechanisms for cell migration. Since parameters were estimated, as far as possible, from available experimental data, this model permitted both qualitative and quantitative comparisons with in vivo networks. However, the model was unable to reproduce the brush-border effect.

Anderson and Chaplain (5) adopted a different approach to the development of a discrete mathematical model of tumoral angiogenesis. They discretized the model equations developed for the continuous case (described in section 3.1), on a five

point stencil, using standard finite-difference methods. The resulting coefficients in the endothelial cell equation were used to generate movement probabilities of the cells, resulting in a biased random walk governing the motion of each cell. In turn, it was assumed that each tip cell pulled behind it a capillary. Biologically motivated rules for branching and anastomoses were prescribed. Numerical simulations of the model showed that as in the continuous case, including haptotaxis leads to a slow migration rate of tips, and increased frequency of branching near the tumor source. Further, as observed experimentally, the sprout tips reach a relative steady state before reaching the tumor, in the absence of cell proliferation. When cell mitosis is included in the model, a well developed branching network is observed to form earlier and this does connect with the tumor.

However, this method suffers from a major disadvantage - the choice of numerical schemes used to discretize the diffusion-advection equations can influence the simulation results. The choice of numerical scheme is not straightforward if the advection velocities are non-constant, and written in the conservative form. Since the approach followed by Anderson and Chaplain relies on the scheme being explicit, they use a central-differencing scheme to discretize the cellular velocity, which is unconditionally unstable in this case. Further, while cell division has been incorporated in the model, it is assumed to occur only once every 18 hours, and results in a forward motion of the developing sprout by a single cell length. This implies that in any sprout, only a single cell is undergoing mitosis at any given time point. This is contrary to experimental observations that up to 30% of the cells in a sprout are undergoing mitosis at any given time (134).

An alternative approach is based on the theory of reinforced random walks, applied to model the movement of cells under the influence of a chemical attractant in their

local environment by Othmer et al (105). Plank and Sleeman (116) modified this technique to simulate tumoral angiogenesis. They began with a probability master equation describing a biased random walk of an endothelial cell. The translation probabilities were assumed to be functions of VEGF, a proteolytic enzyme, and angiostatin - an angiogenesis inhibitor. If a constant mean waiting time for the cell at a lattice site was assumed, it could be shown that the master equation translates to the familiar diffusion-chemotaxis equation for the motion of a cell, of the form used in continuum models of angiogenesis. Using this approach, capillary networks in qualitative agreement with experimental observations could be generated. A novel feature of this model is the explicit inclusion of cell proliferation and cell death.

From the above review, it is clear that mathematical modelling of tumor angiogenesis has come a long way since the publication of the first model. However, as new experimental data becomes available, and new therapeutic strategies are being developed, there is a need to expand the scope of these models to include the current knowledge in the field. In this research, we will focus on the following:

- The uptake and binding of chemokines to cell surface receptors will be studied in greater detail. For instance, the validity of assuming a monomeric uptake of VEGF by VEGFR2 instead of a biochemically correct dimeric uptake will be investigated. The validity of the quasi steady state assumption applied to VEGF-VEGFR2 binding reaction will also be studied.

- All the models reviewed here have the common feature that EC or sprout tips react to free chemokine concentrations. However, it is the presence of activated receptors on the cell surface that elicit a response from ECs. For instance, during the process of chemotaxis, ECs actually sense a gradient of chemokine bound to their surface, which results in their polarization, and bias to movement

in a particular direction. Responses such as proliferation are a result of the integration of the total amounts of activated receptors on their surfaces (47). This issue will be addressed in our model as well.

- A truly multiscale model of angiogenesis will be developed, that will incorporate details of newly discovered intracellular signalling pathways such as the VEGF-Bcl-2-CXCL8 pathway. It will therefore be possible to quantitatively analyze the potential of various apoptosis-inducing anti-angiogenic therapies under development, which are targeted at the Bcl-2 family of proteins.

- Currently, the receptor-kinetic law remains the most popular choice for the chemotaxis sensitivity of ECs to growth factors. However, this suffers from three major drawbacks. The sensitivity of cells is at its maximum when the chemokine concentration is zero. It also makes the assumption that ECs migrate in response to free chemokine concentrations. Finally, it does not account for the fact that the level of chemokine at which desensitization of receptors occurs, should in fact be a function of the EC density. 0.1 pM VEGF may be enough to saturate the receptors of a single cell, but it might not be enough for 10 cells. In the later part of this thesis, a hybrid model of tumor neovascularization will be developed, using a biologically realistic chemotaxis sensitivity function.

CHAPTER IV

Modelling Vascular Endothelial Growth Factor Binding Dynamics

Vascular Endothelial Growth Factor (VEGF) is an endothelial cell (EC) specific pro-angiogenic cytokine. It is a crucial regulator of physiological angiogenesis, during embryonic development, cartilage vascularization, skeletal growth and endochondral bone formation, ovarian angiogenesis and wound healing. It also plays a central role in several pathologic conditions such as vascularization of solid tumors and hematologic malignancies, and has been implicated in various inflammatory disorders and the development of brain edema (37). An accurate description of the mechanism by which VEGF exerts its biological influence, would therefore be a valuable addition to any mathematical representation of VEGF's role in angiogenesis. To this end, we develop a detailed molecular level model of VEGF binding and activating cell surface receptors.

4.1 The VEGF Molecule

The human VEGF family consists of five glycoproteins; namely VEGF-A, VEGF-B, VEGF-C, VEGF-D, and placental growth factor (PlGF). VEGF-A, also referred to as VEGF, is a tumor-secreted homodimeric glycoprotein, with a molecular mass of approximately 45 kDa (20). Alternative exon splicing of the VEGF gene yields

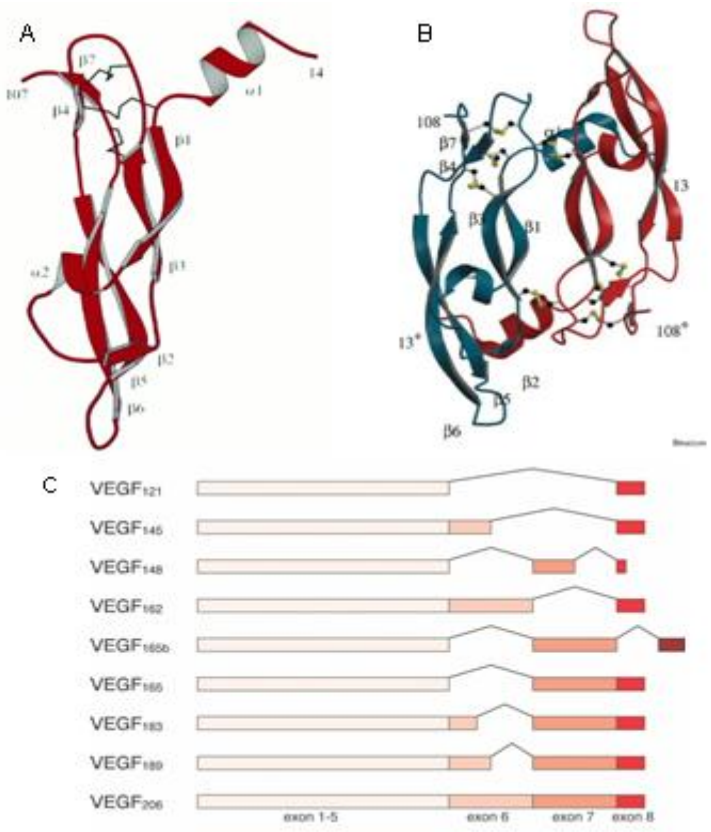

Figure 4.1: (A) Ribbon representation of the receptor-binding domain of the VEGF monomer as observed by X-ray crystallography (89). (B) Ribbon representation of the structure of the receptor-binding domain of the VEGF dimer (90). (C) Alternative exon splicing results in the generation of several isoforms of VEGF-A (143).

several mature isoforms. Of these, the principal forms are $VEGF_{121}$, $VEGF_{165}$, $VEGF_{189}$, and $VEGF_{206}$. While $VEGF_{121}$ is freely diffusible, $VEGF_{189}$ and $VEGF_{206}$ are almost completely bound to, and sequestered in the extra cellular matrix (ECM). $VEGF_{165}$ is the predominantly expressed isoform, and is over-expressed in a variety of solid tumors in humans (106). It is partially diffusible in vivo, and about 50-70% remains bound to the ECM and cell surface, giving it optimal characteristics of bioavailability and biological potency (37; 124). Figures 4.1A, and B show ribbon representations of the VEGF monomer and dimer, respectively, taken by X-ray crystallography. Figure 4.1C shows a comparison of structures of the various isoforms of

VEGF.

In vitro, VEGF has been shown to induce capillary-like tubule formation by microvascular endothelial cells grown on collagen gels (97; 111). In addition to eliciting a mitogenic response, it induces cell chemotaxis and exerts a pro-survival effect by up-regulating intracellular levels of anti-apoptotic proteins such as Bcl-2 and survivin (20; 97; 98; 106). In vivo, VEGF also causes vasodilation and increases vascular permeability, thereby, allowing the leakage of plasma proteins which further promote cell growth (20; 106). For the reasons stated above, we will focus on VEGF (specifically the $VEGF_{165}$ isoform) in this study. A brief introduction to the other VEGF glycoproteins is however, presented below.

VEGF-B, which is also called VEGF-related factor (VRF), is expressed beginning early in fetal development. It also appears to be required for normal heart function in adults. It has been shown to modulate EC mitosis and vessel growth, however, its precise role in vivo remains unclear (106; 124; 159). VEGF-C, also called VEGF-related protein, and VEGF-D, also referred to as c-Fos-induced growth factor (FIGF), have both been shown to induce lymphangiogenesis (159). VEGF-C signalling is, in fact, crucial to the migration and survival of lymphatic endothelial cells, and formation of lymph sacs. Additionally, both are known to induce EC mitogenesis, migration and survival (106; 124; 159). The final member of the VEGF family, PlGF, is a homodimeric glycoprotein like VEGF-A. It was originally discovered in the human placenta, and is also expressed in the heart and lungs, and a variety of tumors. It enhances VEGF signaling, and its expression may diminish the efficacy of therapy targeted against VEGF (124; 159).

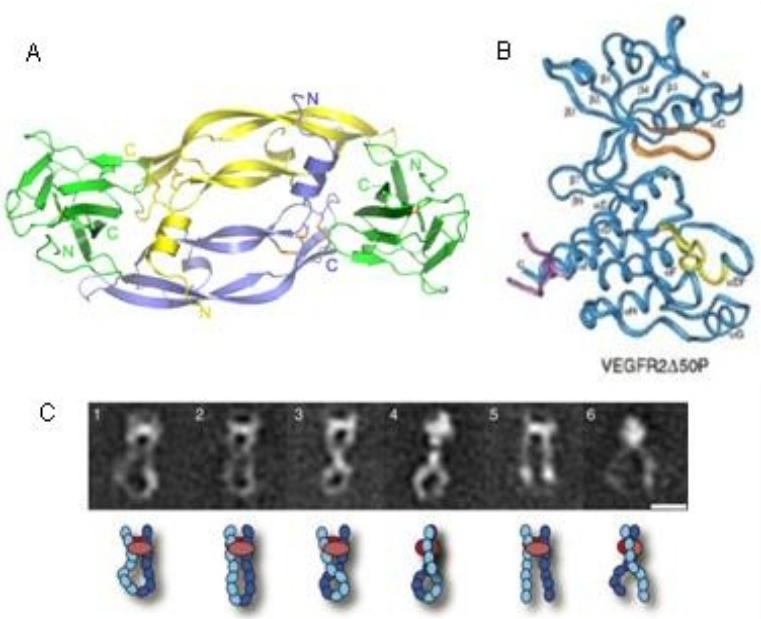

Figure 4.2: (A) Ribbon representation of a dimerized VEGF-VEGFR1 receptor complex. Two monomers of VEGF (blue and yellow) are shown bound to domain 2 of VEGFR1 (green) (155). (B) Backbone representation of structures of the kinase domains of VEGFR2 (85). (C) Class averages (top) and graphic representations (bottom) of the VEGFR-2 extracellular domain in complex with VEGF. Visualization of proteins carried out by negative-stain electron microscopy. Scale bar, 15 nm (124)

4.1.1 VEGF Receptors

The biological effects of VEGF are mediated by interactions with its cell surface receptors. These are the receptor tyrosine kinases (RTKs), VEGFR1 (fms-like tyrosine kinase/Flt-1) and VEGFR2 (kinase insert domain-containing receptor/Flk-1), which are selectively expressed on vascular endothelial cells and the non-enzymatic neuropilin receptors NP1 and NP2, which are expressed on vascular endothelium and neurons (106). Activation of VEGF RTKs occurs through ligand binding, which facilitates receptor dimerization and autophosphorylation of tyrosine residues in the cytoplasmic portion. The phosphotyrosine residues either enhance receptor catalytic activity or provide docking sites for downstream signaling proteins (85).

VEGFR1 is a 210 kDa protein, which binds VEGF with a high affinity. Fig-

ure 4.2A shows a ribbon representation of the structure of the complex formed when VEGF binds two VEGFR1 monomers. It is expressed in various cell types, including ECs, osteoblasts, and macrophages. Its expression is up-regulated by hypoxia via a hypoxia-inducible factor-1 (HIF-1) dependent mechanism. Even though VEGFR1 has a higher affinity for VEGF than VEGFR2, it only undergoes weak tyrosine autophosphorylation in response to ligand induced activation. Furthermore, it has been shown that this does not directly effect cell proliferation. Therefore, it has been proposed that a key function of VEGFR1 is to act as a decoy receptor by preventing VEGF from binding VEGFR2, rather than regulating angiogenesis (37; 106; 124).

VEGFR2 is a 200 kDa protein (139), and is considered to be the principal mediator of the chemotactic, angiogenic, and permeability enhancing effects of VEGF. It undergoes ligand-induced dimerization, and strong tyrosine autophosphorylation (96; 124). Figure 4.2B shows a ribbon representation of the kinase domains of VEGFR2, as observed by X-ray crystallography. Figure 4.2C shows photographs of the extracellular domains of VEGFR2 bound to VEGF, taken by negative-stain electron microscopy. VEGFR2 activation elicits a proliferative response from ECs through activation of the Raf-Mek-Erk pathway. It has also been shown that in human umbilical-vein endothelial cells (HUVECs), and human dermal microvascular endothelial cells (HDMECs), VEGFR2 signalling induces an anti-apoptotic effect through the PI-3 kinase-Akt pathway (37; 97; 106). Figure 4.3 shows a schematic diagram illustrating some of the downstream intracellular signalling pathways activated as a result of dimerization of VEGFR2 by VEGF.

The neuropilins NP1 and NP2 are glycoproteins with a molecular weight of 120-140 kDa, and are expressed on certain ECs, neurons, and tumor cells (37; 124). They are $VEGF_{165}$ isoform specific receptors which enhance the binding of VEGF to

VEGFR2, by forming complexes with VEGFR1. This has been proposed as a possible explanation for increased effectiveness of VEGFR2 mediated signal transduction when the neuropilins are co-expressed in cells with VEGFR2. (37; 106).

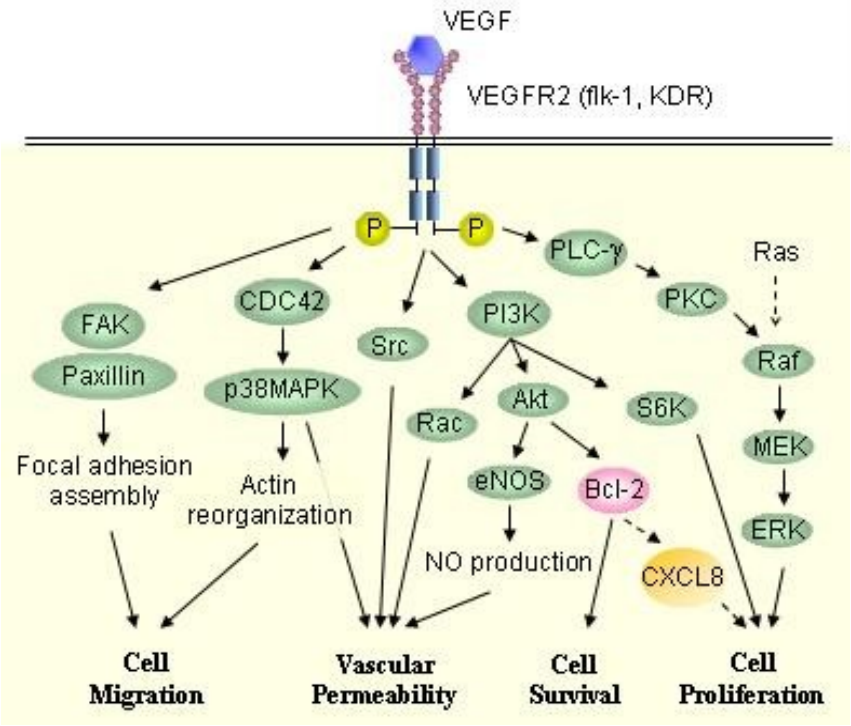

Figure 4.3: Schematic diagram illustrating downstream VEGFR2 signalling pathways, adapted from (105; 143).

4.2 Previous Mathematical Investigations

To date, there have been a number of mathematical models that explicitly incorporate the effects of growth factors such as VEGF on ECs in both, tumor-induced and wound healing angiogenesis. The early models treated the entire panel of angiogenic factors as a single chemokine. In the case of tumor induced angiogenesis, these were collectively referred to as tumor angiogenic factors (TAFs). One of the earliest models of tumor-induced angiogenesis was published by Balding and McElwain in 1985 (11). In this, the TAF concentration was held at a steady state, and binding

and uptake by ECs was neglected. Diffusion of the chemokines was the only mechanism by which such a steady state profile was reached. Stokes and Lauffenburger published the first stochastic model of angiogenesis in 1991 (140). In this model too, the TAF concentration was held fixed in time. Subsequent models added features such as production and decay of TAFs (133), decay of TAFs only (118; 103), and their removal by newly developed vasculature (112), continuing however, to neglect the uptake of TAFs by ECs.

Chaplain and Stuart (23) was one of the first models to explicitly incorporate a term in the TAF evolution equation corresponding to loss due to uptake by ECs. They assumed that this decay rate was governed by Michaelis-Menten kinetics. Other models of angiogenesis used similar Michaelis-Menten like terms for the uptake of TAFs (24; 53), or simplified this still further to a constant rate of uptake (113; 5; 145; 117).

These models represented significant advances in the field of angiogenesis modelling. However, they suffered from several drawbacks, as discussed in Chapter III. Many ignored the uptake of chemokines by the ECs, sometimes assuming them to be in a quasi steady state. A generic chemokine was used to represent an entire panel of angiogenic factors. This meant that the traits of many diffusible angiogenic chemokines are presented as a combined effect of the generic chemokine. However, the current trend in anti-angiogenic therapy research is to develop antagonistic compounds directed against specific chemokines. To accurately simulate these, specific characteristics of that chemokine would have to be modelled. Finally, there is now an abundance of data relating to cellular and subcellular processes governing angiogenesis. This has resulted in the identification of new targets for the development of anti-angiogenic therapy. In order to investigate the therapeutic potential of these

targets, there is a need to expand the current models of angiogenesis to incorporate these advances.

Levine et al (73; 74; 75) published the first models of angiogenesis to incorporate details of interaction of angiogenic growth factors such as VEGF with growth factor receptors on the surface of endothelial cells. Specifically, in (73) it is assumed that one molecule of VEGF binds to a receptor on an endothelial cell surface to produce an intermediate complex. This complex is considered to be an activated state of the receptor that results in the production and secretion of a proteolytic enzyme and a modified intermediate receptor. The intermediate receptor is subsequently removed from the cell surface after which it may be recycled to form the original receptor or a new one is synthesized and moves to the cell surface. Michaelis-Menten kinetics are assumed for this standard catalytic reaction where receptors at the surface of the cell function the same way an enzyme functions in classical enzymatic catalysis. The model of angiogenesis presented in (74; 117) makes similar assumptions regarding receptor-ligand interactions. In (75), the fact that a single molecule of VEGF signals a cascade of intracellular events, which results in the production of several (perhaps hundreds) of molecules of proteolytic enzymes, is addressed. However, there are two main issues with this approach: it does not account for VEGF induced receptor dimerization, and assumes Michaelis-Menten kinetics throughout. This is not a valid assumption in cases where the ligand concentration is not significantly greater than its receptor density.

Mac Gabhann et al (78; 79; 80; 81) were the first to develop computational models of VEGF binding to cell surface receptors at a molecular level. Their models primarily focussed on in vitro assays. The first of these (78) described the competitive binding between VEGF and PlGF to VEGFR1, whilst another (79) described the

interactions of VEGF isoforms $VEGF_{121}$ and $VEGF_{165}$ with VEGFR2 and NP1. In both, it was assumed that VEGF binds to and activates pre-dimerized receptors in a single binding step, referred to as the 1:1 binding model. The 1:1 ligand-receptor binding model was compared to several possible mechanisms of receptor dimerization in (80), including ligand binding to pre-dimerized receptors (static pre-dimerization or SPD, in which VEGF binds pre-dimerized receptors in two steps), receptors dimerizing and dissociating independent of ligand (dynamic pre-dimerization or DPD), and ligand-induced receptor dimerization (LID). They concluded that the average fractional occupancy of receptors and variability in the binding for each mechanism was similar to the 1:1 binding model. Recent studies demonstrate that VEGF receptors can aggregate in the absence of ligand (95). This means that both the DPD and LID mechanisms may exist for ligand induced receptor activation. Mac Gabhann and Popel conducted a study in (81), to try and determine the dominant mechanism. Simulation results suggested the existence of a threshold level of initial VEGF concentration below which all three mechanisms (1:1, DPD, LID) predicted similar binding to cell surface. Above this threshold, a high-dose inhibition was observed for the LID model, due to increase in inactive monomeric receptor-ligand complexes. This lack of observed difference between the 1:1 and other dimerization models of VEGF uptake could be due to three main assumptions in the framework of these models:

- In both (80) and (81), it was assumed that on average there are 25,000 VEGF receptors (VEGFR2) per cell. However, the number of receptors on the EC surface varies considerably with cell type, tissue, and vessel of origin. For instance, in microvascular ECs used in many experiments, designed to study angiogenesis, this number is as high as 231,300 (152).

- In most simulations, it was assumed that the ligand was in far greater concentration than its receptors.

- Finally, in (80), receptor-ligand internalization was ignored. Natural decay of the ligand was ignored in (80) as well as (81). Thus, unbound ligand concentration would remain largely unaffected by receptor uptake.

If any of the above conditions are relaxed, so that the ligand concentration falls relative to the receptor numbers, a divergence of results is possible when investigating 1:1 binding versus ligand-induced receptor dimerization.

4.3 Modelling VEGF Uptake by VEGFR2

A review of the modelling literature shows that existing models of intra-tumoral and wound healing angiogenesis which incorporate the effects of pro-angiogenic chemokines such as VEGF, continue to ignore ligand-induced receptor dimerization. These models use a variety of biologically unrealistic uptake forms (constant rate, and Michaelis-Menten like terms), or ignore it altogether. Given that it is impossible to overstate the role played by VEGF in angiogenesis, it is important to accurately describe VEGF receptor dimerization and its cellular uptake. Here, we present a model of VEGF binding to VEGFR2, the primary receptor shown to be capable of promoting angiogenesis, and compare binding data to that obtained by assuming monomeric uptake. We also present a quantitative analysis to illustrate the invalidity of Michaelis-Menten like kinetics in many biologically realistic environments. To the best of our knowledge, this is the first such analysis of its kind.

Mac Gabhann et al have developed models of angiogenesis occurring within skeletal muscles (82), where molecular level details of VEGF uptake by its receptors are included. However, as noted earlier, in these the 1:1 binding data was found to be

similar to LID or DPD models of receptor dimerization. This may not be true for all cell types, or in every experimental condition, as we will demonstrate by our simulations.

4.3.1 Model Development

Due to a lack of experimental data from which ligand-free receptor dimerization rates may be obtained (as the authors in (81) note), we assume ligand-induced dimerization to be the dominant mechanism by which VEGF activates VEGFR2, as shown in Figure 4.4.

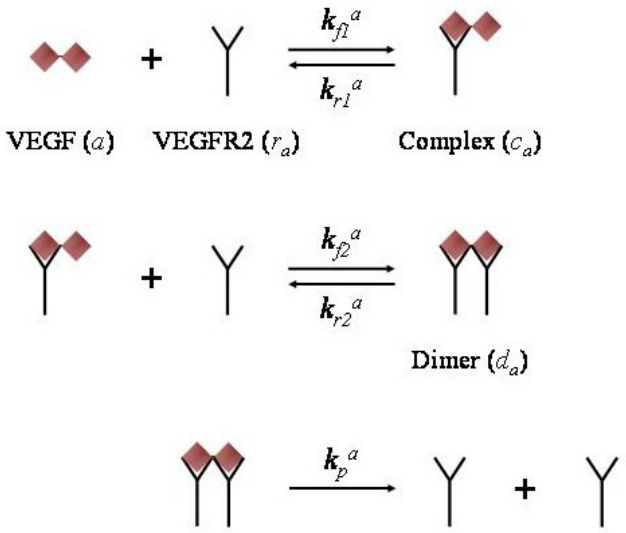

Figure 4.4: A schematic of VEGF-VEGFR2 interactions. VEGF binds to and dimerizes its cell surface receptor VEGFR2. The activated receptor-ligand complex is subsequently internalized, and free receptors recycled.

Lower case letters are used to represent individual molecules and upper case letters are used to represent their concentration (in moles per liter), so that $A = [a]$ is VEGF concentration, $R_a = [r_a]$ is VEGFR2 concentration, $C_a = [c_a]$ is VEGFR2-VEGF monomer complex concentration, and $D_a = [d_a]$ is VEGFR2-VEGF-VEGFR2 dimer complex concentration. The above reaction diagram can be converted to the

following system of equations using the law of mass action.

$$\frac{dA}{dt} = -2\,k^a_{f1}\,A\,R_a + k^a_{r1}\,C_a \tag{4.1}$$

$$\frac{dR_a}{dt} = -2\,k^a_{f1}\,A\,R_a + k^a_{r1}\,C_a - k^a_{f2}\,C_a\,R_a + 2\,k^a_{r2}\,D_a + 2\,k^a_p\,D_a \tag{4.2}$$

$$\frac{dC_a}{dt} = 2\,k^a_{f1}\,A\,R_a - k^a_{r1}\,C_a - k^a_{f2}\,C_a\,R_a + 2\,k^a_{r2}\,D_a \tag{4.3}$$

$$\frac{dD_a}{dt} = k^a_{f2}\,C_a\,R_a - 2\,k^a_{r2}\,D_a - k^a_p\,D_a \tag{4.4}$$

where

k^a_{f1} is an association rate constant and has units (VEGF concentration)$^{-1}$ (time)$^{-1}$

k^a_{r1} is a dissociation rate constant and has units (time)$^{-1}$

k^a_{f2} is an association rate constant and has units (Complex C_a concentration)$^{-1}$ (time)$^{-1}$

k^a_{r2} is a dissociation rate constant and has units (time)$^{-1}$

k^a_p is the rate of receptor internalization/recycling and has units (time)$^{-1}$

The multiplicative factor of 2 in some of the equations accounts for the possibility that there may be two ways for that product to form. For example, in equation (4.2), there are two ways for a VEGF dimer molecule to bind to a single receptor molecule, since there are two binding sites on the VEGF molecule. In experimental assays, the weights of chemokines are often measured in picograms or nanograms. Further, the length scale of experiments is in millimeters. Thus, the above equations are scaled to units of pg/mm^3 by appropriate constants (η^a_i). These represent ratios of the weights of the different molecules involved in the reaction. The values of these constants are given in the table below.

The scaled equation can be written as follows.

Table 4.1: List of parameter values relating to the molecular weights of VEGF and VEGFR2

Parameter	Value	Units
η_0^a	0.1101	pg of VEGF per pg of VEGFR2-VEGF-VEGFR2 complex
η_1^a	0.2250	pg of VEGF per pg of receptor monomer
η_2^a	0.1837	pg of VEGF per pg of VEGFR2-VEGF complex
η_3^a	0.8163	pg of receptor monomer per pg of VEGFR2-VEGF complex
η_4^a	0.4494	pg of receptor monomer per pg of VEGFR2-VEGF-VEGFR2 complex
η_5^a	1.2250	pg of VEGFR2-VEGF complex per pg of receptor monomer
η_6^a	0.5506	pg of VEGFR2-VEGF complex per pg of VEGFR2-VEGF-VEGFR2 complex
η_7^a	2.2250	pg of VEGFR2-VEGF-VEGFR2 complex per pg of receptor monomer

$$\frac{dA}{dt} = -2\,\eta_1^a\,k_{f1}^a\,A\,R_a + \eta_2^a\,k_{r1}^a\,C_a \tag{4.5}$$

$$\frac{dR_a}{dt} = -2\,k_{f1}^a\,A\,R_a + \eta_3^a\,k_{r1}^a\,C_a - k_{f2}^a\,C_a\,R_a + 2\,\eta_4^a\,k_{r2}^a\,D_a + 2\,\eta_4^a\,k_p^a\,D_a \tag{4.6}$$

$$\frac{dC_a}{dt} = 2\,\eta_5^a\,k_{f1}^a\,A\,R_a - k_{r1}^a\,C_a - \eta_5^a\,k_{f2}^a\,C_a\,R_a + 2\,\eta_6^a\,k_{r2}^a\,D_a \tag{4.7}$$

$$\frac{dD_a}{dt} = \eta_7^a\,k_{f2}^a\,C_a\,R_a - 2\,k_{r2}^a\,D_a - k_p^a\,D_a \tag{4.8}$$

4.3.2 Parameter Estimation

The parameter values for VEGF binding dynamics are taken from studies on vascular endothelial cells from the human colon. Equilibrium disassociation constant $k_D^a = k_{r1}^a/k_{f1}^a$ has a value of 30.375 pg per mm^3 of VEGF (152). Cell-free experiments

using human ligand and immobilized human receptors in (78), give $k_{f1}^a = 6.9120$ per VEGF concentration per day and $k_{r1}^a = 11.5776$ per day. However, these give a value of 1.675 pg per mm^3 of VEGF for k_D^a, thus both of these individual rates are scaled by the same constant to get $k_{f1}^a = 1.6232$ per VEGF concentration per day and $k_{r1}^a = 49.3025$ per day so that their ratio is 30.375 pg per mm^3 of VEGF. Due to a lack of experimental data, the values for k_{f2}^a and k_{r2}^a are difficult to estimate, and a sensitivity analysis on the effects of varying these parameters is carried out. We do however, make the following assumption regarding bounds for their values: VEGF binding is known to induce receptor aggregation; therefore, it is reasonable to assume that the rate of formation of a dimerized receptor-ligand complex (k_{f2}^a) is greater than the rate of formation of a monomer receptor-ligand complex (k_{f1}^a). It should be noted that choosing $k_{f2}^a >> k_{f1}^a$ would approximately simulate the static pre-dimerization case. Further, because the dimerized complex D_a is the signaling form of the receptor, it is reasonable to assume that D_a is more stable than the monomer complex C_a. Therefore k_{r2}^a is taken to be less than k_{r1}^a. For baseline simulations, k_{f2}^a is chosen to be greater than k_{f1}^a by a factor of about 100, and likewise, k_{r2}^a is taken to be slower than k_{r1}^a by a factor of about 100. It takes on average, 90 minutes for the receptor-ligand complexes to be internalized and the receptors to be re-released out of the cell (152), which gives a value for k_p^a. The average receptor density per cell R_t^a is taken to be 230000 (78). The tissue half-life of VEGF is about 64 minutes (132).

4.4 Results

4.4.1 Dimeric versus Monomeric Uptake of VEGF in In Vitro Conditions

The model of angiogenesis developed in subsequent chapters is motivated by work carried out by Nör et al (97; 98; 99). Parameter estimation for the full model of angiogenesis presented in Chapters VI and VII is based on in vitro experiments

described therein. These tend to be typically low cell density experiments, by which we mean that VEGF concentrations are far in excess of cell, and hence receptor densities. This is typical of most in vitro settings, including those described in the Mac Gabhann papers. In these cases, monomeric uptake of VEGF by VEGFR2 differs significantly from dimeric uptake. To see this, cell density is fixed at 200 cells per mm^3. Initial concentration of free VEGF is taken as 50 pg per mm^3. These numbers correspond to initial cell and chemokine concentrations in the in vitro experiments in (98).

Figure 4.5 shows graphs of fractional occupancy of activated receptors and free VEGF density versus time, for the two kinds of uptake of VEGF. It can be seen that whilst there does not appear to be any significant difference in free VEGF concentrations (Figure 4.5B), the fractional occupancies of activated cell surface receptors are very different (Figure 4.5A). If the natural decay of VEGF is ignored, and ligand-receptor complexes are assumed not to internalize, the fractional occupancy of receptors reaches a steady state that is about 59% higher in the dimer model than the monomer model of VEGF uptake (Figure 4.5C). Correspondingly, the concentration of VEGF in activated receptor complexes reaches a steady state that is about 25% higher in the monomer model than the dimer model of VEGF uptake. Again, the free VEGF densities do not differ significantly (Figure 4.5D). These results can be explained as follows. In the dimer model, each VEGF molecule occupies two receptors, as opposed to just the one in the monomer model. The assumed stability of the dimer complex may be a contributing factor to the observed differences as well. Free VEGF densities however remain fairly similar across all simulations because in this framework, there is a much higher VEGF concentration than available receptor density.

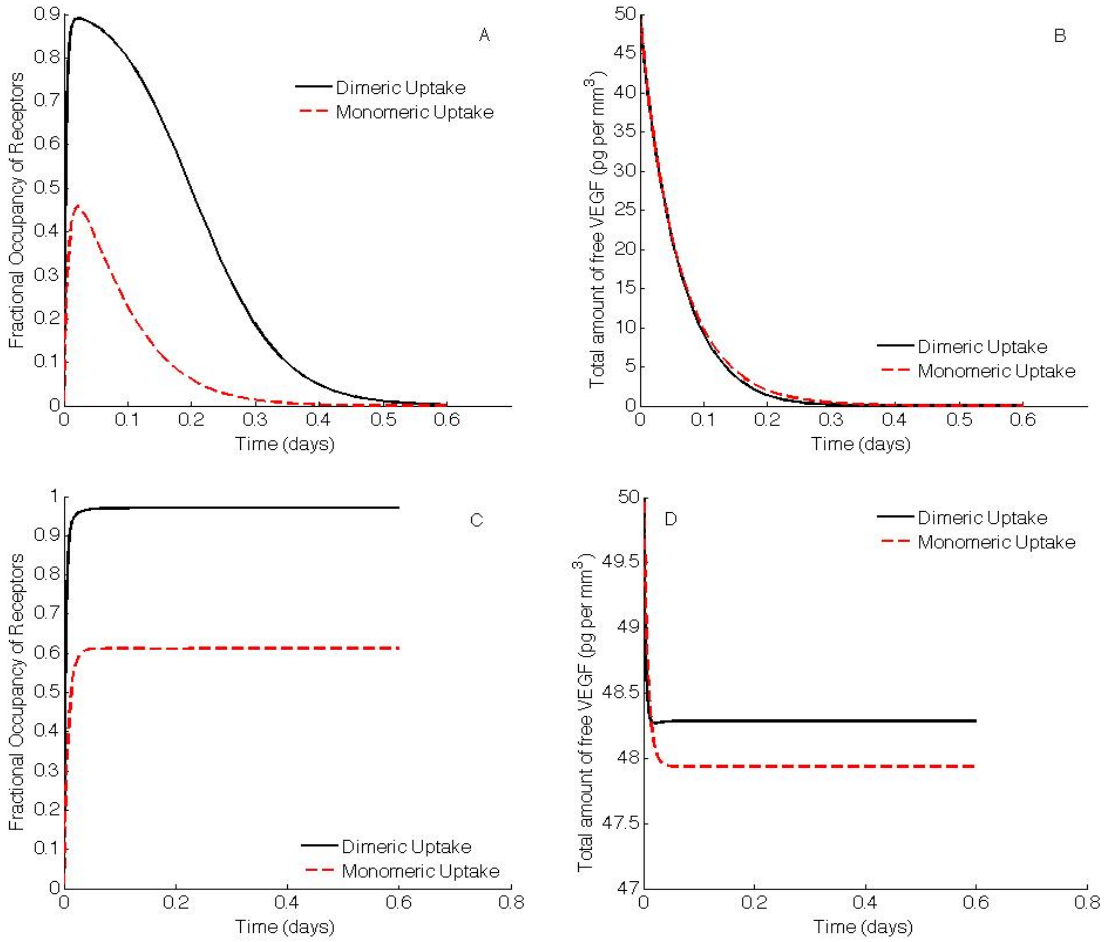

Figure 4.5: Dimeric (black) versus monomeric (red) uptake by of VEGF by VEGFR2 for low cell density experiments, in the case when natural decay of VEGF and receptor-ligand complex internalization are included (A,B), and when they are excluded (C,D). (A,B) VEGFR2 dimerization predicts higher fractional occupancies of receptors (A), even though free VEGF concentration profiles in the two forms of uptake are very similar (B). (C,D) Ignoring loss of VEGF due to natural decay and receptor-ligand complex internalization predicts a steady state of fractional occupancies of VEGFR2 that is 59% higher in the dimeric uptake model as compared to the monomeric uptake model (C). Free VEGF concentration profiles remain similar (D).

Next, the effects of varying the association rate constant k_{f2}^a, and disassociation rate constant k_{r2}^a on fractional occupancy of VEGFR2 and free VEGF density is studied in the dimer model (Figure 4.6). As k_{f2}^a is varied through a range of values from $k_{f1}^a \times 10^2$ to $k_{f1}^a \times 10^0$, with k_{r2}^a kept constant, fractional occupancy of receptors varies significantly, with maximum values ranging from 0.89 to 0.35, an

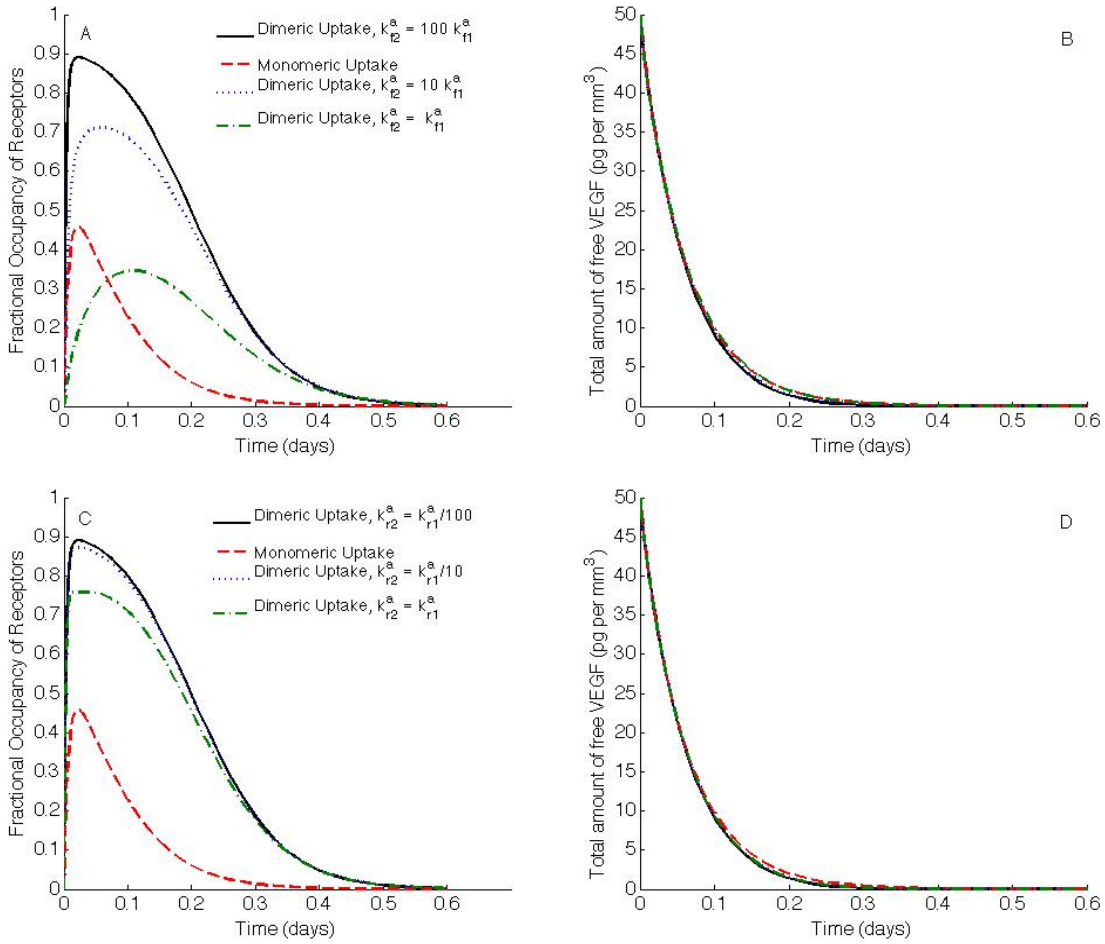

Figure 4.6: Effect of association rate constant k^a_{f2}, and disassociation rate constant k^a_{r2} on dimeric uptake of VEGF, for low cell density experiments. (A) As the value of k^a_{f2} is increased from $k^a_{f1} \times 10^2$ to $k^a_{f1} \times 10^0$, keeping k^a_{r2} fixed, fractional occupancies of VEGFR2 vary from 89% to 35%. (B) Free VEGF concentrations remain unaffected. (C) As the value of k^a_{r2} is increased from $k^a_{r1}/10^2$ to $k^a_{r1}/10^0$, keeping k^a_{f2} constant, fractional occupancies of VEGFR2 vary from 89% to 76%. (D) Again, Free VEGF concentrations remain unaffected.

overall change of 61%, as seen in Figure 4.6A. Correspondingly, maximum values of bound VEGF density vary from 1.50 pg per mm^3 to 0.59 pg per mm^3. However, free VEGF concentration does not differ appreciably (Figure 4.6B). The rate constant k^a_{f2} is a measure of how rapidly a VEGFR2 monomer-VEGF complex binds another VEGFR2 monomer, to create an activated complex. Thus, in cells where clustering of VEGF receptors is observed, k^a_{f2} would have a higher value. Consequently, higher

levels of receptor activation would be predicted. Finally, k_{r2}^a is varied through a range of values from $k_{r1}^a/10^2$ to $k_{r1}^a/10^0$, with k_{f2}^a kept constant. Maximum values of the fractional occupancy of receptors vary from 0.89 to 0.76, an overall change of only 14%, as seen in Figure 4.6C. Correspondingly, maximum values of bound VEGF densities range from 1.50 pg per mm^3 to 1.28 pg per mm^3. Thus k_{r2}^a does not appear to have a significant impact on the uptake of VEGF. Again, free VEGF concentration appears unaffected (Figure 4.6D).

4.4.2 Simulating VEGF-VEGFR2 Interactions in In Vivo Conditions

In vivo experiments may involve higher cell numbers per unit volume, that is, high receptor density compared to VEGF concentration. In these cases, when natural decay of VEGF and recycling of bound receptors is included in the model, monomeric uptake of VEGF does not appear to differ significantly from dimeric uptake. To see this, cell density is fixed at 17000 cells per mm^3. Initial concentration of free VEGF is taken as 50 pg per mm^3. These numbers correspond to initial cell and chemokine concentrations in the in vivo experiments in (98). Figure 4.7 shows graphs of fractional occupancy of activated receptors and free VEGF density versus time, for the two kinds of uptake of VEGF. Now, the receptor occupancies do not appear to significantly differ in the two models (Figure 4.7A), although free VEGF concentration decays faster for dimeric uptake of VEGF (Figure 4.7B). However, maximum VEGF bound in activated complexes is 4.51 pg per mm^3 in the dimer model, as opposed to 3.87 pg per mm^3 in the monomer model - a difference of 17%. This may still be enough to influence simulation results when one uptake law is chosen over the other. If the natural decay of VEGF is ignored, and ligand-receptor complexes are assumed not to internalize, the receptor occupancy reaches a steady state that is about 10% lower in the monomer model than the dimer model of VEGF uptake (Figure 4.7C).

The association rate constant k_{f2}^a and disassociation rate constant k_{r2}^a do not have a discernible impact on VEGF uptake (results not shown).

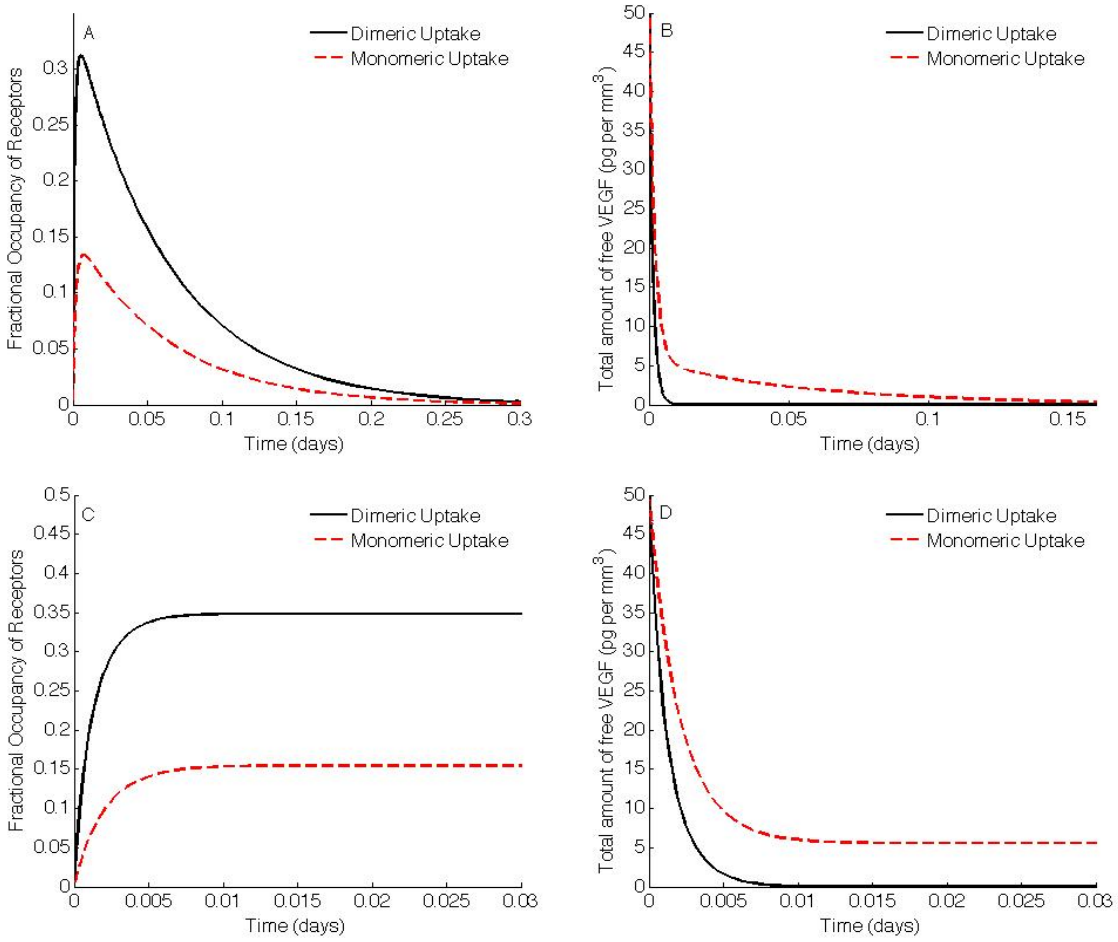

Figure 4.7: Dimeric (black) versus monomeric (red) uptake by of VEGF by VEGFR2 for high cell density experiments, in the case when natural decay of VEGF and receptor-ligand complex internalization are included (A,B), and when they are excluded (C,D). (A,B) VEGFR2 dimerization predicts higher fractional occupancies of receptors (A), and a faster decay in free VEGF concentration (B). (C,D) Ignoring loss of VEGF due to natural decay and receptor-ligand complex internalization predicts a steady state of fractional occupancies of VEGFR2 that is 10% higher in the dimeric uptake model as compared to the monomeric uptake model (C). Free VEGF concentration shows a rapid decay in the dimeric uptake model as compared to the monomeric uptake model (D).

4.4.3 The Quasi Steady State Assumption

In 1989, Segel and Slemrod (131) published a detailed perturbation analysis of the quasi steady state assumption (QSSA) in the case of a monomeric substrate-enzyme binding model. This assumption states that if the rate of reaction is approximately constant over the time period of interest, then some of the dependant variables (the enzyme, or in our case the free and complexed receptor densities) may be regarded in steady state with respect to the instantaneous values of the other dependant variable (the substrate or free VEGF concentration). The rationale behind the QSSA is as follows. If the substrate is in sufficiently large quantities, it will quickly bind to free enzyme, in what is called the 'pre steady-state period'. A steady state is then achieved for which the enzyme is always saturated with substrate. Segel and Slemrod argue that this naturally introduces two time-scales into the problem - a fast time-scale corresponding to the pre steady-state period, and a slow time-scale, corresponding to the decay of the substrate. The QSSA is then valid only if the slow time-scale is much larger than the fast time-scale. This leads to the identification of a parameter, say ϵ, representing the ratio of the fast to the slow time-scales. Once the reaction equations are non-dimensionalized, with the time variable being rescaled by the slow time-scale, standard methods of singular perturbation theory can then applied to obtain series solutions of the resulting enzyme and substrate concentrations, in terms of ϵ. If $\epsilon << 1$, first order and higher terms can be ignored, so that the enzyme concentration remains approximately constant over the slow time-scale. This is equivalent to assuming the rate of reaction of the enzyme is negligible. The main result in (131) is the identification of $\epsilon = E_0/(K_m + S_0)$, where S_0 is initial substrate concentration, E_0 is initial enzyme concentration, and K_m is the concentration of the substrate at which half the true maximum velocity of

the enzyme-substrate reaction is achieved , which is often called Michaelis-Menten constant for the binding of substrate to enzyme.

To reduce complexity of our model of VEGF binding VEGR2, the possibility of simplifying the reaction equations (4.5)-(4.8) using the QSSA as described above, is investigated. In order to calculate the slow and fast time scales, an analytical solution of the non-linear system of differential equations (4.6)- (4.8) is required. However, such a solution is difficult to obtain, and it is not possible to replicate the analysis in (131) for our dimeric substrate-enzyme binding model. Instead, we adopt a numerical approach to test the validity of the QSSA.

As per the discussion above, if the QSSA is valid, the rates of change of free receptors (dR_a/dt), intermediate complex (dC_a/dt), and dimerized receptor-VEGF complex (dD_a/dt) can be ignored to first order. The left hand sides of equations (4.6)-(4.8) are set to zero, and the equations solved to obtain R_a, C_a and D_a in terms of A. As the EC population is held fixed, with no cell death or multiplication assumed to be occurring, C_a may be eliminated using conservation of total receptor numbers: $R_a+\eta_3^a C_a+2\eta_4^a D_a = R_t^a\, M_0$, where R_t^a is the total number of receptors per endothelial cell and M_0 is EC density. The remaining two equations can be scaled to appropriate units and added to get the following expression for R_a.

$$-2\,k_{f1}^a\,A\,R_a + k_{r1}^a\,(R_t^a\,M_0 - R_a - 2\,\eta_4^a\,D_a) + k_p^a\,\eta_4^a\,D_a = 0 \tag{4.9}$$

$$\Rightarrow \quad k_{r1}^a\,R_t^a\,M_0 - (2\,k_{f1}^a\,A + k_{r1}^a)\,R_a + \eta_4^a\,(k_p^a - 2\,k_{r1}^a)\,D_a = 0 \tag{4.10}$$

We solve for R_a to get:

$$\Rightarrow \qquad R_a = \frac{k^a_{r1}\, R^a_t\, M_0 + \eta^a_4\, (k^a_p - 2\, k^a_{r1})\, D_a}{2\, k^a_{f1}\, A + k^a_{r1}} \tag{4.11}$$

$$= \alpha + \beta\, D_a, \qquad \text{say} \tag{4.12}$$

An expression for D_a can now be obtained from (4.8) as follows.

$$\eta^a_7\, \eta^a_5\, k^a_{f2}\, (R^a_t\, M_0 - R_a - 2\, \eta^a_4\, D_a)\, R^a = (2\, k^a_{r2} + k^a_p)\, D_a \tag{4.13}$$

$$\Rightarrow \qquad (R^a_t\, M_0 - \alpha - (\beta + 2\, \eta^a_4)\, D_a)\, (\alpha + \beta\, D_a) = \gamma\, D_a \text{ say} \tag{4.14}$$

$$\Rightarrow \qquad D_a = \frac{-2\,\alpha\,\delta - \gamma + \theta_a\,\beta + \sqrt{(2\,\alpha\,\delta + \gamma - \theta_a\,\beta)^2 + 4\,\alpha\,\beta\,(\eta^a_4 + \delta)\,(\theta_a - \alpha)}}{2\,\beta\,(\eta^a_4 + \delta)} \tag{4.15}$$

where,

$$\alpha = \frac{k^a_{r1}\, R^a_t}{2\, k^a_{f1}\, A + k^a_{r1}} \tag{4.16}$$

$$\beta = \frac{\eta^a_4\, (k^a_p - 2\, k^a_{r1})}{2\, k^a_{f1}\, A + k^a_{r1}} \tag{4.17}$$

$$\gamma = \frac{2\, k^a_{r2} + k^a_p}{\eta^a_5\, \eta^a_7\, k^a_{f2}} \tag{4.18}$$

$$\delta = \eta^a_4 + \beta \tag{4.19}$$

$$\theta_a = R^a_t\, M_0 \tag{4.20}$$

Adding equations (4.6) and (4.8) gives $-2\, k^a_{f1}\, A\, R_a + \eta^a_3\, k^a_{r1}\, C_a = -k_p\, \eta^a_4\, D_a$, and this can be used in (4.5) to get the rate of change of free VEGF concentration.

$$\frac{dA}{dt} = -2\, \eta^a_1\, k^a_{f1}\, A\, R_a + \eta^a_2\, k^a_{r1}\, C_a \tag{4.21}$$

$$= -\eta^a_0\, k^a_p\, D_a \tag{4.22}$$

where D_a has the expression given in (4.15). As proven in (131), the QSSA is valid when receptor concentration is low compared to ligand concentration. We now test whether this assumption is valid in the two cases we have considered - low and high cell density experiments. For the first set of simulations, cell density is fixed at 200 cells per mm^3, and initial VEGF concentration is taken as 50 pg per mm^3. Figure 4.8A,B compares receptor occupancy, and free VEGF concentration respectively for the full versus the QSSA model. Internalization and subsequent recycling of receptors is included, and natural decay of VEGF is ignored. The two models appear to be in excellent agreement, and the QSSA is valid, in this case. However, if the natural decay of VEGF is now included, while free VEGF concentrations are still in good agreement (Figure 4.8C), the fractional receptors occupancy begins to differ (Figure 4.8D).

Next, the cell density is increased to 17000 cells per mm^3, keeping the initial VEGF concentration at 50 pg per mm^3. As before, activated receptor complex internalization is included initially, while natural decay of VEGF is ignored. In this case, the QSSA is not valid. This can be seen from Figure 4.9A,B, where time course data of both receptor occupancy and free VEGF concentration are very different in the two models. Including VEGF decay has little effect on receptor occupancy (Figure 4.9C). However, free VEGF concentration goes to zero marginally quicker than in the previous case (Figure 4.9D).

4.4.4 A Comparison of the LID and the 1:1 Binding Models

Finally, the validity of the 1:1 uptake of VEGF as described in Mac Gabhann et al (78; 79; 80; 81) is tested for the two experimental cases that we are considering. As mentioned earlier, the 1:1 model makes the simplifying assumption that a VEGF molecule binds to pre-dimerized receptors in a single step. Figure 4.10 presents a

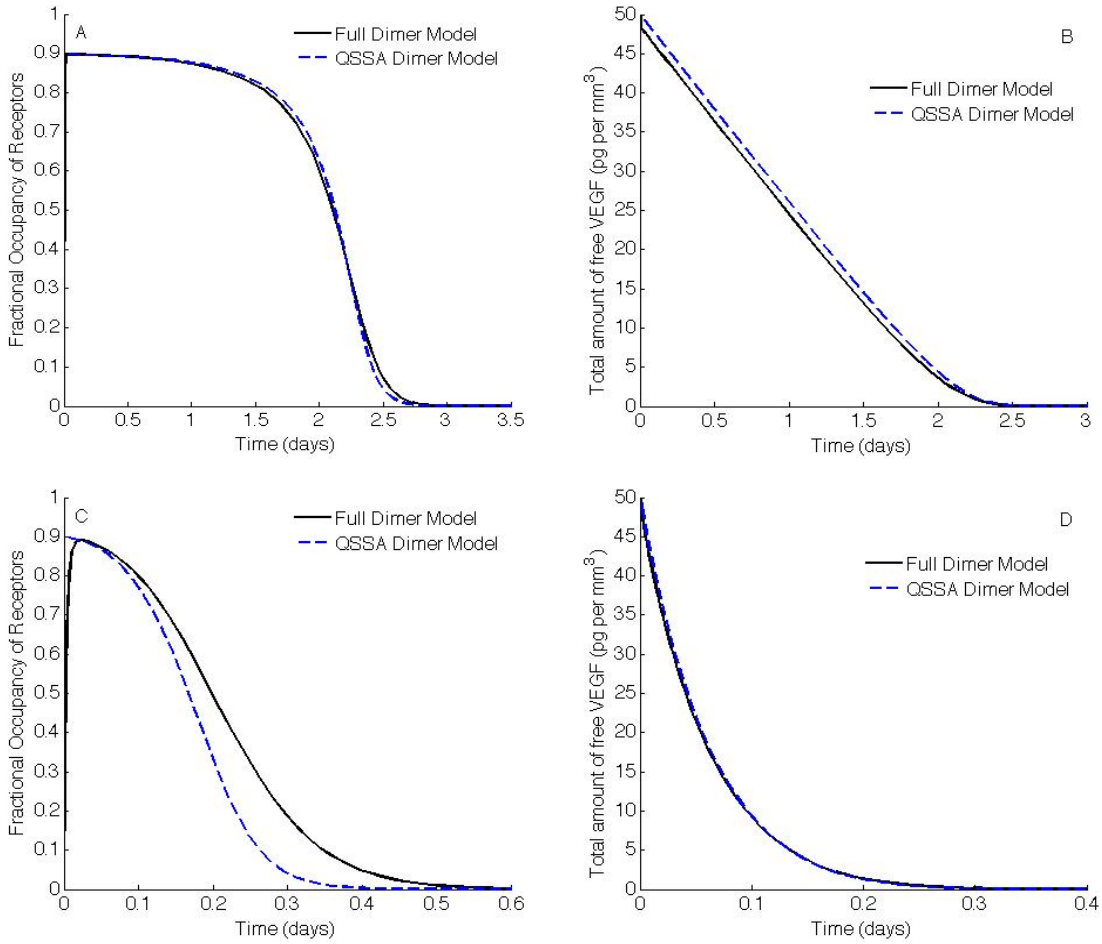

Figure 4.8: Full dimer model (black) versus QSSA (blue) uptake by of VEGF by VEGFR2 for low cell density experiments, in the cases when natural decay of VEGF is excluded (A,B), or included (C,D). (A,B), Both, fractional occupancies of VEGFR2 (A) and free VEGF concentration (B) have similar profiles when the full dimer model is solved or the QSSA is applied. (C,D) However, including the natural decay of VEGF predicts different time courses for fractional occupancies of VEGFR2 in the cases when the full dimer model is solved, as compared to applying the QSSA (C). Free VEGF concentration profiles still appear to be similar (D).

schematic of the 1:1 model.

In the first set of simulations, the low cell density environment is considered, and predictions of the 1:1 model are compared to the full dimer or LID model (Figure 4.11). If the natural decay of VEGF and the internalization of activated receptors is included, we observe that while free VEGF concentrations for both models are sim-

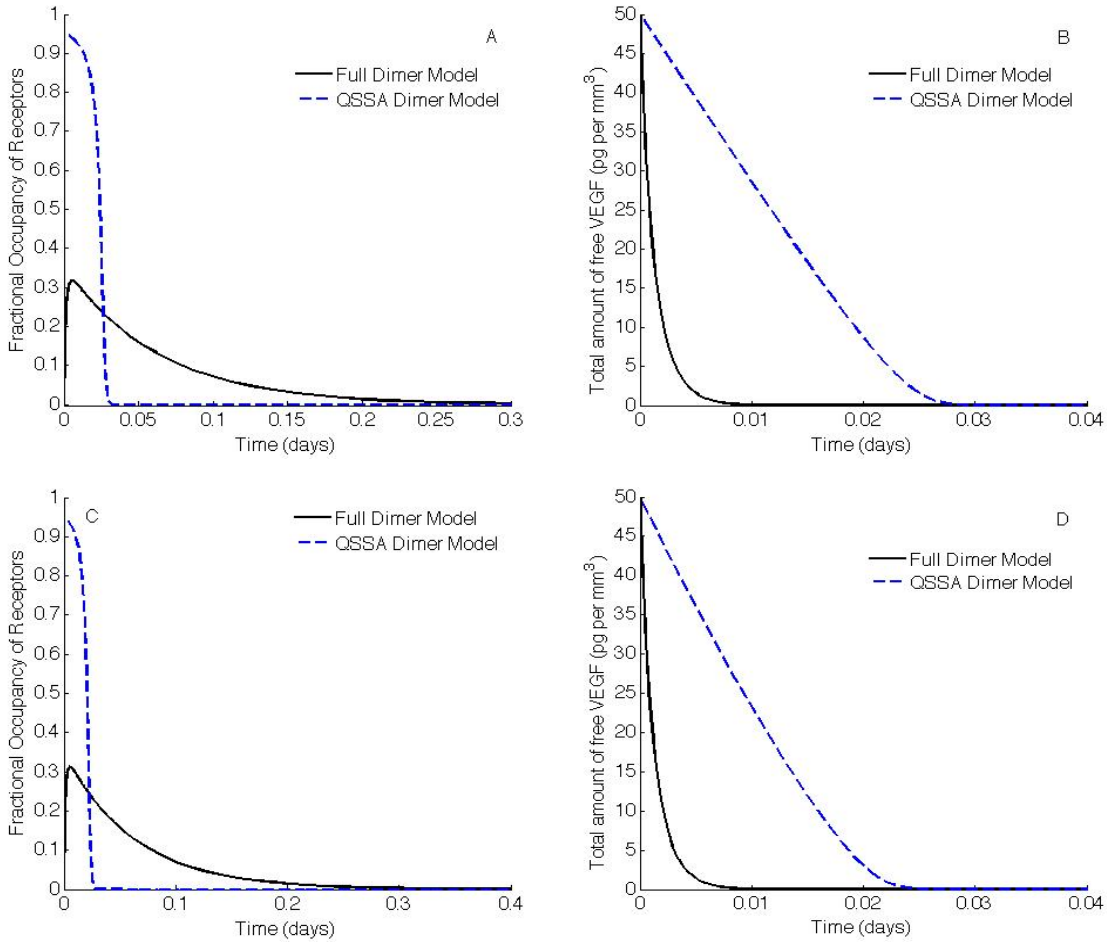

Figure 4.9: Full dimer model (black) versus QSSA (blue) uptake by of VEGF by VEGFR2 for high cell density experiments, in the cases when natural decay of VEGF is excluded (A,B), or included (C,D). (A,B), The QSSA no longer appears to be valid, as the fractional occupancies of VEGFR2 follow divergent temporal profiles when the full dimer model is solved, as compared to applying the QSSA (A). Free VEGF concentrations are also predicted to be dissimilar in the two cases (B). (C,D), Including the natural decay of VEGF does not change the results observed in the previous case. Both receptor occupancies (C) and free VEGF concentrations (D) follow different profiles when the full dimer model is solved.

ilar (Figure 4.11B), there is a marked difference in receptor occupancies. In the 1:1 case, the maximum occupancy of receptors is only 52% of that in the case of LID (Figure 4.11A). The two models would be in agreement only if the disassociation constant k_D^a in the 1:1 case were decreased to 0.122 pg per mm^3 of VEGF, which is much lower even than the value of 1.675 pg per mm^3 of VEGF considered in (78). To

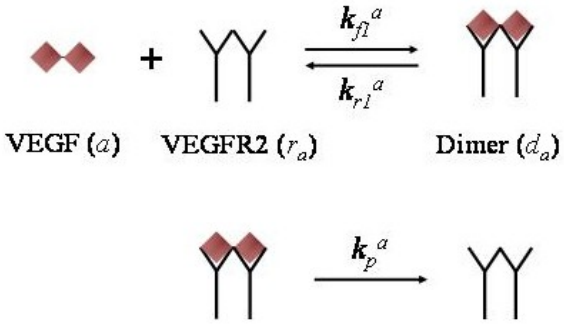

Figure 4.10: VEGF uptake by pre-dimerized endothelial cell surface receptors, as per the 1:1 model of Mac Gabhann et al (81).

replicate conditions in (81), we now ignore natural decay of VEGF. In this case, both fractional occupancy of receptors (Figure 4.11C), and unbound VEGF concentration (Figure 4.11D) profiles are highly dissimilar for the two models. In the LID case, VEGF levels decay to zero much faster compared to the 1:1 case. These results are in direct contrast to those observed in (81).

Finally, a high cell density environment is simulated. When natural decay of VEGF is included, both models predict similar receptor occupancies (Figure 4.12A), although unbound VEGF profiles are quite different (Figure 4.12B). If the decay of VEGF is ignored, the profiles of receptor occupancy begin to diverge from each other (Figure 4.12C), even though their maximum values differ only by 5%.

4.5 Discussion

VEGF is one of the most potent, specific and intensively studied tumor angiogenic factors. Together with its receptors, it plays a crucial role in vascular development, both pathologic, as well as physiological. We have developed a model of VEGF's interaction with VEGFR2, investigating in particular, the importance of incorporating ligand-induced receptor dimerization and activation in models of VEGF's role in

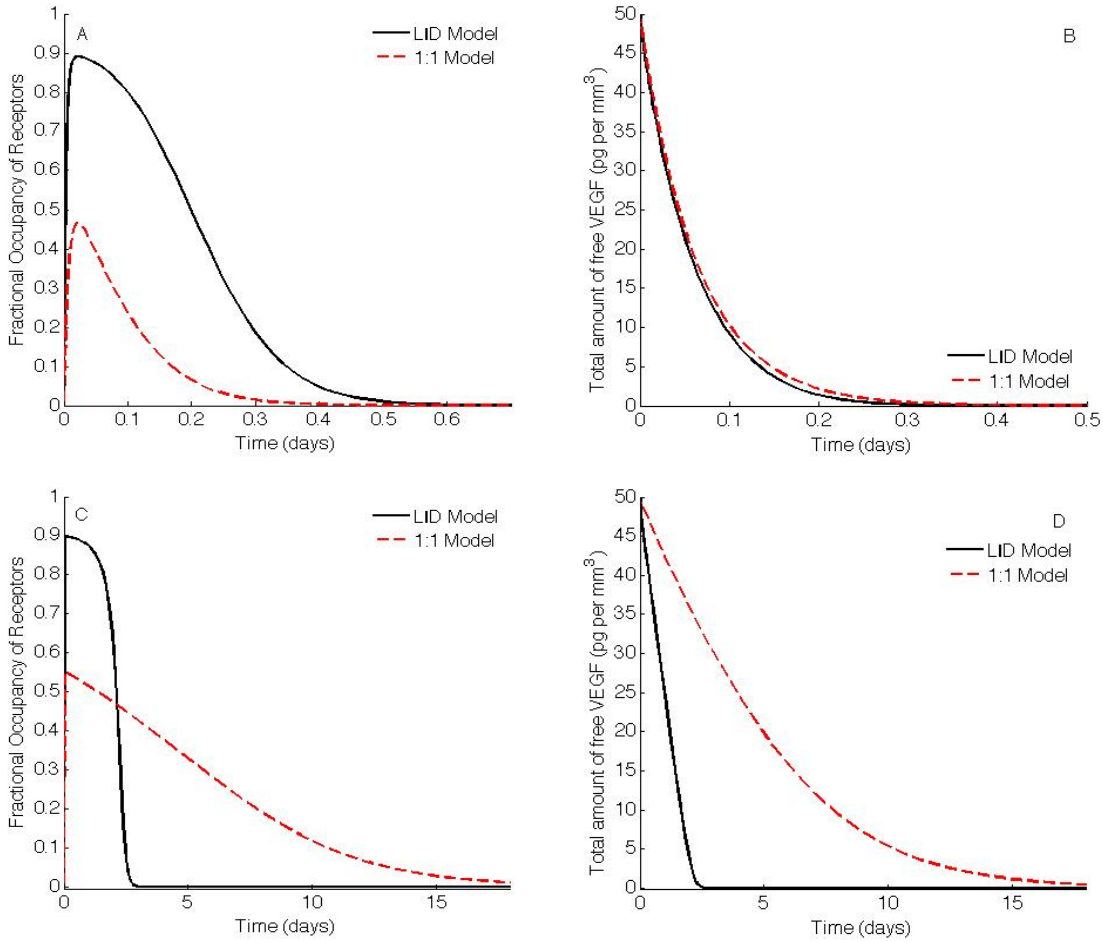

Figure 4.11: A comparison of the LID model (black) and 1:1 model (red) for low cell density experiments. If the natural decay of VEGF and receptor-ligand complex internalization are included, maximum receptor occupancy in the 1:1 model is only 52% of the maximum occupancy in the LID case (A). Free VEGF profiles look similar in both cases (B). However, both fractional occupancies (C) as well as free VEGF concentration (D) follow very dissimilar profiles in the two models if natural decay of VEGF is excluded.

angiogenesis.

The VEGF receptors, like all receptor tyrosine kinases, require dimerization to be activated, ligand-independent pre-associated receptor dimers are not active (82). We therefore assumed ligand-induced dimerization to be the dominant mechanism by which VEGFR2 is activated by VEGF. The law of mass action was used to derive a system of ordinary differential equations governing the interactions between VEGF

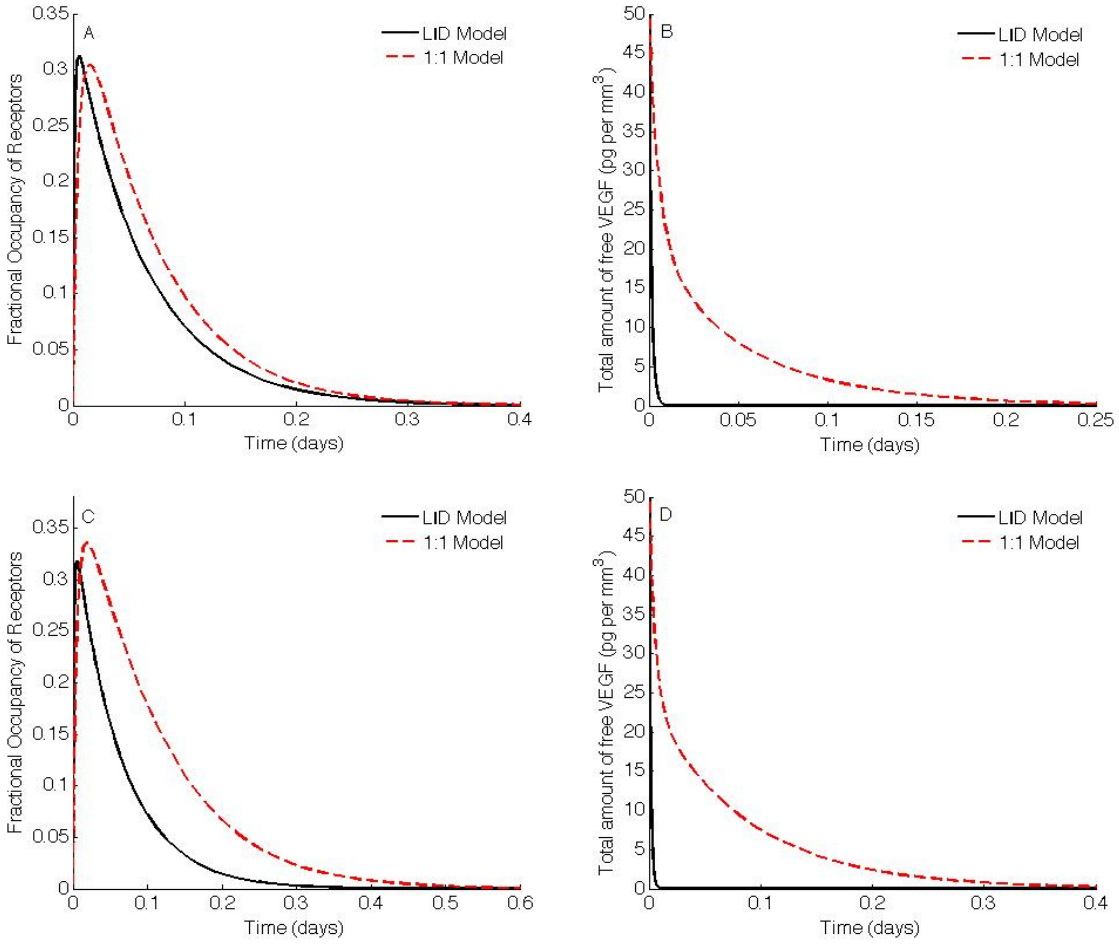

Figure 4.12: A comparison of the LID model (black) and 1:1 model (red) for high cell density experiments. If the natural decay of VEGF and receptor-ligand complex internalization are included, both models predict similar receptor occupancies (A), although free VEGF concentrations are very different (B). Ignoring the decay of VEGF causes the profiles of receptor occupancies to diverge for the two models (C). Free VEGF profiles remain very different (D).

and VEGFR2. Endothelial cells have a pro-angiogenic response to VEGF due to the presence of activated receptors on their surfaces. Despite this, most existing models of tumor or wound-healing angiogenesis incorporate cellular response to angiogenic cues, as being a function of free or unbound chemokine concentration. Therefore, we kept track of temporal changes in the fraction of activated receptors on the cell surface, as well as free VEGF concentration in all our simulations.

In models of tumor induced angiogenesis including (73; 74; 75; 117), wherein details of VEGF-VEGF receptor interactions are included, the form of the loss term in the VEGF evolution equation is derived by assuming that VEGF binds and activates a receptor monomer. We tested the validity of this assumption, by presenting a comparison of the binding data obtained by assuming a monomeric uptake of VEGF, with that obtained from our model. Typically, parameters relating to EC response to VEGF that are used in models of angiogenesis occurring in vivo, are derived from in vitro experiments. Therefore, comparison of the monomeric and dimeric models was carried out for both cases. In simulations representing in vitro assays, where the initial concentration of VEGF was assumed to be much higher than cell density, free VEGF concentration profiles remained fairly similar for both models. These profiles were observed to diverge slightly when the cell density was taken to be high compared to initial VEGF concentration. This is typical of situations in vivo (80). However, the fractional occupancies of activated receptors followed very different trajectories in both in vitro, as well as in vivo simulations, especially if the natural decay of VEGF, and activated receptor complex internalization and subsequent recycling of receptors was ignored. These results underscore the fact that a free VEGF concentration-dependent endothelial cell response may not be a valid assumption. In fact, endothelial cells have a proliferative or chemotactic response dependant on the concentration of activated receptor complexes on their surface. Choosing the correct form of VEGF binding and uptake is essential for accurately capturing these cellular responses. A sensitivity analysis performed on the rate constants relating to the formation of the VEGF-VEGFR2 dimer complex, revealed that cells where receptors tend to cluster, rather than be distributed throughout the plasma membrane, exhibited higher levels of activation. This could have a significant impact on

models of angiogenesis incorporating VEGF, especially if cells only respond when their activation level reaches a minimum threshold.

Next, the possibility of using the quasi steady state assumption as a model simplification was investigated. In low cell density experiments where VEGF was far in excess of receptor density, the QSSA appeared to be valid. However, if the natural decay of VEGF was included, the QSSA was observed to be invalid. This is possibly due the fact that in this case, the time-scale of the decay of VEGF is lowered, and may no longer be significantly greater than the time-scale of VEGF binding to VEGFR2. As expected, the QSSA was found to be invalid in high cell density experiments. This was irrespective of inclusion of the natural decay of VEGF, possibly due to an abundance of VEGF receptors, causing it to be taken up by the ECs at a rate faster than the time-scale of its decay. These results accentuate the need for the inclusion of greater molecular level detail when considering the uptake of chemoattractants such as VEGF by ECs, and their resultant activation, in models of angiogenesis. Approximating the effects of the chemokines through their unbound concentrations, or using Michaelis-Menten like kinetics to approximate their uptake, could lead to erroneous results.

Finally, the validity of simplifying the model by assuming that a VEGF molecule bound to, and activated pre-dimerized receptors in a single step (1:1 model) was tested. In simulations of a low cell density environment, fractional occupancies of activated receptors were seen to differ considerably. The fraction of activated receptors in the ligand-induced dimerization (LID) model was higher than that in the 1:1 model. This could be due to the assumption made in the LID case, whereby the dimerized receptor-VEGF complex is assumed to be very stable as compared to the monomer receptor-VEGF complex. Ignoring the natural decay of VEGF had the

effect of causing free VEGF to decay faster in the LID case as compared to the 1:1 model. This could be due to additional sequestering of VEGF on the cell surface in the form of receptor monomer-VEGF complexes. These quickly form the more stable receptor dimer-VEGF complexes, which are then internalized into the cell. This intermediate step thus appears to facilitate the uptake of VEGF from the cell's environment, leading to a more rapid consumption of the chemokine. Simulations of a high cell density environment predicted a faster decay of VEGF in the LID case as compared to the 1:1 model, independent of the inclusion of natural decay of VEGF. As explained above, this difference can be accounted for by the facilitated uptake of VEGF by ECs in the LID model.

We have presented a detailed quantitative analysis of the validity of various assumptions commonly made in modelling VEGF interactions with VEGFR2. The results of our model evince the impact of incorporating ligand-induced dimerization on the binding of VEGF to VEGFR2, and the formation of active signaling receptor complexes. Simulations with various initial conditions demonstrate that receptor numbers and initial concentration of ligand have a considerable influence on the activation of ECs. During angiogenesis, both these variables are expected to be highly dynamic. This highlights the impact of incorporating molecular level detail on a model of cellular response to VEGF, say during angiogenesis. In Chapters V and VII, we develop models of intra-tumoral angiogenesis, in which VEGF is assumed to be the principle tumor-secreted chemokine. For the reasons outlined in this chapter, ligand-induced dimerization of VEGFR2 is applied to both these models. This is an improvement over existing models of angiogenesis is several ways. Our models incorporate a much higher level of biochemical detail. ECs are activated by, and respond to VEGF bound on their surface receptors, rather than to free VEGF. Fur-

ther, anti-angiogenic therapy which results in the decrease of EC population, or of VEGF concentrations, may easily be tested without worrying about the validity of the QSSA. Finally, the models are sensitive enough to differentiate response to inhibition of VEGFR2, from inhibition of the VEGF molecule itself. Thus, they provide a useful framework in which to test the potential of anti-VEGF therapies that may target VEGFR2 (for instance the small molecule inhibitor PTK787/ZK222584), or the VEGF molecule (for instance the humanized monoclonal anti-VEGF antibody Avastin).

CHAPTER V

The VEGF-Bcl-2-CXCL8 Pathway

5.1 Novel Experimental Techniques in Intra-tumoral Angiogenesis

Recent advances in tissue engineering have allowed for the development of novel approaches to study the in vivo growth of human blood vessels within a mouse model system. Human dermal microvascular endothelial cells (HDMECs) along with oral squamous cell carcinoma (OSCC-3) or Kaposi's Sarcoma (SLK) are transplanted into severe combined immunodeficient (SCID) mice on biodegradable polymer matrices, fabricated from poly-L-lactic acid (PLLA) (97; 98; 99) (Figure 5.1A). These matrices have an average pore diameter of 250 μm, which allows for easy penetration and entrapment of the HDMECs. The PLLA sponges thus function as temporary scaffolds that maintain transplanted cells in a defined space and therefore guide new tissue growth and organization. HDMECs transplanted in this way differentiate into functional human microvessels that anastomose with the mouse vasculature thus generating human tumors vascularized with human microvessels. A graphical representation of this experimental system is shown in Figure 5.1B. It is interesting to note that 7 days post transplantation, 60% of the microvessels within the implants test positive for being of human origin. At 14 days this proportion is reduced to approximately 25% (99).

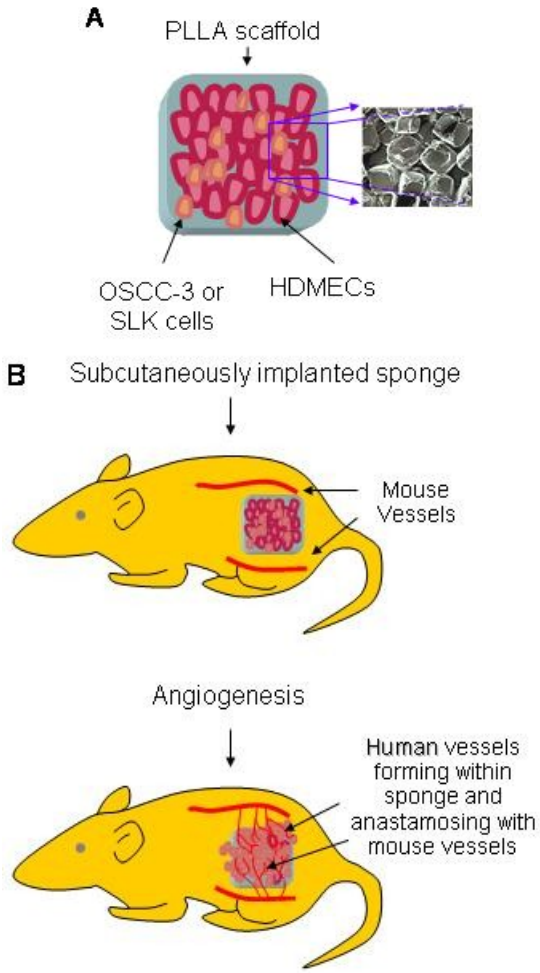

Figure 5.1: (A) Graphic representation of a poly-L-lactic acid matrix, seeded with HDMECs and OSCC-3 cells. The insert is a photograph showing HDMECs dispersed in the scaffold taken by a scanning electron microscope (96). (B) Graphic representation of the experimental system described in (96; 97; 98). HDMECs along with OSCC-3 or SLK cells are transplanted subcutaneously in the flank region of SCID mice. These implants eventually develop into human tumors, populated with human microvessels.

Using such experimental systems, Nör et al have shown that the pro-angiogenic growth factor VEGF mediates a strong survival signal to the HDMECs, by up-regulating the expression of the anti-apoptotic intracellular protein Bcl-2 (97). A series of experiments are carried out (described in (98)), in order to substantiate these findings. Briefly, HDMECs stably transduced to over-express Bcl-2, were implanted along with OSCC-3 in SCID mice. The resultant tumors were observed to

be significantly larger in volume and weight as compared with tumors in implants containing empty vector control HDMEC-LXSN and OSCC-3. (Figure 5.2C,D). Further, the implants populated with HDMEC-Bcl-2 and tumor cells displayed a higher degree of vascularization, and a reduction in the number of endothelial cells undergoing apoptosis, than implants containing HDMEC-LXSN and tumor cells.

Nör et al have also demonstrated that Bcl-2 can function as a proangiogenic signalling molecule, independent of its ability to enhance cell survival (59). It activates nuclear factor-κB (NF-κB), which regulates the expression of chemotactic cytokines or chemokines, by the cell. In particular, the activation of NF-κB results in up-regulated production and secretion of interleukin-8 (CXCL8) (98). CXCL8 is a proangiogenic chemokine that simulates both endothelial cell proliferation and migration (67; 136). Experiments designed to assess the contribution of CXCL8 expression to tumor growth in vivo, are described in (98). Briefly, SLK cells were implanted together with HDMECs in PLLA scaffolds, into SCID mice. Polyclonal antihuman CXCL8 antibody was delivered to these mice either by intraperitoneal injections given on alternate days, or locally by incorporating the antibody to the scaffolds before implantation. After 1 week of therapy, a 50% reduction in tumor weight compared to control implants, was reported in both cases. Mice treated systematically with i.p. injections showed a 33% reduction in tumor volume, whilst implants passively immunized by the anti-CXCL8 antibody showed a 50% reduction in tumor volume. Tumors treated with anti-CXCL8 antibody showed a dramatic reduction in intratumoral microvascular density, as can be seen in Figure 5.2A,B.

Thus, VEGF has been demonstrated to be the crucial mediator of downstream events that ultimately lead to enhanced endothelial cell survival and increased vascular density within many tumors. The newly discovered pathway involves up-

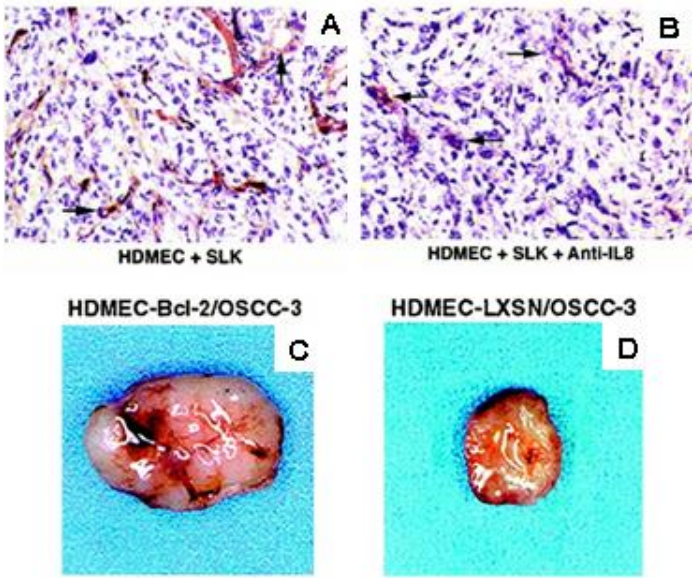

Figure 5.2: Results from experiments designed to assess the contribution of Bcl-2 and CXCL8 over-expression to tumor growth, taken from (97). (A,B), Anti-CXCL8 antibodies decrease intratumoral microvascular density and reduce tumor growth. Sponges seeded with HDMECs and SLK tumor cells were implanted in SCID mice. Polyclonal antihuman CXCL8 antibody was delivered by passive immunization with i.p. injections every 2 days. Photomicrographs of representative fields at $\times 200$ magnification showing CD34 (reddish-orange) staining of microvessels (black arrows) in tumors populated with HDMECs and SLK cells of SCID mice that were injected with PBS (A) or injected with a polyclonal antihuman CXCL8 antibody (B). (C,D), Tumors populated with HDMECs over-expressing Bcl-2 (C) are significantly larger than those populated with control HDMECs (D). Macroscopic view of representative implants at the time of retrieval from SCID mice are shown.

regulation of the anti-apoptotic protein Bcl-2, which in turn leads to increased production of CXCL8. The VEGF - Bcl-2 - CXCL8 pathway suggests new targets for the development of anti-angiogenic strategies, including short interfering RNA (siRNA) that silence the CXCL8 gene and small molecule inhibitors of Bcl-2. Quantitative modelling of this pathway may have profound implications for the development of novel therapies directed against specific proteins and chemokines to alter tumor progression.

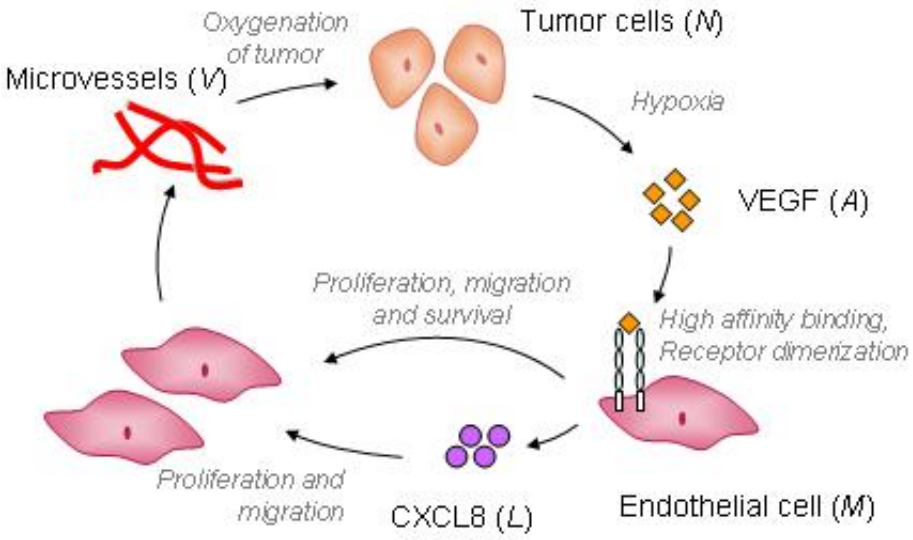

Figure 5.3: Tumor cells under conditions of hypoxia produce VEGF, which binds to endothelial cells via cell surface receptors and causes receptor dimerization and activation. This elicits a proliferative, chemotactic, and pro-survival response from the endothelial cells, and also results in up-regulation of CXCL8 production by them. CXCL8 in turn induces cell proliferation and chemotaxis. The endothelial cells begin to aggregate and differentiate into microvessels, that eventually fuse with mouse vessels and become blood borne, resulting in oxygenation of the tumor.

5.2 Model Development

Mathematical models of intra-tumoral angiogenesis have been developed in a number of papers including (5; 11; 24; 27; 53; 73; 74; 75; 94; 103; 116; 118; 133; 140; 145). The focus of these studies has mainly been the growth of capillary sprout tips or the initiation of capillary sprout formation from pre-existing vasculature in close proximity of a tumor. Here, we develop a quantitative model based on the experiments in (97; 98), wherein the vasculature that develops within the tumor space arises from free human endothelial cells, rather than from pre-existing mouse vessels. Therefore, this model needs to capture the process of microvessel formation from individual endothelial cells which align themselves to form blood vessels, which then anastomose with the existing mouse vasculature. A primary objective of our modelling is to better understand the precise role the VEGF - Bcl-2 - CXCL8 pathway plays in tumor

development and to predict the anti-angiogenic effect of the therapeutic blockade of VEGF, CXCL8, and Bcl-2 at early and late stages of tumor progression.

The mathematical model describes the temporal changes in tumor cell density $N(t)$, HDMEC density $M(t)$, free VEGF concentration $A(t)$, free CXCL8 concentration $L(t)$, and microvessel density $V(t)$. A system of delay differential equations is used to model the evolution of these species with time. A partial model schematic is shown in Figure 5.3. The different components of the model equations, beginning with the effects of oxygen and blood-bearing vessels on growing tumor cells, followed by the molecular events associated with the chemical mediators as well as the endothelial cell response to these chemokines, and finally the microvessel formation rate are discussed below, along with the assumptions that underlie them.

5.2.1 Tumor Cell Equation

Following (44; 155), an empirical model is used to govern tumor cell growth, as given in equation (5.1). The tumor cells proliferate and undergo apoptosis at rates which depend on the local oxygen concentration, C. As oxygen concentration increases to a maximum value (normoxia), the rate of tumor cell proliferation increases until it reaches a maximum value, while the programmed cell death rate decreases to a minimum level. The cell death rate also reflects the limited carrying capacity of the environment.

$$\frac{dN}{dt} = r_1 \frac{C^2}{C_1^2 + C^2} N - r_2 \left(1 - \sigma \frac{C^2}{C_2^2 + C^2}\right) N^2 \tag{5.1}$$

To simplify the model, oxygen concentration is treated as a function of blood-bearing vessel density. That is, oxygen is supplied to the implant by the microvessels that have blood flow established in them. The exact form relating the oxygen density C

and microvessel density V is taken from (94), and is given in equation (5.2).

$$C = C(V) = C_m \frac{V_0 + V}{k + V_0 + V} \tag{5.2}$$

Here, C_m is the maximum oxygen concentration, under normoxia (20% oxygen (44)). Because mouse vessels surround the scaffold, and some oxygen may diffuse through to the tumor cells from these, a fixed minimum vessel density V_0 is assumed in the region of the implant.

5.2.2 VEGF Uptake and Binding

A model for the binding of VEGF to receptors (VEGFR2), their subsequent dimerization, and activation, has already been developed in Chapter IV. Briefly, A is free VEGF concentration, R_a is VEGFR-2 density, C_a is density of the complex formed when VEGF binds a single molecule of VEGFR-2, and D_a is density of the complex formed when VEGF binds two receptor molecules. As before, the units of concentration have been chosen as pg per mm^3. This introduces scaling factors η_i^a that represent ratios of the weights of the different molecules involved in the reaction.

$$\begin{aligned} \frac{dA}{dt} &= -2\,\eta_1^a\,k_{f1}^a\,A\,R_a + \eta_2^a\,k_{r1}^a\,C_a - \lambda_a\,A \\ &\quad + r_3\,N\left(1 + \tanh\left(\frac{V_{char} - (V + V_0)}{\epsilon}\right)\right) \end{aligned} \tag{5.3}$$

$$\frac{dR_a}{dt} = -2\,k_{f1}^a\,A\,R_a + \eta_3^a\,k_{r1}^a\,C_a - k_{f2}^a\,C_a\,R_a + 2\,\eta_4^a\,k_{r2}^a\,D_a + 2\,\eta_4^v\,k_p^a\,D_a \tag{5.4}$$

$$\frac{dC_a}{dt} = 2\,\eta_5^a\,k_{f1}^a\,A\,R_a - k_{r1}^a\,C_a - \eta_5^a\,k_{f2}^a\,C_a\,R_a + 2\,\eta_6^a\,k_{r2}^a\,D_a \tag{5.5}$$

$$\frac{dD_a}{dt} = \eta_7^a\,k_{f2}^a\,C_a\,R_a - 2\,k_{r2}^a\,D_a - k_p^a\,D_a \tag{5.6}$$

Also included in equation (5.3) is the rate of decay λ_a of VEGF in tissue. (The tissue half-life of VEGF is about 64 minutes (132)). Further, oxygen tension has been

shown to play a key role in regulating the expression of VEGF in tumor cells (124; 135). Briefly, under conditions of hypoxia, the intracellular levels of hypoxia inducible factor-1α (HIF-1α) are up-regulated. This results in the initiation of the transcription of various target genes including VEGF (124). Therefore , we assume that VEGF is produced by tumor cells under conditions of hypoxia, which occurs when the density of the microvessels is very low. Specifically, the production of VEGF is 'switched on' when the microvessel density falls below a threshold level V_{char}, and 'switched off' when the density exceeds this value. It should be noted that this angiogenic switch causes the microvessel density to stabilize at a maximum level, at around V_{char}. Thus, a production term is added in the equation (5.3) governing free VEGF concentration, following (112).

Note that conservation of total receptor numbers is ensured by setting the sum of the free and bound receptor densities equal to the product of the average VEGFR2 density per endothelial cell and the total (free + differentiated) endothelial cell density. That is, we require the following condition to be satisfied.

$$R_a + \eta_3^a\, C_a + 2\,\eta_4^a\, D_a \;=\; R_t^a\,(M + \alpha_1\, V) \tag{5.7}$$

Here, R_t^a is the total VEGFR2 density in pg per cell, and α_1 is the average number of endothelial cells per microvessel. This introduces production and loss terms corresponding to changes in HDMEC density in equations (5.4)- (5.6). The altered equations are presented in section 5.2.5.

5.2.3 CXCL8 Uptake

A novel feature of this model is the incorporation of a second potent angiogenic stimulator, CXCL8. CXCL8 is an 8kDa chemokine (83) produced by many cell types

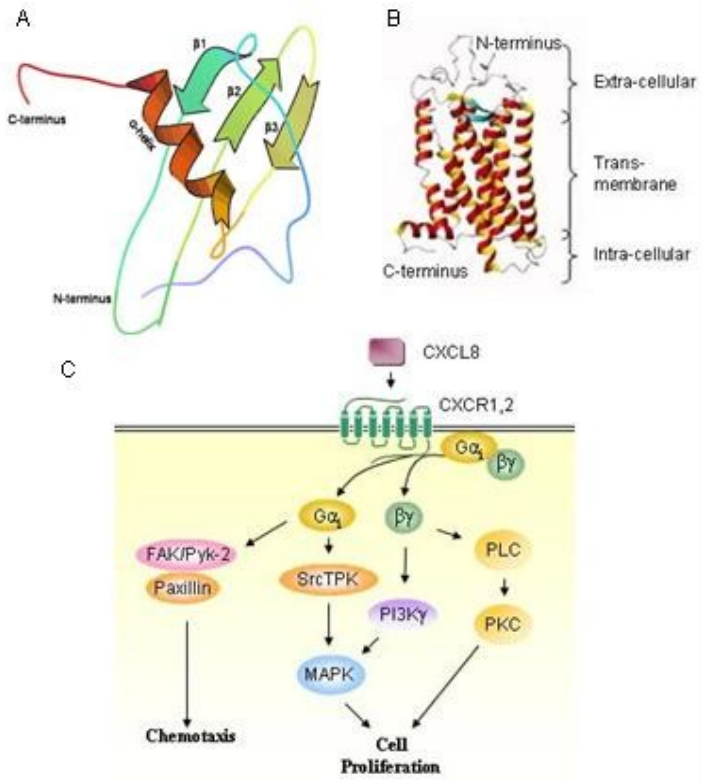

Figure 5.4: (A) Schematic diagram showing the restrained minimized average structure of the CXCL8 monomer as obtained by nuclear magnetic resonance, adapted from (118), and RCSB Protein Data Bank. (B) Ribbon representation CXCR1 structure, after homology modelling and energy minimization taken from (34). (C) Schematic diagram of some of the intracellular signalling pathways activated by CXCRs, adapted from (145)

including monocytes, T cells, neutrophils, endothelial cells, and epithelial cells (89). It has been shown to induce cell migration, and proliferation, more so than VEGF for HDMECs (67; 136; 141). CXCL8 binds to two distinct membrane bound receptors, CXCR1 (molecular weight 62kDa (127)) and CXCR2 (molecular weight 60kDa (55)), that mediate signal transduction through G proteins (89). These receptors dimerize independently of the presence of the ligand (147; 157) and they undergo heterodimerization as well (157). Figure 5.4A and B show the structure of the CXCL8 monomeric unit, and a ribbon representation of CXCR1, respectively. Figure 5.4C shows a graphical representation of a typical receptor for CXCL8, embedded in the lipid bilayer of the cell surface. For simplicity, CXCR1 and CXCR2 are not distin-

guished between in the model. Further, there is no conclusive evidence that two CXCL8 molecules are required to internalize this complex. Thus it is assumed that one molecule of CXCL8 is sufficient to activate its receptors, as shown in Figure 5.5

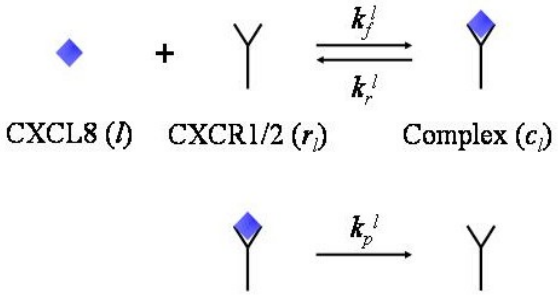

Figure 5.5: A schematic of CXCL8-CXCL8R1/2 interactions. CXCL8 binds to its cell surface receptors CXCL8R1/2 . The activated receptor-ligand complex is subsequently internalized, and the free receptor recycled.

Lower case letters are used to represent individual molecules and upper case letters are used to represent their concentration (in moles per liter), so that $L = [l]$ is CXCL8 concentration, $R_l = [r_l]$ is CXCR1/2 density, and $C_l = [c_l]$ is CXCL8-CXCR1/2 complex density. The above reaction diagram can be converted to the following system of equations using the law of mass action.

$$\frac{dL}{dt} = -k_f^l\, L\, R_l + k_r^l\, C_l \tag{5.8}$$

$$\frac{dR_l}{dt} = -k_f^l\, L\, R_l + k_r^l\, C_l + k_p^l\, C_l \tag{5.9}$$

$$\frac{dC_l}{dt} = k_f^l\, L\, R_l - k_r^l\, C_l - k_p^l\, C_l \tag{5.10}$$

where,

k_f^l is the association rate constant and has units (CXCL8 concentration)$^{-1}$ (time)$^{-1}$

k_r^l is the dissociation rate constant and has units (time)$^{-1}$

k_p^l is the rate of receptor internalization/recycling and has units (time)$^{-1}$

As earlier, the above equations are scaled to units of pg/mm^3 by appropriate constants (η_i^l). The choice of units of concentration introduces scaling factors η_i^l that represent ratios of the weights of the different molecules involved in the reaction. The scaled equation can be written as follows.

$$\frac{dL}{dt} = -\eta_1^l\, k_f^l\, L\, R_l + \eta_2^l\, k_r^l\, C_l - \lambda_l\, L + \beta_l\, M + \beta_a\, \phi_a\, M \tag{5.11}$$

$$\frac{dR_l}{dt} = -k_f^l\, L\, R_l + \eta_3^l\, k_r^l\, C_l + \eta_3^l\, k_p^l\, C_l \tag{5.12}$$

$$\frac{dC_l}{dt} = \eta_4^l\, k_f^l\, L\, R_l - k_r^l\, C_l - k_p^l\, C_l \tag{5.13}$$

where,

$$\phi_a = \phi_a(D_a, M, V) = \frac{D_a}{M + \alpha_1 V} \tag{5.14}$$

A natural decay rate λ_l of CXCL8 in tissue is also included in equation (5.11). Further, it is known that HDMECs maintain a basic concentration of CXCL8, through a background production rate β_l. It's production by the endothelial cells is up-regulated, in response to up-regulation of Bcl-2 by VEGF. Due to its intracellular nature, Bcl-2 concentration is taken to be directly proportional to HDMEC density, and a separate equation for Bcl-2 is not included Instead, it's effects are modelled using activated VEGF-receptor complex concentration per cell, ϕ_a, as defined in equation (5.14). Here, $D_a(t)$ is the overall concentration of activated VEGF-receptor complexes, as given by equation (5.6). This is divided by the total endothelial cell density which includes free cells as well as those cells that have differentiated to form microvessels. Note that vessel cells are capable of binding VEGF, and although they may not necessarily respond by proliferating, we assume that VEGF leads to

up-regulated survival in the cells lining immature vessels as well. The parameter α_1 is the number of cells on average per microvessel.

Again, conservation of total receptor numbers is ensured by setting the sum of the free and bound receptor densities equal to the product of the average VEGFR2 density per endothelial cell and the total (free + differentiated) endothelial cell density. That is, we require the following condition to be satisfied.

$$R_l + \eta_3^l \, C_l \;=\; R_t^l \, (M + \alpha_1 \, V) \tag{5.15}$$

Here, R_t^l is the total CXCL8R1/2 density in pg per cell. This introduces production and loss terms corresponding to changes in HDMEC density, in equations (5.12)-(5.13). The altered equations are presented in section 5.2.5.

5.2.4 Endothelial Cell Response to VEGF and CXCL8

In contrast to other models which assume that endothelial cell proliferation depends on extra-cellular growth factor concentrations or on monomeric binding of VEGF, our model assumes that HDMEC proliferation and death rates as well as the CXCL8 production rate are directly proportional to the amount of VEGF bound (in dimer form) to receptors on cell surfaces. In the previous chapter, we have presented simulations of biologically realistic situations where choosing an unbound chemokine concentration-dependant endothelial cell proliferation rate is an invalid assumption. In fact, endothelial cells have a proliferative or chemotactic response dependant on the concentration of activated receptor complexes on their surface. To our knowledge this has never before been considered in a mathematical model of tumor-induced angiogenesis or vascular tumor growth. The rate of change of the free HDMEC population is represented in equation (5.16). The units of endothelial cell ($M(t)$) and

vessel ($V(t)$) densities are number per mm^3. It should be noted that we have simplified the vascular network into a series of equal length units, and 'a microvessel' is one segment between adjacent branching points that can fit into a cube of side one millimeter.

$$\frac{dM}{dt} = (\mu_a \phi_a + \mu_l \phi_l - (\lambda_m - \delta \phi_a))\ M \left(1 - \frac{M}{M_0 - \alpha_1 V}\right) \tag{5.16}$$

where,

$$\phi_l = \phi_l(C_l, M, V) = \frac{C_l}{M + \alpha_1 V} \tag{5.17}$$

The HDMECs are assumed to grow logistically, as the carrying capacity M_0 of this experimental environment is limited. M_0 is estimated to be 17,000 cells per mm^3 from the experiments in (98). The endothelial cells lining the microvessels also compete with the free endothelial cells for space and nutrients. This is incorporated into the logistic term by reducing the carrying capacity by the density of endothelial cells lining the microvessels, $\alpha_1 V$. Note that the vessel density is bounded near a level at which the tumor is nourished by enough vessels to be in normoxia, so $\alpha_1 V$ does not exceed 2,000 cells per mm^3. Since the value of M_0 is far greater than that of $\alpha_1 V$, the effective carrying capacity of the environment, $M_0 - \alpha_1 V$, will never become negative.

The first two terms in equation (5.16) give endothelial cell proliferation rates. While there is no explicit experimental evidence to prove that effects of VEGF and CXCL8 on HDMECs are additive, we believe that this is a reasonable assumption in the absence of data to the contrary. Our rationale for making this choice stems from the knowledge that VEGF is a potent mitogenic and chemokinetic factor for

endothelial cells, and that CXCL8 alone is also capable of inducing cell proliferation and differentiation (97). These cellular responses are a result of the activation of cell surface receptors for these two chemokines. Hence, the proliferation rate of HDMECs due to VEGF is taken to be proportional to the average density of activated VEGF-receptor complexes per cell (ϕ_a, as defined in equation (5.14)). Likewise, the proliferation rate of HDMECs due to CXCL8 is taken as proportional to the average density of activated CXCL8-receptor complexes per cell (ϕ_l, as defined in equation (5.17)). It should be noted that vessel cells also have receptors for CXCL8, so its uptake by these cells is included. This reduces the amount of free CXCL8 available to free endothelial cells. Here $C_l(t)$ is the overall concentration of activated CXCL8-receptor complexes, as given by equation (5.13).

Moving now to the third term in equation (5.16), λ_m gives the natural death rate of endothelial cells. The anti-apoptotic effect of the intracellular protein Bcl-2, whose expression is up-regulated in presence of VEGF, is also incorporated here. As mentioned in the previous section, the effects of Bcl-2 are modelled using activated VEGF-receptor complex concentrations and the natural death rate λ_m of HDMECs is reduced by a factor dependant on ϕ_a. Conservation of receptors ensures that the total number of VEGF receptors per cell R_t^a is fixed; this also ensures that the densities of VEGF-receptor complexes per mm^3 - C_a and D_a - are bounded above by $R_t^a \times M_0$, and that the density of activated VEGF-receptor complexes per cell ϕ_a is bounded above by R_t^a. Since the Bcl-2 dependent death rate of HDMECs cannot be negative, this gives a natural upper bound (λ_m/R_t^a) for the multiplicative factor δ.

5.2.5 Microvessel Formation and Degradation

As endothelial cells grow in number, they begin to come together and arrange themselves into microvessels during the process of vascular inclusion. Previous mod-

els of angiogenesis have looked at microvessel formation in response to growth factor stimuli from a hypoxic tumor including (5; 24; 94) or in the context of wound healing (112; 113). In their model of angiogenesis in wound healing, Pettet et al (112; 113) assume an initial condition of preformed capillary tips, that migrate towards the hypoxic center of a wound, pulling behind them blood vessels contiguous with parent vessels. Anderson et al (5) begin with a tumor source located at a certain distance from parent vessels. It is assumed that sprout tips have already formed along this vessel and these tips migrate toward the tumor in response to growth factors. Both papers address blood vessel formation which results from pre-existing vasculature. However, here we need to model the process of microvessel formation via alignment and differentiation of individual endothelial cells. Nagy (94) incorporates the formation of new vessels that arise from (free) activated vascular endothelial cells at a constant rate, independent of growth factor concentration. In our model however, growth factor concentration is taken into account during vessel formation. Further in (94), the vessel degradation rate depends on limitations of space and growth factor availability. Here, the limitation of resources have already been included in the logistic term of equation (5.16).

Equation (5.18) gives the rate of change of microvessel density. VEGF and CXCL8 are both believed to be strong chemoattractants for the HDMECs, so that the cells align and form microvessels at a rate dependant on the activated receptor density functions ϕ_a and ϕ_l, which appear in the first two terms of equation (5.18). This process of vascular inclusion results in a corresponding decrease in the free endothelial cell density. Thus, a vascular inclusion term is subtracted from the endothelial cell equation and equation 5.16 changes to equation (5.19). Here, α_1 is the average number of cells per microvessel. Vessel maturation is not part of this model. Therefore,

when cells lining an immature vessel die, it is assumed to become dysfunctional at rate, α_4. In addition, the microvessel degradation rate includes a term to study the anti-apoptotic effect of Bcl-2. Like the death term in the free endothelial cell equation (5.19), up-regulated levels of Bcl-2, i.e., high numbers of active VEGF-receptor complexes on the cells lining the microvessels reduce their death rate. The density of cells that have rolled up to form microvessels is given by $\alpha_1 V$.

Since the ODE model presented here is independent of space, chemotaxis is not included explicitly. Budding and anastomoses have also not been included in this model, since this would present further unknown parameters, and there does not appear to be any conclusive evidence that these processes significantly affect microvessel densities within the implant.

$$\frac{dV}{dt} = (\alpha_2\,\phi_a + \alpha_3\,\phi_l)\;M_\tau - \alpha_4\;(\lambda_m - \delta\,\phi_a)\;\alpha_1\,V \tag{5.18}$$

$$\begin{aligned}\frac{dM}{dt} &= (\mu_a\,\phi_a + \mu_l\,\phi_l - (\lambda_m - \delta\,\phi_a))\;M\left(1 - \frac{M}{M_0 - \alpha_1 V}\right)\\ &\quad - \alpha_1\;(\alpha_2\,\phi_a + \alpha_3\,\phi_l)\;M_\tau\end{aligned} \tag{5.19}$$

An assumption of this model is that the numbers of VEGF and CXCL8 receptors per cell are constant. Therefore, as HDMECs grow due to proliferation, or are lost due apoptosis, and as microvessels regress, total receptor (bound + free) densities change correspondingly. For instance, the creation of an EC would add to the free VEGFR2 and CXCL8R1/2 densities, while the death of an EC would lead to loss of free and bound VEGFR2 and CXCL8R1/2 densities. Thus the equations (5.4)-(5.6), (5.12)- (5.13) governing the rates of change of these receptors densities need to be amended in the following way:

$$\frac{dR_a}{dt} = -2\,k^a_{f1}\,A\,R_a + \eta^a_3\,k^a_{r1}\,C_a - k^a_{f2}\,C_a\,R_a + 2\,\eta^a_4\,k^a_{r2}\,D_a + 2\,\eta^v_4\,k^a_p\,D_a + R^a_t\,\mathrm{Prod}(M,V) - \frac{R_a}{R_a + \eta^a_3\,C_a + 2\,\eta^a_4\,D_a}\,R^a_t\,\mathrm{Death}(M,V) \tag{5.20}$$

$$\frac{dC_a}{dt} = 2\,\eta^a_5\,k^a_{f1}\,A\,R_a - k^a_{r1}\,C_a - \eta^a_5\,k^a_{f2}\,C_a\,R_a + 2\,\eta^a_6\,k^a_{r2}\,D_a - \frac{C_a}{R_a + \eta^a_3\,C_a + 2\,\eta^a_4\,D_a}\,R^a_t\,\mathrm{Death}(M,V) \tag{5.21}$$

$$\frac{dD_a}{dt} = \eta^a_7\,k^a_{f2}\,C_a\,R_a - 2\,k^a_{r2}\,D_a - k^a_p\,D_a - \frac{D_a}{R_a + \eta^a_3\,C_a + 2\,\eta^a_4\,D_a}\,R^a_t\,\mathrm{Death}(M,V) \tag{5.22}$$

Likewise,

$$\frac{dR_l}{dt} = -k^l_f\,L\,R_l + \eta^l_3\,k^l_r\,C_l + \eta^l_3\,k^l_p\,C_l + R^l_t\,\mathrm{Prod}(M,V) - \frac{R_l}{R_l + \eta^l_3\,C_l}\,R^l_t\,\mathrm{Death}(M,V) \tag{5.23}$$

$$\frac{dC_l}{dt} = \eta^l_4\,k^l_f\,L\,R_l - k^l_r\,C_l - k^l_p\,C_l - \frac{C_l}{R_l + \eta^l_3\,C_l}\,R^l_t\,\mathrm{Death}(M,V) \tag{5.24}$$

Here, $\mathrm{Prod}(M,V)$ is the rate of production of free and differentiated HDMECs, while $\mathrm{Death}(M,V)$ is the rate of loss of free and differentiated HDMECs. These rates can be obtained from equations (5.19) and (5.18) as follows. Note that the number of differentiated HDMECs is given by $\alpha_1\,V$.

$$\mathrm{Prod}(M,V) = (\mu_a\,\phi_a + \mu_l\,\phi_l)\;M\;\left(1 - \frac{M}{M_0 - \alpha_1 V}\right) \tag{5.25}$$

$$\mathrm{Death}(M,V) = (\lambda_m - \delta\,\phi_a)\,M\;\left(1 - \frac{M}{M_0 - \alpha_1 V}\right) + \alpha_1\,\alpha_1\,\alpha_4\;(\lambda_m - \delta\,\phi_a)\;V \tag{5.26}$$

We can ensure that the equations (5.20)- (5.22) do in fact conserve VEGFR2 numbers as per the relation given by (5.7). Consider the sum $\frac{dR_a}{dt} + \eta^a_3\,\frac{dC_a}{dt} + 2\,\eta^a_4\,\frac{dD_a}{dt}$. From

equations (5.20)- (5.22) it can be seen that the chemical binding terms cancel, and we are left with R_t^a (Prod(M, V) − Death(M, V)). But, it may be verified that this sum is simply $\frac{dM}{dt} + \alpha_1 \frac{dV}{dt}$, as given by equations (5.18) and (5.19). Thus, the condition (5.7) is met. A similar computation shows that the condition for the conservation of CXCL8R1/2 given by (5.15) is also satisfied by the equations (5.23)-(5.24).

A delay τ is incorporated in the vessel formation rate, to account for experimentally observed time delay between an endothelial cell receiving a signal in the form of activated cell surface receptors, and differentiating to form mature, blood-bearing microvessels. The principle steps leading to the formation of microvessels via the processes of vasculogenesis and angiogenesis are described in (108). Briefly, the cells, upon receiving a chemical stimulus, may proliferate or migrate towards this signal in a process known as chemotaxis. As the cells begin to align together, they abandon their invasive phenotype, and begin forming cell-cell adhesions and reassociate with the extracellular matrix, via cell surface molecules such as integrins. This is followed by stretching and thinning of the cells, and their alignment in bipolar mode. The next step is vacuole and lumen formation. As more and more cells come together intracellular vacuoles fuse, and the lumens enlarge to generate tubular structures. Finally, these structures are stabilized, by specialized cells such as pericytes and smooth muscle cells that assist in basement membrane formation, to produce a microvessel capable of carrying blood. The steps involved in capillary formation detailed above are accounted for by the inclusion of a delay in vessel formation. Time delays in vessel formation/regression terms have been used previously in (27) wherein ODE models are presented for tumor induced angiogenesis.

In the experiments in (98), the first vessels in the scaffold are seen only about 5

days after implantation, indicating that the value for the delay τ is 5. It should be noted that a delay of zero days implies that endothelial cells differentiate into vessels as soon as any chemical stimulus is provided, in essence completing all the steps that must precede the differentiation instantaneously. Further, the first of these vessels would already be blood bearing. Whilst blood flow can only be established once the vasculature within the implant has had time to anastomose with neighboring mouse vessels.

For a complete list of model equations, please refer to Appendix B.

5.3 Parameter Estimation

Where possible, the choice of parameter values is based on estimates derived from experimental data or from values given in the literature. In cases where no experimental data could be found, those values of parameters were chosen for which the solution profiles best fit the experimental observations.

5.3.1 Parameters Associated with CXCL8

As mentioned previously, the molecular weight of CXCL8 is 8 kDa, while that of its receptors is taken to be the average of the molecular weights of CXCR1 and CXCR2, equal to 61 kDa. This allows us to calculate the scaling constants η_i^l appearing in equations (5.11)- (5.13). These values are given in Table 5.1.

In the absence of data available for endothelial cells, some of the parameter values relating to the binding kinetics of CXCL8 and its receptors CXCR1/2 are taken from studies on human neutrophils. For instance, the disassociation constant $k_D^l = k_r^l/k_f^l$ has a value of 0.8 nM, or 6.4 pg of CXCL8 per mm^3 (54). Since it takes 60 minutes for a CXCL8 receptor to internalize and reappear (89), k_p^l is taken to have a value of 24 per day. Due to a lack of available data, the natural decay rate of CXCL8 is taken

to be the same as that of VEGF, so that $\lambda_l = 15.5958$ per day. Finally, the total receptor density is taken to be 31000 $\times$ endothelial cell density (54). Thus, taking R_t^l to be the weight of receptors per EC, we have $R_t^l = .00041$ pg per HDMEC.

This still leaves us with a number of unknown parameters, which are estimated by fitting simulation results of the model to experiments. In a series of in vitro capillary sprouting assays described in (97), 3×10^5 human dermal microvascular endothelial cells (HDMECs) were seeded with 1.5 ml collagen (type I), in the absence of any chemokine, and were observed to maintain their numbers and appeared to be in steady state over a period of 7 days. We can reduce the full model system to represent this, for parameter estimation purposes. The resulting equations are listed below. It should be noted that the ECs are still producing constitutive levels of CXCL8.

$$\frac{dM}{dt} = \left(\mu_l \frac{C_l}{M} - \lambda_m\right) M \tag{5.27}$$

$$\frac{dL}{dt} = -\eta_1^l \, k_f^l \, L \, R_l + \eta_2^l \, k_r^l \, C_l - \lambda_l \, L + \beta_l \, M \tag{5.28}$$

$$\begin{aligned} \frac{dR_l}{dt} &= -k_f^l \, L \, R_l + \eta_3^l \, k_r^l \, C_l + \eta_3^l \, k_p^l \, C_l \\ &\quad + R_t^l \, \mathrm{Prod}(M) - \frac{R_l}{R_l + \eta_3^l \, C_l} \, R_t^l \, \mathrm{Death}(M) \end{aligned} \tag{5.29}$$

$$\begin{aligned} \frac{dC_l}{dt} &= \eta_4^l \, k_f^l \, L \, R_l - k_r^l \, C_l - k_p^l \, C_l \\ &\quad - \frac{C_l}{R_l + \eta_3^l \, C_l} \, R_t^l \, \mathrm{Death}(M) \end{aligned} \tag{5.30}$$

where

$$\mathrm{Prod}(M) = \mu_l \frac{C_l}{M} \, M \tag{5.31}$$

$$\mathrm{Death}(M) = \lambda_m \, M \tag{5.32}$$

The death rate of HDMECs is 0.12 per day (74). Thus, the unknown parameters in the above equations are μ_l (CXCL8 dependent HDMEC proliferation rate), k_f^l and β_l (constitutive production rate of CXCL8 by HDMECs). Since the cells are assumed to be in steady state, the left hand sides of the above equations may be set to zero. This implies that Michaelis-Menten like kinetics must be valid for the uptake of CXCL8 by its receptors, and the system reduces to:

$$\frac{dM}{dt} = \left(\mu_l \frac{C_l}{M} - \lambda_m\right) M \tag{5.33}$$

$$\frac{dL}{dt} = -\eta_2^l \, k_p^l \, C_l - \lambda_l \, L + \beta_l \, M \tag{5.34}$$

$$C_l = \eta_4^l \frac{R_t^l \, M \, L}{K_M^l + L} \tag{5.35}$$

Here, $K_M^l = \dfrac{k_r^l + k_p^l}{k_f^l}$ is the Michaelis-Menten constant for the binding of CXCL8 with CXCLR1/2. We solve for β_l in terms of the other parameters, and the steady state values of the endothelial cells M_s and that of CXCL8 L_s to get:

$$L_s = \frac{\lambda_m \, K_M^l}{\eta_4^l \, \mu_l \, R_t^l - \lambda_m} \tag{5.36}$$

$$\beta_l = \frac{\lambda_l \, L_s}{M_s} + \eta_2^l \frac{\lambda_m \, k_p^l}{\mu_l} \tag{5.37}$$

The value for M_s may be read off the experimental data, so that we have reduced the number of parameters to be fitted to just two. A table of the known parameters is given in Table 5.1.

In order to estimate the remaining parameters, we again consider experimental data from (97). Here 3×10^5 HDMECs are now seeded with 1.5 ml collagen (type I), and grown in the presence of CXCL8 for seven days. Their numbers are recorded

[2]In the absence of experimental data, the half-life of CXCL8 was taken to be the same as that of VEGF for purposes of simplicity.

Table 5.1: List of parameter values associated with CXCL8 uptake by HDMECs

Parameter	Value	Units	Source
λ_m	0.12	per day	(74)
k_p^l	24.0	per day	(89)
η_1^l	0.1311	pg CXCL8 per pg R_l	(55), (83), (127)
η_2^l	0.1159	pg CXCL8 per pg C_l	(55), (83), (127)
η_3^l	0.8841	pg R_l per pg C_l	(55), (83), (127)
η_4^l	1.1311	pg C_l per pg R_l	(55), (83), (127)
λ^l	15.5958	per day	$(132)^2$

at daily intervals. CXCL8 dosage of 50 ng per ml, or 50 pg per mm^3 is given every two days. However, to fit the parameters in this model, only the first 4 days worth of data is considered, since after this the HDMEC cell numbers are seen to decline, which is attributed to a hostile in vitro environment. This is something we chose not to factor into the model as this might lead to further undetermined parameters. The equations (5.27)- (5.30) reflect this setup as well, with the only change that a dosage term needs to be added to equation (5.28), to mimic the treatment regime. The unknown parameters are k_f^l and μ_l, together with that given by equation (5.37). These are determined by fits in the least squares sense to experimental data presented in (97). The resultant fit is shown in Figure 5.6A. The parameter values thus obtained are listed in Table 5.2.

Table 5.2: List of parameter values associated with CXCL8 uptake by HDMECs contd.

Parameter	Value	Units
μ_l	12.8810	HDMECs per pg of C_l per day
k_f^l	6.7587	per CXCL8 concentration per day
k_r^l	43.2557	per day
β_l	8.0924×10^{-4}	pg of CXCL8 per HDMEC per day

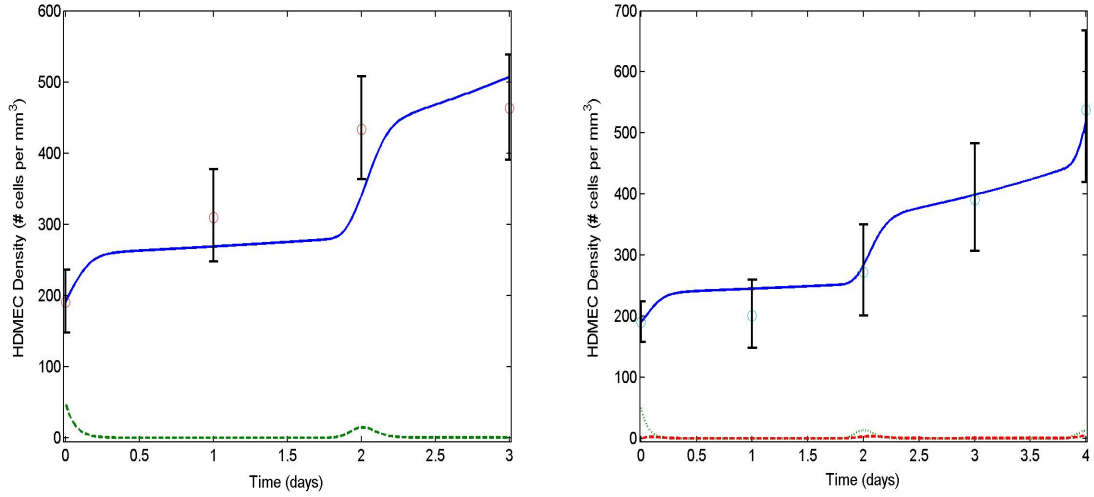

Figure 5.6: Fits to time-course data taken from in vitro capillary sprouting assays described in (96), with HDMECs cultured in the presence of either 50 ng/ml CXCL8 (A), or 50 ng/ml VEGF (B)

5.3.2 Parameters Associated with VEGF

The kinetic parameters relating to VEGF uptake by VEGFR2 have already been estimated in Chapter IV. We present here an estimation of the parameters relating to the effect of VEGF on HDMEC behavior. We again look at the capillary sprouting assays described in (97). In a final set of experiments, Nor et al seeded 3×10^5 HDMECs with 1.5 ml collagen (type I), and treated them with 50 pg/mm^3 VEGF every two days. The total (free + differentiated) number of HDMECs were counted every day. The full model system is reduced to represent this, for parameter estimation purposes. The resulting equations are listed below.

$$(5.38)\quad \frac{dM}{dt} = \left(\mu_a \frac{D_a}{M} + \mu_l \frac{C_l}{M} - \left(\lambda_m - \delta \frac{D_a}{M}\right)\right) M$$

$$(5.39)\quad \frac{dA}{dt} = -2\,\eta_1^a\,k_{f1}^a\,A\,R_a + \eta_2^a\,k_{r1}^a\,C_a - \lambda_a\,A$$

$$(5.40)\quad \frac{dR_a}{dt} = -2\,k_{f1}^a\,A\,R_a + \eta_3^a\,k_{r1}^a\,C_a - k_{f2}^a\,C_a\,R_a + 2\,\eta_4^a\,k_{r2}^a\,D_a + 2\,\eta_4^v\,k_p^a\,D_a$$
$$+R_t^a\,\mathrm{Prod}(M) - \frac{R_a}{R_a + \eta_3^a\,C_a + 2\,\eta_4^a\,D_a}\,R_t^a\,\mathrm{Death}(M)$$

$$(5.41)\quad \frac{dC_a}{dt} = 2\,\eta_5^a\,k_{f1}^a\,A\,R_a - k_{r1}^a\,C_a - \eta_5^a\,k_{f2}^a\,C_a\,R_a + 2\,\eta_6^a\,k_{r2}^a\,D_a$$
$$-\frac{C_a}{R_a + \eta_3^a\,C_a + 2\,\eta_4^a\,D_a}\,R_t^a\,\mathrm{Death}(M)$$

$$(5.42)\quad \frac{dD_a}{dt} = \eta_7^a\,k_{f2}^a\,C_a\,R_a - 2\,k_{r2}^a\,D_a - k_p^a\,D_a$$
$$-\frac{D_a}{R_a + \eta_3^a\,C_a + 2\,\eta_4^a\,D_a}\,R_t^a\,\mathrm{Death}(M)$$

$$(5.43)\quad \frac{dL}{dt} = -\eta_1^l\,k_f^l\,L\,R_l + \eta_2^l\,k_r^l\,C_l - \lambda_l\,L + \beta_l\,M + \beta_a\,D_a$$

$$(5.44)\quad \frac{dR_l}{dt} = -k_f^l\,L\,R_l + \eta_3^l\,k_r^l\,C_l + \eta_3^l\,k_p^l\,C_l$$
$$+R_t^l\,\mathrm{Prod}(M) - \frac{R_l}{R_l + \eta_3^l\,C_l}\,R_t^l\,\mathrm{Death}(M)$$

$$(5.45)\quad \frac{dC_l}{dt} = \eta_4^l\,k_f^l\,L\,R_l - k_r^l\,C_l - k_p^l\,C_l$$
$$-\frac{C_l}{R_l + \eta_3^l\,C_l}\,R_t^l\,\mathrm{Death}(M)$$

where

$$(5.46)\quad \mathrm{Prod}(M) = \left(\mu_a \frac{D_a}{M} + \mu_l \frac{C_l}{M}\right) M$$

$$(5.47)\quad \mathrm{Death}(M) = \left(\lambda_m - \delta \frac{D_a}{M}\right) M$$

The unknown parameters are μ_a (VEGF dependent HDMEC proliferation rate), δ (measure of the protective effect of VEGF on HDMECs, due to Bcl-2 up-regulation), and β_a (rate of CXCL8 production by HDMECs, under the influence of up-regulated

levels of Bcl-2). These are determined by fits in the least squares sense to experimental data presented in (97). The resultant fit is shown in Figure 5.6B. The parameter values thus obtained are listed in Table 5.3.

Table 5.3: List of parameter values associated with VEGF uptake by HDMECs

Parameter	Value	Units
μ_a	14.0875	# HDMECs per pg of D_a per day
δ	21.56	# HDMECs per pg of D_a per day
β_a	3.3766	pg of CXCL8 per pg of D_a per day

5.3.3 Vessel Formation

The estimation of parameters relating to HDMEC differentiation into microvessels are presented in Chapter VI.

5.3.4 Tumor Cell Growth Parameters

Parameters relating to the proliferation and death of tumor cells, appearing in the equation (5.1) governing the rate of change of tumor cell density are taken from Gammack et al (44). These are presented in Table 5.4.

Table 5.4: List of parameter values associated with tumor growth.

Parameter	Value	Units	Source
r_1	1.2924	per day	(44)
C_1	0.1	Oxygen concentration	(44)
r_2	0.001	per Tumor cell density per day	[3]
σ	1.0029	dimensionless	(44)
C_2	0.054	Oxygen concentration	(44)
C_m	0.2	Oxygen concentration	(44)
k	8.0	# Microvessels per mm^3	[3]

[3] In the absence of experimental data, biologically realistic values for these parameters were chosen so that the solution profiles best fit experimental observations.

5.4 Results

5.4.1 Vascular Tumor Growth

All numerical simulations of the model described in the previous section were carried out using RADAU IIA methods adapted to solve delay differential equations, as implemented by the numerical package RADAR5 Version 2.1 (48). Two key indicators of tumor development were studied in particular - maximal steady state values of tumor cell and vessel densities, and the time taken to reach these.

First, a series of numerical simulations are performed to illustrate tumor growth dynamics in the absence of anti-angiogenic or any other anti-cancer therapies. Two parameters were varied: tumor cell sensitivity to oxygen deprivation, that is the rate at which cells become necrotic in a low oxygen environment (r_2), and tumor cell ability to produce VEGF which captures the variation in the production of VEGF by different tumor cell lines (r_3). The results are summarized below.

With parameters at their baseline values, the tumor cell density reaches it's maximum level (1.149×10^4 cells per mm^3) about 28 days after implantation (Figure 5.7A). The first blood-bearing vessels are seen 5 days after implantation, reaching their steady state of about 53 vessels per mm^3, 19 days later (Figure 5.7B). During the first five days, the scaffold is hypoxic and a transient decrease in tumor cell density is observed that may be attributed to necrosis (Figure 5.7A, inset).

Next, a sensitivity analysis is carried out on the tumor cell oxygen sensitivity parameter (r_2). Numerical simulations indicate that maximal tumor cell density reached is exponentially related to r_2. As r_2 is varied from 10% to 150% of its control value, the maximal tumor cell densities decrease from 11.58×10^4 cells per mm^3 to 0.76×10^4 cells per mm^3 - a change of about 93%. However, the maximal vascular densities reached vary only from 54 to 52 vessels per mm^3 - change of only

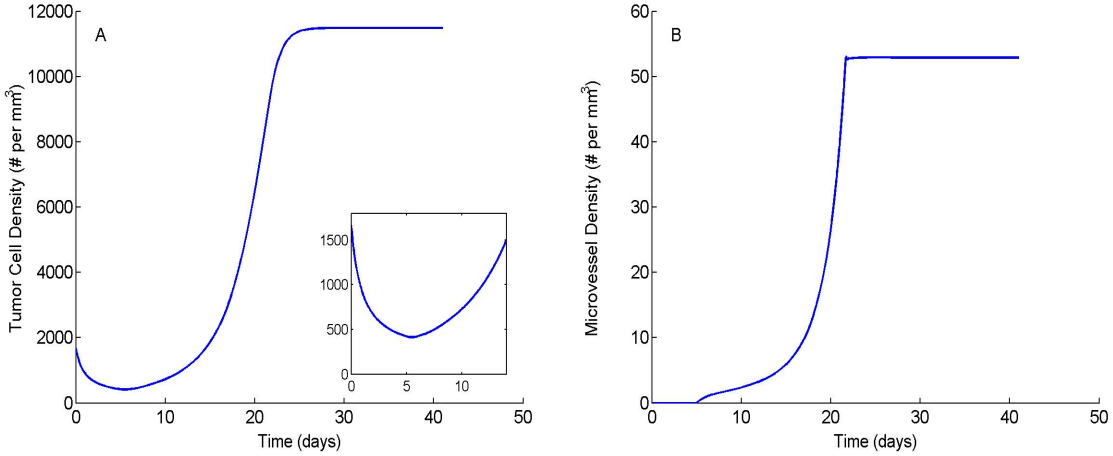

Figure 5.7: Vascular tumor growth in the absence of therapeutic intervention. (A) Tumor cell density reaches its steady state of 1.149×10^4 cells per mm^3 about 28 days post implantation. A transient decrease in tumor cell density is observed due to hypoxic conditions within the implant for the first week (inset). (B), Blood borne vessels are first seen 5 days after implantation, and reach their maximal level of 53 vessels per mm^3 about 24 days post implantation.

4% - and appear to be linearly related to the oxygen sensitivity parameter. These cell and vessel densities are normalized by their respective maximum values, and plotted versus r_2. (Figure 5.8A). For the same variation in the oxygen sensitivity parameter, the time taken by the tumor cells to reach maximal density increases from 18 to 62 days, and the time taken to reach maximum vascular densities increases from 12 to 57 days (Figure 5.8B). Thus, tumor growth and vascular development occur at a similar pace, and seem to vary exponentially with tumor cell sensitivity to oxygen deprivation. These results can be explained by the fact that a delay in tumor cell growth results in a delay in VEGF concentration reaching its maximum level, which correspondingly causes a delay in vasculature development. However, tumor cells are still producing VEGF at the same rate, and while the VEGF concentration falls with a reduction in tumor cell density, the change is not large enough to significantly alter the steady state reached by the vasculature. Therefore, tumor cells that are

more sensitive to local oxygen concentrations give rise to tumors that have very low tumor cell density, but are still highly vascularized. On the other hand, tumor cells with greater resistance to hypoxic conditions produce highly vascularized tumors with very high tumor cell densities.

Finally, a sensitivity analysis is carried out on the rate of VEGF production (r_3). This captures the variation in production of VEGF by different types of cancer cells and can also describe therapeutic intervention associated with administering small molecule inhibitors of VEGF. As expected, the numerical simulations predict that decreasing VEGF production rate delays tumor growth and vascular development. As VEGF production by tumor cells is decreased, the time taken by the tumor cells to reach maximum densities increases, from 17 days to 61 days, and time taken by the vessels to reach maximum densities increases from 13 to 57 days (Figure 5.8D). The relationship between VEGF production rate and both these times appears to be exponential. On the other hand, maximum tumor cell densities reached decrease by only 1%, from 1.157×10^4 to 1.144×10^4 per mm^3, and maximum vessel densities reached decrease by about 4% from 54 to 52 per mm^3, for the same variation in r_3. These cell and vessel densities are normalized by their respective maximum values, and plotted versus r_3. (Figure 5.8C). Thus, decreasing VEGF production rate has a far greater impact on the time taken to reach maximal cell and vessel densities than on their actual maximum values. This indicates that the fall in VEGF production is enough to significantly retard vessel formation, but not enough to affect the steady state reached by the vessel density. Since the other parameters including tumor cell growth and necrosis rates are kept fixed, the tumor cells are able to grow to roughly the same steady states.

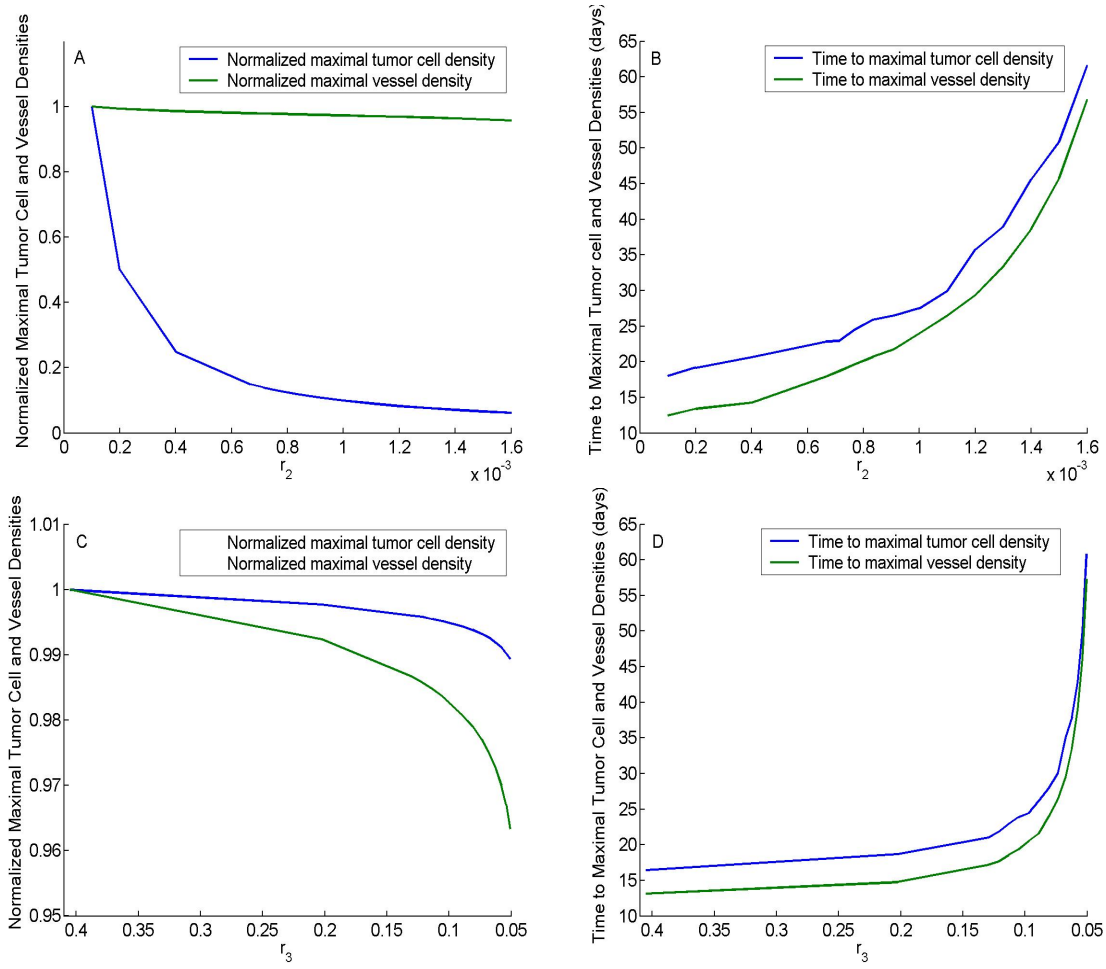

Figure 5.8: Tumor cells with high oxygen deprivation sensitivity give rise to highly vascularized tumors with low tumor cell densities. Decreasing tumor cell VEGF production rate delays tumor growth significantly. (A,B), Effect of increasing tumor cell oxygen deprivation sensitivity from 10% to 150% of its baseline value is simulated. Numerical results predict a 93% reduction in maximal tumor cell density. The corresponding reduction in maximal vessel density is only 4% (A). The time taken to reach maximal tumor cell density increases by a factor of 3.5, while that to reach maximal vessel density increases by a factor of 4.8 (B). (C,D), Effect of decreasing VEGF production rate from 500% to 62.5% of its baseline value is simulated. Numerical results predict a reduction of only 1% in maximal tumor cell density and a reduction of only 4% in maximal vessel density (C). However, the corresponding increase in time taken to reach maximal tumor cell and vessel density is as much as 3.6 and 4.4 fold respectively (D).

5.4.2 Anti-angiogenic Therapy Targeted at the VEGF-BCL-2-CXCL8 Pathway

The main focus of this model is to investigate the importance of the downstream effect of the VEGF - Bcl-2 - CXCL8 pathway in tumor progression. The pathway

suggests two targets for the development of anti-angiogenic therapies: inhibiting the production of CXCL8 by HDMECs and blocking the VEGF mediated up-regulation of Bcl-2 by HDMECs. Numerical simulations of both these cases are carried out keeping all previously introduced parameters fixed at their estimated pre-treatment values. The results are presented and discussed below.

Anti CXCL8 Therapy

The effect of inhibiting the production of CXCL8 from the first day of implantation is investigated. Experimental data is taken from (98), where polyclonal antihuman CXCL8 antibody was delivered locally, by incorporation into the scaffolds implanted in the SCID mice. The mice were then sacrificed after 21 days and vascular densities noted. The vasculature in treated tumors reached a density of around 20 vessels per mm^3 after 21 days, as opposed to a tumor that was allowed to grow without the application of any anti-cancer therapy, in which the density was double this value, at around 42 vessels per mm^3 after the same length of time (Figure 5.9C). The anti-CXCL8 antibody binds to free CXCL8, effectively reducing the bio-availability of free CXCL8 for endothelial cells. In modelling terms, this can be thought of as a reduction in the production rate of CXCL8, which would mean lower levels of free CXCL8 available to the endothelial cells. Thus, anti CXCL8 therapy can be modelled via a parameter ϵ_l, which is a measure of therapy efficacy, and multiplies the CXCL8 production term in equation (5.11). It varies from 1 (no therapy applied) to 0 (100% efficacious therapy). Inclusion of anti-CXCL8 therapy changes equation (5.11) as follows.

$$\frac{dL}{dt} = -\eta_1^l\, k_f^l\, L\, R_l + \eta_2^l\, k_r^l\, C_l - \lambda_l\, L + \epsilon_l\, (\beta_l\, M + \beta_a\, \phi_a\, M) \tag{5.48}$$

Numerical simulations show that as ϵ_l is varied from 1 to 0, the vessel density after 21 days changes from 42 to 12 vessels per mm^3. Comparison with experimental results allows us to calculate that the in vivo therapy in (98) has an efficacy level between 20% ($\epsilon_l = 0.8$) and 100% ($\epsilon_l = 0$) (Figure 5.9C, $\epsilon_l = 0.589$, efficacy level of 41.1%). This range of values for ϵ_l is obtained from experimental error bars. The tumor cell density in a tumor growing without treatment is 48% higher than in a tumor treated with the above level of anti CXCL8 therapy after in 21 days (Figure 5.9A). Correspondingly, the treated tumor is nourished by only half the vasculature in a non-treated tumor, at this point of time (Figure 5.9B).

It is also important to determine how varying CXCL8 therapy levels affects the delay in tumor development. As can be seen from Figure 5.9D, time taken to reach maximal tumor cell and vessel densities appears to vary linearly with ϵ_l. A 100 % efficacious therapy level, corresponding to $\epsilon_l = 0$ introduces a delay of 6 days in tumor development, while the delay is only 2 days corresponding to the in vivo therapy in (98) ($\epsilon_l = 0.589$). Note that in Figure 5.9D, ϵ_l varies from 1 to 0 on the abscissa, which should be interpreted as level of therapy increasing from 0 to 100%. Thus, anti CXCL8 therapy delays tumor growth, but the delay is not very large. Further, the maximal levels of tumor cell and vessel densities remain unaffected upon application of therapy. This can be explained by observing that CXCL8 is not directly related to enhanced endothelial cell survival, it induces cell proliferation and migration. But these functions are also performed by VEGF which in addition exerts a pro-survival effect on the endothelial cells though up-regulation of Bcl-2. So, reducing CXCL8 levels can be expected to produce a delay in vascular development, which correspondingly delays tumor cell growth. However, tumor cell VEGF production rate remains unchanged, which explains the relatively small value of the delay, and

also accounts for the unchanged maximal vessel density. This in turn means that maximal tumor cell density remains unchanged, since it is a function of the blood-bearing vessel density.

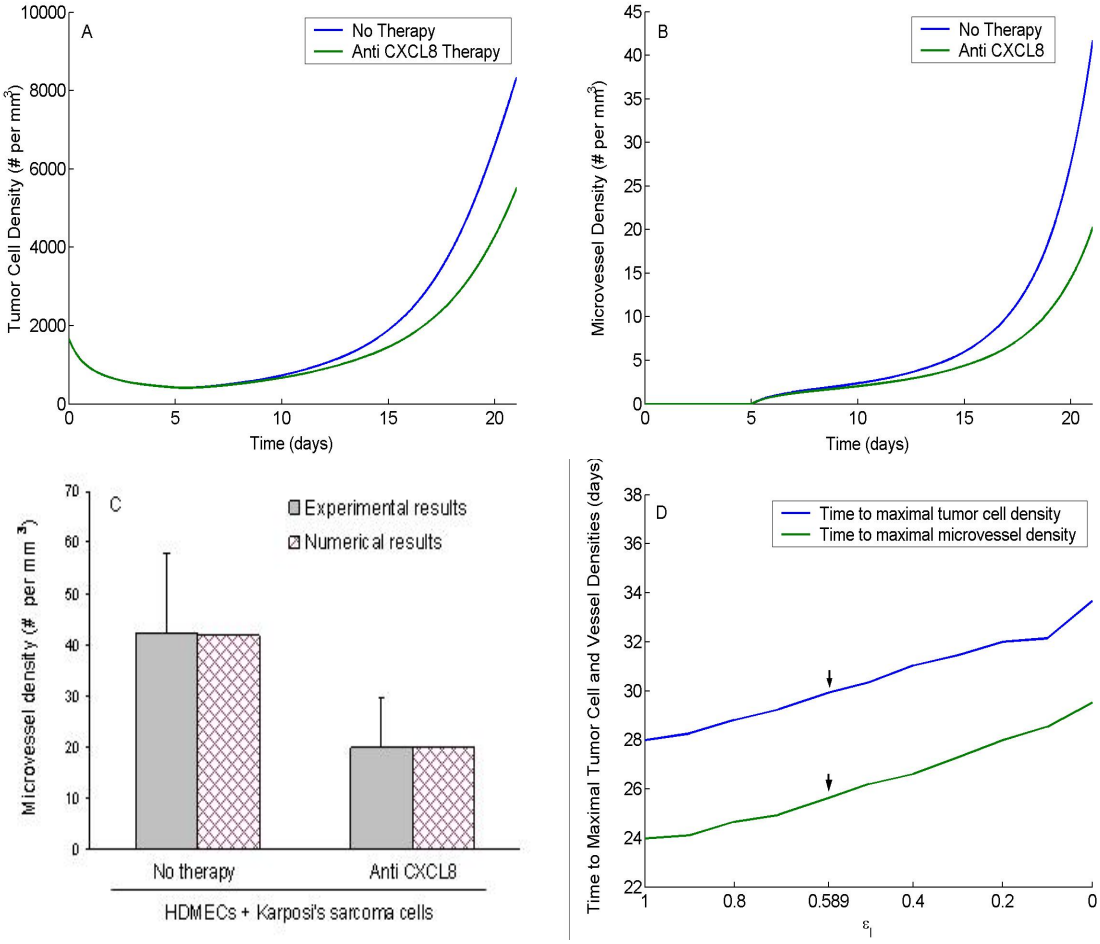

Figure 5.9: Anti CXCL8 therapy applied on the first day of implantation delays both tumor growth and vascular development. (A,B), Numerical simulations of anti CXCL8 therapy applied from the first day, predict that after 21 days, the tumor cell density is about 32% lower than its value in the case when no therapy is applied (A). Likewise, the vessel density in the anti CXCL8 case is 50% lower than its value in the case with no therapy applied (B). (C) Comparison of experimental and numerical predictions of microvessel densities (vessels per mm^3) after 21 days of exposure to anti CXCL8 therapy. Experimental data taken from (97), where sponges seeded with HDMECs and Kaposi's sarcoma cells were implanted in severe combined immunodeficient mice. Polyclonal antihuman CXCL8 antibody was delivered by incorporation into scaffolds implanted in the mice. (D) Time to both maximal tumor cell and vessel densities increases by about 6 days for a 100% efficacious therapy level, as opposed to the no therapy case. $\epsilon_l = 0.589$ corresponds to the in vivo therapy in (97).

Anti Bcl-2 Therapy

Numerical simulations of the clinically interesting situation corresponding to intercepting the effect of VEGF on Bcl-2 levels within HDMECs both in vitro and in vivo were performed. In (59) in vitro capillary sprouting assays with HDMECs exposed to 50 ng/ml of VEGF are compared to HDMECs cultured in the presence of 50 ng/ml VEGF and exposed to anti Bcl-2 therapy starting on day 5, in the form of a small molecule inhibitor BL193. The model equations are modified to simulate the in vitro experiments. Notably, there are no tumor cells present and free VEGF concentration is held fixed at 50 ng/ml. Constitutive CXCL8 production rate by endothelial cells and environmental carrying capacity for endothelial cells are re-evaluated from the control (no therapy) simulations. To model the effect of anti Bcl-2 therapy, a parameter ϵ_a is introduced as a measure of the level of blockage of Bcl-2 up-regulation by BL193. This affects the cell death terms in the free HDMEC and vessel equations, and CXCL8 up-regulation by HDMECs in the presence of VEGF. The equations (5.11), (5.18) and (5.19) change as follows.

$$\frac{dL}{dt} = -\eta_1^l\, k_f^l\, L\, R_l + \eta_2^l\, k_r^l\, C_l - \lambda_l\, L + \beta_l\, M + \epsilon_a\, \beta_a\, \phi_a\, M \tag{5.49}$$

$$\frac{dV}{dt} = (\alpha_2\, \phi_a + \alpha_3\, \phi_l)\; M - \alpha_4\; (\lambda_m - \epsilon_a\, \delta\, \phi_a)\; \alpha_1\, V \tag{5.50}$$

$$\frac{dM}{dt} = (\mu_a\, \phi_a + \mu_l\, \phi_l - (\lambda_m - \epsilon_a\, \delta\, \phi_a))\; M\; \left(1 - \frac{M}{M_0 - \alpha_1 V}\right) \tag{5.51}$$

$$- \alpha_1\; (\alpha_2\, \phi_a + \alpha_3\, \phi_l)\; M \tag{5.52}$$

The level of Bcl-2 up-regulation blockage ϵ_a may be varied between 1 (no therapy) and 0 (complete blockage of Bcl-2 up-regulation), and the results compared with experimental outcomes. Note that setting $\epsilon_a = 0$ forces Bcl-2 to remain at its normal, constitutive levels and ensures that production of CXCL8 is not up-regulated. It is

observed that the model provides a good fit to the no therapy case (Figure 5.10C). The numerical and experimentally observed vessel densities are seen to be in good agreement when the blockage level of Bcl-2 up-regulation by VEGF is between 85% and 100% (Figure 5.10D, complete blockage of Bcl-2 up-regulation).

Next, the effect of small molecule inhibition of Bcl-2 may be numerically investigated in vivo. The model predicts that after 21 days, when Bcl-2 up-regulation is blocked completely ($\epsilon_a = 0$), post-therapy tumor cell and vasculature densities drop to levels 27.5% and 14% respectively of their values when no therapy is applied, (Figures 5.10A,B). Further, the maximal tumor cell and vessel densities may also be plotted as the level of blocking of Bcl-2 up-regulation is varied (Figure 5.10E). Interestingly, there appears to be a minimum level of blockage of Bcl-2 up-regulation by VEGF required for the therapy to be effective. For $\epsilon_a < 0.4$, anti Bcl-2 therapy has comparatively little effect on tumor development, and maximal tumor cell and vessel densities do not change appreciably. With a reduction in Bcl-2 up-regulation levels, the endothelial cell death rate increases, and CXCL8 production by endothelial cells decreases, but these effects are balanced out to some extent by an unchanged tumor cell VEGF production rate. However, as ϵ_a is reduced further, the endothelial cell apoptosis rate becomes very large, and consequently, maximal vessel densities begin to fall drastically. This causes a drop in maximal tumor cell densities as well, since there are fewer blood-bearing vessels supplying nutrients and oxygen to the tumor. Eventually, corresponding to in vitro therapy levels ($\epsilon_a = 0$), tumor cell density stabilizes at 68% and vessel density stabilizes at 41% of their values in the no therapy case. This sensitivity of the tumor to anti Bcl-2 therapy levels is also apparent from the graphs of time taken to reach maximal cell and vessel densities versus therapy level (Figure 5.10F). For $\epsilon_a < 0.4$, the delay in vessel and tumor development in-

creases fairly slowly, with an increase in therapy level. Near $\epsilon_a = 0.4$, the rates of change of both these times are maximum. For higher therapy levels, these rates seem to level out, but are still high. Overall, it takes about 30 days longer for the tumor to develop when Bcl-2 up-regulation is completely blocked. These results underscore the use of this model as a predictive tool to guide in vivo experiments aimed at testing anti Bcl-2 therapies. They suggest that below a certain threshold, anti Bcl-2 therapy elicits little response from the tumor, but as therapy is increased beyond this threshold, the tumor and vascular development is arrested at much lower levels. Thus, anti Bcl-2 therapy is considerably more effective than anti CXCL8 therapy, if given in the right quantities. It should be noted that in Figures 5.10E and F, ϵ_a varies from 1 to 0 on the abscissa, which should be interpreted as level of therapy increasing from 0 to 100%.

Treatment of Fully-Formed Tumors

We investigate the effect of various anti angiogenic therapies applied to a tumor that has been allowed to reach maximal tumor cell and microvessel densities (Figure 5.11A,B). The model predicts that anti CXCL8 treatment has little or no effect on the tumor when applied at this late stage. The vessel density is seen to decrease only slightly, but the tumor cells appear to compensate for this decrease in CXCL8 levels by increasing VEGF production. The vessel density soon returns to its pre-treatment level. However, if the up-regulation of Bcl-2 in HDMECs is blocked, the tumor begins to regress and finally stabilizes at lower cell and vasculature densities. This underscores the importance of enhanced HDMEC survival in the progression of a tumor. Note that in Figure 5.11B, a sudden drop in the vessel density is observed when anti Bcl-2 therapy is applied. In actual experiments this drop may be more gradual. In the numerical simulation, at the point of application of the therapy, the

Bcl-2 levels in the cells are set to non up-regulated levels while in all probability, it would take some time for these to be achieved *in vivo*.

5.4.3 Effect of the Delay τ

An important feature of this model is the inclusion of a delay in the microvessel formation, to account for the various biological steps that precede the differentiation of free endothelial cells into capillaries. We are not the first to use a delay in this way - in (68), Kuang et al use a delay to account for the time it takes activated vascular precursor cells to mature into functional microvessels. Time delays in vessel formation have also been used in angiogenesis models to rationalize empirical observations (27). Experimental observations allow us to fix this delay at 5 days. Various numerical experiments were carried out to test the stability of steady states of the model revealed that the introduction of the delay did not produce any oscillatory behavior.

To investigate the importance of the delay, the model equations are simulated with $\tau = 0$ representing the non-delay case. In setting the delay to zero, we are making the biologically unreasonable assumption that the endothelial cells begin to form vessels as soon as they detect any sort of chemical stimulus, and these vessels are also blood bearing immediately. It is observed that tumor cell density stabilizes almost 12 days earlier and vessel density stabilizes almost 10 days earlier than if the delay is fixed at 5 days. In fact, after 21 days, the tumor cell and vessel densities have already reached their maximal levels, and the vessel density is 27% higher than the value observed experimentally in the case when the delay is set to zero (Figures 5.12A,B). Thus, the tumor vasculature is developing at a rate that is much faster than what is observed in vivo.

Next, the effect of the length of the delay on time taken to reach maximal tumor

and vessel densities is studied. The delay is varied between biologically realistic values of 0.5 days to 10 days. The time taken to maximal tumor cell density increases from 18 days to 34 days - a change of 89%. The time taken to reach maximal vessel density also increases by about 88% from 16 days to 30 days. (Figure 5.12C) Interestingly, for τ between 0.5 and 3 days, the delay between tumor cell and vessel development is about 2 days, but for τ greater than 4 days, this delay increases to 4 days (Figure 5.12D).

5.5 Discussion

There have been numerous advances in the development of experimental models to study angiogenesis, recasting these in mathematical terms can provide valuable insights into understanding the processes that govern angiogenesis and suggest new methods of treatment of cancers. We set out to explore quantitatively one such experimental model that investigated the importance of the VEGF - Bcl-2 - CXCL8 pathway in sustained angiogenesis of a developing tumor. The main goal of this research was to derive a mathematical model of the experiments in (97; 98), in order to better understand those features of the pathway which play the most crucial role in sustaining the growth of a tumor. Further, numerical simulations of the model could be used to suggest new areas for the development of anti-angiogenic therapies targeted at the proteins and chemokines involved in the pathway and to assess their effects on tumor progression. We recognize that this experimental system does not exactly replicate the formation of human tumors in vivo, however this experimental approach has lead to several significant discoveries about the molecular events involved in angiogenesis, and by developing a model specific to these experiments we are able to validate our predictions by direct comparison with the available data.

It would be a straight forward task to change initial conditions to better describe traditional vascular tumor growth.

Numerical simulations of the full model provide insight into the growth dynamics of tumors with different sensitivities to oxygen deprivation and various rates of VEGF production. Results obtained showed that as tumors with increasing sensitivities to local oxygen concentration were considered, the time taken to reach maximum cell densities by the tumor increased, and tumor cell growth was significantly affected, but this had little impact on the vascular development of the tumor. Tumor cells highly sensitive to local oxygen concentrations were found to give rise to highly vascularized tumors, with very low tumor cell densities that were at just 7% of their values in tumors with very low local oxygen concentration sensitivity. The vessel densities in these two kinds of tumors did not differ significantly. VEGF production rate was found to have a more significant impact on the time taken to reach maximal cell and vessel densities. As VEGF production rate was decreased from a maximum by 87.5%, it took 264% more time for tumor cell density to reach its maximal level and 335% more time for the vasculature to fully develop. These results suggested that possible anti-angiogenic therapies targeting VEGF may result in significant delays in tumor progression.

The VEGF - Bcl-2 - CXCL8 pathway also presented two new potential areas for the development of cancer treatment. Numerical results indicated that inhibiting the production of CXCL8 by HDMECs from day zero delayed the tumor progression, but did not affect the maximal tumor cell and vessel densities. The most promising strategy however was to block the up-regulation of Bcl-2 by VEGF in HDMECs, this resulted in a tumor with low vascular density and a correspondingly low tumor cell density. The tumor responded much better to treatment after a certain minimum

level of therapy was applied. Anti Bcl-2 therapy significantly delayed tumor development as well. In a simulation carried out to test these two strategies on a fully developed tumor, we found that blocking CXCL8 production had virtually no effect on the tumor, but down regulation of Bcl-2 resulted in the tumor stabilizing at low cell and vessel densities. Hence, the dual role played by VEGF namely, enhanced endothelial cell survival due to up-regulation of Bcl-2 and increased endothelial cell proliferation and migration due to up-regulation of CXCL8 played a crucial role in the development of the tumor. Indeed, it appeared that increased endothelial cell half life was necessary for rapid growth and progression of the tumor. Finally, the effect of the delay parameter was investigated numerically, and it was observed that without any delay, the vasculature developed too rapidly. For the control value of the delay parameter, a time lag of 4 days was observed between tumor cell and vessel development.

Nör et al have already demonstrated that BL193, a small molecule inhibitor of Bcl-2 has a strong inhibitory effect on the angiogenic potential of endothelial cells in vitro (98; 59). However, the anti-angiogenic potential of BL193 in vivo is not clear. In Chapter VII we extend the modelling approach present here to explicitly incorporate the pro-apoptotic as well as anti-apoptotic members of the Bcl family, in order to better understand the mechanism of action of BL193 and to relate its binding efficiency to its therapeutic efficacy. For future work, we also plan to investigate in greater detail the ability of our mathematical model to predict a response to anti-CXCL8 treatment, as well as to differentiate the response to inhibition of the ligand (CXCL8) from inhibition of its receptor (CXCR2). The ligand can be experimentally inhibited by polyclonal anti-human CXCL8 antibody and the receptor by polyclonal anti-human CXCR2 antibody.

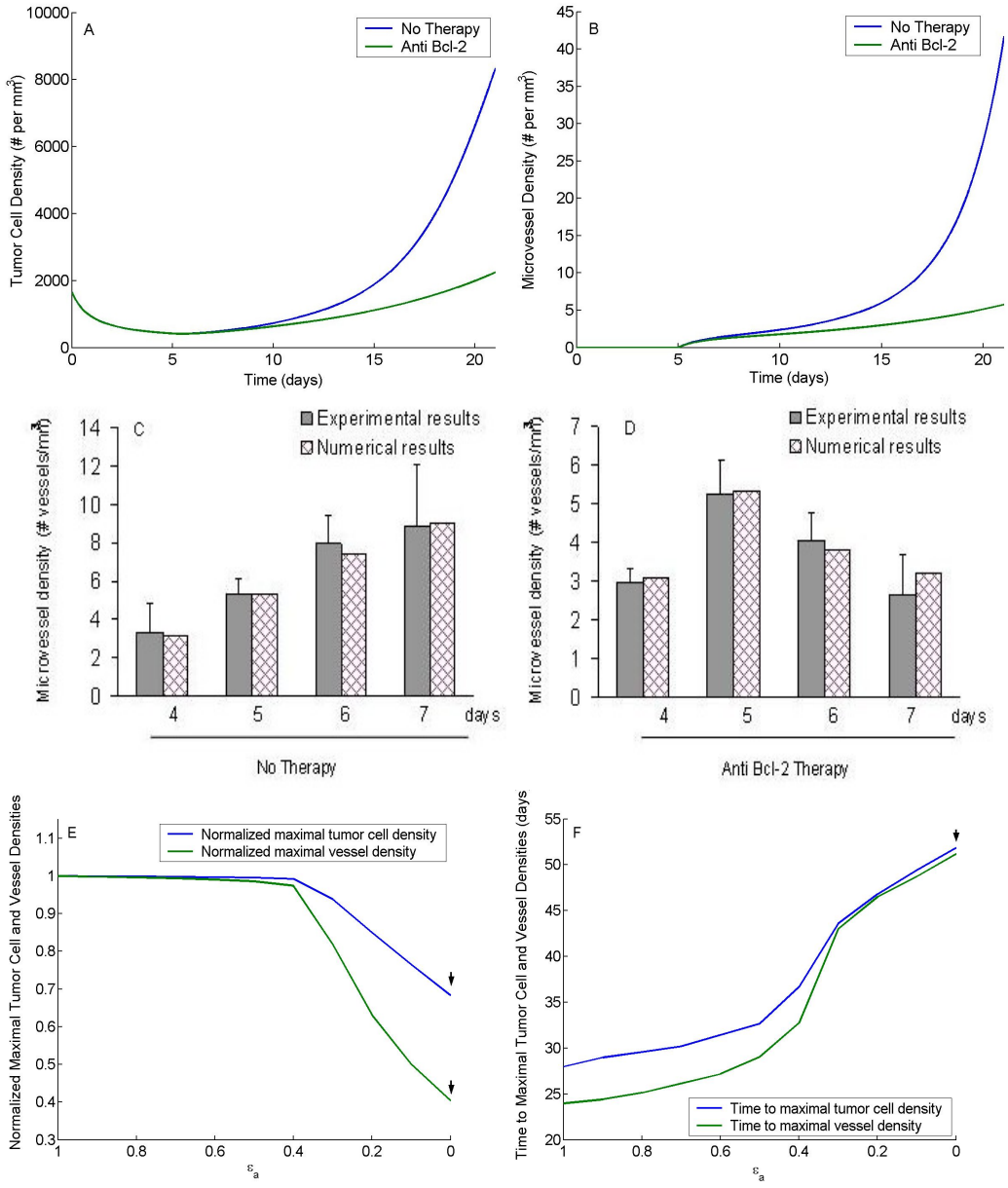

Figure 5.10: Anti Bcl-2 therapy is highly effective in controlling tumor growth and vascular development. (A,B), Numerical simulations of in vivo anti Bcl-2 therapy corresponding to 100% blockage of Bcl-2 up-regulation by VEGF applied from the first day predict that after 21 days, the tumor cell density is only about 27.5% of its value in the case when no therapy is applied (A). Likewise, the vessel density in the anti Bcl-2 case is about 14% of its value in the case with no therapy applied (B). (C,D), Comparison of numerical simulations and experimental results of in vitro capillary sprouting assays with HDMEC exposed either to 50 ng/ml VEGF (C) or 50 ng/ml VEGF and anti Bcl-2 therapy starting on day 5 in the form of 0.5 M of BL193, a small molecule inhibitor of Bcl-2 (D). Experimental data taken from (59). (E,F), Anti Bcl-2 therapy appears to have a major effect only after a minimum level of therapy, corresponding to $\epsilon_a = 0.4$, is provided. Maximal tumor cell density and maximal microvessel density show a drop of 30% and 59% respectively as level of anti Bcl-2 therapy is increased from no therapy to 100% blockage of Bcl-2 up-regulation (E). Time taken to maximal tumor cell density increases by 90% and to maximal vessel density increases by 112% for this range of therapy (F).

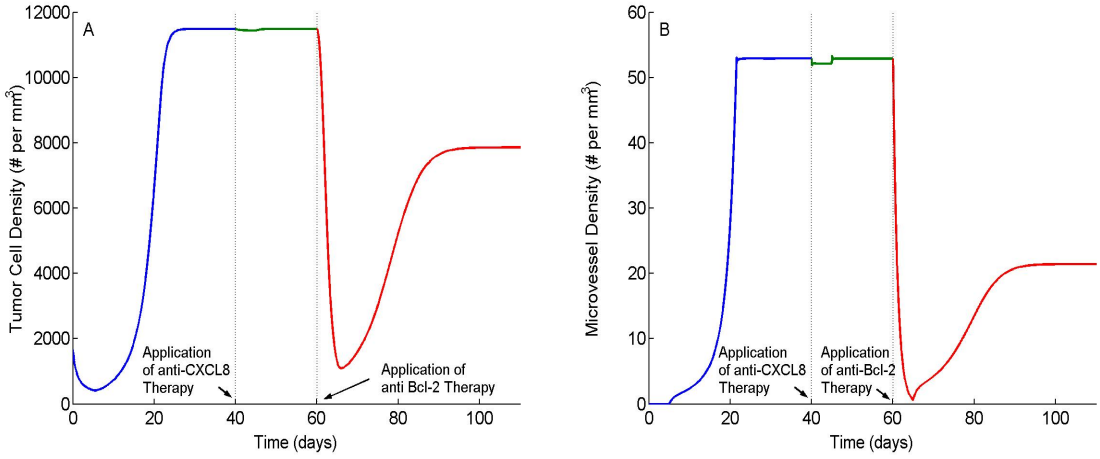

Figure 5.11: A fully formed tumor responds to anti Bcl-2 therapy, while anti CXCL8 therapy appears to have little or no impact.(A,B), Anti CXCL8 and anti Bcl-2 therapies are applied in turn on a fully developed tumor, and their effects on tumor cell and microvessel density graphed. The anti CXCL8 therapy is applied on the 40th day, and the anti Bcl-2 therapy is applied on the 60th day. It can be seen that while the anti CXCL8 therapy has little affect the tumor cell and microvessel densities, anti Bcl-2 therapy produces a significant drop in both of these.

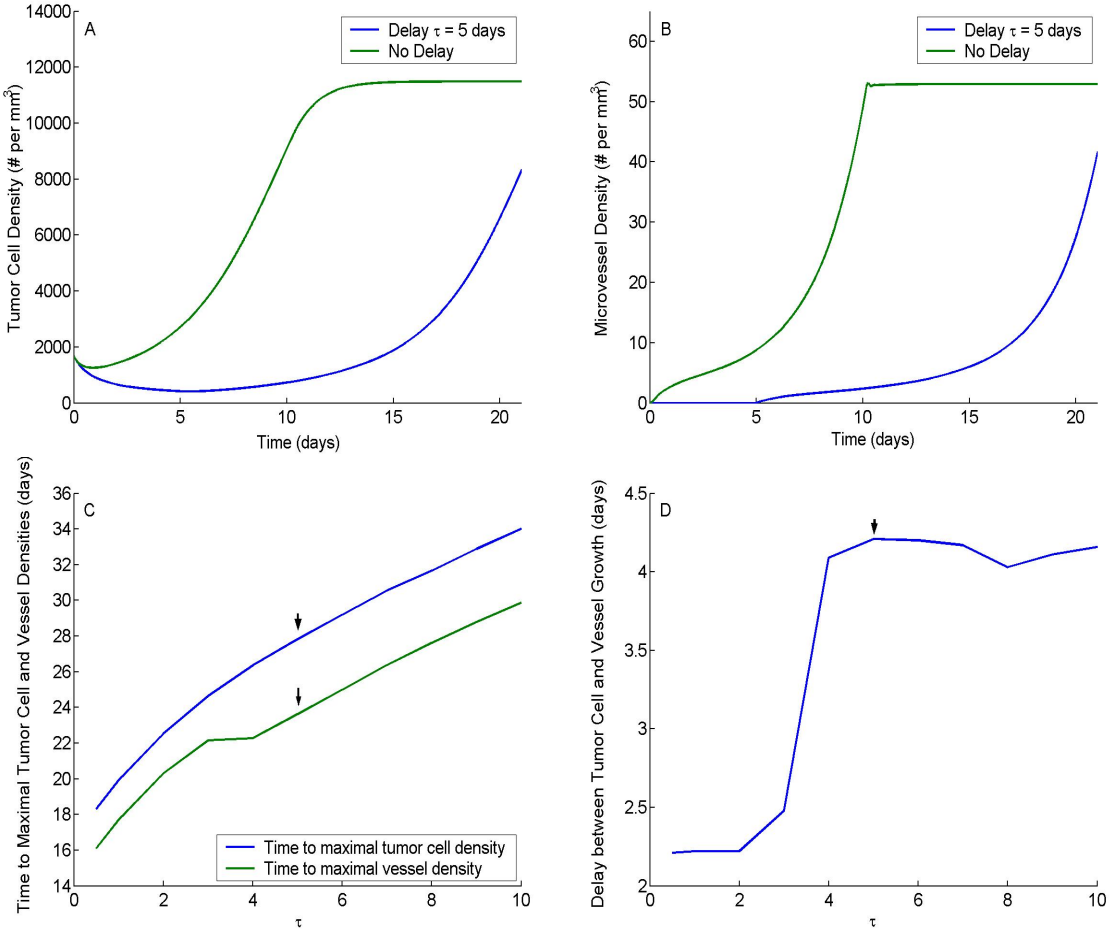

Figure 5.12: Effect of the delay τ on tumor growth and vascular development. (A,B), Comparison of tumor cell and vessel densities in the non-delay case ($\tau = 0$) versus the delay held at its baseline value ($\tau = 5$). The tumor cell density has already reached its maximal level by day 16 in the non-delay case (A). The vessel density reaches its maximal level by day 14 in the non-delay case, and are blood borne as soon as they are formed (B). (C,D), As the delay is varied between biologically realistic values of 0.5 days to 10 days, the time taken to maximal tumor cell density increases by 89% while the time taken to reach maximal vessel density increases by about 88% (C). For τ between 0.5 and 3 days, the delay between tumor cell and vessel development is about 2 days, but for τ greater than 4 days, this delay increases to 4 days (D).

CHAPTER VI

Apoptotic Requirement for Disruption of Microvessels

6.1 Introduction

In the previous chapter, we investigated the importance of the VEGF-Bcl-2-CXCL8 pathway in intra-tumoral angiogenesis. Model simulations showed that the pro-survival influence of VEGF on the microvascular endothelial cells was crucial in the growth and maintenance of tumor vasculature. In fact, anti-Bcl-2 therapy aimed at inducing endothelial cell death or apoptosis, was predicted to be the most promising target for the development of anti-angiogenic therapy. Thus, apoptosis was shown to be an important factor in determining tumor progression.

Apoptosis was first described by Kerr et al, in 1972 (64). They defined it as a form of programmed cell death that occurs in multicellular organisms. It involves a series of biochemical events leading to changes in cellular morphology, including blebbing, chromatin condensation, nuclear fragmentation, and cell shrinkage, which eventually lead to cell death. Apoptosis is an integral part of the normal development and maintenance of tissue homeostasis. However, it is also involved in a variety of pathologic conditions such as neurodegenerative diseases, cardiovascular diseases, immunological diseases, and cancer (161). In this chapter, we aim to quantify the role played by programmed cell death, or apoptosis, in the disruption of blood vessels,

mediated by anti-angiogenic drugs.

6.1.1 Biological Motivation

There exists an abundance of laboratory as well as clinical evidence of the hypothesis that cancer is an angiogenesis-dependent disease (40; 41). Angiogenesis, in turn, is strongly dependent on the suppression of endothelial cell apoptosis (26). In fact, pro-angiogenic growth factors such as VEGF have been shown to potently induce cell survival (46; 59; 97). This has led to a widespread interest in the development of anti-angiogenic therapies, aimed at blocking pro-survival signals and inducing cellular apoptosis, in order to treat a growing tumor (41; 162). In particular, it has been shown that blocking VEGF is sufficient to induce EC apoptosis (65; 66; 120). This resulted in the development of the first anti-angiogenic agent to be approved by the FDA - Bevacizumab (Avastin), a humanized anti-VEGF monoclonal antibody (38). Other molecules such as angiostatin, endostatin, and thrombospondin-1 have also been characterized as anti-angiogenic compounds. For instance, angiostatin and endostatin have been shown to inhibit vessel formation, both in vitro and in vivo, inducing endothelial cell apoptosis (30; 31). Matrix-bound thrombospondin-1 has been shown to promote endothelial cell apoptosis and inhibit angiogenesis (128). There has also been considerable interest in the development of therapies targeted against the anti-apoptotic members of the Bcl family of proteins, which have been identified as crucial mediators of cell death (59; 154; 160).

The mechanism of action of the anti-angiogenic agents described above, is largely based on the induction of endothelial cell apoptosis, resulting in vessel disruption. A question that arises with regard to the evaluation of these compounds is 'what is the minimum level of endothelial cell apoptosis required for significant microvascular regression?' Apoptosis in cells is brought about by the activation of intra-cellular

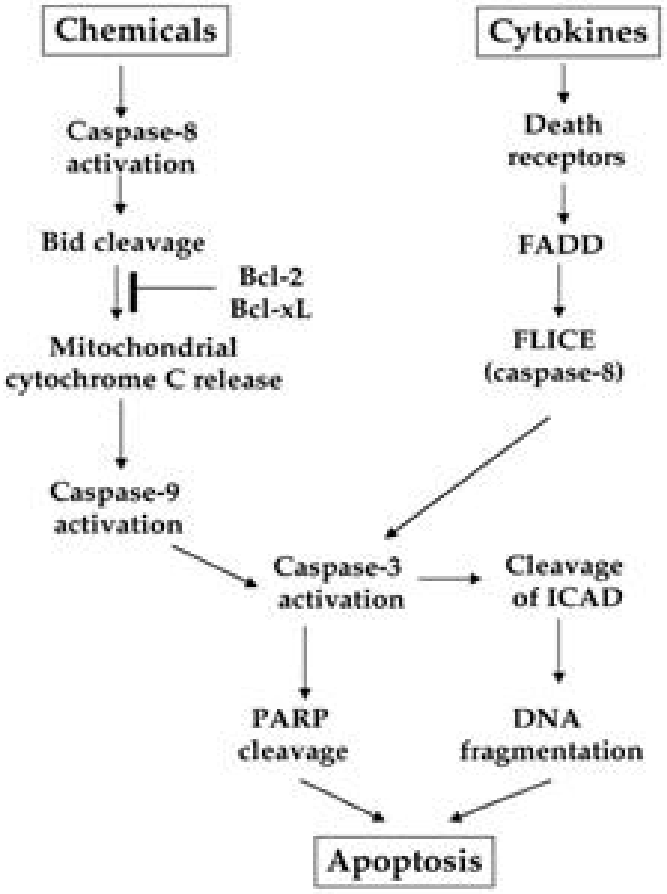

Figure 6.1: Figure showing two distinct pathways leading to cellular apoptosis, taken from (7). Apoptosis can be initiated by internal events involving the release of cytochrome C from the mitochondria, in turn leading to the downstream activation of caspases. Alternatively, cell surface receptors can be activated by specific ligands that bind to 'death receptors'. This pathway is typically mediated by immune cells, to initiate intracellular signaling and the downstream activation of relevant caspases.

cysteine proteases called caspases (3) (Figure 6.1). Dong et al (32) constructed an experimental system based on an inducible caspase (iCaspase-9) in order to address this question. Upon exposure to a dimerizer drug, this caspase induced selective and controlled cellular apoptosis. Using this artificial death switch construct, Dong et al were able to identify the minimum value for the apoptotic threshold. However, the determination of the exact proportion of apoptotic cells needed for vessel disruption, required the formulation of a mathematical model of the experimental system. In the following sections, we present a brief introduction to this experimental setup,

followed by model development and simulation results.

6.2 Experimental Setup

In (32), Dong et al generated HDMECs stably expressing the death switch, or iCaspase-9 (HDMEC-iCaspase-9). These cells underwent apoptosis in vitro upon exposure to the dimerizer drug AP20187. The drug was non toxic to untransduced cells, so that empty vector control or parental HDMECs (HDMEC-LXSN) were left unharmed upon application of AP20187. Next, capillary sprouts were engineered in vitro with varying proportions (6:0, 5:1, 4:2, 3:3, 2:4, 1:5, 0:6) of HDMEC-iCaspase-9, and empty vector control HDMECs. Application of the dimerizer drug to this system induced apoptosis of a pre-determined cohort of ECs. Thus, it was possible to determine the resistance of blood vessels to EC apoptosis, before a significant drop in vessel density was observed. This experiment was then replicated in vivo. Human blood vessels were generated in vivo, with the same proportions of HDMEC-iCaspase-9 and HDMEC-LXSN, as in the in vitro case. Again, application of AP20187 induced apoptosis of a known percentage of ECs causing blood vessels lined with these cells to be disrupted. Hence, a range for the apoptotic requirement percentage in both in vitro, and in vivo, was obtained.

6.2.1 In vitro Capillary Tube Assays

A total of 1.5×10^5 cells (in varying ratios of HDMEC-iCaspase-9 and empty vector control) were cultured in 1.5 ml of type-I collagen, in the presence of 50 ng/ml VEGF. Starting on day 4, and continuing to day 11, the cells were exposed to 0 (control) or 100 nM of AP20187. The number of capillary tubes were counted daily. A significant decrease (p-value ≤ 0.05) in the number of capillary tubes was observed, when at least 33.33% (HDMEC-iCaspase-9:HDMEC-LXSN = 2:4) of the HDMECs were killed. It

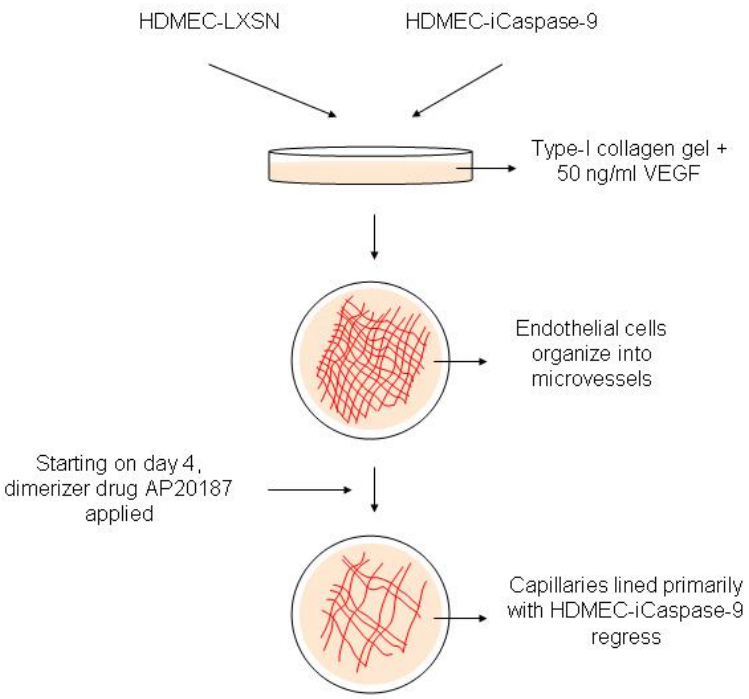

Figure 6.2: Figure showing a schematic of the in vitro capillary sprouting assays described in (32). Briefly, HDMEC-iCaspase-9 and empty vector control HDMECs were cultured in the presence of 50 ng/ml VEGF. Starting on day 4, and continuing to day 11, the cells were exposed to 0 (control) or 100 nM of the dimerizer drug AP20187. Capillaries lined with HDMEC-iCaspase-9 were observed to regress. The number of capillary tubes were counted at daily intervals.

was also observed that VEGF did not affect the ability of AP20187 to mediate cell death. A schematic of these experiments is shown in Figure 6.2.

6.2.2 In vivo Model of Human Angiogenesis

The mouse experimental system used to generate human blood vessels in vivo has already been described in Chapter V. Briefly, varying proportions of HDMEC-iCaspase-9 and HDMEC-LXSN were seeded on PLLA biodegradable scaffolds, and implanted subcutaneously in SCID mice. Eleven days post transplantation, 2 mg/kg AP20187 was given daily for 3 days. Sprouts were counted on day 14, and once again a significant decrease (p-value ≤ 0.05) in the number of capillary tubes was observed, when at least 33.33% of the HDMECs were killed.

6.3 Mathematical Model Development

Results from the in vitro capillary tube assays suggest that an initial ratio of 2:4 HDMEC-iCaspase-9:HDMEC-LXSN, which is equivalent to killing 33% of the endothelial cells by day 8, leads to significant (p=0.002 (32)) reduction in vessel density. However, the next experimental ratio tested here (1:5 HDMEC-iCaspase-9:HDMEC-LXSN) results in a p-value of 0.495, which does not reflect a significant reduction in vessel density. In order to further rigorously investigate the proportion of endothelial cells that must be killed in order obtain a significant reduction in blood vessel density, a mathematical model of the experimental procedure described above is formulated. In the preceding chapter, we have already developed a model for capillary tube formation in vitro, as well as tumor vascularization in vivo wherein, we were able to capture the process of vessel formation from free HDMECs. This modelling framework can easily be adapted to represent the experimental system described above. The resulting model consists of a system of five differential equations describing the temporal changes in the two populations of endothelial cells - HDMEC-LSXN (M_1) and HDMEC-iCaspase-9 (M_2) - the angiogenic factors VEGF (A) and CXCL8 (L), and the capillary tubes (V), coupled with a further five equations describing the binding dynamics of CXCL8 and VEGF to their endothelial cell surface receptors.

6.3.1 Pre-treatment Equations

Prior to treatment, the endothelial cells are assumed to follow the following statement of balance.

rate of change of HDMEC density	=	VEGF and CXCL8-dependent proliferation	-	VEGF-dependent death	-	VEGF and CXCL8-dependent vascular inclusion

This translates to the following equations. Note that our terminology and notation remains the same as in preceding chapters.

$$\begin{aligned}(6.1)\qquad \frac{dM_1}{dt} &= (\mu_a\,\phi_a + \mu_l\,\phi_l - (\lambda_m - \delta\,\phi_a))\;M_1\left(1 - \frac{M_1+M_2}{M_0-\alpha_1 V}\right)\\ &\quad -\alpha_1\;(\alpha_2\,\phi_a + \alpha_3\,\phi_l)\;M_1\\ (6.2)\qquad \frac{dM_2}{dt} &= (\mu_a\,\phi_a + \mu_l\,\phi_l - (\lambda_m - \delta\,\phi_a))\;M_2\left(1 - \frac{M_1+M_2}{M_0-\alpha_1 V}\right)\\ &\quad -\alpha_1\;(\alpha_2\,\phi_a + \alpha_3\,\phi_l)\;M_2\end{aligned}$$

where,

$$(6.3)\qquad \phi_l = \phi_l(C_l, M_1, M_2, V) = \frac{C_l}{M_1+M_2+\alpha_1 V}$$

$$(6.4)\qquad \phi_a = \phi_a(D_a, M_1, M_2, V) = \frac{D_a}{M_1+M_2+\alpha_1 V}$$

Equations (6.1) and (6.2) give the rates of change of HDMEC-LXSN (M_1) and HDMEC-iCaspase9 (M_2) densities, respectively. Both VEGF and CXCL8 stimulate HDMEC division and the proliferation rate depends on the functions ϕ_a and ϕ_l, which represent amounts of these chemokines bound to cell surface receptors on the HDMECs. The function ϕ_a is computed by writing down the biochemical reaction diagram corresponding to dimeric binding of VEGF to its receptors on endothelial cell surfaces (cf. Chapter IV, D_a is the density of activated dimerized VEGFR2-VEGF complexes). The law of mass action is applied to obtain the corresponding differential equations for the various species involved. Finally, dividing the dimerized receptor-ligand complex density by total number of endothelial cells gives the average density of VEGF bound to cell surface receptors. The function ϕ_l is computed in a similar way, except CXCL8 is assumed to undergo monomeric binding to its receptors (cf. Chapter V, C_l is the density of activated CXCR1/2-CXCL8 complexes).

Endothelial cell death incorporates the anti-apoptotic effect of the intracellular protein Bcl-2, whose expression is up-regulated in presence of VEGF. As assumed previously in Chapter V, since Bcl-2 is an intracellular protein, a separate equation for it is not included; instead its effects are modelled using VEGF concentrations. Natural cell death rate is given by λ_m, however in the presence of bound VEGF, this is reduced by a factor δ. The HDMECs are assumed to grow logistically, as the carrying capacity of this experimental environment is limited. As endothelial cells grow in number, they begin to come together and arrange themselves into microvessels. When this happens, they are no longer considered a part of the free endothelial cell population as they have now become part of the microvasculature. Thus, vascular inclusion of the HDMECs results in a decrease in the free endothelial cell density, and a corresponding increase in the microvessel density.

$$\frac{dA}{dt} = r_3 - \lambda_a A - f(M_1, M_2, V) \tag{6.5}$$

$$\frac{dA}{dt} = 0 \tag{6.6}$$

Equation (6.5) gives the rate of change of free VEGF (A) for the in vivo experimental system. Here a constant, background rate of VEGF production r_3, (by mouse cells or the implanted endothelial cells) is assumed. VEGF undergoes natural decay at a rate λ_a, and is taken up by the endothelial cells, as per the uptake function $f(.)$. A precise form of f is given by equation (5.3) in Chapter V. Equation (6.6) gives the rate of change of free VEGF for the in vitro experimental system, where the cells are cultured in the presence of 50 ng/ml of VEGF. The cell surface receptors still bind to free VEGF but because it is being replenished externally, it is assumed that this uptake does not significantly change free VEGF concentrations. Thus the rate

of change is taken to be zero.

$$\frac{dL}{dt} = (\beta_l + \beta_a\,\phi_a)\;(M_1 + M_2) - \lambda_l\,L - g(M_1, M_2, V) \tag{6.7}$$

Equation (6.7) gives the rate of change of free CXCL8 (L). Endothelial cells naturally synthesize it, which is represented in the equation by the parameter β_l. The production of CXCL8 is up regulated when Bcl-2 levels are elevated (in the presence of bound VEGF), at a rate proportional to β_a. CXCL8 is lost due to natural decay at a rate λ_a and uptake by HDMECs as per the uptake function $g(.)$. A precise form of g is given by equation (5.11) in Chapter V.

$$\frac{dV}{dt} = (\alpha_2\,\phi_a + \alpha_3\,\phi_l)\;(M_1 + M_2) - \alpha_4\;(\lambda_m - \delta\,\phi_a)\;\alpha_1\,V \tag{6.8}$$

Equation (6.8) gives the rate of change of functional microvessel density (V). The vessels are produced by the HDMECs in the process of vascular inclusion. Both VEGF and CXCL8 are strong chemoattractants for the HDMECs, so that they aggregate to form microvessels at rates proportional to the amounts of these chemokines bound to the endothelial cells, with rate constants α_2 and α_3. As the endothelial cells lining vessels apoptose, the vessels become dysfunctional at a rate α_4, which is proportional to the number of endothelial cells lining the vessels per unit volume.

6.3.2 Post-treatment Equations

$$\begin{aligned}\frac{dM_1}{dt} &= (\mu_a\,\phi_a + \mu_l\,\phi_l - (\lambda_m - \delta\,\phi_a))\;M_1\left(1 - \frac{M_1 + M_2}{M_0 - \alpha_1 V}\right)\\ &\quad -\alpha_1\;(\alpha_2\,\phi_a + \alpha_3\,\phi_l)\;M_1\end{aligned} \tag{6.9}$$

Treatment using the dimerizer drug AP20187 is given in vitro starting from day 4 of seeding the endothelial cells. Equation (6.9) gives the rate of change of HDMEC-LXSN density post treatment. HDMEC-LXSN cells are left unharmed by AP20187, thus their rate of change remains unaffected, so that equations (6.9) and (6.1) are the same.

$$\frac{dM_2}{dt} = -\chi_1 M_2 - \alpha_1 \left(\alpha_2 \phi_a + \alpha_3 \phi_l\right) M_2 \tag{6.10}$$

Equation (6.10) gives the rate of change of HDMEC-iCaspase9 density post treatment. The drug causes these cells to die at a rate χ_1 that is determined by forcing 90% of these cells to die 4 days after treatment, as observed in the experiments. Thus, the growth terms in equation (6.2) is replaced by a constant rate of death.

The rate of change of free VEGF concentration post treatment is not effected by the addition of the dimerizer drug to the system, and is assumed to be the same as that pre-treatment, given by equation (6.5) in the in vivo case, or equation (6.6) in the in vitro case.

$$\frac{dL}{dt} = \left(\beta_l + \beta_a \phi_a\right) M_1 - \lambda_l L - g(M_1, M_2, V) \tag{6.11}$$

Equation (6.11) gives the rate of change of free CXCL8 concentration post treatment. It is assumed that endothelial cells marked to die (HDMEC-iCaspase9) are not able to synthesize CXCL8 any more. Thus equation (6.11) may be obtained from equation (6.7) by altering the CXCL8 production term to exclude production by HDMEC-iCaspase9 (M_2).

$$\frac{dV}{dt} = \left(\alpha_2 \phi_a + \alpha_3 \phi_l\right)\left(M_1 + M_2\right) - \alpha_4 \left(\lambda_m - \delta \phi_a\right) \alpha_1 V - \chi_2 V \tag{6.12}$$

Equation (6.12) gives the rate of change of microvessel density post treatment. Since the HDMEC-iCaspase9 lining the microvessels die under due to the action of the drug, an additional term is included in the microvessel equation to incorporate the resulting loss of functionality. AP20187 induced microvessel dysfunctional rate χ_2 is proportional to χ_1 times the number of HDMEC-iCaspase9 lining the vessels per unit volume. It also depends on the proportion of iCaspase9 cells that were lining the vessels when treatment began.

6.3.3 Parameter Estimation

Most of the model parameters have been already been estimated from existing experimental literature and by fitting the model to the in vitro data of (97; 98). This has been discussed in detail in section 5.3 of Chapter V. The remaining parameters, relating to the rates of vascular inclusion of HDMECs are estimated so that microvessel densities best fit pre-treatment experimental data taken from (32).

Briefly, 1.5×10^5 HDMECs were seeded in a 1.5 ml layer of gelled type I collagen, and grown in the presence of 50 n/ml VEGF. The number of capillary tubes were counted at daily intervals. The pre-treatment model equations (6.1)- (6.8) are applicable in this case. The two cell populations need not be distinguished between, since we are considering pre-treatment data. In this case, the unknown parameters are α_1, the average number of cells per microvessel, α_2 and α_3, the VEGF and CXCL8 dependent microvessel formation rates, and α_4, the rate at which a microvessel becomes dysfunctional when the cells lining it die. Note that, as mentioned previously, we have simplified the vascular network into a series of equal length units, and 'a microvessel' is one segment between adjacent branching points that can fit into a cube of side one millimeter. In this case, α_1 may be estimated to have a value of 30 cells per vessel, considering average HDMEC sizes as reported in (74; 100; 126).

The resultant fit for the remaining three parameters is shown in Figure 6.3. The parameter values are listed in Table 6.1.

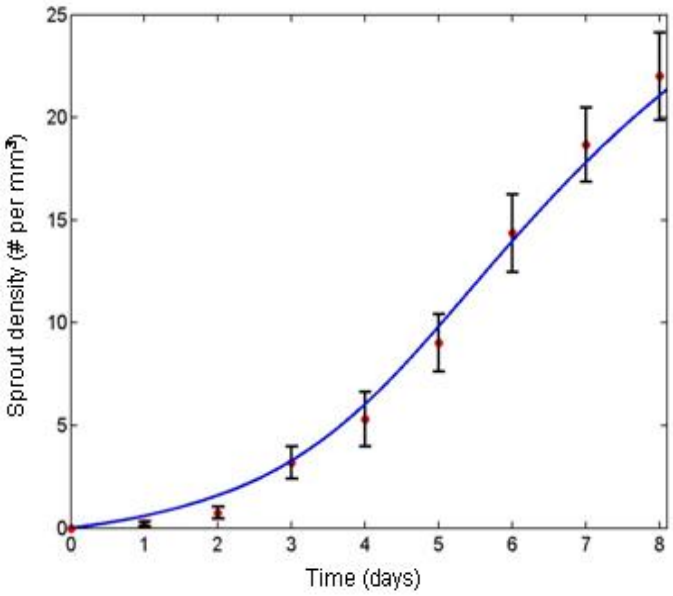

Figure 6.3: Fit to time-course data taken from in vitro capillary sprouting assays, with HDMECs cultured in the presence of 50 ng/ml VEGF

Table 6.1: List of parameter values relating to microvessel formation rates

Parameter	Value	Units
α_1	30.0	# HDMECs per Microvessel
α_2	0.2577	# Microvessels per pg of D_a per day
α_3	0.6741	# Microvessels per pg of C_l per day
α_4	0.24845	# Microvessels per HDMEC

For the post-treatment case, it is known that AP20187 induced HDMEC-iCaspase9 apoptosis level is 90% four days post treatment, which determines drug induced cell death rate $\chi_1 = 0.5756$ per day.

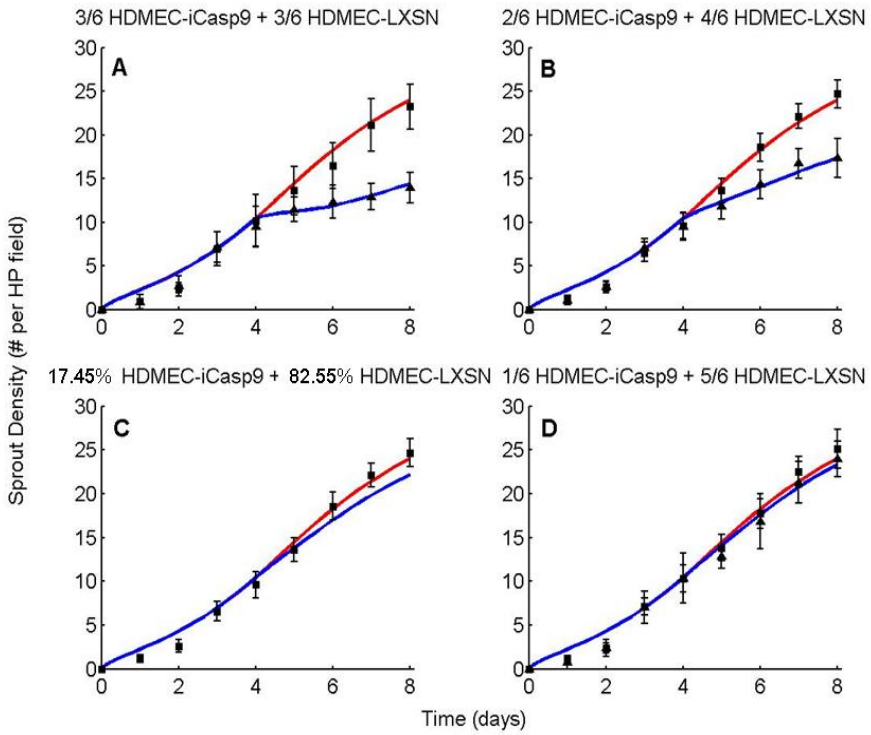

Figure 6.4: Mathematical modelling of the effect of endothelial cell apoptosis on angiogenesis. A system of differential equations describing the two populations of endothelial cells (HDMEC-iCaspase-9 and HDMEC-LSXN), angiogenic factors, and capillary tubes was derived for evaluation of inaccessible HDMEC-iCaspase-9:HDMEC-LXSN ratios in vitro. (A,B,D) Data from the in vitro control experiments in which cells were supplemented with 50 ng/ml of VEGF alone (squares) are plotted together the best fit of the mathematical model (red line) to this data. Post treatment experimental data (triangles) is plotted along with fits of the mathematical model, obtained by varying the rate of vessel dysfunction associated with HDMEC-iCaspase-9 cells (χ_2) (blue line). (C) The mathematical prediction of sprout number when a culture containing 19.39% HDMEC-iCaspase-9 and 80.61% HDMEC-LXSN are exposed to 50 ng/ml VEGF + 100 nM AP20187 (blue line). The model predicts that at this critical percentage (corrected to 17.45% to account for 90% effectiveness of drug) of apoptotic endothelial cells, there is a significant decrease ($p = 0.0498$) in capillary sprouting in vitro.

6.4 Results

6.4.1 Apoptotic Requirement for Capillary Disruption In Vitro

Figures 6.4 shows microvessel counts from the in vitro experiments in which cells were supplemented with 50 ng/ml of VEGF alone (squares). These are plotted together with the best fit of the mathematical model in the pre-treatment case (red line). Using the post-treatment data (triangles), the rate of vessel dysfunction as-

sociated with HDMEC-iCaspase-9 cells, χ_2, is estimated from the experiments in which varying ratios of HDMEC-iCaspase-9 cells are present. The resultant fits are shown in Figures 6.4A,B,D (blue line). It should be noted that the only parameter being varied to get these fits is χ_2. The model can now be used to focus on the experimentally inaccessible ratios between 2:4 and 1:5 HDMEC-iCaspase-9:HDMEC-LXSN in order to precisely determine the percentage of cells that must be killed so that a significant reduction in vessel density is obtained. The model predicts that starting with 19.39% HDMEC-iCaspase-9 and 80.61% HDMEC-LXSN cells leads to a significant reduction in vessel density (p=0.0498) (Figure 6.4C, blue line). When corrected for the fact that 90% of the HDMEC-iCaspase-9 cells are dead 4 days after exposure to AP20187 in vitro, the critical percentage of apoptotic endothelial cells required to mediate a significant decrease in capillary sprouting is 17.45%.

Further, we can use the mathematical model to investigate the efficacy of AP20187 therapy in vitro versus different VEGF concentrations. The percentage of apoptotic cells is fixed at 17.45% - a level at which a significant reduction in vessel density is predicted in the presence of 50 ng/ml VEGF. After 4 days of treatment with AP20187, the model predicts an increase of 2.6% in the vessel density, if the cells are cultured in the presence of 100 ng/ml VEGF, as opposed to 50 ng/ml VEGF. Likewise, a decrease of 91% is predicted in vessel density on the fourth day of treatment, if the cells are cultured in the presence of 1 ng/ml VEGF. If no VEGF is added to the system, the decrease in vessel density is 99.9%. Taken together, this data indicates that the protective effect of VEGF on in vitro sprouting of endothelial cells is dose dependent.

6.4.2 Apoptotic Requirement for Blood Vessel Disruption In Vivo

This mathematical model can be modified to simulate the in vivo data, by adding background VEGF production by the host. The VEGF production rate r_3 in vivo is obtained from control experiments in which no HDEMC-iCaspase9 cells were present. This was achieved by fitting the vessel count 14 days post-implantation to the single data point available. The in vivo experiments indicated that 15-30% of cells need to be killed for a significant reduction in blood vessel density. Our mathematical model predicts that starting with 74.08% HDMEC-LXSN and 24.92% HDMEC-iCaspase-9 will cause a significant reduction in vessel density (p=0.0498) (Figure 6.5A). When adjusted for the percentage of HDMEC-iCaspase-9 cells that undergo apoptosis when treated with AP20187, the critical percentage for achieving a significant decrease in microvessel density in vivo comes to 22.43%.

We can also use the model to investigate the effect of anti-VEGF therapy on the apoptotic requirement of endothelial cells. In modelling terms, we treat the effect of anti-VEGF therapy to be a reduction in the bio-availability of VEGF to the endothelial cells. This therapy is applied at the same time as AP20187, starting on day 11, and is continued for four days. The model predicts that there is a significant reduction in microvessel density for therapy with an efficacy level greater than 15%, even when we begin with no HDMEC-iCaspase-9 cells. However, for therapy that is 10% efficacious, the critical percentage for achieving a significant reduction in capillary sprouting is predicted as 16.92%, and this increases to 19.73% for anti-VEGF therapy which is only 5% efficacious (Figure 6.5B).

6.5 Discussion

One of the hallmarks of tumors is their ability to induce sustained angiogenesis, and their dependence on it (40; 49). Tumors 'turn on' the angiogenic switch by the release of angiogenic factors, of which the most commonly expressed is VEGF (49). This has led to the development of a number of anti-angiogenic therapies, targeting VEGF, or its receptors or the endothelial cells lining the newly formed blood vessels themselves. Despite these differences in the target molecule, a feature common to most of these therapies is the induction of endothelial cell apoptosis resulting in disruption of the vasculature. Therefore, it is essential to improve our knowledge of the mechanisms underlying the maintenance of blood vessels. One such experimental system aimed to fix the percentage of apoptotic cells required for blood vessel regression, is described in (32). In this chapter, we have devised a mathematical model representing these experiments in order to evaluate experimentally inaccessible percentages of apoptotic cells. This can be used to predict this threshold with greater accuracy.

Experimental data suggested that between 16.67 - 33.33% cells need to be killed in order to disrupt capillaries in vitro. Using our mathematical model, the exact percentage was predicted to be 17.45% (Figure 6.4C). It is known that VEGF promotes endothelial cell survival by up-regulating intra-cellular levels of Bcl-2 (59; 98). However, the target of the dimerizer drug AP20187 used in the experiments to induce cell death is caspase-9, which acts downstream of Bcl-2. Thus, VEGF was unable to protect the cells against AP20187-induced apoptosis. Interestingly, the model simulations predicted an increase in the threshold of apoptotic requirement with increasing VEGF concentrations. This could be due to the fact that VEGF is

a potent inducer of cell proliferation, and it is likely that this compensates to some extent for the loss of cells due to apoptosis.

The model was then modified to simulate the experiments designed to fix the apoptotic requirement of cells in vivo. A percentage of 22% was predicted using the model (Figure 6.5A). Thus, the apoptotic requirement appears to be slightly greater in vivo than that predicted in vitro. This could be due to the process of vessel maturation that occurs in vivo, which would result in the stabilization of the microvessels. The model was then used to investigate the effect of anti-VEGF therapy on the apoptotic requirement of endothelial cells. As expected, it was found that increasing levels of anti-VEGF therapy resulted in lowering of the apoptotic requirement (Figure 6.5B). This is because the entire cell population is effected by the anti-VEGF therapy, as opposed to only the caspase-induced cells. However, a modelling assumption is that VEGF is the only angiogenic factor in the in vivo system. In reality, there may be many others such as the FGFs, that would offset the efficacy of anti-VEGF therapy to varying degrees.

Mathematical modelling such that described here can play an important role in the determination of parameters relating to anti-angiogenic therapy regimes, as well as aid in evaluation of current anti-vascular compounds under development. We began with the model of angiogenesis developed in Chapter V, and were able to modify it easily to simulate the in vitro and in vivo experiments of Dong et al, illustrating it's flexibility. Data from the in vivo simulations underscored the capability of blood vessels to maintain their integrity even under significant loss of endothelial cells. This provides a reference point for the preclinical testing of new anti-angiogenic drugs aimed at inducing endothelial cell apoptosis. The results further showed that VEGF did not prevent EC apoptosis and capillary tube disruption, induced by caspase-9

activation. The lack of VEGF's protective effect may reflect the fact that caspase-9 functions downstream from Bcl-2 in the cellular apoptotic pathway. This suggests that EC apoptosis-inducing therapy may be a promising target for the development of anti-angiogenic drugs. There is therefore, a need to study cell death pathways in greater detail. In the next chapter, we develop a model of tumoral angiogenesis that explicitly incorporates the intra-cellular apoptotic pathways mediated by the Bcl-family of proteins. We also test the potential of targeting the Bcl-2 molecule as a possible anti-vascular therapy.

In this chapter, we have demonstrated that it is possible to answer questions relating to the biology of vascular regression, which would otherwise have been difficult or even impossible to do experimentally. Taken together, our results support the concept that anti-angiogenic drugs that induce apoptosis of 17.45% or more cells in vitro, have the best probability to have a significant anti-angiogenic effect in vivo. Given the high financial as well as human costs of clinical trials, decisions in regards to allowing for a new drug to be tested in patients, or not, are of paramount importance. Here, we established a fairly straight-forward criterium - induction of at least 22% apoptosis in vivo is capable of consistently resulting in a significant drop in microvessel density. This parameter, together with other analyses of drug effectivity in laboratory studies and mathematical modelling of response to treatment, might be helpful to decide in favor or against clinical trial.

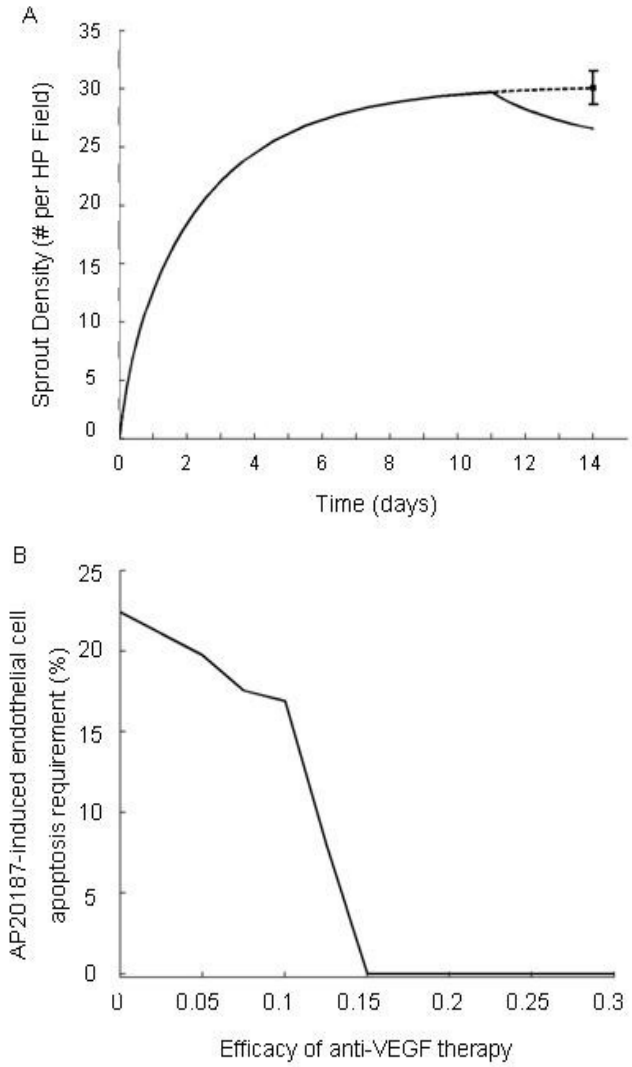

Figure 6.5: Mathematical modelling of the effect of endothelial cell apoptosis on angiogenesis. A system of differential equations describing the two populations of endothelial cells (HDMEC-iCaspase-9 and HDMEC-LSXN), angiogenic factors, and capillary tubes was derived for evaluation of inaccessible HDMEC-iCaspase-9:HDMEC-LXSN ratios in vivo. (A) The single data point from the in vivo control experiments in which no HDMEC-iCaspase-9 cells are present (square) is plotted together with the best fit of the mathematical model (dashed line) as well as the mathematical prediction of sprout number when 24.92% of the cells are HDMEC-iCaspase-9 (solid line). The model predicts that at this critical percentage (corrected to 22.43% to account for 90% effectiveness of drug) of apoptotic endothelial cells, there is a significant decrease ($p = 0.0498$) in capillary sprouting in vivo. (B) Apoptotic requirement of endothelial cells is plotted versus increasing efficacy of anti-VEGF treatment that is applied continuously from day 11 for four days, along with 100 nM of AP20187. The model predicts that for a level of therapy at least 15% efficacious, a significant reduction in vessel density is obtained without the presence of HDMEC-iCaspase-9. As the efficacy of anti-VEGF treatment is reduced further, the critical percentage of apoptotic cells required increases to a maximum of 22.43% (in the case of no anti-VEGF being applied).

CHAPTER VII

Anti-Bcl-2 Therapy Inhibits Tumor Vascularization and Retards Tumor Growth

7.1 Introduction

In Chapter V, we developed a model of intra-tumoral angiogenesis, which was the first to connect the molecular events associated with VEGFR2 dimerization and intra-cellular signaling with the temporal changes in endothelial cell proliferation, migration and survival. We were able to use this model to predict the effect of decreasing the bio-availability of VEGF, CXCL8 and Bcl-2 on tumor growth and vascular structure. Our preliminary results suggested that Bcl-2 is the most promising target for anti-angiogenic therapies along the VEGF pathway of interest. These results also led to the hypotheses that anti-Bcl-2 therapies applied at early and late stages of tumor growth will significantly affect, with a dose-dependent threshold, both, the time course of tumor development, as well as the maximum tumor cell and blood vessel densities. In this chapter, we will test this hypothesis by explicitly modelling the cellular response to the administration of specific anti-angiogenic therapies targeted against the Bcl-2 molecule at different stages of tumor development.

7.1.1 Bcl Family of Proteins

The Bcl family of proteins have been identified as crucial mediators of apoptosis, a form of cell death in which a programmed sequence of events leads to the disintegration of cells without releasing harmful substances into the surrounding tissue. There are anti-apoptotic Bcl proteins including Bcl-2 and Bcl-X_L, as well as their pro-apoptotic counterparts Bax, Bad, Bak, and Bid. These proteins are constitutively expressed within cells and it is the interaction between these molecules that determines cellular response to apoptotic signals such as intra-cellular damage and deprivation of or exposure to cytokines and growth factors (3; 123; 154). Bcl proteins all differ slightly in size and intra-cellular location. Bcl-2 is a 26-kDa protein (122), while Bcl-X_L is reported to be slightly smaller (14). They are located mainly in the nuclear envelope, parts of the endoplasmic reticulum, and outer mitochondrial membrane (122; 129). Bax is a 21-kDa protein (88), and is localized to the outer mitochondrial membrane (129). The 18.4-kDa protein Bad can be found on the mitochondrial outer membrane, as well as the cytoplasm (158), while the 23.4-kDa protein Bak is a single-pass membrane protein (158). Bid is a 22-kDa protein and resides in the cytoplasm (158).

Apoptosis in cells is brought about by the activation of intra-cellular cysteine proteases called caspases (3). This occurs due to the presence of cytochrome c in the cell cytoplasm, which together with Apaf1 activates caspase 9. This in turn activates downstream effector caspases like caspase 3, which induce cell death (2). The Bcl family of proteins helps regulate this process by controlling the release of cytochrome c, typically from the mitochondrial outer membrane. Broadly speaking, the pro-apoptotic members of the Bcl family may be divided into two sub-families. Members of the Bax-like sub-family include Bax and Bak, and are very similar to

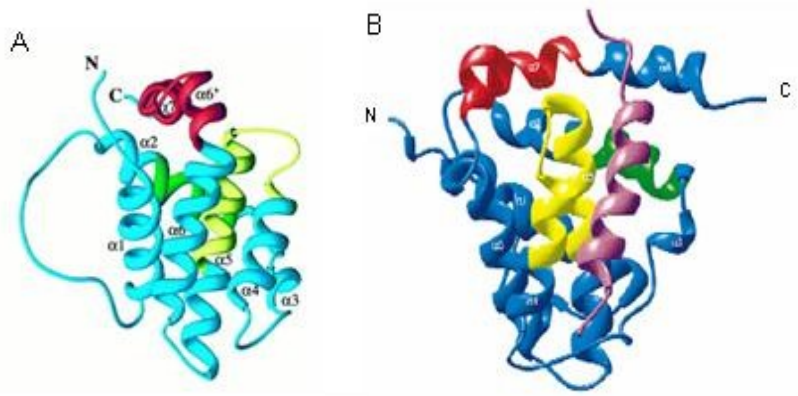

Figure 7.1: (A) Ribbons depiction of the average minimized structure for Bcl-2 (113). (B) A Ribbons depiction of the averaged, minimized NMR structure of the Bcl-X_L-Bad complex. The BH1, BH2, and BH3 domains of Bcl-xL are colored yellow, red, and green, respectively. The Bad peptide is shown in purple (114).

Bcl-2 in sequence. The BH3-only proteins including Bad, Bid, and Bak are sequentially unrelated to any Bcl family proteins, apart from containing a BH3 binding domain (2). Members of the BH3-only sub-family bind to BH3 binding pockets that form on the anti-apoptotic proteins like Bcl-2 and Bcl-X_L, preventing them from inhibiting activation of members of the Bax-like sub-family. It is believed that this results in the release of cytochrome c into the cell cytoplasm (154; 2). Thus, the anti-apoptotic function of Bcl-2 and Bcl-X_L is at least partly due to their ability to heterodimerize with Bax, Bad, Bak and Bid, inhibiting their pro-apoptotic function (154). The various pathways that Bcl-2 and its family are involved in, are shown in Figure 7.2.

The Bcl family proteins have been shown to play a key role in tumor development and progression. Tumor cells in several types of cancers such as prostrate, breast, colorectal, head and neck cancers, and melanoma are known to over-express either Bcl-2, or Bcl-X_L, or both (154). In addition to promoting cell survival, this could provide cancer cells with some measure of protection from chemo- and radiotherapy, especially if these therapies directly or indirectly induce apoptosis (154). Further,

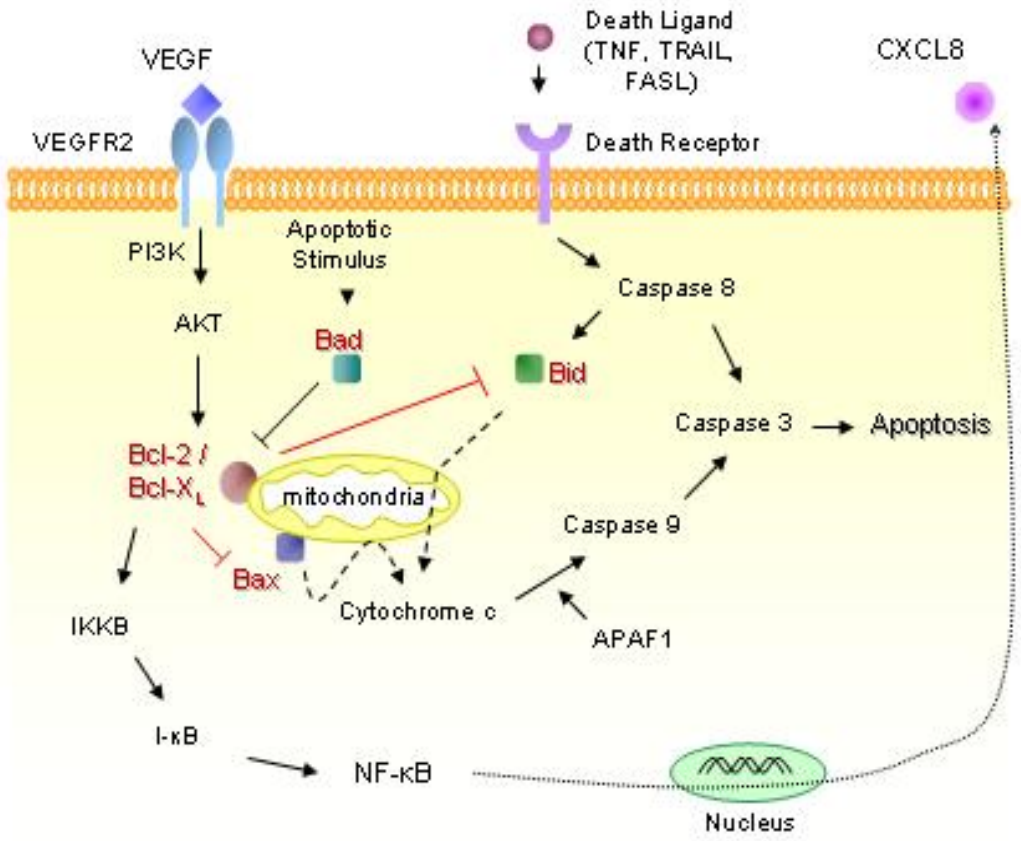

Figure 7.2: Schematic diagram showing intra-cellular functions of the Bcl family of proteins. VEGF induces Bcl-2 expression via the VEGFR-2, PI3K/Akt signalling pathway. Pro-apoptotic proteins such as Bad and Bid heterodimerize with Bcl-2/Bcl-X_L thus regulating their ability to inhibit activation of other pro-apoptotic proteins like Bax. Activation of Bax results in the release of cytochrome c from the mitochondrial outer membrane, which together with Apaf1, causes caspase activation. This induces cell apoptosis. Bcl-2 also acts as a pro-angiogenic signalling molecule, by activating the NF-κB signaling pathway, inducing expression of the pro-angiogenic chemokine, CXCL8.

Nör et al have demonstrated that in the case of some head and neck cancers, cancer cells are able to extend this protective effect to the endothelial cells lining the blood vessels in the vicinity of the tumor by up-regulating levels of Bcl-2 within these cells, thus enhancing intra-tumoral angiogenesis (97; 98; 99). This makes Bcl-2 and Bcl-X_L attractive targets for the development of anti-cancer drugs. In fact, several forms of therapy targeting Bcl-2/Bcl-X_L are under development. These include antisense *bcl-2* and *bcl-X_L* oligonucleotides that work by inhibiting Bcl-2/Bcl-X_L ex-

pression levels, single chain antibodies and peptides that bind to the Bcl-2 molecule inhibiting it's functions, and an anti-*bcl-2* ribozyme, that works by degrading *bcl-2* mRNA (154). However, Wang et al (154) propose that nonpeptidic, cell-permeable small molecule inhibitors of Bcl-2 and Bcl-X_L may have greater potential as anti-cancer drugs than the therapies mentioned above for a variety of reasons including better bio-availability, stability, low cost and the ability to penetrate the blood-brain barrier of the central nervous system. These inhibitor molecules act as antagonists of Bcl-2/Bcl-X_L by binding to their BH3 binding pocket, thus preventing pro-apoptotic members such as Bax, Bad, Bak from binding to Bcl-2/Bcl-X_L.

7.2 Development of a Multiscale Model of Tumor Vascularization, Incorporating Interactions of the Bcl-family of Proteins

With all of these new possibilities, a critical challenge in experimental therapeutics for cancer is to decide which drugs are the best candidates for clinical trials. Mathematical modelling, such as that developed here can help to determine which anti-cancer drugs have the most potential for therapeutic benefit. In this chapter, we concentrate on the anti-angiogenic potential of therapies targeted at Bcl-2, in the form of small molecule inhibitors such as BL193 (59; 160) and TW37 (160); both of which have been shown to cause a marked decrease in angiogenic potential of endothelial cells in vitro. Since BL193 has similar inhibition constants for both Bcl-2 and Bcl-X_L, we focus on this as our drug of choice. Our model is based on the experiments of Nör et al (97; 98; 99). A brief overview of these experiments is included in Chapter V, where we have already developed and presented a mathematical model describing them. It is our goal to extend this model to explicitly incorporate the pro-apoptotic as well as anti-apoptotic members of the Bcl family, so that we can better understand the implications and effects of therapy targeted against these proteins.

In particular, our preliminary model could not address the mechanism of action of BL193 and could not relate its binding efficiency to its therapeutic efficacy. The model presented here will be able to study both of these important issues as well as predict tumor response with increased accuracy.

7.2.1 Model Foundation

A biochemically motivated, ordinary differential equation model is developed to capture the essential intra-cellular dynamics of the Bcl family of proteins governing programmed cell death. The mathematical model has as its foundation specific biological assumptions that are based on the accepted knowledge of the function of and cellular response to various pro and anti-apoptotic proteins. Specifically, the intra-cellular concentration, in femtograms per cell, of a single anti-apoptotic protein Bcl-2, and a single pro-apoptotic representative of the Bcl family, Bad, will be tracked in time. Using one representative of the pro and anti apoptotic family members allows us to avoid involving a number of intra-cellular binding parameters for which there is no experimental data. The particular choice of the representative proteins was made for the following reasons: (1) BL193 has similar binding affinities to both of the anti-apoptotic proteins, Bcl-2 and Bcl-X_L, on which it has been shown to act (160), (2) it is intra-cellular levels of Bcl-2 that are up-regulated in response to a VEGF stimulus (98) and (3) Bad binds to Bcl-2 with a higher affinity than the other Bcl proteins (154). It also acts upstream of the Bax-like members of the Bcl family, making it the protein of choice to represent the pro-apoptotic members of the Bcl family. The intra-cellular concentration of Bcl-2 will be represented by the letter B, while that of Bad will be represented by the letter X.

It is known that Bcl-2 and Bad interact with each other within the endothelial cell to form heterodimers. This balance between pro- and anti-apoptotic proteins

regulates cell death rate. In an endothelial cell, unbound Bcl-2, unbound Bad and Bcl-2-Bad dimers will be present at their respective constitutive levels. We assume that the amount of unbound protein Bad determines the cell death rate, since it is the pro-apoptotic members of the Bcl family that are directly responsible for regulating caspase activation within the cells (2). It has experimentally been shown that Bcl-2 induces the expression of CXCL8 in endothelial cells through its ability to activate the NF-κB signaling pathway (59). Therefore, we assume that the amount of unbound Bcl-2 is responsible for CXCL8 production by the endothelial cells. At background levels of Bcl-2 and Bad, the cell death rate is taken to be 0.12 per day (74) and HDMEC CXCL8 production rate is fit to experiments in (98). The VEGF-Bcl-2-CXCL8 pathway discovered in the experiments of Nör et al (97; 98) is explicitly included in this model by allowing for the up-regulation of Bcl-2 in the presence of VEGF. In turn, this up-regulates production of CXCL8 by the endothelial cell. This is due to increase in free Bcl-2 levels within the cell. High levels of Bcl-2 would mean low levels of Bad in its unbound state since it would be taken up as Bcl-2-Bad dimers. This would result in a decrease in cell death rate. Thus, we are able to capture the essential principles of cell death regulation by the Bcl family proteins, as well as account for the pro-survival, and pro-angiogenic effect of Bcl-2 in particular. The complete derivation of equations is discussed in the sections that follow.

Note that throughout this chapter, we adopt the following notation for the various species being modelled.

M = Human dermal microvascular endothelial cell density

A = Unbound VEGF concentration

R_a = VEGFR-2 density

C_a = VEGF - VEGFR-2 complex density

D_a = VEGF- VEGFR-2 - VEGF complex density

L = Unbound CXCL8 concentration

R_l = CXCL8 receptor density

C_l = CXCL8-receptor complex density

V = Microvessel density

B = Intracellular unbound Bcl-2 concentration

X = Intracellular unbound Bad concentration

C_{bx} = Intracellular Bcl-2 - Bad complex concentration

I = Intracellular unbound BL193 concentration per cell

C_{bi} = Intracellular Bcl-2 - BL193 complex concentration

N = Tumor cell density

7.2.2 Modelling Bcl family protein interactions within a single cell

We begin our model development at the single cell level, so that we may include the role of the Bcl family proteins in cell apoptosis explicitly. Once we are able to describe the relevant apoptotic pathways within a single cell, we can scale the model up to the population level, and thus obtain a better quantitative understanding of the role of these intra-cellular molecular pathways in determining vascular development in tumors.

Bcl-2 - Bad and Bcl-2- BL193 interactions

Following the general approach of Levine et al (75), the law of mass action is used to translate the reaction diagram in Figure 7.3, which describes the hetero-dimerization of Bcl-2 and Bad as well as the inhibition of Bcl-2 by BL193, into a system of differential equations (7.1) - (7.5) that govern the temporal changes in the intra-cellular concentrations of these proteins. Specifically, the upper case letters in equations (7.1) - (7.5) represent chemical concentrations, measured in femtograms per cell. Then, B is unbound Bcl-2 protein per cell, X is unbound Bad protein per cell, C_{bx} is the quantity per cell of the heterodimer formed when one molecule of Bcl-2 binds to one molecule of Bad, I is the amount of small molecule inhibitor or BL193 per cell, and C_{bi} is quantity per cell of the complex formed when one molecule of Bcl-2 binds to one molecule of BL193.

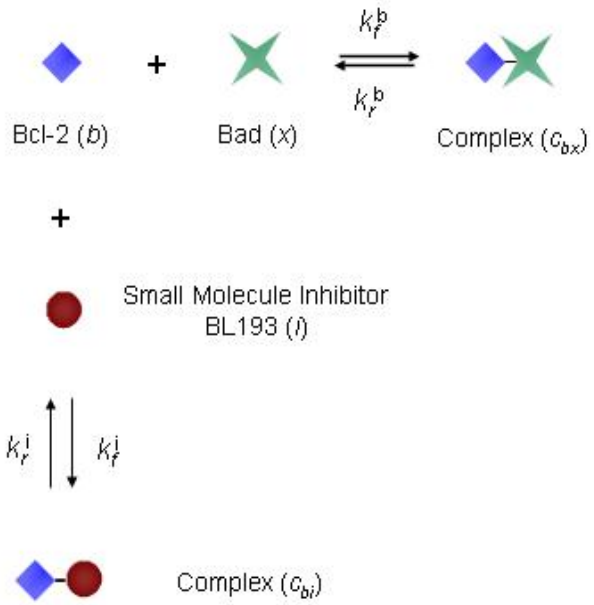

Figure 7.3: Reaction diagram showing the heterodimerization reaction between the Bcl-2 (b) and Bad (x) molecules, and the inhibition of Bcl-2 by a small molecule inhibitor, BL193 (i).

It is assumed that upon application of therapy, the inhibitor molecules diffuse into the endothelial cell across the cell membrane. This is consistent with the design strategy behind these small molecule inhibitors (BL193 has a molecular weight of only 0.5 kDa (160)). Thus, there is a source term in equation (7.4), where the rate of entry of the inhibitor molecules into an endothelial cell is proportional to the difference of extracellular and intra-cellular BL193 concentrations. The extracellular concentration, I_0, of BL193 in the local environment of a cell is a parameter that varies as the dosage level of therapy changes, and is fit to match such experiments. The constant D_i is a measure of cell wall permeability to BL193, and has units of 1/day. We can write the rate D_i as $-(\ln 1/2)/t_{1/2}$, where $t_{1/2}$ is the amount of time it takes half the drug, external to a cell, to be internalized. The inhibition constant K_i of BL193, which is given by the ratio of k_r^i to k_f^i, is 320 nM (160). The effect on intra-cellular Bcl-2 and Bad densities of the addition of varying amounts of BL193 can be seen from Figure 7.4A. As BL193 level within a cell increases from 0 to 0.9 femtograms, free Bcl-2 concentration is seen to decrease by 79%, causing free Bad concentration to increase by 13%, over their respective constitutive levels.

$$\frac{dB}{dt} = -k_f^b\, B\, X + k_r^b\, C_{bx} - k_f^i\, B\, I + k_r^i\, C_{bi} \tag{7.1}$$

$$\frac{dX}{dt} = -k_f^b\, B\, X + k_r^b\, C_{bx} \tag{7.2}$$

$$\frac{dC_{bx}}{dt} = k_f^b\, B\, X - k_r^b\, C_{bx} \tag{7.3}$$

$$\frac{dI}{dt} = -k_f^i\, B\, I + k_r^i\, C_{bi} + D_i\, (I_0 - I) \tag{7.4}$$

$$\frac{dC_{bi}}{dt} = k_f^i\, B\, I - k_r^i\, C_{bi} \tag{7.5}$$

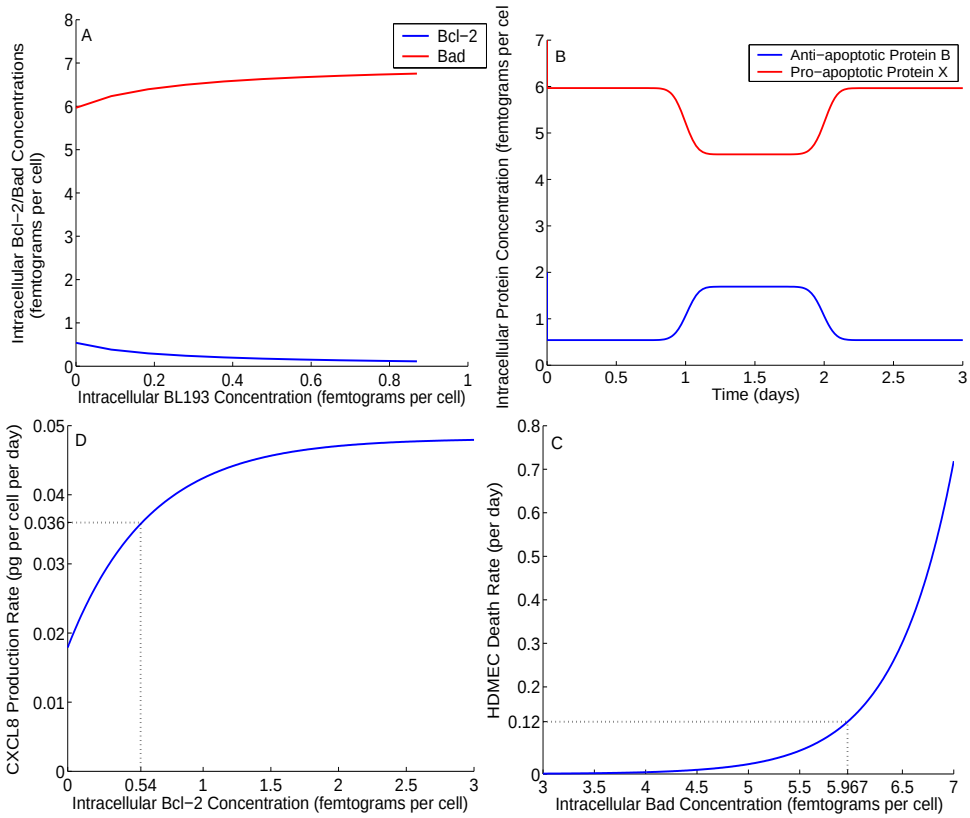

Figure 7.4: Intra-cellular Bcl-2 and Bad concentrations, and their effect on cell death rate and CXCL8 production rate. (A), Bcl-2 levels within a single cell are seen to decline, as increasing amounts of BL193 therapy are administered, causing a corresponding increase in Bad levels. (B), Upon application of 50 ng/ml VEGF, Bcl-2 level within a cell is seen to increase 3.1 fold, causing a 22% decrease in the level of Bad. As VEGF is consumed, Bcl-2 and Bad protein levels return to their constitutive state. (C), CXCL8 production rate by HDMECs increases to a maximum, as intra-cellular Bcl-2 levels increase. At the constitutive level of Bcl-2, CXCL8 production rate is fixed at 0.0358 pg of CXCL8 per HDMEC per day (see parameter estimation, Chapter V). The model allows for CXCL8 production independent of Bcl-2 up-regulation as well. (D), HDMEC death rate is taken to increase exponentially with the amount of intra-cellular Bad protein. At the constitutive level of Bad, cell death rate is taken to be 0.12 per day (73).

Modelling the effect of VEGF on Bcl-2

Extracellular concentrations of cytokines and growth factors influence intracellular concentrations of the Bcl family proteins. In order to capture the effect of VEGF on Bcl-2 and Bad levels within each cell, we postulate that the amount of Bcl-2 produced is directly proportional to the number of active VEGF-receptor dimer complexes per cell. A corresponding source term for Bcl-2 may be included in Equation (7.1), which

changes to equation (7.6) given below.

$$\frac{dB}{dt} = -k_f^b\, B\, X + k_r^b\, C_{bx} - k_f^i\, B\, I + k_r^i\, C_{bi} + \beta_a \frac{d}{dt}\,(\phi_a) \tag{7.6}$$

Here, ϕ_a is the density of active VEGF-receptor dimer complexes in pg per cell. In the presence of 50 ng per ml VEGF, it is observed that Bcl-2 is up-regulated 3.1 fold (98). This is used to fix the constant β_a, which determines the level of up-regulation of Bcl-2 by VEGF. In Figure 7.4B, levels of Bcl-2 and Bad within a single cell are plotted versus time. An external dose of 50 ng/ml VEGF is given after 1 day, and lasts for 1 day. It can be observed that unbound Bcl-2 density increases by 3.1-fold as VEGF is taken up by the cell. Correspondingly, unbound Bad density decreases. As the VEGF is consumed, the amounts of Bcl-2 and Bad proteins eventually fall back to constitutive levels.

The VEGF-dependent CXCL8 production rate of HDMECs used in equation (5.11), in Chapter V, can now be replaced with a rate, denoted by β_l, that is dependent on intracellular Bcl-2 concentration, B. The functional form of $\beta_l(B)$ is taken as follows:

$$\beta_l(B) = \beta_m + a_p\,(1 - e^{-b_p\, B}) \tag{7.7}$$

The CXCL8 production rate by HDMECs is assumed to increase to a maximum level, as intra-cellular Bcl-2 concentration increases, under the effect of VEGF. We also allow for the possibility that CXCL8 could be produced by endothelial cells independent of Bcl-2. Thus, if intra-cellular Bcl-2 levels fall to zero, there is still a constant background rate of CXCL8 production, namely β_m. Figure 7.4C shows a graph of the CXCL8 production rate. We can see that as intra-cellular Bcl-2 levels

increase, which may be in response to the presence of VEGF, the production rate of CXCL8 also increases.

7.2.3 Modelling programmed cell death regulation at the population level

Temporal changes in Bcl-2 concentration, within a single cell, will now be explicitly incorporated into the population level model of tumor growth and sustained angiogenesis described in Chapter V. To accomplish this, the VEGF-dependent death rate used in equation (5.19), in Chapter V, is replaced with a rate, denoted by λ_m, that is dependent on intracellular Bad concentration, X. In this way, the behavior predicted by the single cell model described in the previous section is used to determine the response of a population of cells to their microenviroment. The functional form of λ_m is taken as follows:

$$\lambda_m(X) = a_d\, e^{b_d\, X} \tag{7.8}$$

In the absence of experiments designed to determine the precise functional dependence of cell death on pro-apoptotic members of the Bcl family, we choose an exponential form of the death rate. This reflects the fact that cells are highly sensitive to pro-apoptotic signals such as intra-cellular Bad levels, which are normally tightly controlled and balanced by anti-apoptotic proteins like Bcl-2. There is some indirect experimental justification for this, which can be seen from a comparison of the model predictions to in vitro therapy results, presented in the next section. Figure 7.4D shows a graph of HDMEC death rate as a function of its intra-cellular environment. The graph also gives insight into the effect of extracellular events on the fate of the cell. For instance, if as a result of anti Bcl-2 therapy, 0.5 femtograms of BL193 are incorporated by an endothelial cell, then free Bcl-2 level within the cell falls by 66%,

and free Bad level increases by 11 %, over their respective constitutive values (Figure 7.4A). This causes an increase in cell death rate from 0.12 per day to 0.37 per day.

We have thus developed a truly multi-scale model of intra-tumoral angiogenesis; providing greater insight into vascular development and tumor growth dynamics. The complete model equations are listed in Appendix C.

7.3 Parameter Estimation

Most of the parameters in the model have already been determined in Chapter V. However, the addition of equations governing the rates of change of Bcl-2, Bad, and BL193 introduces new parameters relating to these rates, and the effect of these molecules on cellular behavior such as CXCL8 production and death rates.The estimation of these parameters is described in greater detail below.

7.3.1 Experimental conditions

In a series of in vitro capillary sprouting assays described in (97), 3×10^5 human dermal microvascular endothelial cells (HDMECs) were seeded with 1.5 ml collagen (type I), and treated with 50 pg/mm^3 VEGF. The total (free + differentiated) number of HDMECs were counted every day. We can reduce the full model system to represent this, for parameter estimation purposes. The resulting equations are listed below.

$$\frac{dM}{dt} = \left(\mu_a \frac{D_a}{M} + \mu_l \frac{C_l}{M} - \lambda_m(X)\right) M \tag{7.9}$$

$$\frac{dL}{dt} = -\eta_1^l \, k_f^l \, L \, R_l + \eta_2^l \, k_r^l \, C_l - \lambda_l \, L + \beta_l(B) \, M \tag{7.10}$$

$$\begin{aligned}\frac{dR_l}{dt} &= -k_f^l \, L \, R_l + \eta_3^l \, k_r^l \, C_l + \eta_3^l \, k_p^l \, C_l \\ &\quad + R_t^l \, \mathrm{Prod}(M) - \frac{R_l}{R_l + \eta_3^l \, C_l} \, R_t^l \, \mathrm{Death}(M)\end{aligned} \tag{7.11}$$

$$\begin{aligned}\frac{dC_l}{dt} &= \eta_4^l \, k_f^l \, L \, R_l - k_r^l \, C_l - k_p^l \, C_l \\ &\quad - \frac{C_l}{R_l + \eta_3^l \, C_l} \, R_t^l \, \mathrm{Death}(M)\end{aligned} \tag{7.12}$$

$$\frac{dA}{dt} = -2 \, \eta_1^a \, k_{f1}^a \, A \, R_a + \eta_2^a \, k_{r1}^a \, C_a - \lambda_a \, A + s_a(t) \tag{7.13}$$

$$\begin{aligned}\frac{dR_a}{dt} &= -2 \, k_{f1}^a \, A \, R_a + \eta_3^a \, k_{r1}^a \, C_a - k_{f2}^a \, C_a \, R_a + 2 \, \eta_4^a \, k_{r2}^a \, D_a + 2 \, \eta_4^v \, k_p^a \, D_a \\ &\quad + R_t^a \, \mathrm{Prod}(M) - \frac{R_a}{R_a + \eta_3^a \, C_a + 2 \, \eta_4^a \, D_a} \, R_t^a \, \mathrm{Death}(M)\end{aligned} \tag{7.14}$$

$$\begin{aligned}\frac{dC_a}{dt} &= -2 \, \eta_5^a \, k_{f1}^a \, A \, R_a + k_{r1}^a \, C_a - \eta_5^a \, k_{f2}^a \, C_a \, R_a + 2 \, \eta_6^a \, k_{r2}^a \, D_a \\ &\quad - \frac{C_a}{R_a + \eta_3^a \, C_a + 2 \, \eta_4^a \, D_a} \, R_t^a \, \mathrm{Death}(M)\end{aligned} \tag{7.15}$$

$$\begin{aligned}\frac{dD_a}{dt} &= \eta_7^a \, k_{f2}^a \, C_a \, R_a - 2 \, k_{r2}^a \, D_a - k_p^a \, D_a \\ &\quad - \frac{D_a}{R_a + \eta_3^a \, C_a + 2 \, \eta_4^a \, D_a} \, R_t^a \, \mathrm{Death}(M)\end{aligned} \tag{7.16}$$

$$\frac{dB}{dt} = -k_f^b \, B \, X + \eta_1^b \, k_r^b \, C_{bx} + \beta_a \, \frac{d}{dt} \left(\frac{D_a}{M + \alpha_1 V}\right) \tag{7.17}$$

$$\frac{dX}{dt} = -\eta_2^b \, k_f^b \, B \, X + \eta_3^b \, k_r^b \, C_{bx} \tag{7.18}$$

$$\frac{dC_{bx}}{dt} = \eta_4^b \, k_f^b \, B \, X - k_r^b \, C_{bx} \tag{7.19}$$

Here,

$$\mathrm{Prod}(M) = \left(\mu_a \frac{D_a}{M} + \mu_l \frac{C_l}{M}\right) M \tag{7.20}$$

$$\mathrm{Death}(M) = \lambda_m(X) \, M \tag{7.21}$$

The function $s_a(t) = d_a\,(e^{-((t-2)^2)/.01} + e^{-((t-4)^2)/.01})$, corresponds to the dosage of VEGF given externally, around day 2, and day 4. The parameter d_a is fixed by ensuring that the area under s_a equals the total amount of chemokine administered. The initial condition for VEGF is also set at 50 pg per mm^3, to reflect the first dose. It is known that at constitutive intracellular Bad concentration, the death rate of HDMECs is 0.12 per day (74). Further, in the presence of 50 ng per ml VEGF, it is observed that Bcl-2 is up-regulated 3.1 fold (98). Consequently the level of Bad falls by a factor of 0.77 (Figure 7.4B) . We assume a very low death rate (0.005 per day, for example) corresponding to this low level of Bad. From these two observations, the constants a_d and b_d may be fixed. Next, a relation between the constants β_m, a_p and b_p may be found by observing that at constitutive Bcl-2 levels, the production rate of CXCL8 is 0.0358 pg of CXCL8 per HDMEC per day (as estimated in Chapter V). β_a is a constant that determines the level of Bcl-2 up-regulation by activated VEGF-receptor complexes on a cell surface. Its value may be fixed since we know that 50 ng/ml of VEGF up-regulates intracellular Bcl-2 amounts by a factor of 3.1 (98). A list of parameter values relating to VEGF - VEGFR2 binding dynamics available from existing literature are given in Table 4.1, and Section 4.3.2 in Chapter IV, while those relating to Bcl-2 - Bad binding dynamics are given in Table 7.1.

Table 7.1: List of parameter values relating to Bcl-2 and Bad interactions

Parameter	Value	Units	Source
k_f^b	4	per Bad concentration per day	[4]
k_r^b	8.832	per day	(154)
η_1^b	0.5856	fg Bcl-2 per fg C_{bx}	(122), (158)
η_2^b	0.4144	fg Bad per fg C_{bx}	(122), (158)
η_3^b	0.7077	fg Bad per fg Bcl-2	(122), (158)
η_4^b	1.7077	fg C_{bx} per fg Bcl-2	(122), (158)
β_a	40.0	fg Bcl-2 per pg of D_a	(98)

[4] In the absence of experimental data, it is assumed that forward rates of reaction for Bcl-2 binding to Bad are

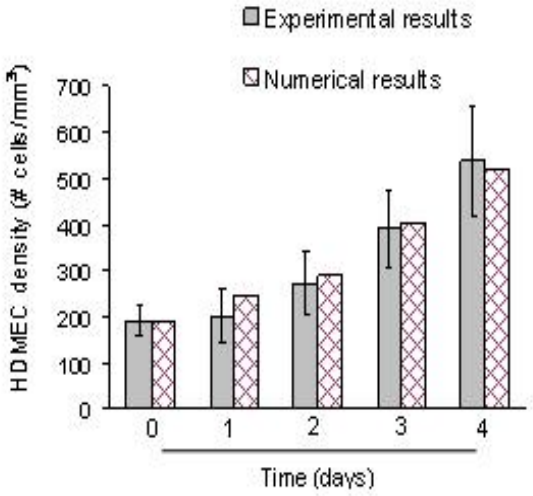

Figure 7.5: Fits to experimental data taken from (95), with cells cultured in the presence of 50 ng/ml VEGF

Thus, the unknown parameters/functions are μ_a (VEGF dependent HDMEC proliferation rate), a_p and b_p (governing the rate of CXCL8 production by HDMECs). These are determined by fits in the least squares sense to experimental data presented in (97). The resultant fit is shown in Figure 7.5. The parameter values thus obtained are listed in Table 7.2.

Table 7.2: List of parameter values relating to the effect of VEGF on HDMECs

Parameter	Value	Units
μ_a	12.8810	HDMECs per pg of D_a per day
a_d	3.878×10^{-6} [5]	per day
b_d	1.7329 [5]	per Bad concentration
β_m	8.1139×10^{-4} [6]	pg of CXCL8 per HDMEC per day
a_p	6.9620×10^{-4} [6]	pg of CXCL8 per HDMEC per day
b_p	1.6185 [6]	per Bcl-2 concentration

about the same order of magnitude as CXCL8 binding to its receptors, or VEGF binding to its receptors.

[5] Note that a_d and b_d which determine HDMEC death rate were fixed prior to running the curve fitting algorithm.

[6] Note that we had derived a relation between the parameters β_m, a_p and b_p, so that effectively only two of these was an unknown while running the curve fitting algorithm.

7.3.2 Anti-Bcl-2 Therapy in the Form of a Small Molecule Inhibitor BL193

To incorporate the effect of anti Bcl-2 therapy in the form of the small molecule inhibitor BL193, we include a further two equations in our model above representing intracellular concentrations of BL193, and Bcl-2 - BL193 complex The revised equations for Bcl-2, BL193 and Bcl-2 - BL193 complex are given below.

$$(7.22)\quad \frac{dB}{dt} = -k_f^b\, B\, X + \eta_1^b\, k_r^b\, C_{bx} - k_f^i\, B\, I + \eta_1^i\, k_r^i\, C_{bi} + \beta_a \frac{d}{dt}\left(\frac{D_a}{M + \alpha_1 V}\right)$$

$$(7.23)\quad \frac{dI}{dt} = -\eta_2^i\, k_f^i\, B\, I + \eta_3^i\, k_r^i\, C_{bi} + D_i\ (I_0 - I)$$

$$(7.24)\quad \frac{dC_{bi}}{dt} = \eta_4^i\, k_f^i\, B\, I - k_r^i\, C_{bi}$$

A source term is included in the equation for intracellular BL193 concentration. Briefly, we assume that BL193 is a small enough molecule (it has a molecular weight of 0.5 kDa (160)) to permeate through the cell wall, and that the rate of change of intracellular BL193 is proportional to the difference of extracellular and intracellular BL193 concentrations. The constant D_i is a measure of cell wall permeability to BL193. The extracellular concentration I_0 of BL193 in the local environment of a cell is a parameter that varies as the dosage level of therapy changes. In the absence of experimental data, we assume that it takes about 4-5 hours for the concentration of BL193 within a cell to equal half that in its immediate environment. The parameter values available from existing literature are given in Table 7.3. k_D^i is the inhibition constant for BL193 binding to Bcl-2, given by the ratio of k_r^i to k_f^i.

7.4 Results

A series of numerical experiments using the model described in the previous sections are carried out to simulate both, microvessel formation in vitro, as well as

Table 7.3: List of parameter values relating to Bcl-2 and BL193 interactions

Parameter	Value	Units	Source
k_D^i	64	fg BL193 per cell	(160)
η_1^i	0.9811	fg Bcl-2 per fg C_{bi}	(122), (160)
η_2^i	0.0189	fg BL193 per fg C_{bi}	(122), (160)
η_3^i	0.0192	fg Bcl-2 per fg Bcl-2	(122), (160)
η_4^i	1.0192	fg C_{bi} per fg Bcl-2	(122), (160)

tumor induced angiogenesis in vivo. To date, the effect of the small molecule inhibitor BL193 of Bcl-2, on sprout formation, has only been tested experimentally in vitro (59; 160). Therefore, we first validate our model by presenting a comparison of model simulations to these in vitro experiments. This is followed by in vivo simulations designed to predict the effects of the administration of BL193 on intra-tumoral angiogenesis. The dependence of drug efficacy on its 50% inhibition constant of Bcl-2, and on the permeability of the endothelial cell wall to the drug are studied in particular. These are both key factors in drug design strategy. Therefore the results of our simulations may be used to guide in vivo experimentation.

7.4.1 In Vitro Therapy Results Provide Model Validation

In a series of in vitro experiments described in (59), capillary sprouting assays were carried out on HDMECs. The endothelial cells were exposed to 50 ng per mL VEGF for 5 days and then to 50 ng/mL VEGF in the presence of 0 to 5 μmol per L BL193 thereafter, and the number of sprouts counted at daily intervals. To represent this experimental system, our model of intra-tumoral angiogenesis needs to be modified slightly by removing the tumor cell equation, and keeping free VEGF concentrations fixed at 50 ng/ml. The resulting system of equations is listed in Appendix B. The values of all parameters barring the amount of drug administered I_0, were estimated prior to simulation of treatment strategies, and these values were

kept constant thereafter. This allows us to validate our model by direct comparison of model predictions of treatment by BL193, with experimental observations.

Numerical and experimental observations are compared in Figures 7.6A, C and E, where the dosage of BL193 administered starting from day 5 increases from 0.05 μM, to 0.5 μM, and finally to 5 μM. The model predictions of microvessel densities are seen to match the experimental observations well, thus validating our model. It should be noted that at this final concentration of BL193, the cells simply die from too much chemical within them, rather than from a disruption in the Bcl-2 regulated anti-apoptotic pathway. The model does not account for such a possibility, and the last data point in Figure 7.6E therefore does not match in vitro observations. The effect of therapy on intracellular protein levels can be seen in Figures 7.6B, D, and E which plot the amounts of Bcl-2, Bad and BL193 per cell, corresponding to therapy levels of 0.05 μM, 0.5 μM, and 5 μM respectively, of BL193.

7.4.2 BL193 Therapy is Highly Effective in Treating Early Stage Tumors

Having validated our model by comparison to in vitro experimental results, we can now perform a series of numerical simulations to investigate the effect of BL193 therapy on in vivo tumor growth dynamics when applied at an early stage of tumor development.

First, a series of numerical simulations are performed to investigate the effect of therapy on tumor growth dynamics when applied at an early stage of tumor development. Prior to treatment, with parameters at their baseline values, the tumor cell density reaches it's maximum level (8.669×10^3 cells per mm^3) about 28 days after implantation (Figure 7.7A). The first blood-bearing vessels are seen 5 days after implantation, reaching their steady state of about 53 vessels per mm^3, 19 days later (Figure 7.7B). When a dose of 0.05 μM of BL193 is administered, it takes about a

week longer for the vasculature to fully develop, and the tumor cell density to reach its maximal value, when compared to the no therapy case. If the dosage is increased to 0.5 μM, the delay in vascular development increases by 16 days, while the tumor cells take 18 days longer to reach their steady state. A dosage level of 5 μM BL193 appears to be enough to cause the tumor to regress (Figure 7.7A,B). Thus, based on these numerical predictions, anti-angiogenic therapies directed at Bcl-2, such as the use of small molecule inhibitors of Bcl-2, appear to be highly efficacious, especially when administered to an early stage tumor.

Next, we investigate the effect of application of BL193 to a tumor that has been allowed to reach maximal tumor cell and microvessel densities (Figure 7.7C,D). Therapy is applied continuously from day 60 of implantation. The model predicts that at a dosage level of 5 μM BL193, the vessel density is seen to decrease (Figure 7.7D), leading to a corresponding decrease in tumor cell density (Figure 7.7C). However, the tumor cells appear to compensate for this loss of blood supply by increasing VEGF production. The vessel density soon returns to its pre-treatment level, and the tumor recovers rapidly. In fact, we need to increase the dosage of BL193 to approximately 24.5 mM to induce tumor regression. In this case, the microvessel density is observed to fall to a level that is too low for the tumor to recover from as a result of anti-Bcl-2 therapy (Figure 7.7D).

7.4.3 Sensitivity analysis on drug design parameters

There are two important considerations behind the design strategy of small molecule inhibitors of Bcl-2 such as BL193. Firstly, to maximize the inhibition of Bcl-2 by the molecule. Secondly, to maximize the cell-permeability of the molecule. We therefore carry out a sensitivity analysis on the inhibition constant K_{Di} of BL193, and the rate of diffusion D_i of BL193 across the cell wall. In all the simulations carried out

here, the drug is administered to a late stage tumor, and the least amount of drug required to induce tumor regression is observed. Numerical simulations predict that decreasing K_{Di}, decreases exponentially the amount of drug required to effect a cure (Figure 7.8A). For instance, the required dosage of an inhibitor with a K_{Di} 25% lower than that of BL193 is 0.52 mM, while that of an inhibitor with a K_{Di} 50% lower than that of BL193 is 11.04 μM. The required dosage for BL193 is 27.26 mM. Likewise, increasing cell-permeability of BL193, i.e. increasing the rate of diffusion of BL193 across the cell wall reduces the level of therapy required (Figure 7.8B). A 10-fold increase in D_i reduces the minimum drug dosage needed for a cure by a factor of 53%, but any increase in D_i beyond this does not significantly affect this dosage further.

7.5 Discussion

A deeper understanding of the cellular and molecular events that govern tumor-induced blood vessel growth is crucial to the development of anti-cancer therapies targeted at angiogenesis. Therefore, it has been the focus of intensive research. Several experimental models have been developed to study it. One such experimental model investigated the importance of the up-regulation of Bcl-2 by VEGF in sustained intra-tumoral angiogenesis (97; 98), and the effect of blocking this by means of a small molecule inhibitor BL193 of Bcl-2 (59). In Chapter V, we presented a mathematical model describing this experimental setup, at an extracellular and tissue level. Here, we incorporated the intra-cellular dynamics of the Bcl family of proteins in our existing model. This enabled us to quantify in a more definitive way, the role Bcl-2 plays in intra-tumoral angiogenesis, and to assess its potential as a target for anti-angiogenic therapy. By building a model specific to this experimental

system, we were able to validate it by direct comparison with experimental results. The model was then used to simulate the application of therapy in vivo, thereby highlighting its usefulness as a guiding tool in the development of anti-angiogenic drugs designed to inhibit the function of Bcl-2.

Numerical simulations of the full model provide valuable insight into the growth dynamics of tumors and their response to the application of BL193 therapy. The model was first calibrated versus control in vitro capillary sprouting assays. It was found to be in good agreement with experimental observations taken after the application of BL193. The model was then used to predict the effect of therapy applied at various stages of tumor growth in vivo. Numerical results indicated that even low levels of BL193 administered to an early stage tumor, induced significant delays in tumor and vascular development. In fact, 5μM Bl193 was sufficient to cause the tumor to regress. This could be due to the fact that if the vasculature has not had a chance to develop in a tumor, then administering anti Bcl-2 therapy has the effect of preventing further vascular development, by inducing cell death. However, in a simulation carried out to test this drug on a fully developed tumor, we found that the amount of therapy required to effect a cure increased by 3-4 orders of magnitude. It was observed that below a certain threshold, anti Bcl-2 therapy elicited little response from the tumor, but as therapy was increased beyond this threshold, the tumor and vascular development were arrested at much lower levels. However, it is possible that this threshold corresponds to an amount of therapy that is toxic for the host, and thus not administrable in practise.

These results accentuated the importance of timely detection and treatment of tumors, and indicated that a single point of attack at a fully developed tumor may be insufficient in order to effect a cure. Finally, numerical experiments were run to

provide an insight into drug design strategies aimed at improving the effectiveness of the small molecule inhibitor therapy, especially in late stage tumors. A small molecule that was only 25% more efficient than BL193 in inhibiting Bcl-2, reduced the required therapy level by as much as 97%. Therefore, even a moderately better inhibitor of Bcl-2 may prove to be a much better target for the development of anti-angiogenic therapy. However, increasing the cell-wall permeability of the drug molecules could reduce the minimum effective therapy level by at most 56%. These numerical simulations suggest that improving drug design in terms of permeability across cell walls has limited potential as far as minimizing drug efficacy level is concerned. Continued quantitative modelling in this direction could have a profound impact on the development of anti-angiogenic drugs aimed at the intra-cellular regulators of cell death.

The mathematical model presented here consists of delay differential equations, and by keeping track of temporal changes in the tumor and endothelial cell densities, VEGF and CXCL8 concentrations and microvessel density, we have been able to study the potential of a number of possible cancer therapies targeted at the VEGF - Bcl-2 - CXCL8 pathway. As the experimental data available is mostly density versus time plots, this approach is the natural first choice. However, the vascular structure within a tumor is highly unorganized and spatially heterogeneous, and it would be instructive to extend this model to include spatial variations in cell densities, chemical concentrations and vascular development. As a first step, we construct a hybrid model of endothelial cell and sprout tip migration in response to a gradient of VEGF in Chapter VIII. The principal dynamics that we wish to capture with the model are the binding and uptake of VEGF by the endothelial cells, the subsequent activation of cell surface receptors, and the chemotactic response of the

cells to this. This approach will later be generalized to incorporate the VEGF - Bcl-2 - CXCL8 pathway, in order to gain further insight into the potential of some of the anti-angiogenic therapies discussed above. This mathematical model together with the extensions mentioned above can provide a useful framework for enhancing the understanding of the interplay between mediators of tumor angiogenesis and for predicting the effectiveness of novel anti-angiogenic treatment strategies.

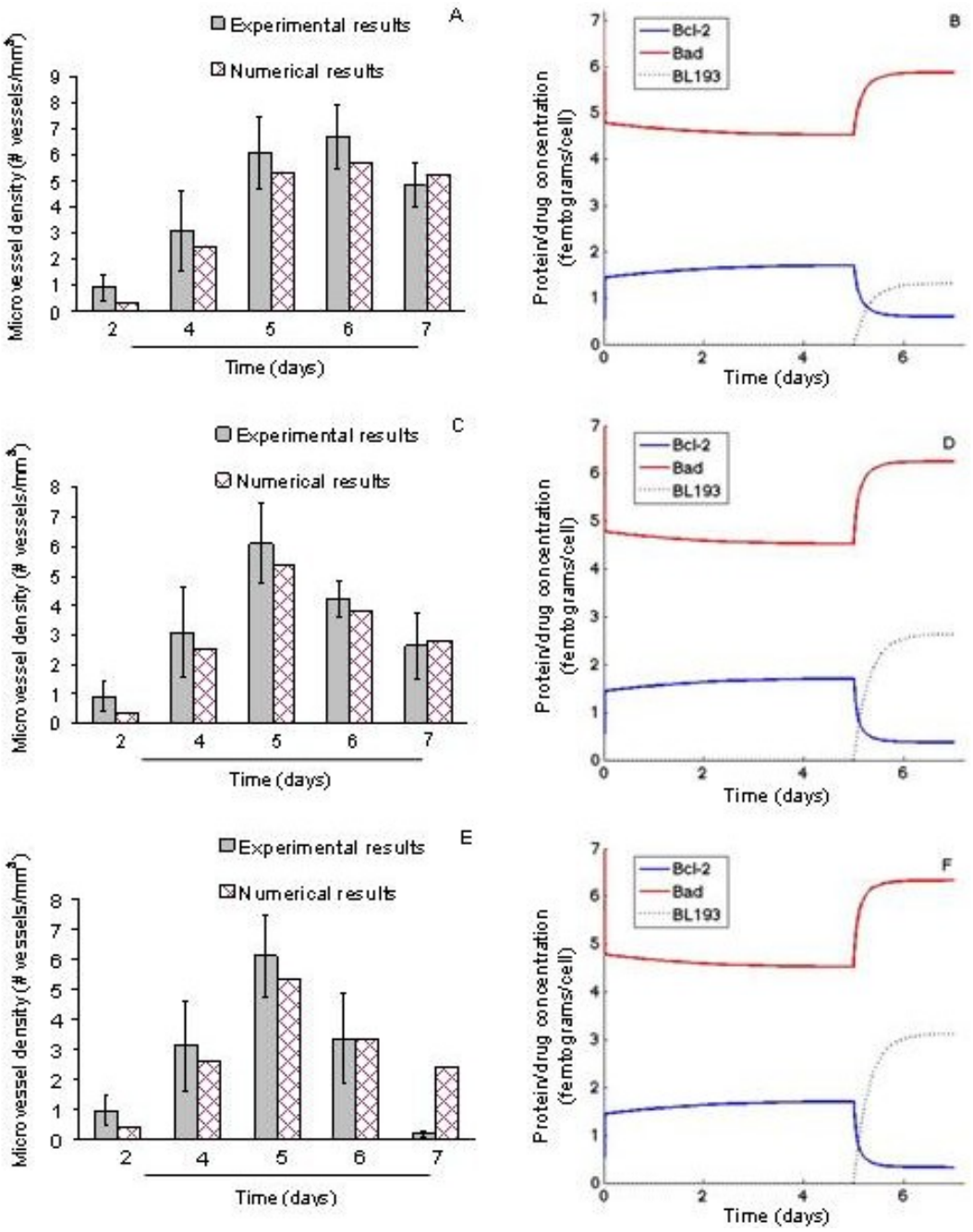

Figure 7.6: Comparison of model simulations to in vitro simulations designed to study the effect of BL193 on capillary formation. (A,C,E), In capillary sprouting assays described in (59), HDMECs were cultured on type I collagen in the presence of 50 ng per ml VEGF. Starting on day 5, BL193 was administered in increasing doses from 0.05 μM (A), 0.5 μM (C), and 5 μM (E), and the number of sprouts counted. Numerical simulations of our model are seen to be in good agreement with experimental data, thus providing a validation for it. (B,D,F), Intra-cellular Bcl-2, Bad and BL193 levels are tracked with time, as therapy is administered in increasing doses from 0.05 μM (B), 0.5 μM (D), and 5 μM (F). Starting on day 5, BL193 levels within a cell begin to increase, causing a decrease in amounts of unbound Bcl-2 protein, and a corresponding increase in unbound Bad protein.

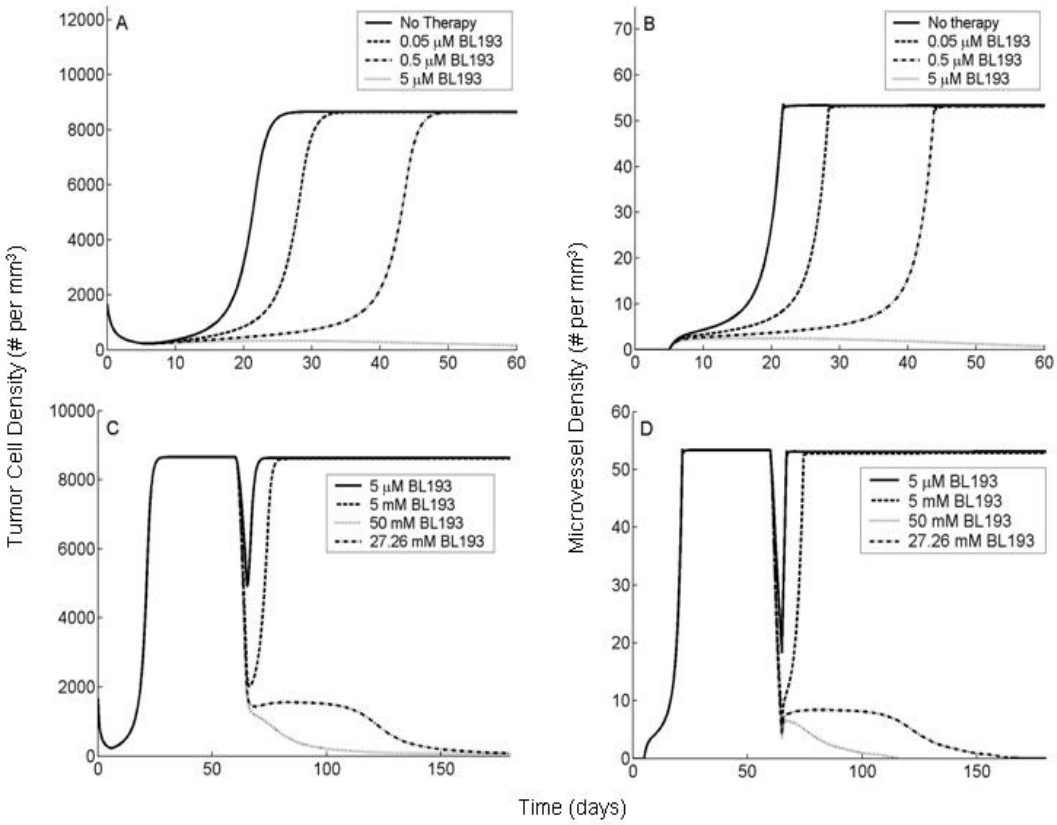

Figure 7.7: In vivo simulations of anti-Bcl-2 therapy applied to a tumor at early and late stages of development. Our model is based on experiments described in (95; 96; 97), wherein HDMECs along with oral squamous carcinoma cells are transplanted into SCID mice, on ploy-L lactic acid matrices. The HDMECs are observed to differentiate into functional microvessels, giving rise to a vascularized tumor. (A,B), BL193 is administered in starting from the day of implantation and continuing thereafter. As therapy levels increase from 0 to 0.05 μM, and to 0.5 μM, time taken to reach maximal tumor cell density increases by 25% and 89% respectively (A). The corresponding increase in time taken to reach maximal vessel density is 37% and 121% respectively (B). 5 μM of BL193 appears to be enough to effect a cure. (C,D), BL193 is administered to a fully developed tumor, starting from day 60 of implantation and continuing thereafter. 5 μM of BL193 is insufficient to effect a cure, and only a temporary reduction in tumor cell (C), and vessel densities (D) is observed. The minimum amount of therapy required in order to cause tumor regression is predicted to be 27.26 mM.

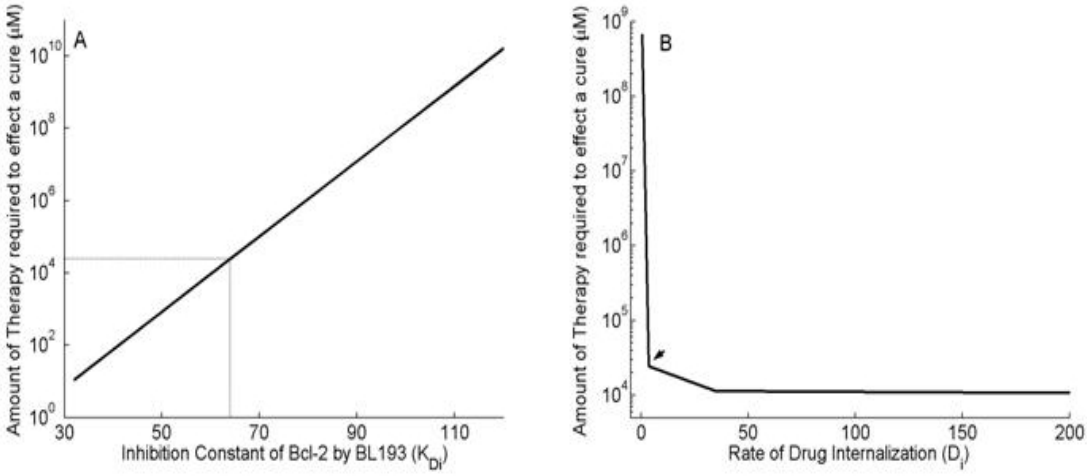

Figure 7.8: Simulations to guide drug design strategies for anti Bcl-2 therapy. (A) Minimum amount of therapy required to induce tumor regression is observed to vary exponentially with the inhibition constant K_{Di} of BL193 for Bcl-2. Reducing K_{Di} from its baseline value by 25% decreases the least amount of therapy required from 27.26 mM to 0.52 mM. (B) As the rate of diffusion D_i of BL193 into the cell is increased, the least amount of efficacious therapy reduces by a maximum amount of 56%, after which no significant change is observed, when compared to baseline values for D_i.

CHAPTER VIII

A Hybrid Model of Capillary Formation

In the preceding chapters, we have developed ordinary and delay differential equation models of tumor induced angiogenesis. In these, we incorporated the downstream molecular signaling pathways of VEGF and investigated the potential of targeting these pathways as possible anti-angiogenic therapies. As the experimental data available are mostly density (cellular or microvascular) versus time plots, this approach is the natural first choice. However, the vascular structure within a tumor is highly unorganized and spatially heterogeneous, and it would be instructive to extend this model to include spatial variations in cell densities, chemical concentrations and vascular development.

Here, we will develop a hybrid model of VEGF-induced angiogenesis, based on the theory of reinforced random walks. We will include in our model, the chemotactic response of endothelial cells to angiogenic factors bound to cell-surface receptors, rather than approximating this as a function of extracellular chemical concentrations. This will allow us to capture biologically observed phenomena such as activation and polarization of endothelial cells in response to VEGF gradients across their lengths. We will also propose a novel and more biologically reasonable functional form for the chemotactic sensitivity of cells, than those currently used. Model validation will be

provided by comparison of simulation results directly with experimental data.

As in (5), we consider a 2 dimensional domain, with a tumor source at $x = 1$, and a parent vessel at $x = 0$, as shown in Figure 8.1. The tumor secretes angiogenic factors under conditions of hypoxia, which diffuse outwards, towards the parent vessel. While an entire panel of factors are known to be secreted by tumors, the primary of these is VEGF, and for the purposes of modelling, this shall be the factor of choice. As mentioned earlier, VEGF will be taken up by cells lining the parent vessel, transforming them into sprout tip cells. These will migrate up the chemical gradient, pulling behind them capillaries. The principal dynamics that we wish to capture with the model are the binding and uptake of VEGF by the sprout tip cells, the subsequent activation of cell surface receptors, and the chemotactic response of the cells to this. To our knowledge, this level of molecular detail has not been implemented previously in a model of tumor induced angiogenesis.

8.1 Single Cell Motion under the Influence of VEGF

We begin our model development by first simulating a single endothelial cell moving under the influence of VEGF. The cell starts out at $x = 0$, $y = 0.5$, and will move in response to a gradient of VEGF, that has its source at $x = 1$, as in Figure 8.1. For the purpose of simplicity, we do not explicitly incorporate an extra cellular matrix. Following Plank et al, we base our spatial discretization on purely biological considerations, by interpreting the cell as a (biased) random walker. As per the approach developed in (116; 117; 118), the following master equation is used to describe a biased random walk (in two dimensions) of the endothelial cell, moving under the influence of VEGF in its local environment.

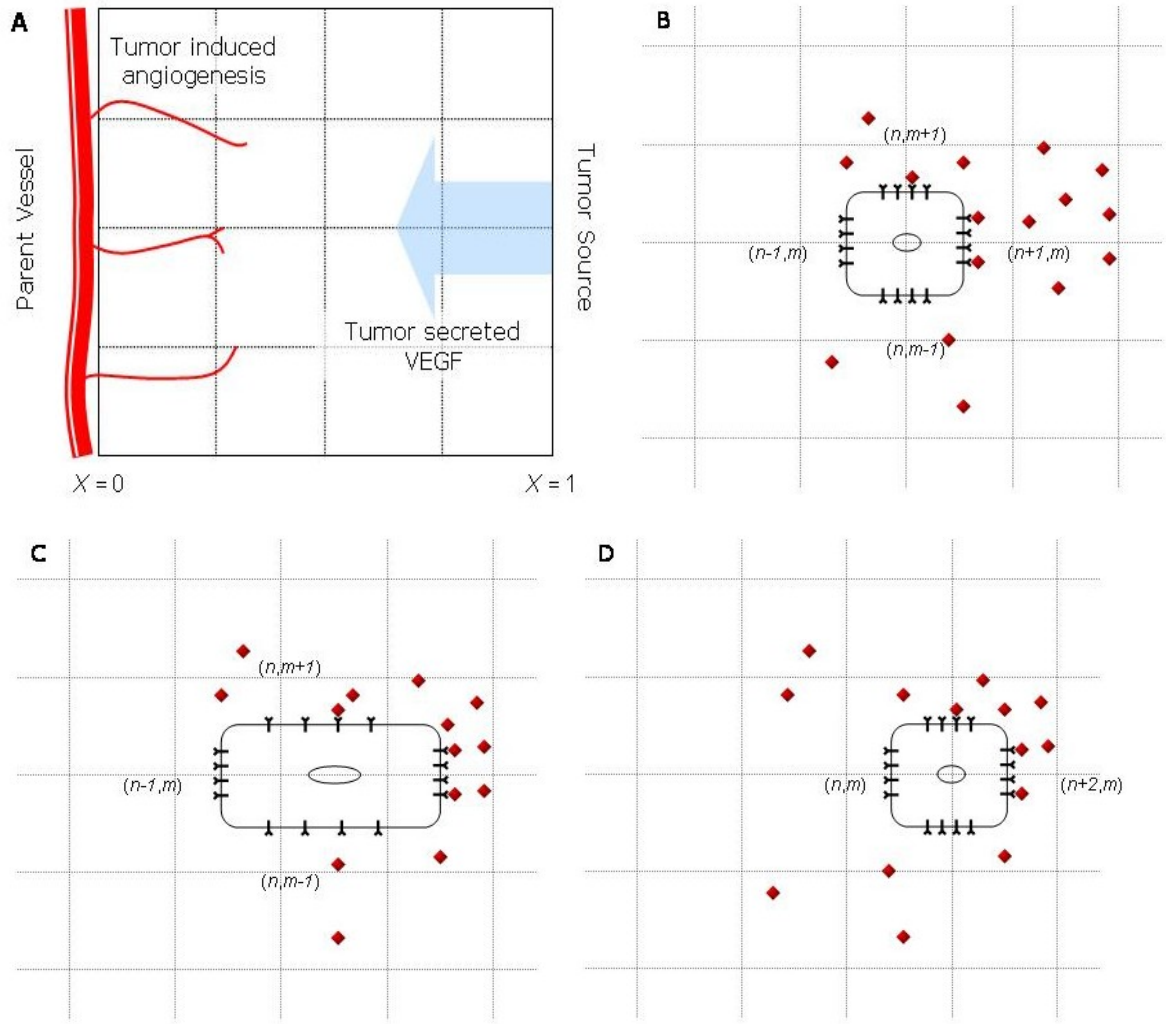

Figure 8.1: (A), Geometry of the model domain. A tumor is present at $x = 1$, which under conditions of hypoxia, secretes angiogenic factors such as VEGF. These diffuse towards a parent vessel located at $x = 0$, and are taken up endothelial cells lining it. The activated cells migrate up gradients of the angiogenic factors, laying down behind them capillaries. (B,C,D), Motion of a cell on a 2-d lattice in response to a chemical stimulus. The cell begins at position (n, m) in B. Chemoattractant molecules are shown in red. The length of the cell in motion is taken to be 40 μm (C), while at resting state to be 20 μm (B,D). The number of activated cell surface receptors is greatest on the cell surface at lattice site $(n+1/2, m)$, and the probability of motion in this direction is the greatest.

$$\frac{\partial p_n}{\partial t} = \hat{\mathcal{T}}^{H+}_{n-1,m}(W)\, p_{n-1,m} + \hat{\mathcal{T}}^{H-}_{n+1,m}(W)\, p_{n+1,m} + \hat{\mathcal{T}}^{V+}_{n,m-1}(W)\, p_{n,m-1} + \hat{\mathcal{T}}^{V-}_{n,m+1}(W)\, p_{n,m+1} - \left(\hat{\mathcal{T}}^{H+}_{n,m}(W) + \hat{\mathcal{T}}^{H-}_{n,m}(W) + \hat{\mathcal{T}}^{V+}_{n,m}(W) + \hat{\mathcal{T}}^{V-}_{n,m}(W)\right) p_{n,m} \tag{8.1}$$

Here, $p_n(t)$ describes the probability that a walker is at site (n, m), at time t. $\hat{\mathcal{T}}^{H\pm}_{n,m}(\cdot)$ and $\hat{\mathcal{T}}^{V\pm}_{n,m}(\cdot)$ are the transition probabilities per unit time for a one step horizontal jump to $(n \pm 1, m)$, or a one step vertical jump to $(n, m \pm 1)$ respectively. The mean waiting time at the (n, m)th site is given by $(\hat{\mathcal{T}}^{H+}_{n,m}(W) + \hat{\mathcal{T}}^{H-}_{n,m}(W) + \hat{\mathcal{T}}^{V+}_{n,m}(W) + \hat{\mathcal{T}}^{V-}_{n,m}(W))^{-1}$. The vector W gives the concentration of the chemoattractant c, at the lattice sites. In order that the master equation translates to the standard diffusion-chemotaxis equation for cell movement in the continuum limit, it is assumed that the dependence of transition rates at lattice site (n, m) is localized to chemoattractant concentration at sites $(n \pm 1/2, m)$ and $(n, m \pm 1/2)$. This is reasonable, since we may think of a cell present at lattice site (n, m), with its boundaries extending to half the lattice length. It can therefore sense the chemical concentrations at these half lattice sites, and make a decision where to move. This is illustrated in Figure 8.1B,C,D. Therefore, $W = (\dots, c_{-n-1/2}, c_{-n}, c_{-n+1/2}, c_{-n+1}, \dots)$. Further, it is assumed that the decision where to move is independent of the decision when to move. Mathematically, this is equivalent to setting

$$\hat{\mathcal{T}}^{H+}_{n,m}(W) + \hat{\mathcal{T}}^{H-}_{n,m}(W) + \hat{\mathcal{T}}^{V+}_{n,m}(W) + \hat{\mathcal{T}}^{V-}_{n,m}(W) \;=\; 4\lambda \tag{8.2}$$

for some constant λ. That is to say, the cell makes a decision to move (or to stay still) after a constant interval of time, say k, also called the mean waiting time at a grid point. In this case, $k = \dfrac{1}{4\lambda}$. One way to satisfy these assumptions is the following choice of transition probabilities, as made by Othmer et al (105):

$$\begin{aligned} \mathcal{T}^{H\pm}_{n,m} &= 4\lambda \frac{\tau(c_{n\pm 1/2,m})}{\tau(c_{n+1/2,m}) + \tau(c_{n-1/2,m}) + \tau(c_{n,m+1/2}) + \tau(c_{n,m-1/2})} \\ \mathcal{T}^{V\pm}_{n,m} &= 4\lambda \frac{\tau(c_{n,m\pm 1/2})}{\tau(c_{n+1/2,m}) + \tau(c_{n-1/2,m}) + \tau(c_{n,m+1/2}) + \tau(c_{n,m-1/2})} \end{aligned} \tag{8.3}$$

for some function $\tau(c)$ of the chemoattractant. This choice of this function is based on the particular form of the chemotactic sensitivity desired, and is explained in Appendix D.2. A grid of mesh size h is taken, and $x = nh$ is set. Passing to the continuum limit $h \to 0$ and $\lambda \to \infty$ such that $h^2\lambda = D_p$ where D_p is the diffusion coefficient of the endothelial cells, Othmer et al show that the master equation (8.1) translates to the familiar diffusion-chemotaxis equation, as given in (8.4), for the motion of a cell. Here, $\chi(c)$ is the chemotactic sensitivity, and it equals $D_p\,(\ln \tau(c))'$. To get a completely discretized model of the motion of the cell, the time derivative of p in equation (8.1) is approximated by a simple forward difference scheme, with k as the time step. For details, refer to Appendix D.1.

$$\frac{\partial p}{\partial t} = D_p\,\Delta\, p - \nabla \cdot (p\,\chi(c)\,\nabla c) \tag{8.4}$$

A diagrammatic representation of the motion of the cell is shown in Figure 8.1. The cell starts out at time t with its center at the lattice site (n, m) (Figure 8.1B). It detects *bio-available* VEGF by taking it up at the half-lattice sites(Figure 8.1B). The model can thus make the crucial distinction between VEGF that is free to bind to the cell, versus VEGF that might be sequestered in the underlying extracellular matrix, unavailable to the cell. This also ensures that molecular fluctuations in VEGF concentrations are significant enough to alter the polarization of the cell, and hence its direction of motion. This is consistent with experimental observations (84). Based on the numbers of activated receptors at its four sides, the cell becomes polarized and attains a bias in a particular direction. It correspondingly elongates in this direction (Figure 8.1C). Finally, the rear of the cell detaches from the underlying matrix and contracts, the cell has now moved to the site $(n + 1, m)$ (Figure 8.1D).

8.1.1 Chemotactic Sensitivity Function - A Biochemical Approach

An important difference that sets this model apart from those preceding it, is the choice of the chemotactic sensitivity function $\chi(c)$. Since ECs respond chemotactically to the presence of activated cell surface receptors rather than extracellular VEGF (47), we propose that $\chi(.)$ should in fact be a function of the activated receptor densities on a cell surface, a. In this case, equation (8.4) for the motion of a cell in 2 dimensions transforms to the following.

$$\frac{\partial p}{\partial t} = D_p \Delta p - \nabla \cdot (\chi(a)\, p \nabla a) \tag{8.5}$$

Correspondingly, the transition probabilities in (8.1) will now be functions of concentration of activated receptor complexes on the cell surface a, and not extracellular VEGF. We of course have to add equations for the binding of chemokine to their cell surface receptors, which will need to be solved wherever a cell is present. Biologically, the chemotactic sensitivity $\chi(a)\,\nabla a$ can be interpreted by breaking it down as follows - a velocity $\chi(a)$ imparted to the cell due to the presence of bound chemokine on its surface, and a gradient ∇a which governs the direction of motion. This gradient simply means that the cell is able to sense the amount of chemokine bound to its various faces, and is correspondingly able to align itself for motion in this direction. Therefore, a is in fact taken to be the amount of activated receptors *per cell face*. We choose a velocity function that satisfies the requirements that there can be no chemotaxis in the absence of a signal, and that the cell gets desensitized in the presence of excess signal. One such functional form is:

$$\chi(a) = \chi_0\, a\, e^{-a/B} \tag{8.6}$$

This is a significant improvement over existing chemotactic sensitivity functions in several ways.

- The simplest choice for χ is to take it as a constant (61; 62), $\chi(c) = \chi_0$. However, this predicts a constant chemotactic sensitivity in the presence of stimulus, and does not account for the desensitization which has been experimentally observed to occur in regions of high chemokine concentrations (69; 70; 151). Our model is able to capture both these features.

- Lapidus and Schiller (71), and later Murray (92) used the functional form $\chi(c) = \chi_0/(K + c)^2$, also known as the receptor-kinetic law. Yet another popular phenomenological choice is $\chi(c) = \chi_0/(K + c)$, where K is the dissociation constant of the chemokine binding to the receptors (5; 11; 117). These have the advantage that they are able to account for the desensitization of receptors when c is large. However, there are a few issues that these choices do not address. They indicate that when no chemokine is present at a site, the chemotactic sensitivity is the greatest, and this decreases as chemokine concentrations increase. This is in contrast to experimental evidence which points towards the existence of a minimum threshold level of chemical stimulus required for the cell surface receptors to get activated, and for the cell to start moving in a directed fashion (33; 77). Our choice for χ accounts for the fact that the cells need a minimum amount of stimulus in order to get activated. A similar threshold has also been incorporated in a Cellular Potts model of tumor-induced angiogenesis by Bauer et al (12).

- Further, the above functions do not account for the fact that the amount of chemokine required to desensitize cells depends on the concentration of cells

present at the lattice site. For instance, while 5 pM VEGF is enough to desensitize a single cell, it is not enough for 10 cells. This issue is taken care of in our model, since desensitization of cells occurs if there is excess VEGF bound to their surface.

- Finally, for an external chemical signal to elicit a chemotactic response from a cell, it needs to be detected by the cell, and transduced into an internal signal controlling cell motion. Neutrophils have been shown to sense chemical gradients of 1% across their lengths, under optimal conditions (76; 153), while this number can be as low as 0.1% for axons (153). In general, eukaryotic cells are reported to be able to polarize and migrate in a directed fashion in alignment with chemical gradients of about 2% across their lengths (43). It is therefore biologically more reasonable to assume that the chemotactic response is dependent on the gradients of activated receptor complexes formed on the cell surface when the chemokine binds to its receptors, rather than gradients of unbound extracellular chemokine concentration.

The maximum of the chemotactic sensitivity function given by equation (8.6) occurs at $a = B$, while its maximum value is given by $\chi_0 B e^{-1}$. In order for this choice to be consistent with the discrete formulation, the function $\tau(a)$, from equation (8.3) must be taken as follows. See Appendix D.2 for details.

$$\tau(a) \;=\; \exp\left[\frac{\chi_0\, B}{D_p}\left(B - (B+a)\, e^{-a/B}\right)\right] \tag{8.7}$$

The parameter B is an unknown in our model formulation, and must be fixed via experimentation. It determines the fractional occupancy of the receptors on the cell surface at which its chemotactic response is the greatest. The parameter χ_0

determines the maximum value of this response. In tumor induced angiogenesis, new capillaries can grow up to a rate of 1 mm per day (9). Once B is determined, this can be used to fix the value of χ_0. For baseline simulations, the value of B is fixed at 7.42 fg of activated VEGF-VEGFR2 receptor complexes. This allows us to fix the value of χ_0 at $4{\times}10^5$. It has units area (of a lattice site) per activated VEGF-VEGFR2 receptor complex density (in pg per cell face) per time (in hours). Figure 8.2A shows the fractional occupancy of receptors on a cell face, and chemotactic sensitivity as a function of activated receptors on a cell face, versus total VEGF at a lattice site, for a particular choice of the parameters B and χ_0. We can see that at zero fractional occupancy, the cell remains inactive. The sensitivity peaks at fairly low fractional occupancy, and decays thereafter. It should be noted that the units of free VEGF at a lattice site are in pg, so that if the concentration of VEGF changes by even 1 pM, cell behavior will be influenced. Figure 8.2B shows the distribution of VEGF at steady state across the domain. For illustration purposes, a line source of tumor cells is considered at $x = 1$, so that VEGF concentration is invariant along the y-axis.

8.1.2 Model Equations Describing VEGF Concentrations in Single Cell Motion

Equations (8.1), (8.3) and (8.7) that describe the biased random walk of a cell under the influence of VEGF have been explained in the preceding sections. No flux boundary conditions are imposed on the cell equation. Equation (8.8) describes the rate of change of free VEGF in the system.

$$\frac{\partial c}{\partial t} = D_c \Delta c - \alpha_c c \tag{8.8}$$

The units of concentration of free VEGF are taken as pg per lattice site volume (taken to have a height equal to a cell length and a base equal to the surface area

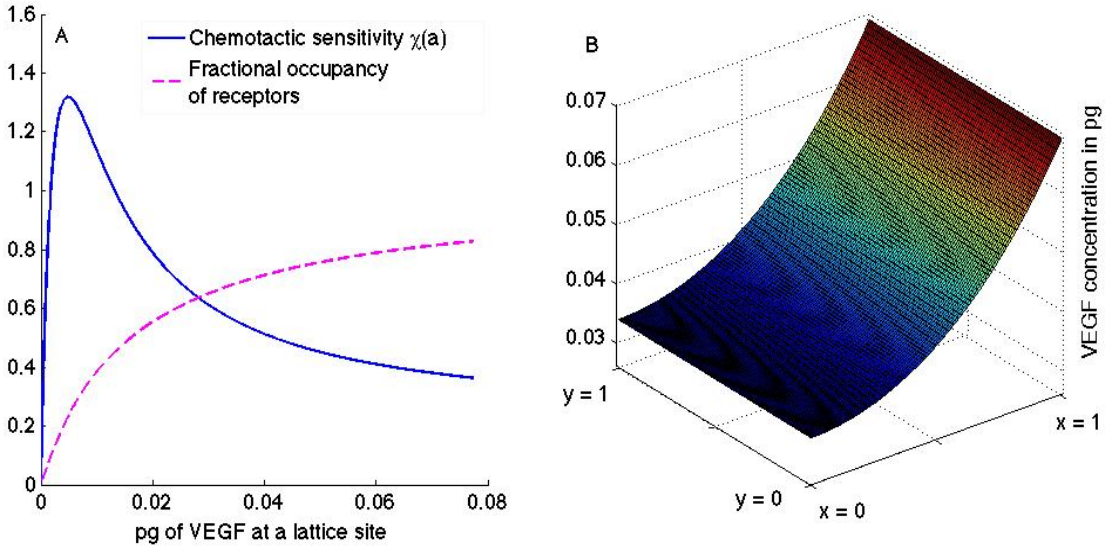

Figure 8.2: (A), Chemotactic sensitivity of an HDMEC to VEGF bound to its surface receptors, as a function of unbound VEGF, in pg per lattice site. Also plotted is the corresponding fractional occupancy of receptors on the cell face. (B), Typical steady state profile of unbound VEGF, the source of which is located at $x = 1$.

of a cell). Here, D_c is the diffusion coefficient of VEGF, and α_c is the rate of decay in tissue. Following (5), the case of a line of tumor cells is considered at the right boundary. Zero flux conditions are imposed on free VEGF at $x = 0$ and $y = 0, 1$. Since VEGF is also taken up by the cell, this introduces new moving boundaries in the system, namely, at the four faces of the cell. Equations (8.9)- (8.10) govern the binding of VEGF to its receptors on the cell surface, to create activated receptor ligand complexes. These are solved at each cell face.

$$\frac{\partial c}{\partial t} = -\eta_1 \, k_f \, c \, r + k_r \, a \tag{8.9}$$

$$\frac{\partial r}{\partial t} = -k_f \, c \, r + \eta_2 \, k_r \, a + \eta_2 \, k_p \, a \tag{8.10}$$

$$\frac{\partial a}{\partial t} = \eta_1 \, k_f \, c \, r - k_r \, a - k_p \, a \tag{8.11}$$

Here, r is the free VEGF receptor density, with units of concentration pg per cell

face, and a is the amount of activated receptor complexes, also in pg per cell face. For simplicity, we consider monomeric binding of VEGF to its receptors on the cell surface. The constants k_f and k_r are the forward and backward rates of reaction of VEGF with its receptor, VEGFR2. The rate of internalization of the activated receptor-ligand complex, and subsequent recycling of free receptors is given by k_p. These equations are scaled to units of pg per cell face by appropriate constants η_i, that represent ratios of the weights of the different molecules involved in the reaction. Conservation of total receptor numbers is ensured by setting the sum of the free and bound receptor densities to the average VEGFR2 density per endothelial cell.

The entire system is re-scaled to introduce non-dimensional variables. x and y are scaled by the distance of the tumor from the parent vessel, L. VEGF density c is scaled by a factor of c_0, the maximum amount of unbound VEGF in the system. This maximum is attained at the source, at $x = L$. r and a are scaled by factors of r_0 and a_0, the maximum possible free receptor density per cell face and activated receptor density per cell face respectively. Finally, the time variable t is scaled by a factor $T = L^2/D_c$, which corresponds to the diffusion time-scale of VEGF. The non-dimensional system reduces to the following.

$$\frac{\partial c^*}{\partial t^*} = \Delta\, c^* - \alpha\, c^* \tag{8.12}$$

The equations at the cell surface transform as follows.

$$\frac{\partial c^*}{\partial t^*} = -\beta_1\, c^*\, r^* + \beta_2\, a^* \tag{8.13}$$

$$\frac{\partial r^*}{\partial t^*} = -\beta_3\, c^*\, r^* + \beta_4\, a^* + \beta_5\, a^* \tag{8.14}$$

$$\frac{\partial a^*}{\partial t^*} = \beta_3\, c^*\, r^* - \beta_4\, a^* - \beta_5\, a^* \tag{8.15}$$

where the * superscripts denote non-dimensional quantities. The movement probability dependence function in non-dimensional terms becomes

$$\tau(a^*) \;=\; \exp\left[\nu\,(1-(1+\gamma\,a^*))\,e^{-\gamma\,a^*}\right] \tag{8.16}$$

The non-dimensional parameters are listed below. Henceforth * superscript shall be dropped as all computations are carried out in non-dimensional terms.

$$\nu \;=\; \frac{\chi_0\,B^2}{D_p} \qquad \alpha \;=\; \alpha_v\,T \qquad \beta_1 \;=\; \eta_1\,k_f\,T\,r_0\,p_0 \qquad \beta_2 \;=\; \frac{k_r\,a_0\,T\,p_0}{v_0}$$

$$\beta_3 \;=\; k_f\,v_0\,T \qquad \beta_4 \;=\; k_r\,T \qquad \beta_5 \;=\; k_p\,T \qquad \gamma \;=\; \frac{a_0}{B}$$

8.1.3 Parameter Estimation

Table 8.1: List of parameter values

Parameter	Value	Units	Source
D_p	3.6×10^{-4}	mm^2 per hour	(117)
D_v	3.6×10^{-1}	mm^2 per hour	(79)
α_v	0.6498	per hour	(132)
k_f	169	per VEGF concentration per hour	(78), (152)
k_r	2.0543	per hour	(78), (152)
k_p	0.6667	per hour	(152)
η_1	0.2250	pg VEGF per pg of receptor	(35), (139)
η_2	4.4444	pg receptor per pg of VEGF	(35), (139)
r_0	0.0191	pg receptors per cell face	(78), (139)
a_0	0.0234	pg activated receptor complexes per cell face	(78), (35), (139)
h	0.02	mm	(148), (75)
B	7.42	fg activated receptor complexes per cell face	[7]

A list of parameter values and sources is given in Table 8.1. The parameter values for VEGF binding dynamics are taken from studies on human colonic vascular endothelial cells. These have already been discussed in Section 4.3.2. The size of

[4] In the absence of experimental data,biologically realistic values for these parameters were chosen.

the lattice on which the cell moves is taken to be 20μm, since typical microvascular endothelial cell volume is about 400μm (148), while thickness is about 1μ (75). This gives a value for h. Finally, the domain size is taken to be 1 mm $\times$ 1 mm.

8.1.4 Numerical Implementation of the Biased Random Walk Model

The time interval over which the movement of the cell is simulated, is divided into subintervals of length k, given by the mean waiting time of the cell at any lattice site. The cell moves on a lattice of step size h. VEGF quantity is calculated at half lattice sites, where the edges of the cell are assumed to exist.

Since the source of VEGF is constant, and it has a very high diffusivity, compared to that of the cell, we assume that the concentration of free VEGF is not affected due to uptake by the cell. In fact, the mean waiting time k of the cell at a lattice site, is much greater than the diffusion time-scale of VEGF, and the constant source ensures that it quickly recovers to the steady state solution of equation (8.12), within each time step. This steady state profile is given by the following function. A typical profile is plotted in Figure 8.2B.

$$c_s(x,y) = \frac{e^{\sqrt{\alpha}\,x} + e^{-\sqrt{\alpha}\,x}}{e^{\sqrt{\alpha}} + e^{-\sqrt{\alpha}}} \tag{8.17}$$

This also implies that Michaelis-Menten like dynamics for the uptake of VEGF are valid (see Section 4.4.3). Thus, the amount of activated VEGF in cell surface receptor-ligand complexes is given by the steady state solution of equation (8.15), or $a = v/(K+v)$, where $K = k_m/v_0$. Here k_m is the Michaelis-Menten constant for VEGF given by $k_m = (k_r + k_p)/k_f$. It should be noted that we are keeping account of VEGF taken up by the cell at each half-lattice site, in other words, by each cell face. Consequently, we assume an equal density of receptors on all the four cell faces, so

that r_0, the maximum receptor density per cell face is one fourth of the total receptor density per cell.

The method of simulation of cell movement is based on that described in (117). Briefly, at each time step, the movement of the cell is simulated according to the master equation (8.1), with the probabilities of moving up, down, left and right calculated according to (8.3). These probabilities depend on the levels of VEGF taken up by the cell via the transition probability function (8.16). This uptake occurs at the half lattice sites, nearest to the site at which the cell is centered. The real interval $[0, 5\lambda]$ is divided into five subintervals, each of length proportional to the probabilities of moving or staying still. A random number q lying within this interval is generated, and depending on the sub-interval in which it lies, the cell either executes a motion in the corresponding direction or stays stationary. Thus, the cell moves left if $q \in [0, \mathcal{T}^{H-}_{n,m})$, moves right if $q \in [\mathcal{T}^{H-}_{n,m}, \mathcal{T}^{H-}_{n,m} + \mathcal{T}^{H+}_{n,m})$ and so on.

8.2 Results for the Motion of a Single Cell

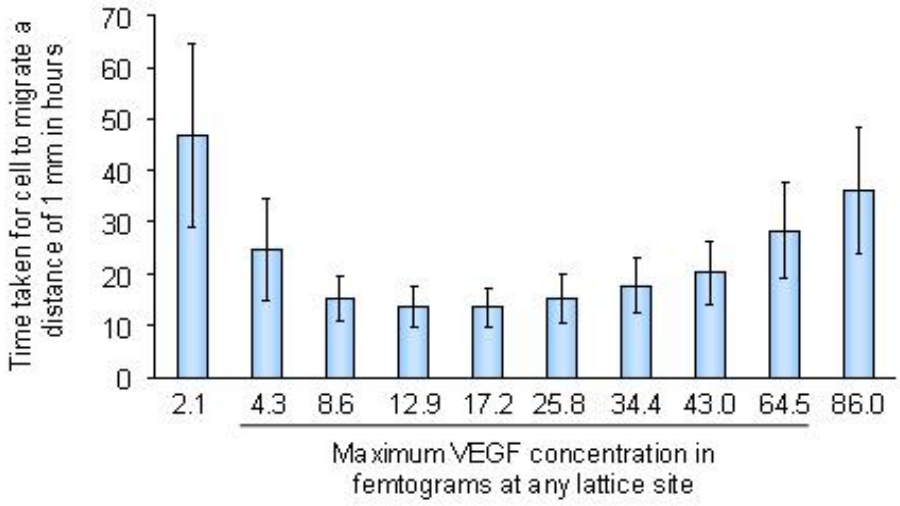

Figure 8.3: Average migration times (in hours) for a single cell to travel across a 1 mm × 1 mm domain, for various values of the maximum free VEGF concentration

Simulations of the system governing the motion of a single cell given by equations (8.1), (8.3), and (8.16) were run in two dimensions, with unbound VEGF profile given by (8.17). Figure 8.3 shows the average time in hours it took the cell to travel across the domain (a distance of 1 mm), for various values of c_0, the maximum VEGF concentration. Standard deviations and average times are computed over 500 runs of the model. Figures 8.4-8.6 show typical trajectories followed by the cell, and movement probabilities at any lattice site. Note that since the VEGF profile is invariant along the y-axis, the movement probabilities are also invariant along this axis - they only vary as x varies.

Figures 8.4A considers the case when the maximum concentration of VEGF c_0 is very low, taken to be 0.0021 pg here. Fractional occupancies of receptors on any cell face range from a low of 0.06% to a high of 0.12%. Also shown is the gradient of activated receptor complexes across the *length* of the cell. This ranges from 0.05% when the cell is at its starting position at $x = 0$, to 3.04% when the cell has reached the source of VEGF at $x = 1$. We can see that the cell exhibits a high degree of randomness in its motion, and takes on average almost 2 days to reach $x = 1$ (Figure 8.3. This is despite the high gradient of activated complexes across the cell length, the maximum of which is well above the reported value of 1-2% at which eukaryotic cells become polarized. Due to the low concentration of VEGF in the system, and hence low fractional occupancies of receptors, the probabilities of stepping up, down, left or right have fairly similar values. This can be seen in Figure 8.4B. It is only close to $x = 1$, that a definite bias is apparent for motion to the right. Thus, the model is able to account for the fact that if chemokine concentrations are too low, cell surface receptors do not achieve a sufficient degree of activation. In this case, the cell will not exhibit a high degree of directed motion,

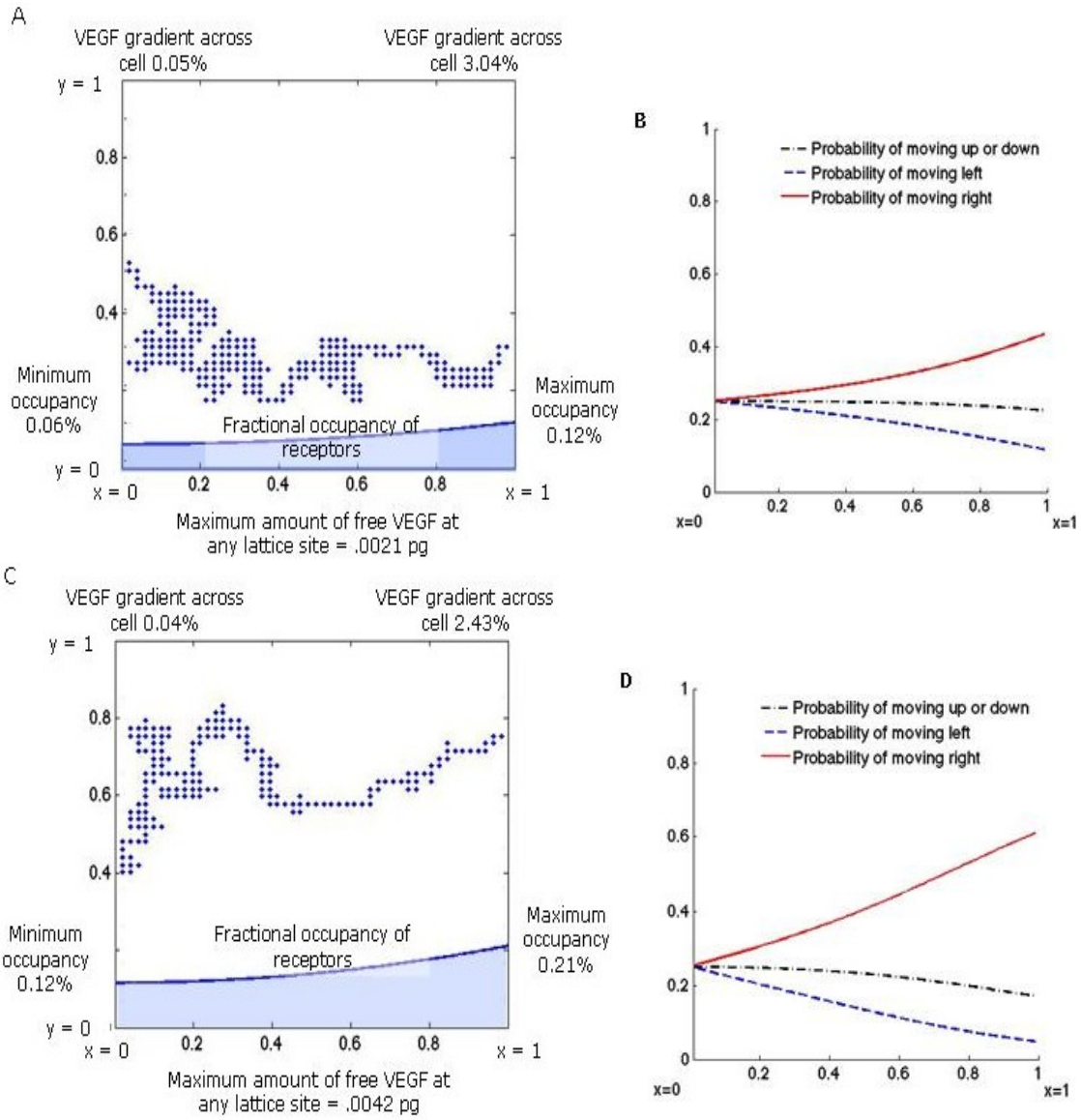

Figure 8.4: Typical trajectories of a cell migrating across a 2-dimensional domain under the influence of VEGF (A,C), and corresponding movement probabilities (B,D) for various values of the maximum VEGF concentration, c_0. Also indicated are maximum and minimum fractional occupancies on any cell face, and upper and lower bounds for the gradient of VEGF in activated receptor complexes across the length of the cell. (A,B) $c_0 = 0.0021$ pg per lattice site. (C,D) $c_0 = 0.0043$ per lattice site.

even if there is enough chemokine present to polarize the cell.

As c_0 is increased, migration times for the cell are observed to decrease, to a low of 13.7 hours, when $c_0 = 0.0172$ pg. (Figure 8.3). The corresponding trajectory is plotted in Figure 8.5C. Here, fractional occupancies of receptors range from 0.35%

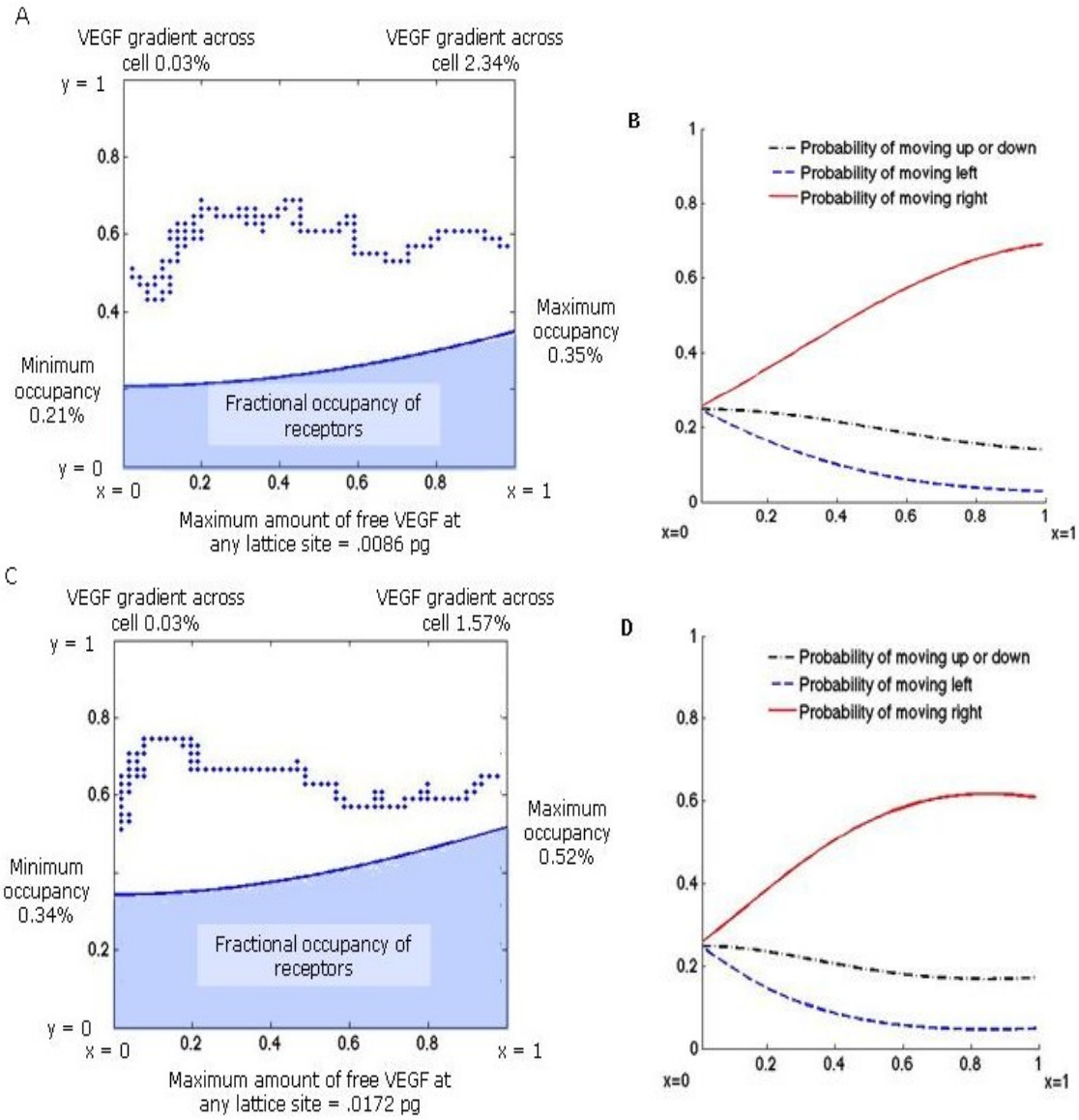

Figure 8.5: Typical trajectories of a cell migrating across a 2-dimensional domain under the influence of VEGF (A,C), and corresponding movement probabilities (B,D) for various values of the maximum VEGF concentration, c_0. Also indicated are maximum and minimum fractional occupancies on any cell face, and upper and lower bounds for the gradient of VEGF in activated receptor complexes across the length of the cell. (A,B) $c_0 = 0.0086$ pg per lattice site. (C,D) $c_0 = 0.0172$ per lattice site.

to 0.52%, while activated receptor gradients vary from 0.03% to 1.57% across the cell length. For our chosen values of the parameters B and χ_0, which determine the chemotactic sensitivity function $\chi(a)$, the above value of c_0 appears to be optimal for the cell to migrate across the domain. A plot of the movement probabilities

shows a large bias towards stepping to the right, while steps to the left are very unlikely to occur (Figure 8.5D). This is due to the following two reasons. Firstly, typical gradients of activated receptors on the cell fall within the reported range of 1-2% required for directed motion, allowing the cell to get polarized in the direction of increasing chemokine. Secondly, the receptors themselves have a high enough occupancy level, so that they are in a highly activated state.

As c_0 is increased further, the model replicates the desensitization effect which has been observed to occur when receptors are over-exposed to chemokines. As can be seen from Figure 8.3, when $c_0 = 0.086$ pg, it takes the cell an average of 1.5 days to migrate across the domain. Typical cell trajectories exhibit a fair degree of random motion, even though there is an overall bias for stepping to the right (Figure 8.6C). A combination of high fractional occupancies, which range from 0.68% to 0.81%, along with low activated receptor gradients across the cell, the maximum of which is only 0.56% contribute to keeping this bias of motion to the right at a low level. This is illustrated in a graph of the corresponding movement probabilities, in Figure 8.6D.

8.3 VEGF-induced Capillary Network Formation

We have developed a model for the motion of a single cell under the influence of VEGF. In this model, we were able to capture biologically observed phenomena such as the polarization of cells in response to activated VEGF-VEGFR2 complexes on their surfaces, requirement of a minimum stimulus in order for the cells to exhibit directed motion and desensitization as a result of excess VEGF signalling. We are now in a position to apply the techniques developed thus far to simulate capillary network formation under the influence of VEGF.

We base our model on the experiments of Sholley et al (134). Briefly, they in-

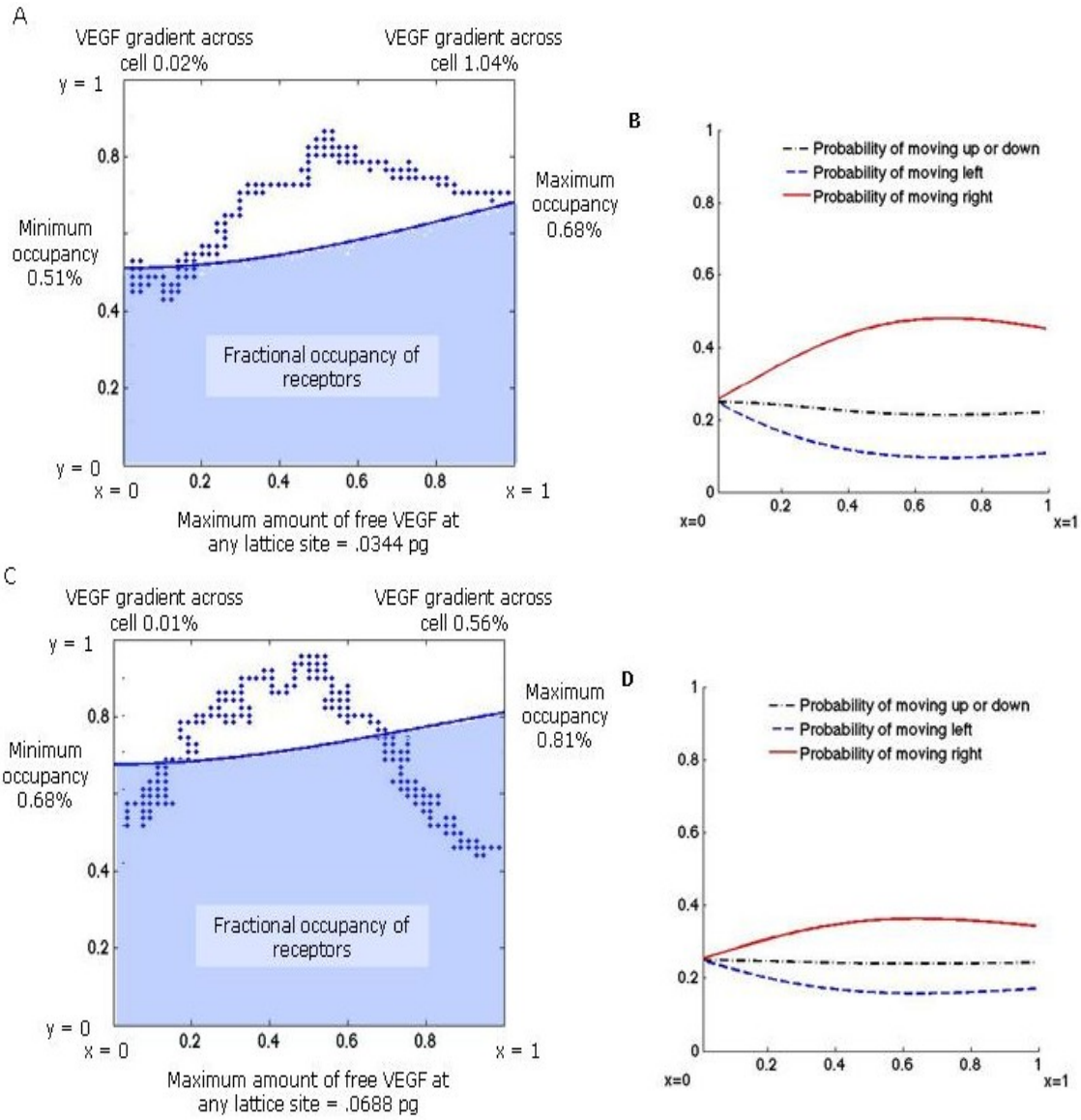

Figure 8.6: Typical trajectories of a cell migrating across a 2-dimensional domain under the influence of VEGF (A,C), and corresponding movement probabilities (B,D) for various values of the maximum VEGF concentration, c_0. Also indicated are maximum and minimum fractional occupancies on any cell face, and upper and lower bounds for the gradient of VEGF in activated receptor complexes across the length of the cell. (A,B) $c_0 = 0.0344$ pg per lattice site. (C,D) $c_0 = 0.0688$ per lattice site.

duced inflammatory neovascularization of the rat cornea by cauterization using silver nitrate. Levels of endothelial cell proliferation and degree of vascular profusion were measured periodically at days 1, 2, 4 and 7 post cauterization. The importance of EC mitosis in the formation of new sprouts was also investigated. The key findings

of this paper were:

1. The first sprouts were formed between day 1 and day 2. The initial vascular sprouting did not depend on cellular mitosis. Rather, these sprouts were likely formed by the migration and redistribution of existing endothelial cells, originating from the limbal vessels.

2. However, continued growth of the sprouts required cellular proliferation. If EC mitosis were prevented, the resulting sprouts stopped growing beyond 4 days, and were severely stunted. The resultant network extended an average of only 0.55 mm into the stroma.

3. If mitosis were allowed to occur, the sprouts continued to grow and by day 4, a dense network of vessels exhibiting branching and anastomoses was formed, extending a mean distance of 1.05 mm into the cornea. By day 7, this network had reorganized itself into fewer, and larger vessels which were radially oriented, extending a distance of 1.88 mm into the stroma. This reorganization was possibly the result of vessel maturation.

4. Proliferative activity of the ECs was observed to be concentrated near the advancing edge of the vessels, extending to 0.5 mm behind the sprout tips.

Several models of the process of vascularization similar to that described here, have been developed. These, together with their limitations, have already been discussed in Chapter III. In the model of angiogenesis developed here, we will aim to improve on these models by incorporating a higher level of detail of the biochemical forces guiding angiogenesis.

For the purposes of our model, we will focus on the vessel growth occurring between days 1 and 4 of the Sholley experiments. The first sprouts are seen after day

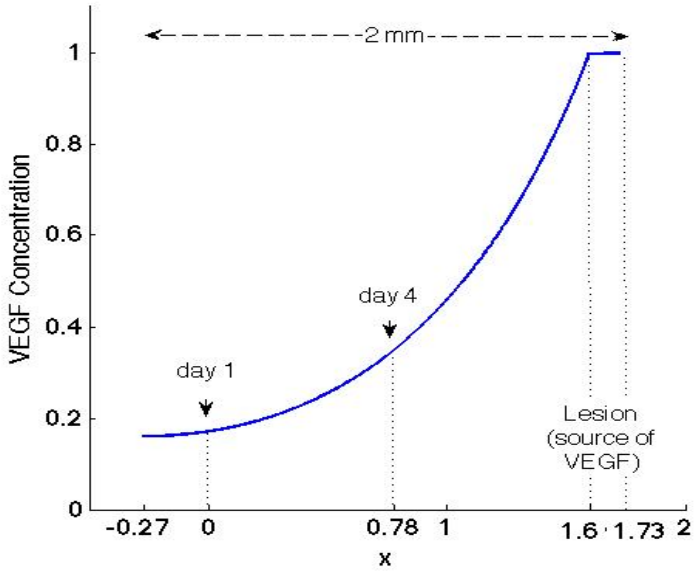

Figure 8.7: The geometry of the domain over which vascular growth in response to tumor-secreted VEGF is being modelled. Capillary growth is modelled from day 1 to day 4. At day 1, the initial sprouts have already formed along the parent vessel. Vessel growth resulting from EC mitosis is assumed to begin at $x = 0$, with the source of growth factors located at a distance 2 mm from the parent vessel between $x = 1.6$ and 1.73

1 in the experiments, and we take this as the starting point of our model. Indeed, a model for capillary network formation in the rat cornea, in the absence of EC proliferation has already been proposed by Anderson and Chaplain in 1998 (4). Since we do not account for vessel maturation, the model simulations are not carried out beyond day 4, after which time this process is observed to occur. The geometry of the domain is shown in Figure 8.7. Initial sprouts, together with the parent vessels, are assumed to extend to a short distance into the cornea. For our simulations this is taken to be approximately 0.27 mm, in keeping with experimentally observed average vessel extension speeds. Vessel growth resulting from EC mitosis begins at $x = 0$. The source of growth factor (assumed to be VEGF) is the center of the lesion which lies at $x = 1.73$. Thus the distance of the lesion from the limbal vessels is about 2 mm, as reported in the experiments. In order that the vessels reach the lesion by day

7, it is taken to have a radius of 0.12 mm, which means that the vessels extend to a mean length of 1.88 mm. Note that, since the initial vascular network is assumed to extend a distance of 0.27 mm by day 1, the sprouts must travel 0.78 mm in 3 days so that a total distance of 1.05 mm is covered in 4 days.

8.3.1 Adaptation of Single Cell Motion to Capillary Formation Model

While the general setup remains the same as described in equations (8.1), (8.16), (8.3), and (8.17), a few changes are implemented to account for the creation of microvessels, under a slightly altered VEGF profile. VEGF is now being secreted at $x = 1.73$, and no flux boundary conditions are imposed at $y = 0$, $y = 1$, and $x = -0.27$. The equation (8.12) for free VEGF is solved for its steady state under these new boundary conditions, and this profile of VEGF is kept constant throughout (see Section 8.1.4).

It is known that specialized ECs situated at the tips of the sprouts, called tip cells, are activated by, and respond to VEGF, by chemotactic migration (47; 50). We therefore keep track of these leading cells in our simulations. We have already presented a model for the motion of a single cell, responding to a gradient of VEGF formed on its surface as a result of receptor activation. This is modified to capture the motion of tip cells, with the only difference being that since a tip cell pulls behind it a vessel, receptors on its tail are made unavailable for binding VEGF at any given time. This eliminates the possibility for the tip cell to back-track. Initially, 5 sprouts are assumed to have formed along $x = 0$.

Empirical evidence points to the existence of a region of proliferating stalk cells just behind the tip cell (47; 110; 134). Sholley et al have also demonstrated that sprout extension cannot occur in the absence of cell division. To account for this, we assume that a tip cell has the freedom to occupy a new lattice site only when a stalk cell has had time to undergo mitosis. Vessel elongation speeds must be approximately

0.27 mm a day in order that a distance of 1.05 mm is traversed in 4 days, as per the observed time-course of vessel formation in (134). Given that typical EC lengths are 0.02 mm, this implies that at least 14 cell divisions must occur per day, which allows us to fix an upper bound for the time-step k, to be 1.7 hours. Recall that k is the mean waiting time at a lattice site. In reality, the mean waiting time is expected to be lower since not every motion of the tip cell is in necessarily in the forward direction. This is a parameter that will be fitted to ensure that simulation and experimental vessel elongation speeds are in agreement. Further, no more than 25 cell divisions may occur at any point of time, since the proliferating zone extends to no more than 0.5 mm behind the tip cell.

Finally, while the migratory response of the tip cell is a result of gradient sensing, . Since the process of branch formation is a result of proliferation of the cells lining the developing microvessel,

The process of branch formation is included explicitly in the model. It is assumed that the generation of new sprouts occurs only from existing sprout tips. This is in keeping with the fact that there is a region of proliferating cells just behind the tip cell, which could give rise to new branches. The proliferation of cells is regulated by total VEGF concentrations on their cell-surface receptors (47). Thus, in our model, the tip cell *integrates* the total VEGF bound to it, and the higher the bound VEGF quantity, the greater the branching probability. Conversely, if the amount of VEGF bound to the cell is very low, branching cannot occur. As the bound VEGF increases, the frequency of branching increases, creating the brush-border effect (5; 112). Similar rules for branching have been applied previously by Anderson et al (5). It is also assumed that branching into a space occupied by another sprout is not possible.

The process of anastomoses or formation of loops by capillary sprouts is also incorporated in the model. At each time step, as the tip cells migrate under the influence of VEGF, probabilities of motion to adjacent lattice sites are calculated. In order to prevent back-tracking, the probability of moving to the lattice site occupied currently is set to zero. Anastomoses may occur if another sprout is present at a neighboring site. Following Anderson et al (5), it is assumed that if another tip cell is encountered at a site, only one of these cells continues to grow, while the rest of the time, a loop is created with the loss of both cells.

8.3.2 Degree and Morphology of Tumor Vascularization is Crucially Mediated by the Bio-availability of VEGF

Simulations of the system governing capillary network formation under the influence of VEGF, described above were run in two-dimensions. The first case considered is when the sprout tips move across the domain in the least amount of time. This occurs at a maximal concentration of VEGF of 0.0047 pg per lattice site. Taking an average over 500 simulations, it is observed that the sprout tips require 49 steps to migrate across the domain, in order to travel 0.78 mm into the stroma after 3 days. Note that the chemotaxis parameters chi_0 and B are fixed in order to minimize this number of steps. Thus, the time-step k must equal 1.47 hours. This is less than the upper bound of 1.7 hours as estimated from (134), due to the fact that even though the bias for movement is overwhelmingly in the forward direction, a few steps are invariably taken in the lateral directions. The results from a typical simulation are shown in Figure 8.8A. We begin with 5 initially formed sprout tips at $x = 0$. As these tip cells migrate across the domain, they lay down behind them capillary sprouts. As the vascular network penetrates deeper into the stroma, branching is observed to occur. Anastomoses is also seen as the sprouts branch further. These

results are qualitatively similar to the networks observed at day 4 in Sholley et al. In Figure 8.8B, we can see the probability of movement for the tip cell across the length of the domain. There is a bias towards forward motion, as the fractional occupancies of receptors on the tip cell increase from a minimum of 20% at $x = 0$, to a maximum of 40% at $x = 1$.

Recent studies have focused on the role of various VEGF isoforms in vascular morphogenesis (47; 72) and have found that VEGF in soluble versus matrix-bound form has a different effect on vascular appearance. Lee et al (72) demonstrated that endothelial cell receptor activation by soluble VEGF induced significant cell proliferation and broad invasion of the stroma.

Recent studies have focused on the role of various VEGF isoforms in vascular morphogenesis (47; 72) and have found that VEGF in soluble versus matrix-bound form has a different effect on vascular appearance. In order to simulate the presence of a more soluble isoform of VEGF, the quantity of bio-available VEGF is increased by increasing c_0. Figure 8.8C shows the vascular network formed in response to these increased levels of bio-available VEGF. As the sprout grows, a greater number of cells are activated and stimulated to proliferate. Thus, extensive branching and anastomoses is observed. In fact, a number of 'loops' in the vasculature can be seen which have been formed by are only a single cell thick. It is reasonable to expect that the cells lining these regions would fuse into one another to give rise to a thicker and more dilated vessel, which is a morphology consistent with vascular hyperplasia, as seen in (72). Furthermore, since the fractional occupancies of tip cell receptors is very high, the tip cell does not have a very strong directional preference (Figure 8.8D). Thus lateral movement of vessels as well as movement against the gradient of VEGF are observed to occur. These are observed phenomenon in vivo,

and have been numerically simulated previously (142).

Finally, the effect of a low maximum VEGF concentration on vascular formation is investigated. c_0 is fixed at a very low value of 5.4×10^{-5} pg per lattice site. Fractional occupancies of receptors on the tip cell now vary from a minimum of 3% to a maximum of 7%. The cell is no longer polarized sufficiently to display directed motion. The total VEGF bound to the cell is also too low to induce proliferation, and hence branch formation. Instead, the vessels tends to loop back on themselves, or loop back towards the limbal vessel, without moving a significant distance into the stroma (Figure 8.8E). Corresponding movement probabilities are shown in Figure 8.8F.

8.4 Discussion

We have developed and presented here an agent based model of cellular chemotaxis, under the influence of VEGF. The first step was the formulation of a chemotaxis sensitivity function that incorporated biological detail hitherto ignored by sensitivity functions currently in use. A stochastic approach to simulate the movement of the cell was followed, based on the theory of biased random walks, popularized by Davis. Using this, the motion of a single cell was simulated on a two-dimensional grid, following the gradient of VEGF laid down by a constant source. An important difference that sets this model apart from those preceding it is the inclusion of a molecular level of detail, used to guide the motion of the cell. VEGF was allowed to bind to cell surface receptors, resulting in polarization of the cell, and a bias toward motion in a particular direction. This is observed experimentally as well - endothelial cells respond to gradients of chemokines *across* their lengths, rather than to free chemokine concentrations. In vitro, these gradients are calculated to be as low as

1%, which was seen in the numerical simulations as well, thus validating our model. Using this setup, we were able to demonstrate its capacity to capture realistic dynamics, such the requirement of a minimum activation level of cell surface receptors, and receptor desensitization in high concentrations of VEGF.

Next, this model was adapted to simulate the neovascularization of the rat cornea, as in the experiments of Sholley et al. Events such as branching and anastomoses, which are observed to occur in vivo, were incorporated explicitly in the model. The time-step was fixed to ensure that vessels elongation speeds matched those observed experimentally. Thus a value of 1.47 hours was fixed for k. It is known that the time taken by a lymph EC to undergo mitosis can be as low as 12 hours (6), while that for pulmonary ECs is about 13 hours (1). This does not, of course, include inter-mitotic times. Given that vessel penetration into the cornea may take place only if ECs lining it undergo mitosis, and assuming an cell cycle time of 13 hours, this implies that at any time 8-9 cells are undergoing division. Further, since we take the length of a resting EC to be 0.02 mm, this allows us to calculate that cell division is occurring in a total length of 0.16-0.18 mm, behind the tip cell. Sholley et al reported that the proliferative region is located up to a distance of 0.5 mm behind a tip cell. Thus, numerical simulation indicate that 32-36% of the cells in the proliferative regions are undergoing mitosis at any point of time, which is in good agreement with the value of 30% as observed empirically (134). This provides excellent validation for our model. Using this framework, we were also able to test the effects of excessive VEGF signalling, which may result if the VEGF isoform is freely soluble, as well as very low levels of VEGF signalling, on vascular development.

Angiogenesis is a highly complex process, and the mechanisms driving it are still unclear to a large extent. Mathematical modelling can go a long way in shedding

light on some of the these mechanisms. To this end, it is vital that modelling effort keeps up with current advances in experimentation. Our model provides such a framework, in which it is easy to build in biochemical and biomechanical forces guiding vessel formation. We have already incorporated VEGF binding to the tip cell. Currently, it is assumed that the tip cell gives rise to new sprouts. In this way, it follows that proliferation occurs just behind the tip. However, it is straightforward to keep track of the ECs lining the vessels as well, so that VEGF uptake by these may be monitored. Since the cell integrates the total amount of VEGF bound to it, in order to decide whether or not to divide (47), proliferation may be kept track of in an explicit manner, and more direct comparisons with experiments that report proliferative regions along the stalk of the capillary may be made. We also plan to include vessel maturation, so that even if there is ample signal for a stalk cell to proliferate, if it is of a certain age, it may not do so. Maturation of the ECs lining a vessel is modulated by the angiopoietins. Ang-1 has been shown to stabilize the blood vessel by maintaining periendothelial cell coverage whereas Ang2 permits the removal of pericytes from the vessel. This induces angiogenesis in the presence of VEGF, and causes regression in the absence of VEGF (10). The angiopoietins exert their influence through the Tie-2 receptors, which are tyrosine kinases like the VEGF receptors. Thus including this system in our model would not be a difficult task.

A vital component that governs vessel formation is the extra cellular matrix or ECM. ECs require the ECM to gain traction in order to move. Activated ECs up-regulate cell surface receptors known as integrins, that help the cell adhere to fibers in the ECM (16; 130). To facilitate their migration, ECs also secrete proteolytic enzymes such as the matrix metalloproteinases (MMPs), that degrade collagen and elastin and clear a path for the ECs to follow. In addition, the plasminogen activator

system plays an important part in the degradation of fibronectin (87). As ECs interact with the matrix, they also cause the release of matrix bound angiogenic factors such as VEGF, which are then available to induce further pro-angiogenic activity (84). The framework presented here is highly flexible, and would allow for the inclusion of the above processes, grounding it further in biology, and enhancing its usefulness as a tool to understanding the process of angiogenesis.

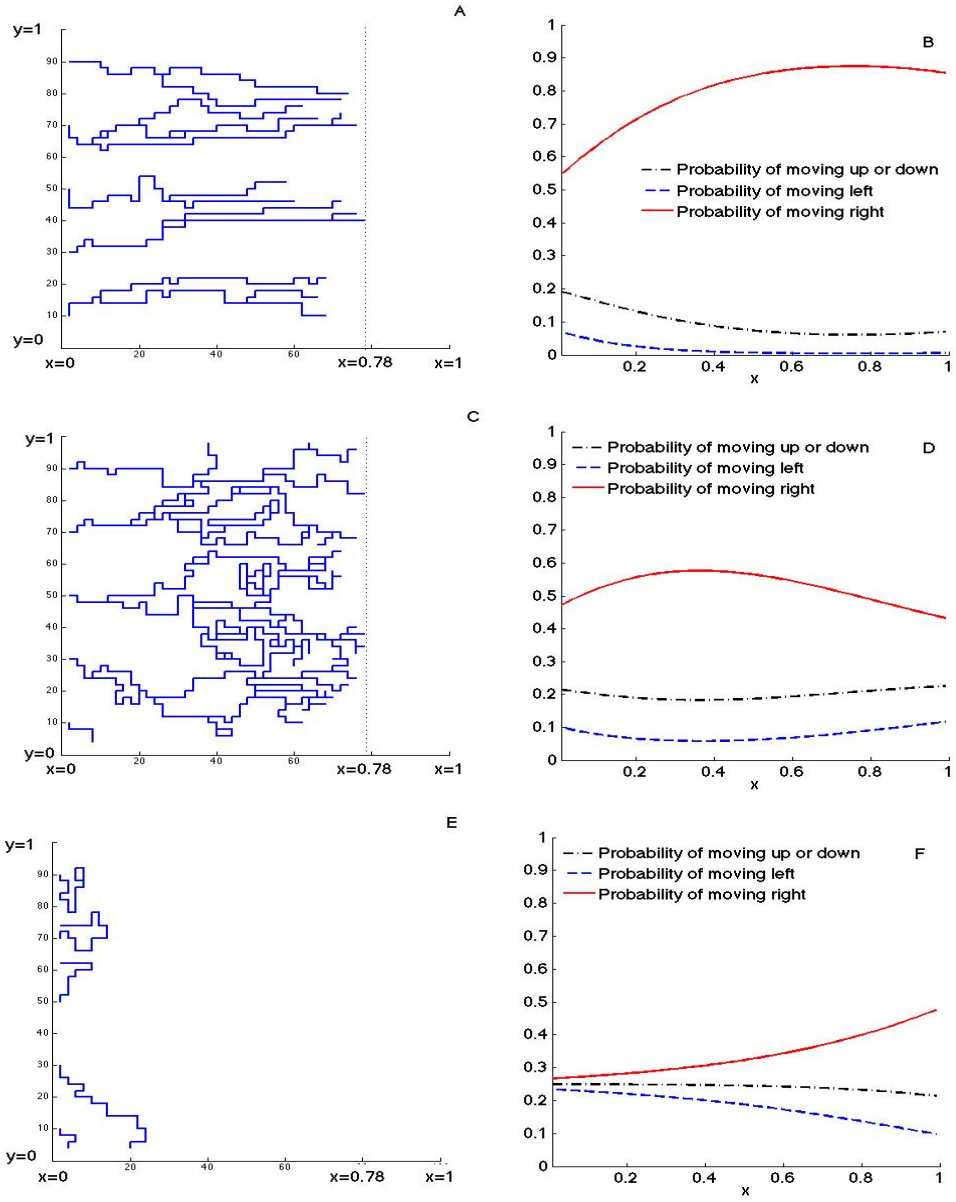

Figure 8.8: Typical vascular networks formed by 5 initial sprouts at $x = 0$, migrating across a 2-dimensional domain under the influence of VEGF (A,C,E), and corresponding movement probabilities (B,D,F) for various values of the maximum VEGF concentration c_0 secreted by the tumor source. (A,B) $c_0 = 0.0047$ pg per lattice site. The bias of movement is overwhelmingly in the forward direction (B). (A) Branching and anastomoses is observed to occur as the vasculature penetrates deeper into the stroma. The resulting networks are qualitatively similar to those observed experimentally in (131). (C,D) $c_0 = 0.0188$ pg per lattice site. (C) Due to high VEGF concentrations, over-stimulation of ECs occurs, and extensive branching, and anastomoses is observed. The resulting vasculature is morphologically consistent with vascular hyperplasia, observed to occur in the presence of high VEGF concentrations. (D) De to high fractional occupancies, the tip cell tends to lose its directional bias. (E,F) $c_0 = 0.000054$ pg per lattice site. (E) The amount of VEGF is too low to induce proliferation or polarization of the tip cell, leading to a poorly developed vasculature that does not reach the tumor source. (F) Due to low fractional occupancies of receptors, the tip cell does not display sufficient bias towards forward motion.

CHAPTER IX

Summary and Future Directions

9.1 Impact of Dissertation Research

Morphologically, tumor vessels and healthy blood vessels are very different. Tumor blood vessels are highly irregular and disorganized structures. They tend to be leaky, tortuous, containing an abnormal basement membrane. As a result, the blood flow in tumors is chaotic. The tumor vessels generally contain poorly oxygenated blood, so that the tumor tissue is relatively hypoxic. This has lead to the theory that normalization of tumor vessels and blood supply achieved by angiogenesis inhibitors could improve drug delivery to the tumor as well as prevent cancer metastasis by limiting the access of cancer cells to the vasculature. Today, therapeutic strategies targeted against angiogenesis are clinically recognized has having enormous potential in the treatment of cancer. Several potent angiogenesis inhibitors have been identified and are currently in various stages of development and clinical trials. However, their underlying mechanisms of action remain poorly understood. Consequently, mathematical modelling of angiogenesis has an increasingly important role in the development and testing of these strategies.

While significant progress has been made in the development of models of tumor-induced angiogenesis, none have been able to capture the dynamics of pro- and

anti-angiogenic molecules, and the downstream signalling cascades that they initiate, at an intracellular or molecular level. Vascular endothelial cell behavior has been treated as a function of free chemokine density, instead of a response to the presence of activated growth factor receptors on their surfaces. This makes it difficult to accurately predict cellular response to therapeutic blockage of angiogenic growth factors. Furthermore, generic chemokines have often been used to represent an entire panel of angiogenic factors. However, many anti-angiogenic molecules being investigated currently target specific chemokines; any mathematical investigation designed to evaluate their potential or elucidate their anti-angiogenic mechanisms would need to incorporate specific details relating to that particular chemokine.

To advance the current state of mathematical investigations of tumor-induced angiogenesis, we developed a multiscale tumor vascularization model explicitly describing the intricate interplay between intracellular regulation in the form of molecular signalling pathways, growth factor-receptor crosstalk at a cellular level, and the resulting intercellular interactions. This model makes novel and significant contributions to the field of angiogenesis modelling in several ways.

We began with a detailed quantitative analysis of the validity of various assumptions such as monomeric uptake of VEGF by VEGFR2, and the quasi-steady state assumption commonly made in modelling VEGF interactions with VEGFR2. The results of this analysis highlighted the impact that incorporating molecular level detail of the biochemical processes that control angiogenesis can have in enhancing the accuracy and usefulness of a mathematical model of angiogenesis. Subsequently, a model of intra-tumoral angiogenesis was developed. This model is the first to connect the molecular events associated with VEGFR2 dimerization and intracellular signaling with the temporal changes in endothelial cell proliferation, migration and

survival. It is also the first to explicitly incorporate details of intracellular molecular events, such as interactions of the Bcl-family of proteins that control cellular apoptosis. This put us in a unique position to explore the therapeutic potential of a small molecule inhibitor of the pro-survival protein Bcl-2. Another novel feature of this model is that it captures the process of microvessel formation from individual endothelial cells which align themselves to form blood vessels.

Finally, a hybrid model of tumor vascularization was proposed. A significant feature that sets this apart from previous such mathematical investigations is that it is the first to allow endothelial cells to detect gradients of bound VEGF across their lengths, and polarize and migrate in response to this gradient. Another important contribution of this model is a novel chemotactic sensitivity function that incorporates a level of biological detail ignored by sensitivity functions currently in use. We are thus able to capture empirically observed phenomena, such the requirement of a minimum activation level of cell surface receptors, and receptor desensitization in high concentrations of VEGF.

The modelling techniques developed here use the behavior predicted by a single cell, guided by cellular and molecular level events, to determine the response of a population of cells. These techniques are useful in studying the relationship between intra-cellular molecular pathways and multicellular behavior. Therefore, they have have applications in other complex biological systems such as immune system response to cancer cells and other pathogens.

Our model of tumor angiogenesis is borne out of close interactions with experimentalists working in the field of anti-angiogenic drug development. This has allowed us to validate the model at every step of development by direct comparison with experimental data, enhancing its usefulness as a predictive tool to experimentalists and

clinicians. Using this modelling framework, we were able to test the potential of a number of targets for the development of anti-angiogenic therapy, and allowed us to answer questions relating to the biology of vascular regression, which would otherwise have been difficult or even impossible to do experimentally. A great strength of the model lies in the flexibility of its framework; it can easily be modified to simulate other experimental assays designed to elucidate the mechanisms of angiogenesis-dependent diseases from a therapeutic point of view. Given the high financial and human costs of clinical trials, such quantitative modelling can have a far-reaching impact in the field of angiogenetic therapeutics.

9.2 Future Directions

A number of questions regarding anti-angiogenic therapy remain unanswered. A deeper understanding of the molecular mechanisms of their action is required to evaluate their potential as a cure for cancer, whether used alone, or in combination with other forms of anti-cancer therapy. To this end, several additional extensions and improvements to the models of tumor angiogenesis developed in this research are planned. These include incorporating the effects of various angiogenic inhibitors targeting different aspects of vessel growth. In addition, other growth factors and their downstream intracellular signaling pathways, as well as regulators of vessel maturation, regression and sprouting, will also be incorporated. The role of the ECM in vascular network formation and modulation, and blood flow through the capillaries will also be considered. Below, we present additional ideas for future model extensions.

9.2.1 An Evaluation of Anti-VEGF Therapy

It has been shown that tumor angiogenesis is crucially mediated by VEGF. Tumor vessels require VEGF for survival and function. It also plays an important part in determining vascular morphology. Consequently, anti-VEGF strategy is considered as the most promising anti-angiogenesis therapy for the treatment of human cancers (21; 58). Several of the anti-VEGF compounds that were efficacious in animal models are currently undergoing clinical trials. However, many of these compounds including avastin, SU5416 (a small molecule inhibitor of the VEGF receptor) and IM862 (a small molecule that blocks VEGF and other targets) have produced disappointing results (45).

Cao (21) considers several possible reasons for this difficulty in replicating results from the animal models in humans. For instance, a late stage tumor may produce many more angiogenic factors than an early stage tumor, so that the efficacy of anti-VEGF treatment becomes crucially dependent on early detection. Variance in growth rates of human tumors versus mouse tumors could also mean that their angiogenic profiles are different resulting in different levels of VEGF receptor expression. A faster growth rate could thus explain a greater dependency of mouse tumors on VEGF. VEGF can be generated as various spliced isoforms and, it is possible that not all VEGF antagonists can block the functions of all VEGF isoforms. In addition, the treatment may not be effective if it relies on blocking intracellular signalling mediated by VEGF receptors, since there may exist other receptor-like molecules on an endothelial cell surface, that bind VEGF (such as neuropilin, which binds several VEGF isoforms) and thereby transduce pro-angiogenic signalling.

Furthermore, anti-VEGF agents may be accompanied by distinct adverse side-effects, hypertension and proteinuria being the most common.These could lead to

renal toxicity and thromboembolic events (58; 104). It is believed that these are downstream effects of VEGF-signalling suppression in ECs of normal organs (58).

Despite these setbacks, certain success stories do exist that have kept the interest in this field alive. In spite of its failure as a treatment option in breast cancer, Avastin has been approved by the FDA as a first- or second-line treatment of metastatic carcinoma of the colon, in combination with chemotherapy, as well as first-line treatment for nonsquamous, non-small lung cancer. Sunitinib has been approved for the treatment of advanced renal cell carcinoma and gastrointestinal stromal tumors (58). Furthermore, anti-VEGF therapy does not lead to side-effects such as myelosuppression, and neutropenia found with conventional chemotherapy.

Thus, it is essential to gain a better understanding of the mechanisms of action of anti-VEGF therapy, and its side-effects, in order to evaluate its therapeutic potential and predict optimal dosing. The kind of modelling developed here provides an ideal platform for such investigations. This could also answer questions relating to variance in efficacy with tumor type, as well as predicting outcomes of clinical trials. We also plan to mathematically and computationally investigate the effect of the small molecule inhibitor of VEGFR2, PTK787/ZK222584, which does not interfere with VEGF binding, though it does neutralize the intracellular signaling that VEGFR2 triggers in order to promote proliferation and survival. The molecular level detail of the biochemical processes guiding angiogenesis incorporated in our model makes it sensitive enough to distinguish between therapy targeted at the VEGF molecule and that targeted against VEGFR2. For instance, the model can differentiate the response of PTK787/ZK222584 and the humanized monoclonal anti-VEGF antibody Avastin on tumor vasculature.

9.2.2 Towards a Comprehensive Multiscale Hybrid Model of Tumor Angiogenesis

In Chapter VIII, we developed a hybrid model of tumor angiogenesis, in which EC response to cell-surface bound VEGF was explicitly included. However, for the purposes of computational ease, certain simplifying assumptions were made. Most notably, unbound VEGF was assumed to be in quasi steady-state. Further only the tip cell was kept track of, while VEGF uptake by stalk cells was ignored. Cell death was also omitted, while cell proliferation was implicit, rather than explicit. We plan to extend this model by relaxing some of these assumptions.

Lattice-based models of angiogenesis face the criticism that the capillary networks generated by them are artificial to a certain extent, as they are forced to follow the lattice used to discretize the model. A first step would therefore be to develop a lattice-free version of our model of capillary formation, in which the ECs move without geometric constraints. Such models have been applied to capillary formation previously (119). Each tip cell is assigned a speed, and a direction of motion. This would be determined by gradient of bound VEGF on its surface.

As mentioned in section 8.1.2, the edges of the tip cell and stalk cells of each capillary represents moving boundaries serving as sinks for free VEGF via cell-surface receptor uptake. The following equations would need to be solved at each such cell face. (n is the unit normal to the cell face, D_c is the diffusion coefficient of VEGF).

$$D_c \frac{\partial A}{\partial n} = -2\, k^a_{f1}\, A\, R_a + k^a_{r1}\, C_a \tag{9.1}$$

$$\frac{dR_a}{dt} = -2\, k^a_{f1}\, A\, R_a + k^a_{r1}\, C_a - k^a_{f2}\, C_a\, R_a + 2\, k^a_{r2}\, D_a + 2\, k^a_p\, D_a \tag{9.2}$$

$$\frac{dC_a}{dt} = 2\, k^a_{f1}\, A\, R_a - k^a_{r1}\, C_a - k^a_{f2}\, C_a\, R_a + 2\, k^a_{r2}\, D_a \tag{9.3}$$

$$\frac{dD_a}{dt} = k^a_{f2}\, C_a\, R_a - 2\, k^a_{r2}\, D_a - k^a_p\, D_a \tag{9.4}$$

Thus, gradients of activated receptors would form on the leading cell, thereby guiding its motion.

Proliferation has been reported to occur in widely different parts of the sprout. While it is generally believe to occur right behind the tip cell, after the ECs have already migrated into the stroma some distance (134), there is evidence of mitotic activity occurring at the base of a newly formed sprout, some distance behind the tip cell, and directly behind the tip cell (110). It is also known that ECs integrate the total amount of VEGF bound to their surfaces before making a decision to proliferate (47). Keeping track of the amount of VEGF bound on each cell would enable us to simulate these various proliferative regions on the capillary, and examine their effect on sprout development. Proliferation also results in branching, thus we would be able to model this in a biochemically motivated fashion rather than laying down phenomenological rules for it, as is currently the trend.

Finally, cell death, regulated by intracellular pathways such as the VEGF-Bcl-2-CXCL8 would be incorporated in the model. This would allow us to investigate the various anti-angiogenic therapies simulated on our DDE model on a biologically more realistic platform.

9.2.3 Other Targets for Development of Anti-angiogenic Therapy

Over-expression of the pro-survival members of the Bcl-family proteins is frequently observed in tumors of diverse origin. This confers a measure of protection to the cancer cells while making them resistant to treatment that induces cell death by targeting the mitochondrial pathway (39). In certain types of tumors, cancer cells are able to extend this protective effect to ECs lining tumor blood vessels (97; 98; 99). Consequently, the Bcl-family of proteins have emerged as key targets for the design of therapeutic strategies aimed at controlling tumor-induced angiogenesis.

Several small molecule compounds such as Tetrocarcin A and H-14A interfering with Bcl-2/Bcl-xL function have been recently identified, and are undergoing preclinical studies (39). Others such as TW37 are still under development (160). The model developed in this dissertation already incorporates the apoptotic regulating pathway of the Bcl-family of proteins. It would therefore be a straightforward task to test the anti-cancer potential of these molecules.

Experimental evidence has shown that ECM regulates angiogenesis by providing not only scaffold support, but also plays an active signaling roles by serving as a reservoir and modulator for angiogenic growth factors. Cellular interactions with the ECM can have a significant impact on new capillary sprout formation and morphology. Consequently, ECM-targeted strategies are being widely accepted as having significant therapeutic potential as a treatment for cancer. Adding ECM as a dynamic variable in our hybrid model of angiogenesis can play an important role in the development and testing of these strategies.

The research carried out in this thesis is noteworthy in the respect that it aids efficient drug design and administration. It has the potential to save significant time and costs relating to drug development and enhances patient care. The research has aided experimentalists in choosing anti-Bcl-2 therapy as the more effective target for the development of an anti-angiogenic drug. One such small molecule inhibitor of Bcl-2 is in pre-clinical trials. The research has also addressed the issue of the minimum level of drug required to significantly impair tumor vasculature. As many anti-angiogenic drugs may have toxic side-effects, this can be an effective method for clinicians to determine drug therapy regimes.

APPENDICES

APPENDIX A

Modelling VEGF-VEGFR2 Interactions

The full system of equations describing ligand-induced dimerization of cell surface receptors used to model VEGF-VEGFR2 interactions in Chapter IV are presented below.

$$\text{(A.1)} \quad \frac{dA}{dt} = -2\,\eta_1^a\,k_{f1}^a\,A\,R_a + \eta_2^a\,k_{r1}^a\,C_a - \lambda_a\,A$$

$$\text{(A.2)} \quad \frac{dR_a}{dt} = -2\,k_{f1}^a\,A\,R_a + \eta_3^a\,k_{r1}^a\,C_a - k_{f2}^a\,C_a\,R_a + 2\,\eta_4^a\,k_{r2}^a\,D_a + 2\,\eta_4^a\,k_p^a\,D_a$$

$$\text{(A.3)} \quad \frac{dC_a}{dt} = 2\,\eta_5^a\,k_{f1}^a\,A\,R_a - k_{r1}^a\,C_a - \eta_5^a\,k_{f2}^a\,C_a\,R_a + 2\,\eta_6^a\,k_{r2}^a\,D_a$$

$$\text{(A.4)} \quad \frac{dD_a}{dt} = \eta_7^a\,k_{f2}^a\,C_a\,R_a - 2\,k_{r2}^a\,D_a - k_p^a\,D_a$$

The full system of equations describing activation of pre-dimerized receptors by VEGF in a single binding step (1:1 model) are presented below.

$$\text{(A.5)} \quad \frac{dA}{dt} = -\eta_8^a\,k_{f1}^a\,A\,P_a + \eta_0^a\,k_{r1}^a\,D_a - \lambda_a\,A$$

$$\text{(A.6)} \quad \frac{dP_a}{dt} = -k_{f1}^a\,A\,P_a + \eta_9^a\,k_{r1}^a\,D_a + \eta_9^a\,k_p^a\,D_a$$

$$\text{(A.7)} \quad \frac{dP_a}{dt} = \eta_{10}^a\,k_{f1}^a\,A\,P_a - k_{r1}^a\,D_a - k_p^a\,D_a$$

Here, P_a is the pre-dimerized VEGFR2 density. As in the full dimer model, the above equations have been scaled to units of pg/mm^3 by appropriate constants (η_i^a). These

Table A.1: List of parameter values relating to the molecular weights of VEGF and VEGFR2

Parameter	Value	Units
η_8^a	0.1125	pg of VEGF per pg of VEGFR2-VEGFR2 complex
η_9^a	0.8989	pg of VEGFR2-VEGFR2 complex per pg of VEGFR2-VEGFR2-VEGF complex
η_{10}^a	1.1125	pg of VEGFR2-VEGFR2-VEGF complex per pg of VEGFR2-VEGFR2 complex

represent ratios of the weights of the different molecules involved in the reaction. The values of these constants are given in the table below.

A.1 Non-dimensionalization of the Model Equations

The system of equations listed above is re-scaled to introduce non-dimensional variables. t is scaled by the slowest time-scale in the reactions, $1/k_{r1}^a$. VEGF concentration A is scaled by a factor of A_0, the initial amount of VEGF. The free and occupied receptor densities are scaled by their maximum possible values. For instance, free VEGFR2 density R_a is scaled by a factor of $R_t^a\, M_0$, where R_t^a is the weight in pg of VEGFR2 per cell. M_0 is the carrying capacity of the environment for endothelial cells. Therefore, we set

$$t^* = \frac{1}{k_{r1}^a} \qquad A^* = \frac{A}{A_0} \qquad R_a^* = \frac{R_a}{R_t^a\, M_0}$$

$$C_a^* = \frac{C_a}{\eta_5^a\, R_t^a\, M_0}$$

$$D_a^* = \frac{D_a}{\eta_7^a\, R_t^a\, M_0}^1 \quad D_a^* = \frac{D_a}{\eta_{10}^a\, R_t^a\, M_0/2}^2 \quad P_a^* = \frac{P_a}{R_t^a\, M_0/2}$$

where, the * superscripts denote non-dimensional quantities. Dropping the asterisks for clarity, the non-dimensional system corresponding to the dimeric uptake model reduces to the following.

[1] In the case of the dimer model, D_a is scaled by a factor proportional to the maximum free VEGFR2 density, whilst in the 1:1 model, it is scaled by factor proportional to the maximum free pre-dimerized VEGFR2 density.

$$\frac{dA}{dt} = -\zeta_1^a\, A\, R_a + \zeta_2^a\, C_a - \psi_a\, A \tag{A.8}$$

$$\frac{dR_a}{dt} = -\zeta_3^a\, A\, R_a + C_a - \zeta_5^a\, C_a\, R_a + \zeta_6^a\, D_a + \zeta_7^a\, D_a \tag{A.9}$$

$$\frac{dC_a}{dt} = \zeta_3^a\, A\, R_a - C_a - \zeta_5^a\, C_a\, R_a + \zeta_6^a\, D_a \tag{A.10}$$

$$\frac{dD_a}{dt} = \zeta_5^a\, C_a\, R_a - \zeta_6^a\, D_a - \frac{\zeta_7^a}{2}\, D_a \tag{A.11}$$

The non-dimensional system corresponding to the 1:1 uptake model reduces to the following.

$$\frac{dA}{dt} = -\zeta_8^a\, A\, P_a + \zeta_0^a\, D_a - \psi_a\, A \tag{A.12}$$

$$\frac{dP_a}{dt} = -\frac{\zeta_3^a}{2}\, A\, P_a + D_a + \frac{\zeta_7^a}{2}\, D_a \tag{A.13}$$

$$\frac{dD_a}{dt} = \frac{\zeta_3^a}{2}\, A\, P_a - D_a - \frac{\zeta_7^a}{2}\, D_a \tag{A.14}$$

The non-dimensional parameters are listed below.

$$\zeta_1^a = \frac{2\,\eta_1^a\, k_{f1}^a\, R_t^a\, M_0}{k_{r1}^a} \quad \zeta_2^a = \frac{\eta_2^a\, \eta_5^a\, R_t^a\, M_0}{A_0} \quad \zeta_3^a = \frac{2\, k_{f1}^a\, A_0}{k_{r1}^a}$$

$$\zeta_5^a = \frac{\eta_5^a\, k_{f2}^a\, R_t^a\, M_0}{k_{r1}^a} \quad \zeta_6^a = \frac{2\, k_{r2}^a}{k_{r1}^a} \quad \zeta_7^a = \frac{2\, k_p^a}{k_{r1}^a}$$

$$\zeta_8^a = \frac{\eta_8^a\, k_{f1}^a\, R_t^a\, M_0}{2\, k_{r1}^a} \quad \zeta_0^a = \frac{\eta_8^a\, R_t^a\, M_0}{2\, A_0} \quad \psi_a = \lambda_a\, k_{r1}$$

It should be noted that the dimer model approximates the 1:1 model under the condition that the binding of the intermediary complex C_a with a free receptor R_a proceeds forward at a very rapid rate. In other words, if k_{f2}^a is very high, the two models will predict similar fractional occupancies of receptors. In non-dimensional terms, this corresponds to high values for the parameter $zeta_5^a$, which governs the rate of reaction between C_a^* and R_a^*.

APPENDIX B

Modelling the VEGF-Bcl-2-CXCL8 Pathway in Angiogenesis

The full system of equations in Chapter V, used to model sustained angiogenesis are given below.

$$\text{(B.1)}\quad \frac{dM}{dt} = (\mu_a\,\phi_a + \mu_l\,\phi_l - (\lambda_m - \delta\,\phi_a))\;M\;\left(1 - \frac{M}{M_0 - \alpha_1 V}\right) - \alpha_1\;(\alpha_2\,\phi_a + \alpha_3\,\phi_l)\;M_\tau$$

$$\text{(B.2)}\quad \frac{dA}{dt} = -2\,\eta_1^a\,k_{f1}^a\,A\,R_a + \eta_2^a\,k_{r1}^a\,C_a - \lambda_a\,A + r_3\,N\;\left(1 + \tanh\left(\frac{V_{char} - (V + V_0)}{\epsilon}\right)\right)$$

$$\text{(B.3)}\quad \frac{dR_a}{dt} = -2\,k_{f1}^a\,A\,R_a + \eta_3^a\,k_{r1}^a\,C_a - k_{f2}^a\,C_a\,R_a + 2\,\eta_4^a\,k_{r2}^a\,D_a + 2\,\eta_4^a\,k_p^a\,D_a + R_t^a\,\mathrm{Prod}(M,V) - \frac{R_a}{R_a + \eta_3^a\,C_a + 2\,\eta_4^a\,D_a}\,R_t^a\,\mathrm{Death}(M,V)$$

$$\text{(B.4)}\quad \frac{dC_a}{dt} = 2\,\eta_5^a\,k_{f1}^a\,A\,R_a - k_{r1}^a\,C_a - \eta_5^a\,k_{f2}^a\,C_a\,R_a + 2\,\eta_6^a\,k_{r2}^a\,D_a - \frac{C_a}{R_a + \eta_3^a\,C_a + 2\,\eta_4^a\,D_a}\,R_t^a\,\mathrm{Death}(M,V)$$

$$\text{(B.5)}\quad \frac{dD_a}{dt} = \eta_7^a\,k_{f2}^a\,C_a\,R_a - 2\,k_{r2}^a\,D_a - k_p^a\,D_a - \frac{D_a}{R_a + \eta_3^a\,C_a + 2\,\eta_4^a\,D_a}\,R_t^a\,\mathrm{Death}(M,V)$$

$$\text{(B.6)}\quad \frac{dL}{dt} = -\eta_1^l\,k_f^l\,L\,R_l + \eta_2^l\,k_r^l\,C_l - \lambda_l\,L + \beta_l\,M + \beta_a\,\frac{D_a}{M + \alpha_1 V}\,M$$

$$\text{(B.7)} \qquad \frac{dR_l}{dt} = -k_f^l\, L\, R_l + \eta_3^l\, k_r^l\, C_l + \eta_3^l\, k_p^l\, C_l + R_t^l\, \text{Prod}(M,V) - \frac{R_l}{R_l + \eta_3^l\, C_l}\, R_t^l\, \text{Death}(M,V)$$

$$\text{(B.8)} \qquad \frac{dC_l}{dt} = \eta_4^l\, k_f^l\, L\, R_l - k_r^l\, C_l - k_p^l\, C_l - \frac{C_l}{R_l + \eta_3^l\, C_l}\, R_t^l\, \text{Death}(M,V)$$

$$\text{(B.9)} \qquad \frac{dV}{dt} = (\alpha_2\, \phi_a + \alpha_3\, \phi_l)\; M_\tau - \alpha_4\; (\lambda_m - \delta\, \phi_a)\; \alpha_1\, V$$

$$\text{(B.10)} \qquad \frac{dN}{dt} = r_1\, \frac{C^2(V)}{C_1^2 + C^2(V)}\, N - r_2\, \left(1 - \sigma\, \frac{C^2(V)}{C_2^2 + C^2(V)}\right)\, N^2$$

where,

$$\text{(B.11)} \qquad C(V) = C_m\, \frac{V_0 + V}{k + V_0 + V}$$

$$\text{(B.12)} \qquad \text{Prod}(M,V) = (\mu_a\, \phi_a + \mu_l\, \phi_l)\; M\, \left(1 - \frac{M}{M_0 - \alpha_1 V}\right)$$

$$\text{(B.13)} \qquad \text{Death}(M,V) = (\lambda_m - \delta\, \phi_a)\; M\, \left(1 - \frac{M}{M_0 - \alpha_1 V}\right) + \alpha_1\, \alpha_1\, \alpha_4\; (\lambda_m - \delta\, \phi_a)\; V$$

$$\text{(B.14)} \qquad \phi_a = \frac{D_a}{M + \alpha_1 V}$$

$$\text{(B.15)} \qquad \phi_l = \frac{C_l}{M + \alpha_1 V}$$

B.1 Non-dimensionalization of the Model Equations

The system of equations listed above is re-scaled to introduce non-dimensional variables. t is scaled by the value of the delay, τ. HDMEC density M is scaled by M_0, the carrying capacity of the environment for endothelial cells. Microvessel density V is scaled by a factor of $\frac{M_0}{\alpha_1}$, the carrying capacity of the environment for microvessels. Tumor cell density N is scaled by a factor of N_0, the maximum possible concentration of tumor cells under conditions of optimal oxygen concentration.

Oxygen concentration C is scaled by C_m, the oxygen concentration under normoxia. VEGF concentration A is scaled by a factor of A_0, chosen chosen so as to eliminate the parameter associated with its rate of production by tumor cells. Likewise, CXCL8 concentration L is scaled by a factor of L_0, chosen chosen so as to eliminate the parameter associated with its rate of production by HDMECs. The free and occupied receptor densities are scaled by their maximum possible values. For instance, free VEGFR2 density R_a is scaled by a factor of $R_t^a\, M_0$, where R_t^a is the weight in pg of VEGFR2 per cell. Therefore, we set

$$
\begin{array}{cccc}
 & t^* = \dfrac{t}{\tau} & \tau^* = 1 & \\
M^* = \dfrac{M}{M_0} & V^* = \dfrac{V}{M_0/\alpha_1} & N^* = \dfrac{N}{N_0} & C^* = \dfrac{C}{C_m} \\
A^* = \dfrac{A}{A_0} & R_a^* = \dfrac{R_a}{R_t^a\, M_0} & C_a^* = \dfrac{C_a}{\eta_5^a\, R_t^a\, M_0} & D_a^* = \dfrac{D_a}{\eta_7^a\, R_t^a\, M_0} \\
L^* = \dfrac{L}{L_0} & R_l^* = \dfrac{R_l}{R_t^l\, M_0} & C_l^* = \dfrac{C_l}{\eta_4^a\, R_t^a\, M_0} &
\end{array}
$$

where

$$
N_0 = \frac{r_1}{r_2}\,\frac{C_m^2}{C_1^2 + C_m^2}\left(1 - \sigma\,\frac{C_m^2}{C_2^2 + C_m^2}\right)^{-1} \tag{B.16}
$$

$$
A_0 = r_3\, N_0\, \tau \tag{B.17}
$$

$$
L_0 = \beta_l\, M_0\, \tau \tag{B.18}
$$

and the * superscripts denote non-dimensional quantities. Dropping the asterisks for clarity, the non-dimensional system reduces to the following.

$$\text{(B.19)} \quad \frac{dM}{dt} = \left(\rho_a\,\bar{\phi}_a + \rho_l\,\bar{\phi}_l - \left(\psi_m - \omega\,\bar{\phi}_a\right)\right)\,M\,\left(1 - \frac{M}{1-V}\right) - \left(\xi_a\,\bar{\phi}_a + \xi_l\,\bar{\phi}_l\right)\,M(t-1)$$

$$\text{(B.20)} \quad \frac{dA}{dt} = -\zeta_1^a\,A\,R_a + \zeta_2^a\,C_a - \psi_a\,A + N\,\left(1 + \tanh\left(\frac{\bar{V}_{char} - (V + \bar{V}_0)}{\bar{\epsilon}}\right)\right)$$

$$\text{(B.21)} \quad \frac{dR_a}{dt} = -\zeta_3^a\,A\,R_a + \zeta_4^a\,C_a - \zeta_5^a\,C_a\,R_a + \zeta_6^a\,D_a + \zeta_7^a\,D_a + \overline{\text{Prod}}(M,V) - \frac{R_a}{M+V}\,\overline{\text{Death}}(M,V)$$

$$\text{(B.22)} \quad \frac{dC_a}{dt} = \zeta_3^a\,A\,R_a - \zeta_4^a\,C_a - \zeta_5^a\,C_a\,R_a + \zeta_6^a\,D_a - \frac{C_a}{M+V}\,\overline{\text{Death}}(M,V)$$

$$\text{(B.23)} \quad \frac{dD_a}{dt} = \zeta_5^a\,C_a\,R_a - \zeta_6^a\,D_a - \frac{\zeta_7^a}{2}\,D_a - \frac{D_a}{M+V}\,\overline{\text{Death}}(M,V)$$

$$\text{(B.24)} \quad \frac{dL}{dt} = -\zeta_1^l\,L\,R_l + \zeta_2^l\,C_l - \psi_l\,L + M + \nu_l\,\frac{D_a}{M+V}\,M$$

$$\text{(B.25)} \quad \frac{dR_l}{dt} = -\zeta_3^l\,L\,R_l + \zeta_4^l\,C_l + \zeta_5^l\,C_l + \overline{\text{Prod}}(M,V) - \frac{R_l}{M+V}\,\overline{\text{Death}}(M,V)$$

$$\text{(B.26)} \quad \frac{dC_l}{dt} = \zeta_3^l\,L\,R_l - \zeta_4^l\,C_l - \zeta_5^l\,C_l - \frac{C_l}{M+V}\,\overline{\text{Death}}(M,V)$$

$$\text{(B.27)} \quad \frac{dV}{dt} = \left(\xi_a\,\bar{\phi}_a + \xi_l\,\bar{\phi}_l\right)\,M(t-1) - \bar{\alpha}\,\left(\psi_m - \omega, \bar{\phi}_a\right)\,V$$

$$\text{(B.28)} \quad \frac{dN}{dt} = \bar{r_1}\,\frac{C^2(V)}{\bar{C}_1^2 + C^2(V)}\,N - \bar{r}_2\,\left(1 - \sigma\,\frac{C^2(V)}{\bar{C}_2^2 + C^2(V)}\right)\,N^2$$

The non-dimensional parameters are listed below.

$$\rho_a = \mu_a\,\eta_7^a\,R_t^a\,\tau \qquad \rho_l = \mu_l\,\eta_4^l\,R_t^l\,\tau \qquad \psi_m = \lambda_m\,\tau$$

$$\omega = \delta\,\eta_7^a\,R_t^a\,\tau \qquad \xi_a = \alpha_1\,\alpha_2\,\eta_7^a\,R_t^a\,\tau \qquad \xi_l = \alpha_1\,\alpha_3\,\eta_4^l\,R_t^l\,\tau$$

$$\zeta_1^a = 2\,\eta_1^a\,k_{f1}^a\,R_t^a\,M_0\,\tau \qquad \zeta_2^a = \frac{\eta_2^a\,\eta_5^a\,k_{r1}^a\,R_t^a\,M_0\,\tau}{A_0} \qquad \zeta_3^a = 2\,k_{f1}^a\,A_0\,\tau$$

$$\zeta_4^a = k_{r1}^a\,\tau \qquad \zeta_5^a = \eta_5^a\,k_{f2}^a\,R_t^a\,M_0\,\tau \qquad \zeta_6^a = 2\,k_{r2}^a\,\tau$$

$$\zeta_7^a = 2\,k_p^a\,\tau \qquad \psi_a = \lambda_a\,\tau \qquad \bar{V}_{char} = \frac{\alpha_1}{M_0}\,V_{char}$$

$$\bar{V}_0 = \frac{\alpha_1}{M_0}\,V_0 \qquad \bar{\epsilon} = \frac{\alpha_1}{M_0}\,\epsilon \qquad \bar{\alpha} = \alpha_1\,\alpha_4$$

$$\zeta_1^l = \eta_1^l\,k_f^l\,R_t^l\,M_0\,\tau \qquad \zeta_2^l = \frac{\eta_2^l\,\eta_4^l\,k_r^l\,R_t^l\,M_0\,\tau}{L_0} \qquad \zeta_3^a = k_f^l\,L_0\,\tau$$

$$\zeta_4^l = k_r^l\,\tau \qquad \zeta_5^l = k_p^l\,\tau \qquad \psi^l = \lambda_l\,\tau$$

$$\nu_m = \frac{\beta_a\,\eta_7^a\,R_t^a}{\beta_l} \qquad \bar{r}_1 = r_1\,\tau \qquad \bar{C}_1 = \frac{C_1}{C_m}$$

$$\bar{C}_2 = \frac{C_2}{C_m} \qquad \bar{r}_2 = r_2\,N_0\,\tau \qquad \bar{k} = \frac{\alpha_1\,k}{M_0}$$

Here,

$$C(V) = \frac{\bar{V}_0 + V}{\bar{k} + \bar{V}_0 + V} \tag{B.29}$$

$$\overline{\text{Prod}}(M,V) = \left(\rho_a\,\bar{\phi}_a + \rho_l\,\bar{\phi}_l\right)\,M\,\left(1 - \frac{M}{1-V}\right) \tag{B.30}$$

$$\overline{\text{Death}}(M,V) = \left(\psi_m - \omega\,\bar{\phi}_a\right)\,M\,\left(1 - \frac{M}{1-V}\right) + \bar{\alpha}\,\left(\psi_m - \omega\,\bar{\phi}_a\right)\,V \tag{B.31}$$

$$\bar{\phi}_a = \frac{D_a}{M+V} \tag{B.32}$$

$$\bar{\phi}_l = \frac{C_l}{M+V} \tag{B.33}$$

APPENDIX C

The Bcl-family of Proteins in Intra-tumoral Angiogenesis

The full system of equations in Chapter VII, used to model sustained angiogenesis in vivo are given below.

$$\text{(C.1)}\quad \frac{dM}{dt} = (\mu_a\,\phi_a + \mu_l\,\phi_l - \lambda_m(X))\;M\left(1 - \frac{M + \alpha_1 V}{M_0}\right) - \alpha_1\;(\alpha_2\,\phi_a + \alpha_3\,\phi_l)\;M_\tau$$

$$\text{(C.2)}\quad \frac{dA}{dt} = -2\,\eta_1^a\,k_{f1}^a\,A\,R_a + \eta_2^a\,k_{r1}^a\,C_a - \lambda_a\,A + r_3\,N\left(1 + \tanh\left(\frac{V_{char} - (V + V_0)}{\epsilon}\right)\right)$$

$$\text{(C.3)}\quad \frac{dR_a}{dt} = -2\,k_{f1}^a\,A\,R_a + \eta_3^a\,k_{r1}^a\,C_a - k_{f2}^a\,C_a\,R_a + 2\,\eta_4^a\,k_{r2}^a\,D_a + 2\,\eta_4^a\,k_p^a\,D_a + R_t^a\,\mathrm{Prod}(M,V) - \frac{R_a}{R_a + \eta_3^a\,C_a + 2\,\eta_4^a\,D_a}\,R_t^a\,\mathrm{Death}(M,V)$$

$$\text{(C.4)}\quad \frac{dC_a}{dt} = 2\,\eta_5^a\,k_{f1}^a\,A\,R_a - k_{r1}^a\,C_a - \eta_5^a\,k_{f2}^a\,C_a\,R_a + 2\,\eta_6^a\,k_{r2}^a\,D_a - \frac{C_a}{R_a + \eta_3^a\,C_a + 2\,\eta_4^a\,D_a}\,R_t^a\,\mathrm{Death}(M,V)$$

$$\text{(C.5)}\quad \frac{dD_a}{dt} = \eta_7^a\,k_{f2}^a\,C_a\,R_a - 2\,k_{r2}^a\,D_a - k_p^a\,D_a - \frac{D_a}{R_a + \eta_3^a\,C_a + 2\,\eta_4^a\,D_a}\,R_t^a\,\mathrm{Death}(M,V)$$

$$\text{(C.6)}\quad \frac{dL}{dt} = -\eta_1^l\,k_f^l\,L\,R_l + \eta_2^l\,k_r^l\,C_l - \lambda_l\,L + \beta_l(B)\,M$$

$$\text{(C.7)}\quad \frac{dR_l}{dt} = -k_f^l\, L\, R_l + \eta_3^l\, k_r^l\, C_l + \eta_3^l\, k_p^l\, C_l + R_t^l\, \text{Prod}(M,V) - \frac{R_l}{R_l + \eta_3^l\, C_l}\, R_t^l\, \text{Death}(M,V)$$

$$\text{(C.8)}\quad \frac{dC_l}{dt} = \eta_4^l\, k_f^l\, L\, R_l - k_r^l\, C_l - k_p^l\, C_l - \frac{C_l}{R_l + \eta_3^l\, C_l}\, R_t^l\, \text{Death}(M,V)$$

$$\text{(C.9)}\quad \frac{dV}{dt} = (\alpha_2\, \phi_a + \alpha_3\, \phi_l)\; M_\tau - \alpha_4\, \lambda_m(X)\, \alpha_1\, V$$

$$\text{(C.10)}\quad \frac{dN}{dt} = r_1\, \frac{C^2(V)}{C_1^2 + C^2(V)}\, N - r_2 \left(1 - \sigma\, \frac{C^2(V)}{C_2^2 + C^2(V)}\right) N^2$$

$$\text{(C.11)}\quad \frac{dB}{dt} = -k_f^b\, B\, X + \eta_1^b\, k_r^b\, C_{bx} - k_f^i\, B\, I + \eta_1^i\, k_r^i\, C_{bi} + \beta_a\, \frac{d}{dt}\left(\frac{D_a}{M + \alpha_1 V}\right)$$

$$\text{(C.12)}\quad \frac{dX}{dt} = -\eta_2^b\, k_f^b\, B\, X + \eta_3^b\, k_r^b\, C_{bx}$$

$$\text{(C.13)}\quad \frac{dC_{bx}}{dt} = \eta_4^b\, k_f^b\, B\, X - k_r^b\, C_{bx}$$

$$\text{(C.14)}\quad \frac{dI}{dt} = -\eta_2^i\, k_f^i\, B\, I + \eta_3^i\, k_r^i\, C_{bi} + D_i\; (I_0 - I)$$

$$\text{(C.15)}\quad \frac{dC_{bi}}{dt} = \eta_4^i\, k_f^i\, B\, I - k_r^i\, C_{bi}$$

where,

$$\text{(C.16)}\quad C(V) = C_m\, \frac{V_0 + V}{k + V_0 + V}$$

$$\text{(C.17)}\quad \text{Prod}(M,V) = (\mu_a\, \phi_a + \mu_l\, \phi_l)\; M \left(1 - \frac{M + \alpha_1 V}{M_0}\right)$$

$$\text{(C.18)}\quad \text{Death}(M,V) = \lambda_m(X)\, M \left(1 - \frac{M + \alpha_1 V}{M_0}\right) + \alpha_1\, \alpha_1\, \alpha_4\, \lambda_m(X)\, V$$

$$\text{(C.19)}\quad \phi_a = \frac{D_a}{M + \alpha_1 V}$$

$$\text{(C.20)}\quad \phi_l = \frac{C_l}{M + \alpha_1 V}$$

$$\text{(C.21)}\quad \lambda_m(X) = a_d\, e^{b_d\, X}$$

$$\text{(C.22)}\quad \beta_l(B) = \beta_m + a_p\, (1 - e^{-b_p\, B})$$

C.1 Non-dimensionalization of the Model Equations

The system of equations listed above is re-scaled to introduce non-dimensional variables. Most of the variables are re-scaled as described in Appendix B. Note that the only change is in the definition of the scaling factor for L, which is now defined as $L_0 = \beta_m M_0 \tau$. The new variables are scaled as follows. Intra-cellular Bcl-2 concentration B and Bad concentration X are scaled by values B_0 and X_0 respectively, that represent their constitutive levels of expression. Intra-cellular BL193 concentration I is scaled by its extra-cellular concentration I_0. The intra-cellular concentrations of the intermediary complexes C_{bx} and C_{bi} are scaled by their respective maximum possible values. Therefore, we set

$$B^* = \frac{B}{B_0} \quad X^* = \frac{X}{X_0} \quad I^* = \frac{I}{I_0} \quad C^*_{bx} = \frac{C_{bx}}{\eta^b_4 B_0} \quad C^*_{bi} = \frac{C_{bi}}{\eta^i_4 B_0}$$

where the * superscripts denote non-dimensional quantities. Dropping the asterisks for clarity, the non-dimensional system reduces to the following.

$$\begin{aligned}
\text{(C.23)} \qquad \frac{dM}{dt} &= \left(\rho_a \bar{\phi}_a + \rho_l \bar{\phi}_l - \bar{\psi}_m(X)\right) M \left(1 - (M+V)\right) \\
&\quad - \left(\xi_a \bar{\phi}_a + \xi_l \bar{\phi}_l\right) M(t-1) \\
\text{(C.24)} \qquad \frac{dA}{dt} &= -\zeta^a_1 A R_a + \zeta^a_2 C_a - \psi_a A \\
&\quad + N \left(1 + \tanh\left(\frac{\bar{V}_{char} - (V + \bar{V}_0)}{\bar{\epsilon}}\right)\right) \\
\text{(C.25)} \qquad \frac{dR_a}{dt} &= -\zeta^a_3 A R_a + \zeta^a_4 C_a - \zeta^a_5 C_a R_a + \zeta^a_6 D_a + \zeta^a_7 D_a \\
&\quad + \overline{\text{Prod}}(M,V) - \frac{R_a}{M+V} \overline{\text{Death}}(M,V) \\
\text{(C.26)} \qquad \frac{dC_a}{dt} &= \zeta^a_3 A R_a - \zeta^a_4 C_a - \zeta^a_5 C_a R_a + \zeta^a_6 D_a \\
&\quad - \frac{C_a}{M+V} \overline{\text{Death}}(M,V) \\
\text{(C.27)} \qquad \frac{dD_a}{dt} &= \zeta^a_5 C_a R_a - \zeta^a_6 D_a - \frac{\zeta^a_7}{2} D_a - \frac{D_a}{M+V} \overline{\text{Death}}(M,V)
\end{aligned}$$

$$\text{(C.28)} \quad \frac{dL}{dt} = -\zeta_1^l\, L\, R_l + \zeta_2^l\, C_l - \psi_l\, L + \bar{\beta}_l(B)\, M$$

$$\text{(C.29)} \quad \frac{dR_l}{dt} = -\zeta_3^l\, L\, R_l + \zeta_4^l\, C_l + \zeta_5^l\, C_l + \overline{\text{Prod}}(M,V) - \frac{R_l}{M+V}\,\overline{\text{Death}}(M,V)$$

$$\text{(C.30)} \quad \frac{dC_l}{dt} = \zeta_3^l\, L\, R_l - \zeta_4^l\, C_l - \zeta_5^l\, C_l - \frac{C_l}{M+V}\,\overline{\text{Death}}(M,V)$$

$$\text{(C.31)} \quad \frac{dV}{dt} = \left(\xi_a\,\bar{\phi}_a + \xi_l\,\bar{\phi}_l\right)\, M(t-1) - \bar{\alpha}\,\bar{\psi}_m(X)\, V$$

$$\text{(C.32)} \quad \frac{dN}{dt} = \bar{r_1}\,\frac{C^2(V)}{\bar{C}_1^2 + C^2(V)}\, N - \bar{r}_2\,\left(1 - \sigma\,\frac{C^2(V)}{\bar{C}_2^2 + C^2(V)}\right)\, N^2$$

$$\text{(C.33)} \quad \frac{dB}{dt} = -\zeta_1^b\, B\, X + \zeta_2^b\, C_{bx} - \zeta_1^i\, B\, I + \zeta_2^i\, C_{bi} + \nu_b\,\frac{d}{dt}\left(\frac{D_a}{M+V}\right)$$

$$\text{(C.34)} \quad \frac{dX}{dt} = -\zeta_3^b\, B\, X + \zeta_4^b\, C_{bx}$$

$$\text{(C.35)} \quad \frac{dC_{bx}}{dt} = \zeta_1^b\, B\, X - \zeta_2^b\, C_{bx}$$

$$\text{(C.36)} \quad \frac{dI}{dt} = -\zeta_3^i\, B\, I + \zeta_4^i\, C_{bi} + \nu_i\,\left(1 - I\right)$$

$$\text{(C.37)} \quad \frac{dC_{bi}}{dt} = \zeta_1^i\, B\, I - \zeta_2^i\, C_{bi}$$

The additional non-dimensional parameters are listed below.

$$\zeta_1^b = k_f^b\, X_0\, \tau \qquad \zeta_2^b = k_r^b\, \tau \qquad \zeta_3^b = \eta_2^b\, k_f^b\, B_0\, \tau$$

$$\zeta_4^b = \frac{\eta_3^b\, \eta_4^b\, k_r^b\, B_0\, \tau}{X_0} \qquad \nu_b = \frac{\beta_a\, \eta_7^a\, R_t^a}{B_0} \qquad \nu_i = D_i\, \tau$$

$$\zeta_1^i = k_f^i\, I_0\, \tau \qquad \zeta_2^i = k_r^i\, \tau \qquad \zeta_3^i = \eta_2^i\, k_f^i\, B_0\, \tau$$

$$\zeta_4^i = \frac{\eta_3^i\, \eta_4^i\, k_r^i\, B_0\, \tau}{I_0} \qquad \bar{a}_d = a_d\, \tau \qquad \bar{b}_d = b_d\, X_0$$

$$\bar{a}_p = \frac{a_p}{\beta_m} \qquad \bar{b}_p = b_p\, B_0$$

Here,

$$C(V) = \frac{\bar{V}_0 + V}{\bar{k} + \bar{V}_0 + V} \tag{C.38}$$

$$\overline{\text{Prod}}(M, V) = \left(\rho_a \, \bar{\phi}_a + \rho_l \, \bar{\phi}_l\right) \, M \, (1 - (M + V)) \tag{C.39}$$

$$\overline{\text{Death}}(M, V) = \bar{\psi}_m(X) \, M \, (1 - (M + V)) + \bar{\alpha} \, \bar{\psi}_m(X) \, V \tag{C.40}$$

$$\bar{\phi}_a = \frac{D_a}{M + V} \tag{C.41}$$

$$\bar{\phi}_l = \frac{C_l}{M + V} \tag{C.42}$$

$$\bar{\psi}_m(X) = \bar{a}_d \, e^{\bar{b}_d \, X} \tag{C.43}$$

$$\bar{\beta}_l(B) = 1 + \bar{a}_p \, (1 - e^{-\bar{b}_p \, B}) \tag{C.44}$$

APPENDIX D

Biased Random Walk Model for Cell Chemotaxis

D.1 Continuum Limit of the Probability Master Equation

A derivation of the continuous diffusion-advection equation from the probability master equation for the biased random walk of a cell is presented here. The basic steps are as in (105). For ease of notation, the derivation is carried out for the 1-d case. The master equation (8.1) in 1-d is:

$$\frac{\partial p_n}{\partial t} = \hat{\mathcal{T}}^+_{n-1}(W)\, p_{n-1} + \hat{\mathcal{T}}^-_{n+1}(W)\, p_{n+1} \tag{D.1}$$

$$- \left(\hat{\mathcal{T}}^+_n(W) + \hat{\mathcal{T}}^-_n(W)\right) p_n \tag{D.2}$$

where

$$\hat{\mathcal{T}}^\pm_n(W) = 2\lambda \frac{\tau(c_{n\pm 1/2})}{\tau(c_{n+1/2}) + \tau(c_{n-1/2})} \equiv 2\lambda \mathcal{N}^\pm_n(W) \tag{D.3}$$

Define a function $N(.,.)$ as follows

$$N(c_{n+1/2}, c_{n-1/2}) = \mathcal{N}^+_n(W) = \frac{\tau(c_{n+1/2})}{\tau(c_{n+1/2}) + \tau(c_{n-1/2})} \tag{D.4}$$

$$N(c_{n-1/2}, c_{n+1/2}) = \mathcal{N}^-_n(W) = \frac{\tau(c_{n-1/2})}{\tau(c_{n+1/2}) + \tau(c_{n-1/2})}$$

Note that, by symmetry, $N(u,v) + N(v,u) = 1$. This renormalization introduces longer range dependence of the transition rates on the chemoattractant, since

$$\text{(D.5)} \qquad \hat{\mathcal{T}}^{+}_{n-1}(W) \;=\; 2\lambda \mathcal{N}^{+}_{n-1}(W) \;=\; 2\lambda\, N(c_{n-1/2}, c_{n-3/2})$$

$$\text{(D.6)} \qquad \hat{\mathcal{T}}^{-}_{n+1}(W) \;=\; 2\lambda \mathcal{N}^{-}_{n+1}(W) \;=\; 2\lambda\, N(c_{n+1/2}, c_{n+3/2})$$

The master equation (D.2) becomes:

$$\begin{aligned}\text{(D.7)} \qquad \frac{1}{2\lambda}\frac{\partial p_n}{\partial t} &= N(c_{n-1/2}, c_{n-3/2})\, p_{n-1} + N(c_{n+1/2}, c_{n+3/2})\, p_{n+1} \\ &\quad - \big(N(c_{n+1/2}, c_{n-1/2}) + N(c_{n-1/2}, c_{n+1/2})\big)\; p_n \\ &= N(c_{n-1/2}, c_{n-3/2})\, p_{n-1} + N(c_{n+1/2}, c_{n+3/2})\, p_{n+1} - p_n\end{aligned}$$

Consider a grid of mesh size h, and let $x = nh$. Then,

$$\begin{aligned}\text{(D.8)}\quad N(c_{n-1/2}, c_{n-3/2}) &= N\left(c(x-h/2), c(x-3h/2)\right) \\ &= N\left(c - \frac{h}{2}\left(c_x - \frac{h}{4}c_{xx}\right), c - \frac{3h}{2}\left(c_x - \frac{3h}{4}c_{xx}\right)\right) \\ &= N - \frac{h}{2}\left(c_x - \frac{h}{4}c_{xx}\right) N_1 - \frac{3h}{2}\left(c_x - \frac{3h}{4}c_{xx}\right) N_2 \\ &\quad + \frac{1}{2}\left[\frac{h^2}{4}\, c_x^2\, N_{11} + \frac{9h^2}{4}\, c_x^2\, N_{22} + \frac{6h^2}{4}\, c_x^2\, N_{12}\right] + \cdots \\ &= N - \frac{h}{2}\,(N_1 + 3N_2)\, c_x + \frac{h^2}{8}\,(N_1 + 9N_2)\, c_{xx} \\ &\quad + \frac{h^2}{8}\,(N_{11} + 9N_{22} + 6N_{12})\, c_x^2 + \cdots\end{aligned}$$

Here, $c(.) \equiv c(x)$, $N(.,.) \equiv N(u,v)$, $N_k \equiv \partial_k N(.,.)$, where ∂_k denotes a derivative with respect to the kth argument, evaluated at $(c(x), c(x))$. As noted earlier, $N(u,v) + N(v,u) = 1$, so that $N_1(u,v) + N_2(u,v) = 0$ and $N_{12}(u,v) = 0$. Equation (D.8) then becomes

$$N(c_{n-1/2}, c_{n-3/2}) = N - h\,N_2\,c_x + h^2\,N_2\,c_{xx} + h^2\,N_{22}\,c_x^2 \tag{D.9}$$

Likewise,

$$N(c_{n+1/2}, c_{n+3/2}) = N + h\,N_2\,c_x + h^2\,N_2\,c_{xx} + h^2\,N_{22}\,c_x^2 \tag{D.10}$$

Next, we expand p_{n-1} and p_{n+1} in a Taylor series about $x = nh$ to second order, as well, and substitute these in equation (D.7). The various terms on the right hand side are

$$\begin{aligned}
\text{Constant term} &= 0 \\
\text{Coefficient of } h &= 0 \\
\text{Coefficient of } h^2 &= \frac{1}{2}\,p + 2\,N_2\,c_x\,p_x + 2\,(N_2\,c_{xx} + N_{22}\,c_x^2)\,p \\
&= \frac{1}{2}\,p - (N_1 - N_2)\,c_x\,p_x - (N_1 - N_2)\,c_{xx}\,p - (N_{11} - N_{22})\,c_x^2\,p
\end{aligned}$$

Equation (D.7) translates to

$$\begin{aligned}
\frac{\partial p}{\partial t} &= h^2\,\lambda\,p_{xx} - 2\,h^2\,\lambda\,\left(p\,(N_1 - N_2)\,c_x\right)_x \\
&\rightarrow D_p\,p_{xx} - 2\,D_p\,\left(p\,(N_1 - N_2)\,c_x\right)_x
\end{aligned} \tag{D.11}$$

where $D_p = \lim_{h\to 0\lambda\to\infty} h^2\,\lambda$ is the diffusion coefficient of endothelial cells. Note also that since $N(c(x), c(y)) = \tau(c(x))/(\tau(c(x)) + \tau(c(y)))$, by definition, $N_1(c(x), c(x)) = (\ln\tau(c(x)))'/4$, and $N_2(c(x), c(x)) = -(\ln\tau(c(x)))'/4$. We then arrive at the classical diffusion-advection equation

$$\frac{\partial p}{\partial t} = D_p\, p_{xx} - D_p\, \frac{\partial}{\partial_x}\left(p\, \frac{\partial}{\partial_x}\, \ln \tau(c)\right) \tag{D.12}$$

This computation can be easily repeated in two dimensions, where the continuous equation for motion of an endothelial cell becomes

$$\frac{\partial p}{\partial t} = D_p\, \Delta\, p - D_p\, \nabla \cdot (p\, (\ln \tau(c))'\, \nabla c) \tag{D.13}$$

The chemotactic sensitivity function is

$$\chi(c) = D_p\, (\ln \tau(c))' \tag{D.14}$$

D.2 Choice of Transition Probability Function

The function $\tau(.)$, from equation (8.3) determines the transition probability functions $\hat{\mathcal{T}}$ in equation (8.1). Its choice will also determine the form of the chemotactic sensitivity $\chi(.)$, through the relationship given in equation (D.14). In equation (8.6), a choice was made for this sensitivity. We now derive the corresponding form of τ, as follows. By (D.14),

$$\begin{aligned} D_p\, (\ln \tau(a))' &= \chi(a) \\ &= \chi_0\, a\, e^{-a/B} \\ \Rightarrow \qquad \ln \tau(a) &= \frac{\chi_0}{D_p}\left[-B\, u\, e^{-u/B}\Big|_0^a + B \int_0^a e^{-u/B} du\right] \\ &= \frac{\chi_0\, B}{D_p}\left[B - (B+a)\, e^{-a/B}\right] \end{aligned} \tag{D.15}$$

Here, a is the amount in pg, of VEGF in activated receptor complexes, per cell face.

BIBLIOGRAPHY

BIBLIOGRAPHY

[1] Absher M, Ryan US. Comparison of pulmonary endothelial cell and fibroblast proliferation using time-lapse cinematographic analysis. Tissue Cell. 1981;13(4):645-50.

[2] Adams JM, Cory S. The Bcl-2 apoptotic switch in cancer development and therapy. Oncogene 2007;26(9):1324-37.

[3] Adams JM. Ways of dying: multiple pathways to apoptosis. Genes Dev 2003;17:248195.

[4] Anderson AR, Chaplain MA. A Mathematical Model for Capillary Network Formation in the Absence of Endothelial Cell Proliferation. Appl Math Lett. 1998 May;11(3)109-14.

[5] Anderson AR, Chaplain MA. Continuous and discrete mathematical models of tumor-induced angiogenesis. Bull Math Biol. 1998 Sep;60(5):857-99.

[6] Ando T, Jordan P, Joh T, Wang Y, Jennings MH, Houghton J, Alexander JS. Isolation and characterization of a novel mouse lymphatic endothelial cell line: SV-LEC. Lymphat Res Biol. 2005;3(3):105-15.

[7] Anto RJ, Mukhopadhyay A, Denning K, Aggarwal BB. Curcumin (diferuloylmethane) induces apoptosis through activation of caspase-8, BID cleavage and cytochrome c release: its suppression by ectopic expression of Bcl-2 and Bcl-xl. Carcinogenesis. 2002 Jan;23(1):143-50.

[8] Auguste P, Lemiere S, Larrieu-Lahargue F, Bikfalvi A. Molecular mechanisms of tumor vascularization. Crit Rev Oncol Hematol. 2005 Apr;54(1):53-61.

[9] Ausprunk DH, Folkman J. Migration and proliferation of endothelial cells in preformed and newly formed blood vessels during tumor angiogenesis. Microvasc. Res. 1977 14(1) :53-65.

[10] Bach F, Uddin FJ, Burke D. Angiopoietins in malignancy. Eur J Surg Oncol. 2007 Feb;33(1):7-15.

[11] Balding D, McElwain DL. A mathematical model of tumour-induced capillary growth. J Theor Biol. 1985 May 7;114(1):53-73.

[12] Bauer AL, Jackson TL, Jiang Y. A cell-based model exhibiting branching and anastomosis during tumor-induced angiogenesis. Biophys J. 2007 May 1;92(9):3105-21.

[13] Baxter LT, Jain RK. Transport of fluid and macromolecules in tumors. III. Role of binding and metabolism. Microvasc Res. 1991 Jan;41(1):5-23.

[14] Boise LH, Gonzalez-Garcia M, Postema CE, et al. Bcl-x, a bcl-2-related gene that functions as a dominant regulator of apoptotic cell death. Cell 199327;74(4):597-608.

[15] Brat DJ, Bellail AC, Van Meir EG. The role of interleukin-8 and its receptors in gliomagenesis and tumoral angiogenesis. Neuro Oncol. 2005 Apr;7(2):122-33.

[16] Breier G. Endothelial receptor tyrosine kinases involved in blood vessel development and tumor angiogenesis. Adv Exp Med Biol. 2000;476:57-66.

[17] Brown LF, Detmar M, Claffey K, Nagy JA, Feng D, Dvorak AM, Dvorak HF. Vascular permeability factor/vascular endothelial growth factor: a multifunctional angiogenic cytokine. EXS. 1997;79:233-69.

[18] Byrne HM, Chaplain MA. Mathematical models for tumour angiogenesis: numerical simulations and nonlinear wave solutions. Bull Math Biol. 1995 May;57(3):461-86.

[19] Carmeliet P, Jain RK. Angiogenesis in cancer and other diseases. Nature. 2000 Sep 14;407(6801):249-57.

[20] Carmeliet P. VEGF as a key mediator of angiogenesis in cancer. Oncology. 2005;69 Suppl 3:4-10.

[21] Cao Y. Antiangiogenic cancer therapy. Semin Cancer Biol. 2004 Apr;14(2):139-45.

[22] Cao Y. Tumor angiogenesis and therapy. Biomed Pharmacother. 2005 Oct;59 Suppl 2:S340-3.

[23] Chaplain MA, Stuart AM. A model mechanism for the chemotactic response of endothelial cells to tumour angiogenesis factor. IMA J Math Appl Med Biol. 1993;10(3):149-68.

[24] Chaplain MA, Giles SM, Sleeman BD, Jarvis RJ. A mathematical analysis of a model for tumour angiogenesis. J Math Biol. 1995;33(7):744-70.

[25] Chaplain MA, Anderson AR. Mathematical modelling, simulation and prediction of tumour-induced angiogenesis. Invasion Metastasis. 1996 16(4-5):222-34.

[26] Chavakis E, Dimmeler S. Regulation of endothelial cell survival and apoptosis during angiogenesis. Arterioscler Thromb Vasc Biol. 2002 Jun 1;22(6):887-93.

[27] Daugulis P, Arakelyan L, Ginosar Y, Agur Z. Hopf point analysis for angiogenesis models. Discret Contin Dyn S - Series B. 2004 4(1):29-38.

[28] Davis B. Reinforced random walks. Prob Thy Rel Fields. 1990 20329.

[29] Deakin AS. Model for initial vascular patterns in melanoma transplants. Growth. 1976 Jun;40(2):191-201.

[30] Digtyar AV, Pozdnyakova NV, Feldman NB, Lutsenko SV, Severin SE. Endostatin: current concepts about its biological role and mechanisms of action. Biochemistry (Mosc). 2007 Mar;72(3):235-46.

[31] Doll JA, Soff GA. Angiostatin. Cancer Treat Res. 2005;126:175-204.

[32] Dong Z, Zeitlin BD, Song W, Sun Q, Karl E, Spencer DM, Jain HV, Jackson T, Nez G, Nör JE. Level of endothelial cell apoptosis required for a significant decrease in microvessel density. Exp Cell Res. 2007 Oct 1;313(16):3645-57.

[33] Favier B, Alam A, Barron P, Bonnin J, Laboudie P, Fons P, Mandron M, Herault JP, Neufeld G, Savi P, Herbert JM, Bono F. Neuropilin-2 interacts with VEGFR-2 and VEGFR-3 and promotes human endothelial cell survival and migration. Blood. 2006 Aug 15;108(4):1243-50.

[34] Fernandez EJ, Lolis E. Structure, function, and inhibition of chemokines. Annu Rev Pharmacol Toxicol. 2002;42:469-99.

[35] Ferrara N. Molecular and biological properties of vascular endothelial growth factor. J Mol Med. 1999 77(7):527-43.

[36] Ferrara N. VEGF and the quest for tumour angiogenesis factors. Nat Rev Cancer. 2002 2:795803.

[37] Ferrara N, Gerber HP, LeCouter J. The biology of VEGF and its receptors. Nat Med. 2003 Jun;9(6):669-76.

[38] Ferrara N, Hillan KJ, Novotny W. Bevacizumab (Avastin), a humanized anti-VEGF monoclonal antibody for cancer therapy. Biochem Biophys Res Commun. 2005 Jul 29;333(2):328-35.

[39] Fischer U, Schulze-Osthoff K. New approaches and therapeutics targeting apoptosis in disease. Pharmacol Rev. 2005 Jun;57(2):187-215.

[40] Folkman J. Tumor angiogenesis: therapeutic implications. N Engl J Med. 1971 Nov 18;285(21):1182-6.

[41] Folkman J. Angiogenesis and apoptosis. Semin Cancer Biol. 2003 Apr;13(2):159-67.

[42] Ford RM, Lauffenburger DA. Analysis of chemotactic bacterial distributions in population migration assays using a mathematical model applicable to steep or shallow attractant gradients. Bull Math Biol. 1991 53(5) :721-49.

[43] Franz CM, Jones GE, Ridley AJ. Cell migration in development and disease. Dev Cell. 2002 Feb;2(2):153-8.

[44] Gammack D, Byrne HM, Lewis CE. Estimating the selective advantage of mutant p53 tumour cells to repeated rounds of hypoxia. Bull Math Biol. 2001 Jan;63(1):135-66.

[45] Garber K. Angiogenesis inhibitors suffer new setback. Nat Biotechnol. 2002 Nov;20(11):1067-8.

[46] Gerber HP, McMurtrey A, Kowalski J, Yan M, Keyt BA, Dixit V, Ferrara N. Vascular endothelial growth factor regulates endothelial cell survival through the phosphatidylinositol 3'-kinase/Akt signal transduction pathway. Requirement for Flk-1/KDR activation. J Biol Chem. 1998 Nov 13;273(46):30336-43.

[47] Gerhardt H, Golding M, Fruttiger M, Ruhrberg C, Lundkvist A, Abramsson A, Jeltsch M, Mitchell C, Alitalo K, Shima D, Betsholtz C. VEGF guides angiogenic sprouting utilizing endothelial tip cell filopodia. J Cell Biol. 2003 Jun 23;161(6):1163-77.

[48] Guglielmi N, Hairer E. Implementing Radau IIA methods for stiff delay differential equations. Computing. 2001 67(1):1-12.

[49] Hanahan D, Weinberg RA. The hallmarks of cancer. Cell. 2000 Jan 7;100(1):57-70.

[50] Hangai M, Kitaya N, Xu J, Chan CK, Kim JJ, Werb Z, Ryan SJ, Brooks PC. Matrix metalloproteinase-9-dependent exposure of a cryptic migratory control site in collagen is required before retinal angiogenesis. Am J Pathol. 2002 Oct;161(4):1429-37.

[51] Heroult M, Schaffner F, Augustin HG. Eph receptor and ephrin ligand-mediated interactions during angiogenesis and tumor progression. Exp Cell Res. 2006 Mar 10;312(5):642-50.

[52] Hicklin DJ, Ellis LM. Role of the vascular endothelial growth factor pathway in tumor growth and angiogenesis. J Clin Oncol. 2005 23(5):1011-27.

[53] Holmes MJ, Sleeman BD. A mathematical model of tumour angiogenesis incorporating cellular traction and viscoelastic effects. J Theor Biol. 2000 Jan 21;202(2):95-112.

[54] Holmes WE, Lee J, Kuang WJ, Rice GC, Wood WI. Structure and functional expression of a human interleukin-8 receptor. Science. 1991 Sep 13;253(5025):1278-80.

[55] Horuk R. The interleukin-8-receptor family: from chemokines to malaria. Immunol Today. 1994 Apr;15(4):169-74.

[56] Huynh N, Mallik B, Zhang L, Martins-Green M, Morikis D. Computational studies of CXCR1, the receptor of IL-8/CXCL8, using molecular dynamics and electrostatics. Biopolymers. 2008 Jan;89(1):52-61.

[57] Jackson TL, Ashkenazi R, Heusel S, Jain HV. Cancer modeling: A perspective on what's new and what's next. Contemp Math. 2006 410:153-72

[58] Kamba T, McDonald DM. Mechanisms of adverse effects of anti-VEGF therapy for cancer. Br J Cancer. 2007 Jun 18;96(12):1788-95.

[59] Karl E, Warner K, Zeitlin B, Kaneko T, Wurtzel L, Jin T, Chang J, Wang S, Wang CY, Strieter RM, Nunez G, Polverini PJ, Nör JE. Bcl-2 acts in a proangiogenic signaling pathway through nuclear factor-kappaB and CXC chemokines. Cancer Res. 2005 65(12):5063-69.

[60] Ke LD, Shi YX, Im SA, Chen X, Yung WK. The relevance of cell proliferation, vascular endothelial growth factor, and basic fibroblast growth factor production to angiogenesis and tumorigenicity in human glioma cell lines. Clin. Cancer Res. 2000 6(6) :2562-72.

[61] Keller EF, Segel LA. Models for chemotaxis. J Theor Biol. 1971 30 :225-34.

[62] Keller EF, Segel LA. Traveling bands of chemotactic bacteria: a theoretical analysis. J. Theor. Biol. 1971 30 :235-48.

[63] Kerbel RS. Tumor angiogenesis: past, present and the near future. Carcinogenesis. 2000 Mar;21(3):505-15.

[64] Kerr JF, Wyllie AH, Currie AR. Apoptosis: a basic biological phenomenon with wide-ranging implications in tissue kinetics. Br J Cancer. 1972 Aug;26(4):239-57.

[65] Kim KJ, Li B, Winer J, Armanini M, Gillett N, Phillips HS, Ferrara N. Inhibition of vascular endothelial growth factor-induced angiogenesis suppresses tumour growth in vivo. Nature. 1993 Apr 29;362(6423):841-4.

[66] Klement G, Huang P, Mayer B, Green SK, Man S, Bohlen P, Hicklin D, Kerbel RS. Differences in therapeutic indexes of combination metronomic chemotherapy and an anti-VEGFR-2 antibody in multidrug-resistant human breast cancer xenografts. Clin Cancer Res. 2002 Jan;8(1):221-32.

[67] Koch AE, Polverini PJ, Kunkel SL, Harlow LA, DiPietro LA, Elner VM, Elner SG, Strieter RM. Interleukin-8 as a macrophage-derived mediator of angiogenesis. Science. 1992 258(5089):1798-1801.

[68] Kuang Y, Nagy JD, Elser JJ. Biological stoichiometry of tumor dynamics. Discret Contin Dyn S - Series B. 2004 4(1):221-40.

[69] Kuppuswamy D, Pike LJ. Ligand-induced desensitization of 125I-epidermal growth factor internalization. J Biol Chem. 1989 Feb 25;264(6):3357-63.

[70] Kurt RA, Baher A, Wisner KP, Tackitt S, Urba WJ. Chemokine receptor desensitization in tumor-bearing mice. Cell Immunol. 2001 Feb 1;207(2):81-8.

[71] Lapidus IR, Schiller R. A model for the chemotactic response of a bacterial population. Biophys. J. 1976 16 :779-89.

[72] Lee S, Jilani SM, Nikolova GV, Carpizo D, Iruela-Arispe ML. Processing of VEGF-A by matrix metalloproteinases regulates bioavailability and vascular patterning in tumors. J Cell Biol. 2005 May 23;169(4):681-91.

[73] Levine HA, Sleeman BD, Nilsen-Hamilton M. A mathematical model for the roles of pericytes and macrophages in the initiation of angiogenesis. I. The role of protease inhibitors in preventing angiogenesis. Math Biosci. 2000 Nov;168(1):77-115.

[74] Levine HA, Pamuk S, Sleeman BD, Nilsen-Hamilton M. Mathematical modeling of capillary formation and development in tumor angiogenesis: penetration into the stroma. Bull Math Biol. 2001 Sep;63(5):801-63.

[75] Levine HA, Tucker AL, Nilsen-Hamilton M. A mathematical model for the role of cell signal transduction in the initiation and inhibition of angiogenesis. Growth Factors. 2002 Dec;20(4):155-75.

[76] Levine H, Kessler DA, Rappel WJ. Directional sensing in eukaryotic chemotaxis: a balanced inactivation model. Proc Natl Acad Sci U S A. 2006 Jun 27;103(26):9761-6.

[77] Liu Y, McCarthy J, Ladisch S. Membrane ganglioside enrichment lowers the threshold for vascular endothelial cell angiogenic signaling. Cancer Res. 2006 Nov 1;66(21):10408-14.

[78] Mac Gabhann F, Popel AS. Model of competitive binding of vascular endothelial growth factor and placental growth factor to VEGF receptors on endothelial cells. Am J Physiol Heart Circ Physiol. 2004 Jan;286(1):H153-64.

[79] Mac Gabhann F, Popel AS. Differential binding of VEGF isoforms to VEGF receptor 2 in the presence of neuropilin-1: a computational model. Am J Physiol Heart Circ Physiol. 2005 Jun;288(6):H2851-60.

[80] Mac Gabhann F, Yang MT, Popel AS. Monte Carlo simulations of VEGF binding to cell surface receptors in vitro. Biochim Biophys Acta. 2005 Dec 15;1746(2):95-107.

[81] Mac Gabhann F, Popel AS. Dimerization of VEGF receptors and implications for signal transduction: a computational study. Biophys Chem. 2007 Jul;128(2-3):125-39.

[82] Mac Gabhann F, Popel AS. Dimerization of VEGF receptors and implications for signal transduction: a computational study. Biophys Chem. 2007 Jul;128(2-3):125-39.

[83] Maher JJ. Rat hepatocytes and Kupffer cells interact to produce interleukin-8 (CINC) in the setting of ethanol. Am J Physiol. 1995 Oct;269(4 Pt 1):G518-23.

[84] Mantzaris NV, Webb S, Othmer HG. Mathematical modeling of tumor-induced angiogenesis. J Math Biol. 2004 49:111-87

[85] McMahon G. VEGF Receptor Signalling in Tumor Angiogenesis. Oncologist. 2000 5:3-10.

[86] McTigue MA, Wickersham JA, Pinko C, Showalter RE, Parast CV, Tempczyk-Russell A, Gehring MR, Mroczkowski B, Kan CC, Villafranca JE, Appelt K. Crystal structure of the kinase domain of human vascular endothelial growth factor receptor 2: a key enzyme in angiogenesis. Structure. 1999 Mar 15;7(3):319-30.

[87] Mignatti P, Rifkin DB. Biology and biochemistry of proteinases in tumor invasion. Physiol Rev. 1993 Jan;73(1):161-95.

[88] Minshall C, Arkins S, Dantzer R, Freund GG, Kelley KW. Phosphatidylinositol 3'-kinase, but not S6-kinase, is required for insulin-like growth factor-I and IL-4 to maintain expression of Bcl-2 and promote survival of myeloid progenitors. J Immunol 1999;162(8):4542-9.

[89] Mukaida N. Pathophysiological roles of interleukin-8/CXCL8 in pulmonary diseases. Am J Physiol Lung Cell Mol Physiol. 2003 284(4):L566-77.

[90] Muller YA, Christinger HW, Keyt BA, de Vos AM. The crystal structure of vascular endothelial growth factor (VEGF) refined to 1.93 A resolution: multiple copy flexibility and receptor binding. Structure. 1997 Oct 15;5(10):1325-38.

[91] Muller YA, Li B, Christinger HW, Wells JA, Cunningham BC, de Vos AM. Vascular endothelial growth factor: crystal structure and functional mapping of the kinase domain receptor binding site. Proc Natl Acad Sci U S A. 1997 Jul 8;94(14):7192-7.

[92] Murry JD. Mathematical Biology II: Spatial models and biomedical applications. 3rd ed. Berlin: Springer-Verlag.

[93] Muthukkaruppan VR, Kubai L, Auerbach R. Tumor-induced neovascularization in the mouse eye. J Natl Cancer Inst. 1982 Sep;69(3):699-708.

[94] Nagy JD. Competition and natural selection in a mathematical model of cancer. Bull Math Biol. 2004 66(4):663-87.

[95] Neagoe PE, Lemieux C, Sirois MG Vascular endothelial growth factor (VEGF)-A165-induced prostacyclin synthesis requires the activation of VEGF receptor-1 and -2 heterodimer. J Biol Chem. 2005 Mar 18;280(11):9904-12.

[96] Neufeld G, Cohen T, Gengrinovitch S, Poltorak Z. Vascular endothelial growth factor (VEGF) and its receptors. FASEB J. 1999 Jan;13(1):9-22.

[97] Nör JE, Christensen J, Mooney DJ, Polverini PJ. Vascular endothelial growth factor (VEGF)-mediated angiogenesis is associated with enhanced endothelial cell survival and induction of Bcl-2 expression. Am J Pathol. 1999 Feb;154(2):375-84.

[98] Nör JE, Christensen J, Liu J, Peters M, Mooney DJ, Strieter RM, Polverini PJ. Up-Regulation of Bcl-2 in microvascular endothelial cells enhances intratumoral angiogenesis and accelerates tumor growth. Cancer Res. 2001 Mar 1;61(5):2183-8.

[99] Nör JE, Peters MC, Christensen JB, Sutorik MM, Linn S, Khan MK, Addison CL, Mooney DJ, Polverini PJ. Engineering and characterization of functional human microvessels in immunodeficient mice. Lab. Invest. 2001 81(4):453-463.

[100] Norrby K. Microvascular density in terms of number and length of microvessel segments per unit tissue volume in mammalian angiogenesis. Microvasc Res. 1998 Jan;55(1):43-53.

[101] Nunez G, Clarke MF. The Bcl-2 family of proteins: regulators of cell death and survival. Trends Cell Biol 1994;4(11):399-403.

[102] Olsson AK, Dimberg A, Kreuger J, Claesson-Welsh L. VEGF receptor signallingin control of vascular function. Nat Rev Mol Cell Biol. 2006 7:359371.

[103] Orme ME, Chaplain MA. Two-dimensional models of tumour angiogenesis and anti-angiogenesis strategies. IMA J Math Appl Med Biol. 1997 Sep;14(3):189-205.

[104] Ostendorf T, De Vriese AS, Floege J. Renal side effects of anti-VEGF therapy in man: a new test system. Nephrol Dial Transplant. 2007 Oct;22(10):2778-80.

[105] Othmer HG, Stevens A. Aggregation, blowup and collapse: The ABCs of generalized taxis in reinforced random walks. SIAM J Appled Math. 1997 57(4):1044 81.

[106] Otrock ZK, Makarem JA, Shamseddine AI. Vascular endothelial growth factor family of ligands and receptors: review. Blood Cells Mol Dis. 2007 May-Jun;38(3):258-68.

[107] Painter KJ, Maini PK, Othmer HG. Development and applications of a model for cellular response to multiple chemotactic cues. J Math Biol. 2000 Oct;41(4):285-314.

[108] Patan S. Vasculogenesis and angiogenesis as mechanisms of vascular network formation, growth and remodeling. J Neurooncol. 2000 50(1-2):1-15.

[109] Papetti M, Herman IM. Mechanisms of normal and tumor-derived angiogenesis. Am J Physiol Cell Physiol. 2002 May;282(5):C947-70.

[110] Paweletz N, Knierim M. Tumor-related angiogenesis. Crit Rev Oncol Hematol. 1989;9(3):197-242.

[111] Pepper MS, Ferrara N, Orci L, Montesano R. Potent synergism between vascular endothelial growth factor and basic fibroblast growth factor in the induction of angiogenesis in vitro. Biochem Biophys Res Commun. 1992 Dec 15;189(2):824-31.

[112] Pettet GJ, Byrne HM, McElwain DL, Norbury J. A model of wound-healing angiogenesis in soft tissue. Math Biosci. 1996 Aug;136(1):35-63.

[113] Pettet G, Chaplain MA, McElwain DL, Byrne HM. On the role of angiogenesis in wound healing. Proc Biol Sci. 1996 Nov 22;263(1376):1487-93.

[114] Petros AM, Medek A, Nettesheim DG, Kim DH, Yoon HS, Swift K, Matayoshi ED, Oltersdorf T, Fesik SW. Solution structure of the antiapoptotic protein bcl-2. Proc Natl Acad Sci U S A. 2001 Mar 13;98(6):3012-7.

[115] Petros AM, Nettesheim DG, Wang Y, Olejniczak ET, Meadows RP, Mack J, Swift K, Matayoshi ED, Zhang H, Thompson CB, Fesik SW. Rationale for Bcl-xL/Bad peptide complex formation from structure, mutagenesis, and biophysical studies. Protein Sci. 2000 Dec;9(12):2528-34.

[116] Plank MJ, Sleeman BD. A reinforced random walk model of tumour angiogenesis and anti-angiogenic strategies. Math Med Biol. 2003 Jun;20(2):135-81.

[117] Plank MJ, Sleeman BD, Jones PF. A mathematical model of an in vitro experiment to investigate endothelial cell migration. J. Theor. Med. 2003 (4):251-70.

[118] Plank MJ, Sleeman BD, Jones PF. A mathematical model of tumour angiogenesis, regulated by vascular endothelial growth factor and the angiopoietins. J Theor Biol. 2004 Aug 21;229(4):435-54

[119] Plank MJ, Sleeman BD. Lattice and non-lattice models of tumour angiogenesis. Bull Math Biol. 2004 Nov;66(6):1785-819.

[120] Prewett M, Huber J, Li Y, Santiago A, O'Connor W, King K, Overholser J, Hooper A, Pytowski B, Witte L, Bohlen P, Hicklin DJ. Antivascular endothelial growth factor receptor (fetal liver kinase 1) monoclonal antibody inhibits tumor angiogenesis and growth of several mouse and human tumors. Cancer Res. 1999 Oct 15;59(20):5209-18.

[121] Rajarathnam K, Clark-Lewis I, Sykes BD. 1H NMR solution structure of an active monomeric interleukin-8. Biochemistry. 1995 Oct 10;34(40):12983-90.

[122] Reed JC. Bcl-2 and the regulation of programmed cell death. J Cell Biol 1994;124(1-2):1-6.

[123] Reed JC. Bcl-2 family proteins. Oncogene 1998;17(25):3225-36.

[124] Roskoski R Jr. Vascular endothelial growth factor (VEGF) signaling in tumor progression. Crit Rev Oncol Hematol. 2007 Jun;62(3):179-213.

[125] Ruch C, Skiniotis G, Steinmetz MO, Walz T, Ballmer-Hofer K. Structure of a VEGF-VEGF receptor complex determined by electron microscopy. Nat Struct Mol Biol. 2007 Mar;14(3):249-50.

[126] Ruhrberg C, Gerhardt H, Golding M, Watson R, Ioannidou S, Fujisawa H, Betsholtz C, Shima DT. Spatially restricted patterning cues provided by heparin-binding VEGF-A control blood vessel branching morphogenesis. Genes Dev. 2002 Oct 15;16(20):2684-98.

[127] Samanta AK, Oppenheim JJ, Matsushima K. Identification and characterization of specific receptors for monocyte-derived neutrophil chemotactic factor (MDNCF) on human neutrophils. J Exp Med. 1989 Mar 1;169(3):1185-9.

[128] Sargiannidou I, Qiu C, Tuszynski GP. Mechanisms of thrombospondin-1-mediated metastasis and angiogenesis. Semin Thromb Hemost. 2004 Feb;30(1):127-36.

[129] Schendel SL, Montal M, Reed JC. Bcl-2 family proteins as ion-channels. Cell Death Differ 1998;5(5):372-80.

[130] Senger DR, Claffey KP, Benes JE, Perruzzi CA, Sergiou AP, Detmar M. Angiogenesis promoted by vascular endothelial growth factor: regulation through alpha1beta1 and alpha2beta1 integrins. Proc Natl Acad Sci U S A. 1997 Dec 9;94(25):13612-7.

[131] Segel LA, Slemrod M. The Quasi-Steady-State Assumption: A Case Study in Perturbation. SIAM Review. 1989 Sep;31(3):446-77

[132] Serini G, Ambrosi D, Giraudo E, Gamba A, Preziosi L, Bussolino F. Modeling the early stages of vascular network assembly. EMBO J. 2003 Apr 15;22(8):1771-9.

[133] Sherratt JA, Murray JD. Models of epidermal wound healing. Proc Biol Sci. 1990 Jul 23;241(1300):29-36.

[134] Sholley MM, Ferguson GP, Seibel HR, Montour JL, Wilson JD. Mechanisms of neovascularization. Vascular sprouting can occur without proliferation of endothelial cells. Lab Invest. 1984 Dec;51(6):624-34.

[135] Shweiki D, Neeman M, Itin A, Keshet E. Induction of vascular endothelial growth factor expression by hypoxia and by glucose deficiency in multicell spheroids: Implications for tumor angiogenesis. Proc Natl Acad Sci U S A. 1995 92(3) :768-72.

[136] Smith DR, Polverini PJ, Kunkel SL, Orringer MB, Whyte RI, Burdick MD, Wilke CA, Strieter RM. Inhibition of interleukin 8 attenuates angiogenesis in bronchogenic carcinoma. J Exp Med. 1994 May 1;179(5):1409-15.

[137] Sottile J. Regulation of angiogenesis by extracellular matrix. Biochim Biophys Acta. 2004 Mar 4;1654(1):13-22.

[138] Spyridopoulos I, Brogi E, Kearney M, Sullivan AB, Cetrulo C, Isner JM, Losordo DW. Vascular endothelial growth factor inhibits endothelial cell apoptosis induced by tumor necrosis factor-alpha: balance between growth and death signals. J Mol Cell Cardiol. 1997 May;29(5):1321-30.

[139] Stewart M, Turley H, Cook N, Pezzella F, Pillai G, Ogilvie D, Cartlidge S, Paterson D, Copley C, Kendrew J, Barnes C, Harris AL, Gatter KC. The angiogenic receptor KDR is widely distributed in human tissues and tumours and relocates intracellularly on phosphorylation. An immunohistochemical study. Histopathology. 2003 Jul;43(1):33-9.

[140] Stokes CL, Lauffenburger DA. Analysis of the roles of microvessel endothelial cell random motility and chemotaxis in angiogenesis. J Theor Biol. 1991 Oct 7;152(3):377-403.

[141] Strieter RM, Kunkel SL, Elner VM, Martonyi CL, Koch AE, Polverini PJ, Elner SG. Interleukin-8. A corneal factor that induces neovascularization. Am J Pathol. 1992 Dec;141(6):1279-84.

[142] Sun S, Wheeler MF, Obeyesekere M, Patrick CW Jr. A deterministic model of growth factor-induced angiogenesis. Bull Math Biol. 2005 Mar;67(2):313-37.

[143] Stupack DG. The biology of integrins. Oncology (Williston Park). 2007 Aug;21(9 Suppl 3):6-12.

[144] Takahashi H, Shibuya M. The vascular endothelial growth factor (VEGF)/VEGF receptor system and its role under physiological and pathological conditions. Clin Sci (Lond). 2005 Sep;109(3):227-41.

[145] Tee D, DiStefano J 3rd. Simulation of tumor-induced angiogenesis and its response to anti-angiogenic drug treatment: mode of drug delivery and clearance rate dependencies. J Cancer Res Clin Oncol. 2004 Jan;130(1):15-24.

[146] Thelen M. Dancing to the tune of chemokines. Nat Immunol. 2001 Feb;2(2):129-34.

[147] Trettel F, Di Bartolomeo S, Lauro C, Catalano M, Ciotti MT, Limatola C. Ligand-independent CXCR2 dimerization. J Biol Chem. 2003 Oct 17;278(42):40980-8.

[148] Vadapalli A,Pittman RN, Popel AS. Estimating oxygen transport resistance of the microvascular wall. Am J Physiol Heart Circ Physiol. 2000 279:65771.

[149] Vestweber D. VE-cadherin: the major endothelial adhesion molecule controlling cellular junctions and blood vessel formation. Arterioscler Thromb Vasc Biol. 2008 Feb;28(2):223-32.

[150] Wang D, Anderson JC, Gladson CL. The role of the extracellular matrix in angiogenesis in malignant glioma tumors. Brain Pathol. 2005 Oct;15(4):318-26.

[151] Wang D, Donner DB, Warren RS. Homeostatic modulation of cell surface KDR and Flt1 expression and expression of the vascular endothelial cell growth factor (VEGF) receptor mRNAs by VEGF. J Biol Chem. 2000 May 26;275(21):15905-11.

[152] Wang D, Lehman RE, Donner DB, Matli MR, Warren RS, Welton ML. Expression and endocytosis of VEGF and its receptors in human colonic vascular endothelial cells. Am J Physiol Gastrointest Liver Physiol. 2002 Jun;282(6):G1088-96.

[153] Wang SJ, Saadi W, Lin F, Minh-Canh Nguyen C, Li Jeon N. Differential effects of EGF gradient profiles on MDA-MB-231 breast cancer cell chemotaxis. Exp Cell Res. 2004 Oct 15;300(1):180-9.

[154] Wang S, Yang D, Lippman ME. Targeting Bcl-2 and Bcl-X_L with nonpeptidic small-molecule antagonists. Semin Oncol 2003;30(5 Suppl 16):133-42.

[155] Ward JP, King JR. Mathematical modelling of avascular-tumour growth. II: Modelling growth saturation. IMA J Math Appl Med Biol. 1999 16(2):171-211.

[156] Wiesmann C, Fuh G, Christinger HW, Eigenbrot C, Wells JA, de Vos AM. Crystal structure at 1.7 A resolution of VEGF in complex with domain 2 of the Flt-1 receptor. Cell. 1997 Nov 28;91(5):695-704.

[157] Wilson S, Wilkinson G, Milligan G. The CXCR1 and CXCR2 receptors form constitutive homo- and heterodimers selectively and with equal apparent affinities. J Biol Chem. 2005 280(31):28663-74.

[158] http://www.genecards.org/index.shtml

[159] Yamazaki Y, Morita T. Molecular and functional diversity of vascular endothelial growth factors. Mol Divers. 2006 Nov;10(4):515-27.

[160] Zeitlin BD, Joo E, Dong Z, et al. Antiangiogenic Effect of TW37, a Small-Molecule Inhibitor of Bcl-2. Cancer Res 2006;66(17):8698-706.

[161] Zimmermann KC, Green DR. How cells die: apoptosis pathways. J Allergy Clin Immunol. 2001 Oct;108(4 Suppl):S99-103.

[162] Zogakis TG, Libutti SK. General aspects of anti-angiogenesis and cancer therapy. Expert Opin Biol Ther. 2001 Mar;1(2):253-75.